Technische Universität Dresden

Remote Assessment of the Cardiovascular Function Using Camera-Based Photoplethysmography

Dipl.-Ing.
Alexander Trumpp

der Fakultät für Elektrotechnik und Informationstechnik der Technischen Universität Dresden

zur Erlangung des akademischen Grades

Doktoringenieur
(Dr.-Ing.)

genehmigte Dissertation

Vorsitzender: Jun.-Prof. Dr.-Ing. Peter Birkholz
Gutachter: Prof. Dr.-Ing. habil. Hagen Malberg
Gutachter: Prof. Dr. Dr. h.c. Robert Riener

Tag der Einreichung: 28.03.2019
Tag der Verteidigung: 12.11.2019

I dedicate this thesis to my wife Sara.

ABSTRACT

Camera-based photoplethysmography (cbPPG) is a novel measurement technique that allows the continuous monitoring of vital signs by using common video cameras. In the last decade, the technology has attracted a lot of attention as it is easy to set up, operates remotely, and offers new diagnostic opportunities. Despite the growing interest, cbPPG is not completely established yet and is still primarily the object of research. There are a variety of reasons for this lack of development including that reliable and autonomous hardware setups are missing, that robust processing algorithms are needed, that application fields are still limited, and that it is not completely understood which physiological factors impact the captured signal. In this thesis, these issues will be addressed.

A new and innovative measuring system for cbPPG was developed. In the course of three large studies conducted in clinical and non-clinical environments, the system's great flexibility, autonomy, user-friendliness, and integrability could be successfully proven.

Furthermore, it was investigated what value optical polarization filtration adds to cbPPG. The results show that a perpendicular filter setting can significantly enhance the signal quality. In addition, the performed analyses were used to draw conclusions about the origin of cbPPG signals: Blood volume changes are most likely the defining element for the signal's modulation.

Besides the hardware-related topics, the software topic was addressed. A new method for the selection of regions of interest (ROIs) in cbPPG videos was developed. Choosing valid ROIs is one of the most important steps in the processing chain of cbPPG software. The new method has the advantage of being fully automated, more independent, and universally applicable. Moreover, it suppresses ballistocardiographic artifacts by utilizing a level-set-based approach. The suitability of the ROI selection method was demonstrated on a large and challenging data set.

In the last part of the work, a potentially new application field for cbPPG was explored. It was investigated how cbPPG can be used to assess autonomic reactions of the nervous system at the cutaneous vasculature. The results show that changes in the vasomotor tone, i.e. vasodilation and vasoconstriction, reflect in the pulsation strength of cbPPG signals. These characteristics also shed more light on the origin problem. Similar to the polarization analyses, they support the classic blood volume theory.

In conclusion, this thesis tackles relevant issues regarding the application of cbPPG. The proposed solutions pave the way for cbPPG to become an established and widely accepted technology.

KURZFASSUNG

Die kamerabasierte Photoplethysmographie (engl. Abk.: cbPPG) ist ein neuartiges Messverfahren, welches die kontinuierliche Erfassung von Vitalparametern mittels herkömmlicher Kameras ermöglicht. In den letzten zehn Jahren hat das Verfahren viel Aufmerksamkeit auf sich gezogen, da es einfach zu konfigurieren ist, kontaktlos angebracht werden kann und neue diagnostische Möglichkeiten eröffnet. Trotz des wachsenden Interesses hat sich die cbPPG jedoch bisher nicht vollständig etabliert und ist hauptsächlich Gegenstand der Forschung geblieben. Gründe dafür sind fehlende zuverlässige und autonome Hardware-Systeme sowie robuste Verarbeitungsalgorithmen, begrenzte Anwendungsfelder und die unzureichend beantwortete Frage, welche physiologischen Faktoren auf das gemessene Signal einwirken. In der Arbeit werden diese Probleme im Einzelnen adressiert.

Es wurde ein neuer und innovativer Messstand für die cbPPG konzipiert, aufgebaut und getestet. Durch drei große Studien aus dem klinischen und nicht-klinischen Umfeld konnte die sehr gute Flexibilität, Autonomie, Bedienerfreundlichkeit und Integrierbarkeit des Systems bestätigt werden.

Weiterhin wurde untersucht, ob der Einsatz von optischen Polarisationsfiltern einen Mehrwert für die Messtechnik leistet. Die Ergebnisse zeigen, dass eine orthogonale Filtereinstellung die Signalqualität signifikant verbessern kann. Die durchgeführten Analysen wurden ebenfalls dazu verwendet, um Rückschlüsse auf die Signalherkunft zu ziehen. Dabei hat sich herausgestellt, dass Blutvolumenschwankungen mit hoher Wahrscheinlichkeit die definierende Größe bei der Signalmodulation sind.

Neben den hardwarespezifischen Themen geht die Arbeit ebenfalls auf die Software ein. Es wurde eine neue Methode für die Auswahl geeigneter Bildregionen (engl. Abk.: ROIs) in cbPPG-Videos entwickelt. Die ROI-Auswahl ist einer der wichtigsten Schritte in der Verarbeitungskette von cbPPG-Software. Die beschriebene Methode arbeitet komplett automatisch, ist kontextunabhängig und universell einsetzbar. Zudem unterdrückt sie ballistokardiografische Effekte durch das geschickte Einbinden eines Level-Set-basierten Ansatzes. Die Effizienz des entwickelten Algorithmus konnte erfolgreich an einem umfassenden und heterogenen Datensatz gezeigt werden.

Im letzten Teil der Arbeit wird ein potenziell neues Anwendungsfeld für die cbPPG beleuchtet. Es wurde untersucht, inwiefern sich autonome Reaktionen des Nervensystems mittels der Messtechnik an der Haut erfassen lassen. Die Auswertung zeigt, dass sich Änderungen des Gefäßtonus (Vasodilatation und -konstriktion) in der Pulsationsstärke des cbPPG-Signals widerspiegeln. Ebenfalls konnten Aussagen zur Signalherkunft getroffen

werden. Analog zu den filterbezogenen Analysen unterstützen die Ergebnisse das klassische Blutvolumenschwankungsmodell.

Insgesamt geht die Arbeit auf relevante Probleme ein, welche die cbPPG bisher in ihrer Anwendung bremsen. Die vorgeschlagenen Lösungen bereiten den Weg für die Technologie sich weiter zu etablieren.

ACKNOWLEDGMENTS

I would like to thank the *Sächsisches Staatsministerium für Wissenschaft und Kunst* and the *Bundesministerium für Bildung und Forschung* for providing most of the funding during my PhD program. The respective projects "Cardio Visio" (ref. 4-7531.60/29/12) and "fast care – Kamerabasiertes Monitoring" (ref. 03ZZ0519C) gave me the opportunity to cooperate with experts from different fields and conduct research that significantly contributed to the outcome of my work. I am especially grateful for the collaboration with Dr. Stefan Rasche whose medical knowledge helped me to better approach complex problems. I consider him not only a great colleague but also a good friend.

I would also like to thank my institute, particularly Prof. Hagen Malberg and Prof. Sebastian Zaunseder. In the course of my program, they took care of the necessary funding, supported me in the decision-making process, and supervised major parts of work. They ensured that I could focus on research, so that I did not had to deal with administrative tasks. Sebastian was always a huge help when it came to the discussion of results. His broad knowledge and skill to assess problems on a more abstract level still impress me until this day. Furthermore, my fellow PhD students Daniel, Fernando, Felix, Martin, Philipp, Jonas, Matthieu and Miriam must be acknowledged. I thank them for their professional assistance, friendship, and for consistently laughing at my bad jokes.

Last but not least, I would like to express gratitude to my family and friends. To my parents who raised me and did not send me to military school during puberty. To my brother whose advice guided me through rough times. To my grandparents whose wisdom I wish to have some day. Most of all, I thank my wife, and the love of my life, Sara. I am very grateful for her support, understanding, and patience. Her endless love fuels me every day. I highly appreciate her for always believing in me, giving me new perspectives on life, and accepting me as the nerd that I am. I also thank my daughter Lorelei who can make a bad day better by simply smiling at me.

CONTENTS

LIST OF FIGURES

LIST OF TABLES

ACRONYMS

AC	alternating current
ANS	autonomic nervous system
a.u.	arbitrary unit
BCG	ballistocardiographic, ballistocardiography
BP	blood pressure
bpm	beats per minute
cbPPG	camera-based photoplethysmography
cd	candela
CFT	cold face test
cm	centimeter
CMOS	complementary metal-oxide-semiconductor
CPT	cold pressor test
CVS	cardiovascular system
°C	degree Celsius
dB	decibel
DBP	diastolic blood pressure
DC	direct current
e.g.	exempli gratia (for example)
etc.	et cetera (and so forth)
fps	frames per second
GB	gigabyte
g/L	grams per liter (of blood)
HDR	heart rate's detection rate
HR	heart rate
Hz	Hertz (1 Hz = 1 s^{-1})
i.e.	id est (that is)
kg	kilogram
LED	light emitting diode

m	meter
MBP	mean blood pressure
min	minute
mm	millimeter
mmHg	millimeters of mercury (1 mmHg = 133 Pascal)
mmol/L	millimoles per liter
ms	millisecond
mW	milliwatt
mW/sr	milliwatt per steredian
µm	micrometer
n.a.	not applied
NIR	near-infrared
nm	nanometer
n/s	not specified
n.s.	not significant
p.	page
pp.	pages
PP	pulse pressure
PPG	photoplethysmography
PSNS	parasympathetic nervous system
PTT	pulse transit time
RGB	red, green, blue
RIH	region of interest - homogeneity
ROI	region of interest
s	second
SBP	systolic blood pressure
SNR	signal-to-noise ratio
SNS	sympathetic nervous system
TB	terabyte
vs.	versus
W	watt

SYMBOLS

C	compliance (in mL/mmHg)
C_s	segmentation contour in image plane
$\mathbf{c}$	color vector which holds a red, green and blue value
d_x	image search range in x-direction (in number of pixels)
d_y	image search range in y-direction (in number of pixels)
δ	penetration depth (in mm)
δ_ϵ	smooth Dirac delta function
e_{mse}	mean squared error (a.u.)
ϵ	tunable parameter for delta function (a.u.)
E	energy functional
E_x	x-component of the electric field
E_y	y-component of the electric field
f	frequency (usually in Hz or bpm)
f_{ref}	heart rate determined from a physiological reference signal (in bpm)
F	feature vector
H_{skin}	histogram for skin colors in the RGB color space
$H_{\neg skin}$	histogram for non-skin colors in the RGB color space
H	Heaviside function
i, j	running indices
I	single channel NIR or three-channel RGB image
I_N	NIR image (gray value)
I_R	red channel of RGB image
I_G	green channel of RGB image
I_B	blue channel of RGB image
J	texture image (single channel)
k	frame index for the RGB and NIR video stream
L	test statistic for Page test (a.u.)
M	number of channels in feature vector F
μ	mean value
μ_a	absorption coefficient (in cm^{-1})

μ_s	scattering coefficient (in cm^{-1})
μ_s'	reduced scattering coefficient (in cm^{-1})
n_{skin}	total number of counts in H_{skin}
$n_{\neg skin}$	total number of counts in $H_{\neg skin}$
n_{AC}	pulsation strength of a non-physiological noise signal (a.u.)
n_{cor}	number of signal segments for which the heart rate was correctly detected
n_{tot}	total number of time segments within a measurement
ν	smoothness factor (a.u.)
∇	nabla operator
Ω	image plane (area)
$\|\Omega\|$	image size (in number of pixels)
$\Omega_{1,2}$	subregions of image plane (area)
Ω_b	square image subregion
Ω_{ROI}	region of interest for an RGB or NIR image
Ω_{SKN}^{RGB}	skin region in RGB image detected by Bayesian classifier
Ω_{ROI}^{RGB}	final region of interest in RGB image
Ω_{REG}^{N}	registered region in NIR image from RGB image
Ω_{ROI}^{N}	final region of interest in NIR image
p	probability density function/ significance probability
P_{tm}	transmural pressure (in mmHg)
P_i	intravascular pressure (in mmHg)
P_e	extravascular pressure (in mmHg)
P_{pp}	pulse pressure (in mmHg)
Φ	level set function
Π	rectangular function
q_{RIH}	quality index assessing the homogeneity in the region of interest ($[0, 1]$)
q_{SNR}	quality index for the signal-to-noise ratio of cbPPG signals (in dB)
q_{HDR}	quality index quantifying the correct heart rate detection ($[0, 100]\,\%$)
ρ	Spearman's rank correlation coefficient
s_{AC}	strength of the plethysmogram's pulsation related to the cardiac cycle (a.u.)
s_{DC}	signal strength of the steady component (a.u.)
σ	standard deviation
σ_{ROI}	standard deviation of the pixel values inside the region of interest
t	time (usually in seconds)

t_0	initialization point in time (a.u.)
t_E	point in time where optimum is achieved (a.u.)
T	measure for vasomotor tone (a.u.)
θ	threshold for the Bayesian skin classifier (a.u.)
V	blood volume (in mL)
$\mathrm{W}_{1-6,1-3}$	evaluation windows for skin heating experiment & cold face test
$\mathrm{W}_{\mathrm{BL}1-2}$	evaluation windows for the cold pressor experiment (during baseline)
$\mathrm{W}_{\mathrm{T}1-2}$	evaluation windows for the cold pressor experiment (during stimulation)
x, y	spatial coordinates in image
$\mathbf{x}$	coordinate vector of image
X	Fourier transform (complex) of a time signal
'o'	symbol referring to the application of no polarization filters
'||'	symbol referring to a polarization filter setting with parallel orientation
'+'	symbol referring to a polarization filter setting with perpendicular orientation

1

INTRODUCTION

1.1 BACKGROUND AND MOTIVATION

Close to 10 % of Germans between the ages of 40 and 79 suffer from cardiovascular diseases [313]. The periodic screening of risk groups is crucial to prevent potential disabilities or even death [379]. However, the necessary means are not always accessible, especially for older people that have impaired mobility and live in remote areas [96]. In the case of blood pressure-related diseases, the affected persons are at least able to themselves check their current health state by using a cuff-based monitor. Those monitors, unfortunately, are not always reliable, are often applied wrong, and only offer a momentary measurement [266]. Furthermore, they restrict the individual flexibility. In the case of other and more dangerous cardiovascular diseases, monitoring is limited to the doctor's office or involves even more inconvenience, for example, when long-term measurements are required (e.g. Holter electrocardiography) [360]. Due to the mentioned problems, there is a general demand for novel technologies that enable easier and continuous screening, can be employed in everyday situations, and allow for flexible application without the need for intervention [80]. Such technologies could eventually prevent the critical progression of diseases as they would provide instant feedback on health hazards. In addition, new diagnostic opportunities could arise from the developments which, in turn, would positively impact the healthcare industry [80].

Camera-based photoplethysmography (cbPPG) is an innovative technology that has the potential of meeting all the desired criteria. The measuring technique enables the remote acquisition of cardiorespiratory signals by using conventional video cameras [202]. In the last decade, cbPPG has gained a lot of attention due to its simple setup and convenient applicability [393] (see Fig. 1). The technique's main advantages are that it does not require any skin contact, can be operated with ambient light, and permits a spatial assessment of the cutaneous perfusion [348]. Despite the growing interest, cbPPG is not completely established yet and is still primarily the object of research. In order to attach more value to the technology and make it applicable to everyday life, four major issues must be addressed. The first issue is the technical setup. Most studies in the field utilize commercial cameras and focus on the processing of the acquired video data [280]. However, possible hardware improvements are barely investigated. Furthermore, there are only a few works

that offer a complete and stand-alone measuring system. The second issue is the selection process for regions of interest (ROIs). Because of the unspecific camera alignment in cbPPG, proper areas, from which biosignals can be eventually extracted, have to be identified in the video images [317]. Available approaches for ROI selection generally lack applicability, robustness, and flexibility. The third issue concerns the application fields of cbPPG. The vast majority of research groups devote themselves to creating a reliable heart rate monitor [209]. Different physiological measures are less often considered. Moreover, the test environments are usually restricted to the laboratory, and the evaluated data sets are rather small and homogeneous [109]. The fourth and last issue is the signal origin. It is not entirely understood yet what bodily processes modulate the cbPPG signal to which extent [393]. Further insights are of high interest as they implicate the technique's benefit and facilitate the exploration of new application fields.

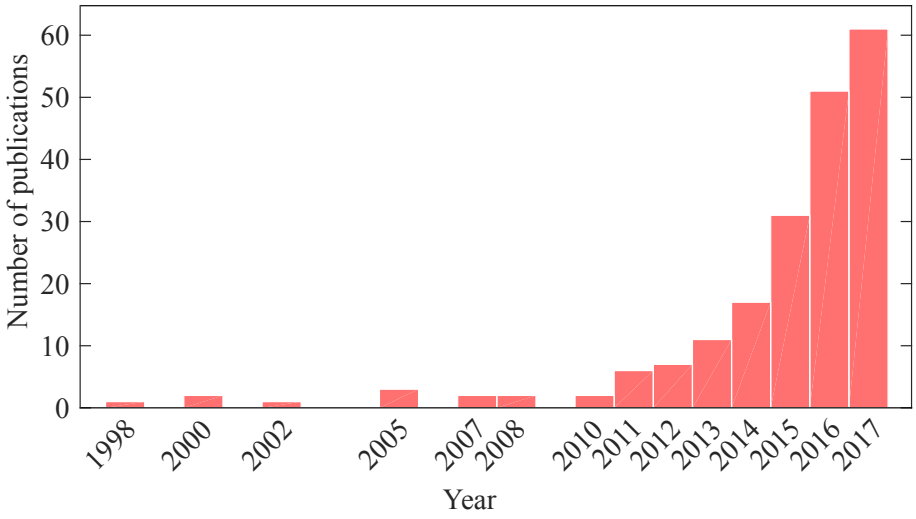

Figure 1: Number of annual publications in the field of cbPPG between 1998 and 2017. Overall 236 articles were taken into account for the illustration.

1.2 AIM OF THIS WORK

In this thesis, the described issues, which hold back the cbPPG's development, will be addressed. The following listing delineates the specific goals:

- *Technical setup* A novel and stand-alone measuring system for cbPPG is introduced. The work intends to demonstrate how conveniently and flexibly the system can be employed in various environments. A further considered hardware aspect concerns optical polarization filtration. The goal is to investigate which polarizer setting creates the most substantial benefit for cbPPG.

- *ROI selection* Another objective of this thesis is to tackle the drawbacks of previous ROI selection methods. A new approach is proposed that is fully automated, universally

applicable, and allows the extraction of high-quality cbPPG signals. It is furthermore able to suppress ballistocardiographic artifacts by utilizing level set methods.

- *Application fields* Broadening the application fields of cbPPG is one of the major priorities here. On the one hand, it is intended to show that cbPPG can be successfully used for heterogeneous subject groups and in different clinical and laboratory environments. More specifically, on the other hand, the work aims at assessing how cbPPG measures reflect the reactivity of the autonomic nervous system with respect to the vasomotor tone.

- *Signal origin* On the basis of the polarization study as well as the analyses regarding the assessment of autonomic functions, the thesis attempts to shed more light on the origin of cbPPG signals. The signals' characteristic behavior in regard to different illumination configurations, filter settings, and vasomotor activation is evaluated to draw the respective conclusions.

Figure 2 provides an overview of the research aspects that are tackled in this thesis.

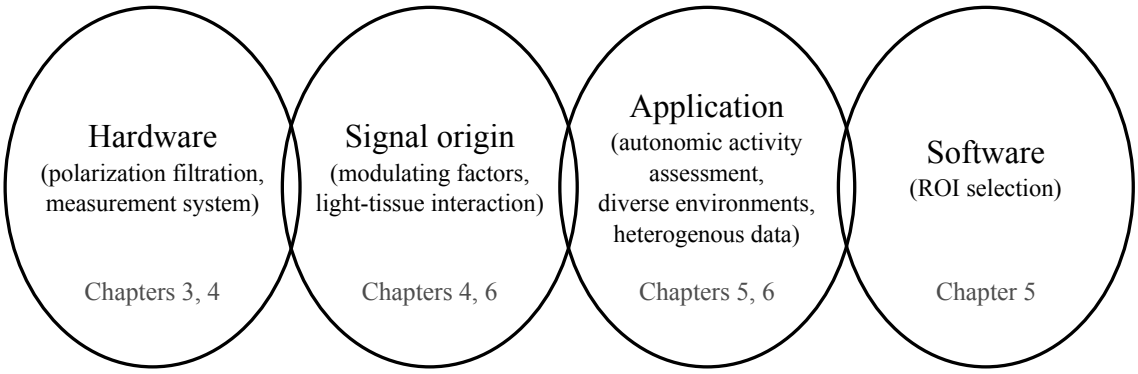

Figure 2: The four major research topics in cbPPG and the specific aspects (in brackets) that are addressed in this thesis. In the lower part of the figure, references to the associated chapters are listed.

1.3 DISSERTATION OUTLINE

Chapter 2 provides medical and technical background knowledge. Detailed descriptions are given concerning the human anatomy and physiology where the skin is addressed in particular. Furthermore, the classic as well as the camera-based photoplethysmography are reviewed. In Chapter 3, the novel measuring system for cbPPG is introduced. Moreover, the clinical and laboratory studies, in which all video data was obtained, are presented. The next three chapters focus on specific research topics and are conventionally structured including a state of the art, method, results and discussion section. Chapter 4 explores the value of polarization filtration with respect to the signal quality and the cbPPG signal origin. Chapter 5 proposes the new method for ROI selection. The performance is extensively

evaluated using data sets from three large studies. Chapter 6 investigates how autonomic reactions of the body reflect in cbPPG measures. The findings are further utilized to shed more light on the signal origin. In Chapter 7, the work is summarized, the final conclusions are drawn, and an outlook for future directions is presented.

2

MEDICAL AND TECHNICAL BACKGROUND

This chapter provides medical and technical background information which is crucial for the understanding of the subsequent chapters. The first two section address the cardiovascular and the autonomic nervous system and explain characteristics and mechanisms that affect the outcome of cbPPG. Since the skin forms the cbPPG's measurement region, the third section focuses on the structure of the skin and assesses its interaction with light. The fourth section describes the classical photoplethysmography because established knowledge about the technique can also be applied to cbPPG, which is introduced in the last section.

2.1 CARDIOVASCULAR SYSTEM

2.1.1 *Anatomy and Physiology*

The cardiovascular system (CVS) consists of three major components, the heart, the blood vessels, and approximately 4 - 6 liters of blood [60, 124]. One of its main functions is the transport of oxygen and nutrients to body cells and the removal of metabolic waste products and carbon dioxide from these cells [291]. The CVS is involved in the intercellular communication by transporting hormones [160], and it contributes to the regulation and stabilization of the body temperature (thermoregulation) [107]. In general, the CVS plays an important role in maintaining the body within defined boundaries, so-called homeostasis [60].

The blood is a complex fluid medium inside the CVS. Besides the transport of essential substances, it fulfills additional functions including immunological tasks, the control of the pH-value and electrolyte concentration, and the arrest of bleeding (hemostasis) [124]. The blood consists of plasma and blood cells, in which the red blood cells (erythrocytes) are of particular importance [60]. Erythrocytes account for 42 % to 47 % of the total blood volume [291] and contain a oxygen-carrying protein called hemoglobin [26]. The concentration of hemoglobin depends on the individual physiology normally ranging between 120 and 180 g/L [160]. Based on the oxygen saturation, it can be divided into oxyhemoglobin and deoxyhemoglobin, which describe the state before and after releasing oxygen to the body tissue [107].

The heart represents the center of the CVS. It can be described as two consecutive pumps, the right and the left heart, that perform at the same pumping rate [160]. Both sides consist of an atrium, a ventricle and two valves which ensure that the blood flows in a certain direction [291]. On the one side, the contraction of the right ventricle allows the right heart to transport deoxygenated blood into the pulmonary circulation where it passes the lungs and flows back into the left heart [26]. In the lungs, the blood is oxygenated again and carbon dioxide is removed [160]. On the other side, the left ventricle ejects blood into the systematic circulation where it supplies the body with oxygen, is deoxygenated, and carries carbon dioxide back to the right heart [26]. The heart pumps blood in a rhythmical manner where each cycle consists of the systole phase, which refers to the ventricles' contraction, and the diastole phase, which refers to their relaxation and refill [129]. The number of cardiac cycles within a minute is defined as the heart rate (HR) and measured in beats per minute (bpm). The HR is an important vital sign that provides information about the CVS. It is a marker for stress [359], a predictor for hypertension[1] and a risk factor for cardiovascular diseases [250], cardiovascular mortality and total mortality [251]. The HR can be determined at various body sites in various technical ways based on electrical, mechanical, acoustical and optical measuring techniques [163].

The third part of the CVS is the vasculature. There are five main types of blood vessels, arteries, arterioles, capillaries, venules and veins, which also appear in this order regarding the direction of the blood flow [291]. The aorta is a special type of vessel in the systematic circulation that connects the left ventricle and larger arteries [107]. Beginning from the aorta, the vessels branch up and bifurcate consistently as far as to the capillaries [160]. Therefore, the number of vessels increases with a higher distance from the heart while their diameters decrease and the total cross-sectional area increases [60] (see Fig. 3 (a) and (b)). The increase in the total cross-sectional area causes the mean blood flow velocity to decline and enables a very slow blood movement inside the capillaries [107, 291] (see Fig. 3 (d)). Starting from the capillaries, a reverse branching structure can be found in the venous system. Throughout the arterial vasculature, the vessel elasticity changes [26, 291]. In general, elastic fibres decrease towards the microvasculature whereas collagen and smooth muscles increases. The capillaries, however, have neither elastic tissue nor smooth muscles. The elasticity of the arterial vasculature coincides with the pulsatile character of the pulse wave meaning that to an almost continuous blood flow exists in the capillaries [107]. A measure for the blood vessels' elasticity is the compliance C which reads [160]:

$$C = \frac{\Delta V}{\Delta P_{tm}} \,, \tag{1}$$

where ΔV is the blood volume change and ΔP_{tm} the corresponding change of the transmural pressure within the same vessel section. The transmural pressure is defined by $P_{tm} = P_i - P_e$ in which P_i depicts the intravascular pressure and P_e the extravascular

1 Hypertension describes a permanent elevation of the arterial blood pressure and is considered a cardiovascular disease [26].

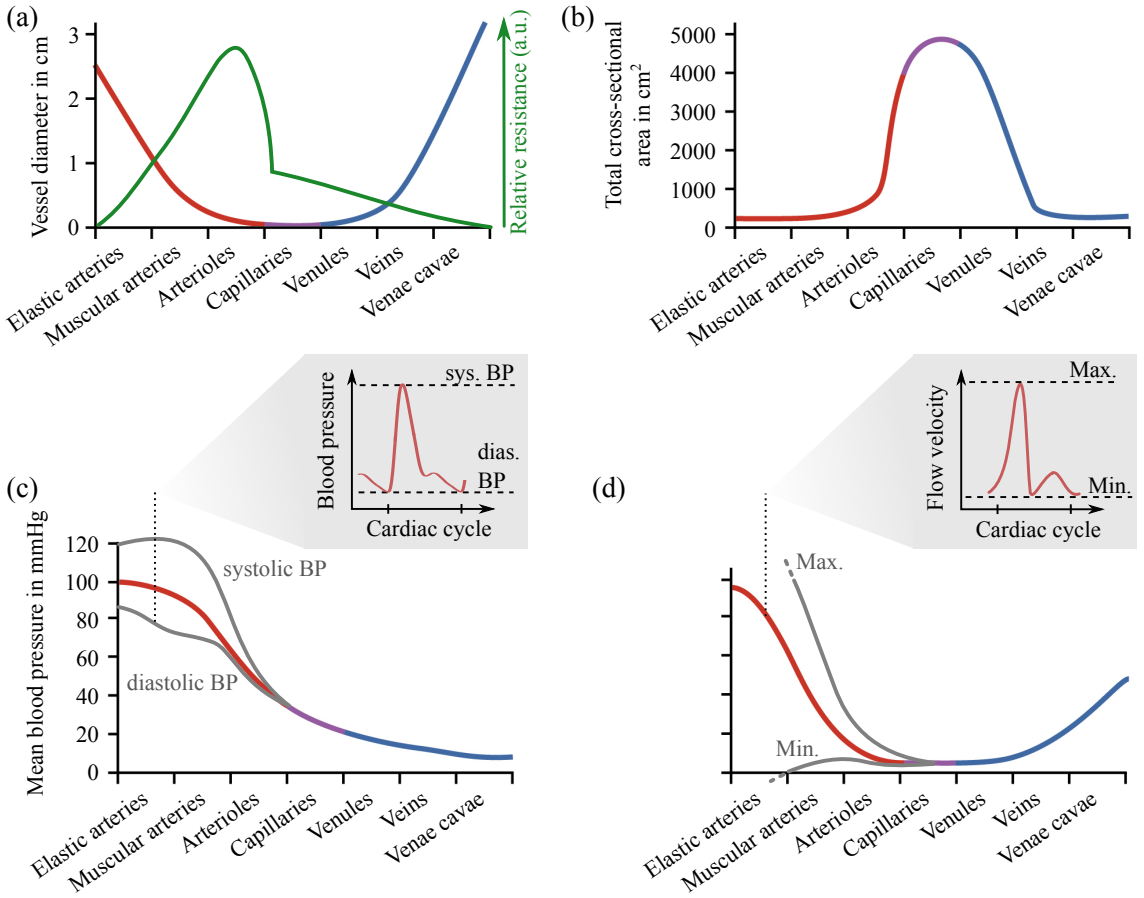

Figure 3: Anatomical and physiological characteristics of the vascular system: (a) Vessel diameter and relative resistance, (b) Total cross-sectional vessel area, (c) Mean BP, (d) Mean blood flow velocity. For Fig. (c) and (d), the minimum and maximum trends of the pressure and velocity parameters are shown as well. Those trends indicate the parameters' pulsatile behavior which is depicted examplarily in the gray areas. (Figure (a)-(d): from [54] - modified in text/ additional plots added, Resistance curve: based on figure in [26, p. 543], Trend curves/ beat waveforms: based on depictions in [160, p. 193])

pressure. Since the pressure by the surrounding tissue is mostly very small, P_e is often ignored [291]. The compliance depends on the vessel type, can be altered by the smooth musculature, and generally changes with age [26, 124].

The terminal arteries and the arterioles together represent the resistance vessels [26]. This denotation refers to their function as they cause a high resistance to the blood flow [124] (see Fig. 3 (a)). Due to the smooth musculature, the resistance can be controlled and allows to influence the perfusion of the body tissue [60, 160]. Vasoconstriction increases the resistance to the incoming flow and, therefore, lowers the pressure inside the capillaries. Vasodilation has the opposite effect. The resistance vessels also play a role for the propagation of the pulse wave. The forward traveling pulse wave is reflected at sites where the vessel resistance changes (bifurcations, changes in cross-section or compliance) creating a backward traveling pulse wave in the periphery which consequently superimposes with the forward wave [291]. The superposition generates a twin peak characteristic in the resulting pulse wave and can be found in various physical measures, such as the blood velocity and

the blood pressure (see Fig. 3 (c) and (d)). The counterpart of the resistance vessels, on the venous side, are the capacitance vessels which hold a large amount of the total blood volume [26]. The respective veins are much more compliant than the arterial vessels, and they allow the control of the blood volume [160].

The (intravascular) blood pressure (BP) is one of the most important vital signs when it comes to examining the CVS [160]. The arterial BP, especially, gains a lot of attention, mainly due to hypertension, which is a very common and serious cardiovascular disease [378] and a risk factor for strokes, heart and renal failure [26]. The arterial BP can be generally described as a product of the total peripheral resistance and the cardiac output [124, 291]. However, the waveform changes throughout the vasculature in which a decreasing trend in the mean value occurs [26] (see Fig. 3 (c)). There are four main BP derivatives that are primarily used for the assessment [160]: (i) the diastolic BP (DBP) which is the minimum in the waveform, (ii) the systolic BP (SBP) which is the maximum, (iii) the pulse pressure (PP) which is the difference between SBP and DBP, and (iv) the mean BP (MBP) which is the average pressure in one cardiac cycle. The arterial BP is most commonly accessed in a non-invasive cuff-based way (Riva-Rocci method) that allows a one-time measurement of the DBP and SBP [160]. In clinical environments, even a continuous BP signal can be obtained by inserting a cannula into an artery [26].

2.1.2 *Microcirculation*

The microcirculation refers to the terminal vessels where different exchange processes take place [107]. It comprises the perfusion-controlling arterioles, the capillaries, venules and the drainage system of the lymphatic vessels [291]. Figure 4 shows the vascular structure with the main components. Between common arterioles and capillaries, a subtype of arterioles arises, called metarterioles, or terminal arterioles [26, 45]. The smooth musculature on metarterioles is incomplete and evolves into precapillary sphincters which allow to control the blood flow at the capillaries' openings. In some body tissues, such as the skin, there are also arteriovenous anastomoses that are shunts between arterioles and venules [124]. These shunts can be opened or closed in order to regulate the substance and heat exchange in the capillary bed of tissue. The capillaries are the smallest vessels in the human body mainly consisting of only one cell layer of endothelium and a basal membrane [291]. They are relatively short and just wide enough (about 5 - 9 µm) to let pass one red blood cell, if the sphincters are opened [26]. In the capillaries, oxygen and nutrients are released to the surrounding tissue while metabolic waste and carbon dioxide enter the bloodstream [26, 160]. The blood flow velocity is low there (0.07 cm/s) and the BP falls from about 30 mmHg to 15 mmHg during the exchange process [291].

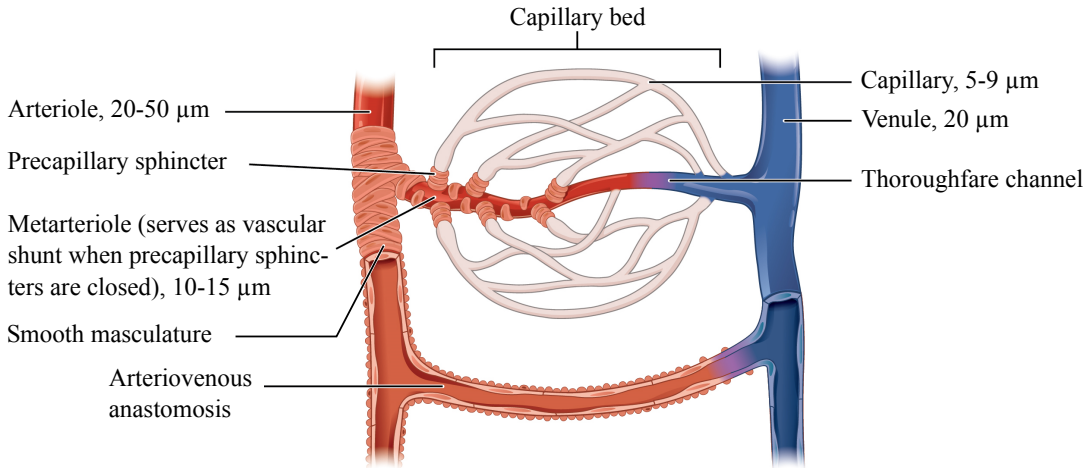

Figure 4: The vasculature of the microcirculation. The different types of vessels are shown with their diameter. (from [53] - modified in text, information from [26])

2.2 AUTONOMIC NERVOUS SYSTEM

2.2.1 *Physiology and Function*

The nervous system is an organ system that coordinates actions within the body and interactions with the environment [60]. From a technical point of view, it can be divided into the following elements [95, 107]:

- *Processor*: The central nervous system is the main functional unit that comprises the brain and the spinal cord. It processes, distributes, and integrates incoming information (sensor data) and creates motor commands.
- *Sensors*: The sensory receptors initiate most of the activities in the nervous system. They are located in different parts of the body (ears, eyes, skin, blood vessel wall, etc.) and consequently vary in their type (auditory, visual, tactile, tensile, etc.).
- *Effectors*: The motor part of the nervous system performs bodily actions that are triggered by the motor commands. These actions contain the contraction of specific skeletal muscles, smooth muscles and the secretion of chemical substances by glands.
- *Transmitters*: The sensory nerve fibers (afferents) transmit impulses from the sensory receptors to the central nervous system. Analogously, the motor nerve fibers (efferents) transmit commands from the central nervous system to the effectors.
- *Storage*: A lot of sensory information is saved for future activities where the cerebral cortex acts as the main storage.

As already implied in the listing, the nervous system holds different components that also fulfill different tasks. More generally, it can be divided into the central and peripheral nervous system where the latter one subdivides into the somatic and autonomic nervous system (ANS) [95]. The terminology of the two subdivisions refers to the way how activities are controlled. While the somatic system coordinates voluntary and conscious action, the ANS mostly coordinates involuntary and unconscious actions [60, 208].

Table 1: Response mechanisms of the parasympathetic and sympathetic nervous system in case of activation, depicted for selected organs or organ systems. (from [291, p. 443] - modified, [26, p. 267] - modified)

ORGAN OR ORGAN SYSTEM	PARASYMPATHETIC RESPONSE	SYMPATHETIC RESPONSE
Heart (myocardium)	Decrease in heart rate	Increase in heart rate
	Decrease in contractility (atria)	Increase in contractility (atria and ventricles)
Arterial vessels		
... in heart (coronary arteries)	–	Vasodilation, Vasoconstriction
... in skin (trunk, extremities)	–	Vasoconstriction
... in skin and mucosa (face)	Vasodilation	Vasoconstriction
Systemic veins	–	Vasoconstriction
Skin		
Pilomotor muscles	–	Contraction
Sweat glands	–	Secretion

The ANS is an essential component for maintaining homeostasis[2] in the body [160]. It innervates all inner organs, with the exception of the skeletal musculature, and adapts their functions to current needs [124]. For this purpose, nerves terminate in smooth muscles, such as in blood vessels, cardiac muscles and glands [26], and allow the control of these organs. The controlling components are located in the brain and primarily encompass the hypothalamus (coordination of regulatory processes), the limbic system (control of emotions) and the reticular formation (transmission of information from hypothalamus and center of many vegetative reflexes) [124]. The ANS can be divided into three parts, the sympathetic nervous system (SNS), the parasympathetic nervous system (PSNS), and the enteric nervous system [291]. For reasons of relevance, this work will only address the SNS and the PSNS. The systems' activation usually has opposing effects on the body in which the SNS places an organ into an emergency mode and the PSNS into a vegetative mode [60, 160]. However, the influence of the respective system varies from organ to organ where some are only affected by one division [124]. Table 1 gives an overview of selected organs with their response in case of the innervation by the ANS. In general, the SNS can be attributed to an increase in HR, BP, and cardiac output, and a decrease in the microcirculatory blood flow and the venous blood volume; the PSNS is associated with a decrease in HR and cardiac output, and with resting functions like digestion, food absorption, and gastric secretion [26, 107, 124].

2 Homeostasis refers to the upkeep of steady conditions within the body's internal environment [107].

2.2.2 *Regulation of Heart Rate, Blood Pressure and Temperature*

The body's circulation is nearly entirely controlled by the ANS in which the SNS plays the major role regarding regulatory mechanisms [107]. The sympathetic stimulation of arterioles and small arteries enables the increase of the peripheral resistance and, consequently, the decrease of the blood flow within the tissues (see Table 1). In fact, the vasomotor vessel tone is continuously maintained through partial vasoconstriction whereas dilation is generally achieved by inhibiting the sympathetic stimulus [124]. The PSNS plays the minor role in the circulatory regulation although it is essential for the control of the HR. The HR is subject to periodic variations that reflect the activation degree of the SNS and the PSNS (vagal function) [404]. These variations can be divided into long-term (>6 s up to several hours) and short-term (2.5 - 6 s) oscillations [314]. While the first ones are associated to numerous mechanisms, the latter ones precisely represent the respiratory rhythm called respiratory sinus arrhythmia. Besides the cyclic variability, the HR changes situation-related in order to impact other intrinsic parameters (see next paragraph).

There are several reflex mechanisms for maintaining the BP of which almost all are negative feedback mechanisms [107]. One of those mechanisms is the baroreflex that is responsible for short-term pressure adjustments mainly concerning minute-based variations [160]. Figure 5 (a) depicts the functional principle. The baroreflex is triggered by stretch receptors (baroreceptors) located in walls of larger systemic arteries, particularly in the aortic arch and certain points of carotid arteries [26]. When the arterial BP rises, the receptors transmit signals to the central nervous system which provokes the ANS to create feedback signals for a certain group of effectors [107]. The resulting effects can be summarized to (i) vasodilation of arterioles, (ii) vasodilation of veins, which leads to a decrease of the blood volume in the heart chambers causing the heart to pump with a lower strength, (iii) decrease in HR, and (iv) decrease in the heart's contractility [107, 124, 291]. These effects consequently reduce the BP by decreasing the peripheral resistance and the cardiac output. In case of low BP, the baroreflex activates the listed effects in the exact opposite way. In some occasions, the body has to adjust the BP rapidly within few seconds. For this purpose, it exploits the same mechanisms, (i) to (iv). Besides regulatory changes in the BP, which are more situation-dependent, two major periodical variations occur in addition to the cardiac cycle [107]. The first are the respiratory waves which are caused by respiration and lead to a fluctuation between 4 - 6 mmHg. The second are vasomotor waves (also called Mayer waves) which stem from the oscillation of pressure control mechanisms and lead a fluctuation between 10 - 40 mmHg within time frames of 7 to 10 seconds.

Similar to the BP, the body temperature is mostly controlled through negative feedback mechanisms [26]. Besides autonomic mechanisms, other strategies exist which will be not discussed here. While the body's core temperature stays mainly constant (37 °C), the peripheral temperature differs between various sites (31 - 36 °C) and underlies permanent fluctuations [160]. From the center of the body towards the skin, it assimilates to the ambient temperature. The body senses varying temperatures using thermoreceptors that

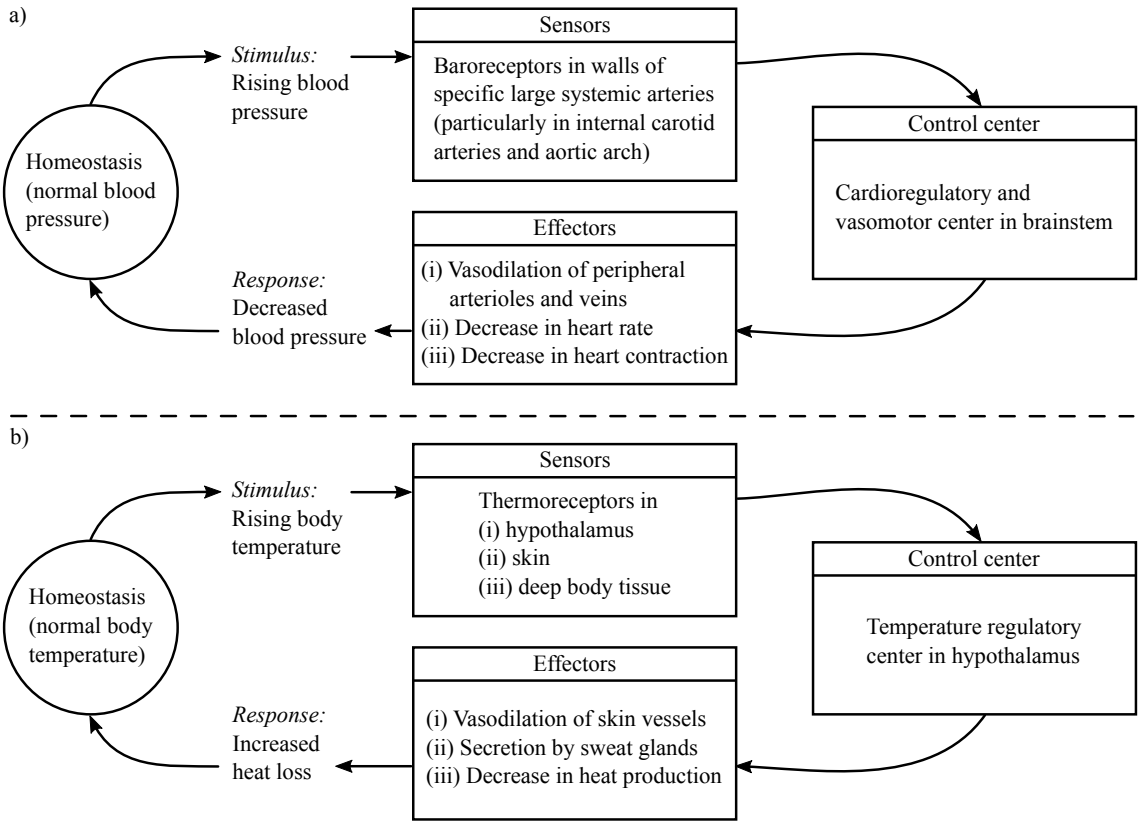

Figure 5: Functional principles of regulatory negative feedback mechanisms: (a) Blood pressure regulation (baroreflex), (b) Thermoregulation. (Fig. (a): adapted from [345] and based on descriptions in [107], Fig. (b): from [345, p. 13] - modified)

can be found in the skin, in deeper body tissues and in the hypothalamus where also the corresponding regulatory center is located [291]. The skin holds warm receptors and the more abundant cold receptors which respond to temperatures between 30 - 45 °C and 15 - 32 °C, respectively [160]. In the face, the sensor density is considerably higher than in the extremities [291]. If the temperature changes, the thermoreceptors transmit signals to the control center in which the actual value is compared to the set value and subsequently a reaction is initiated for the corresponding effectors (see Fig. 5 (b)). The mechanisms for decreasing the temperature are [107, 160]:

1. *Vasodilation of skin vessels*: The heat transfer to the skin decreases due to a higher perfusion.
2. *Sweating*: The secretion by the sweat glands leads to cooling due the liquids' contact with air.
3. *Reduction of heat production*: The mechanisms which are involved in heat production (e.g. shivering and chemical thermogenesis) are inhibited.

Temperature increasing mechanisms are [107, 160]:

1. *Vasoconstriction of skin vessels*: The heat transfer to the skin increases due to a lower perfusion.

2. *Piloerection*: The contraction of the pilomotor muscles causes the hair to be erected and, therefore, to act as an insulator.
3. *Increase in heat production*: The corresponding mechanisms (see above) are promoted.

As can be derived from the listings, the SNS plays a major role for temperature regulation (see also Table 1).

Besides the global temperature reflexes, local reflexes exist as well [107, 291]. If a skin area is locally cooled or heated, vasoconstriction or dilation and the inhibition or promotion of sweating might only occur at this area.

2.3 HUMAN SKIN

2.3.1 *Anatomy and Physiology*

The skin is the biggest organ of the human body which fulfills several functions including the protection of the body, the prevention of water loss, and contributing tasks in the thermoregulatory process [161]. Furthermore, the skin holds different receptors that perform the function of sensing pain, temperature, touch and mechanical impacts [398]. Throughout the body, the skin varies in structure and morphology and is adapted to the needs of the respective region [22]. There are two main types of skin that occur on each individual [270, 398]. On the hand hand, there is the so called 'hairless skin' which is relatively thick and can only be found in the palms and food soles. It has no hair, no sebaceous and scent glands, and its surface shows deep parallel furrows. On the other hand, there is the 'hairy skin' which is thinner and can be found on the rest of the body. It has hair, which varies in density, length, and thickness, as well as sweat and sebaceous glands. Figure 6 depicts the anatomy of the two skin types. An additional factor for differences in the skin's appearance is age [398]. Age generally impacts the thickness, elasticity, and the perfusion.

The skin can be divided into three main layers, the epidermis, the dermis, and the hypodermis (see Fig. 6). The epidermis is the uppermost layer and can be further divided into a non-living and a living component [27]. The non-living part, which is called stratum corneum, is a cornified layer of horny dead cells that function as a protector and a barrier for epidermal water and against external substances [161]. The viable epidermis is the living part that is mostly made up of keratinocytes [398]. Besides this kind of cells, other types exist, namely (i) melanocytes which are responsible for the melanin[3] synthesis, (ii) Merkel cells which are mechanoreceptive and connected to nerve endings, and (iii) Langerhans cells which are part of the immune system [22]. The thickness of the epidermis ranges from about 100 µm in the face up to 1.5 mm on the foot soles [161, 180]. Beneath the epidermis lies a thin junction called basal membrane that represents the interface to the subjacent dermis [214]. The dermis can be described as a connective tissue combined

3 Melanin is a pigment which is released to protect the body from ultraviolet radiation and which leads to a darker appearance of the skin color [22].

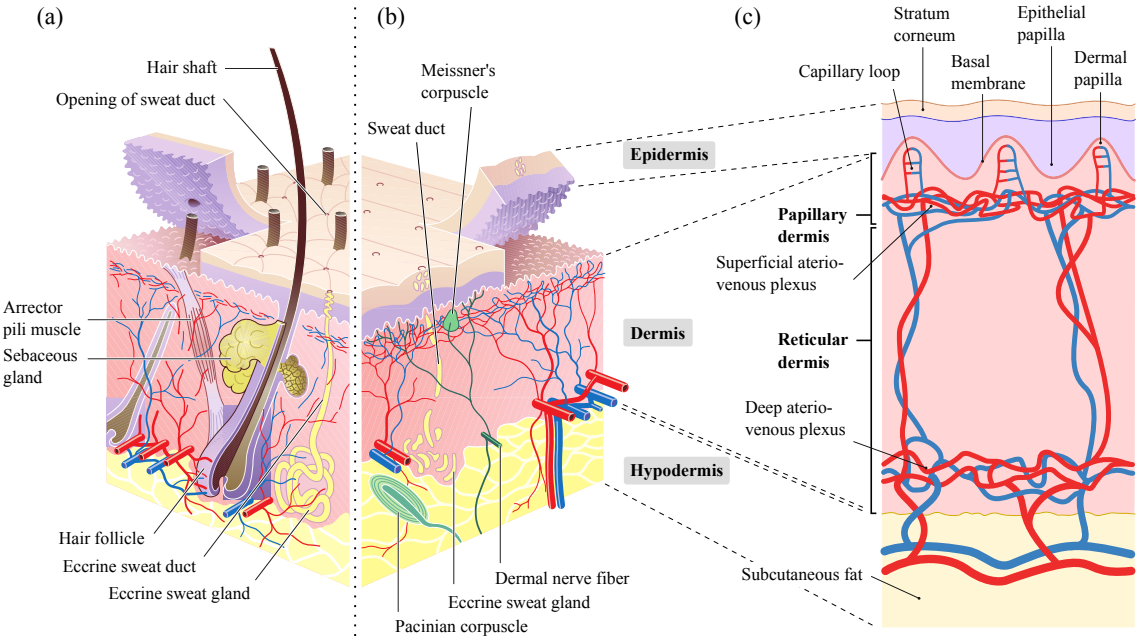

Figure 6: Anatomy of the skin: (a) Thicker hairy skin, (b) Thinner hairless skin, (c) Schematic depiction of the different skin layers including the cutaneous vasculature. (Fig. (a) and (b): from [197] - modified in text and color, Fig. (c): based on figure in [398, p. 588])

with elastic and collagen fibers [22]. It has protective and sensory tasks, and it holds the cutaneous vasculature which fulfills several other functions as will be explained later. The upper part of the dermis, the papillary dermis, is a layer with rather loose connective tissue where blood and lymphatic vessels, nerves, and sensory organs like the Meissner's corpuscle (tactile receptor) are embedded [22, 398]. The lower part, the reticular dermis, is a layer with rather sturdy connective tissue where besides vessels and nerves, hair roots, sebaceous glands, and sweat glands occur [398]. Similar to the epidermis, the thickness of the dermis varies dependent on the body site ranging between 0.5 mm and 4 mm [27, 73]. The last skin layer is called hypodermis which consists of loose connective tissue and fat tissue although the latter is the dominant component [22]. The fat serves as an isolator for pressure and temperature, a storage for energy, water, and heat, as well as a protector in case of injuries [398]. The thickness of the skin layer reaches from 1 mm to 6 mm [27]. To get a better overview, Table 2 summarizes the thickness of the different cutaneous layers for important body sites. It is important to note that not only the region but also the age and the gender affect the thickness [180, 374].

The skin is strongly vascularized and shows a significantly greater blood flow than necessary for the nutrition of the tissue [45]. Investigations concluded that this excess has to be related to thermoregulatory mechanisms [44]. As already mentioned in the previous sections, the perfusion and the heat release in the skin is controlled by the SNS through regulation of the smooth musculature on arterioles and arteriovenous anastomoses. Furthermore, the cutaneous venules significantly affect the heat radiation by changing their diameter [398]. The capillary loop is the closest vasculature to the skin surface and

Table 2: Thickness of skin layers at different body sites. The given values were selected from [27, 180, 276, 374], are depicted with an accuracy of 10 µm, and should be considered as a rough estimate. For the papillary dermis and the plexuses, only static (across the body sites) values could be found. The values of the reticular dermis were calculated.

Skin layer	Forehead	Cheeks	Fingertip	Palm	Inner forearm
Epidermis	90 µm	100 µm	370 µm	600 µm	70 µm
Dermis	790 µm	1080 µm	*n/s*	750 µm	1020 µm
Papillary dermis	150 µm	150 µm	150 µm	150 µm	150 µm
Upper plexus	100 µm	100 µm	100 µm	100 µm	100 µm
Reticular dermis	640 µm	930 µm	*n/s*	600 µm	870 µm
Lower plexus	100 µm	100 µm	100 µm	100 µm	100 µm

n/s No specific values were found (skin type is the same as in the palm)

part of the papillary dermis (see Fig. 6). Although each dermal papilla only holds one loop, the density still varies between different body regions and is the highest in the face ($150\,\mathrm{mm}^{-2}$) [398]. The capillary loop comprises an ascending and a descending limb, as well as the actual intrapapillary loop, which itself bifurcates up to three times [43]. Despite the fact that capillary loops only occur in the skin, certain features resemble conventional structures: The ascending limb partly yields the characteristic of an arterial capillary [45]. The capillary loops are connected to a horizontal net plexus which is also part of the papillary dermis and consists of terminal arterioles, capillaries, and postcapillary venules [43]. There are two kinds of terminal arterioles in the upper plexus. The first kind are relatively wide (17 - 26 µm), likely participate in the peripheral resistance, and have walls that encompass smooth muscle cells and elastin (elastic fiber material) [44]. The second kind (10 - 15 µm) represent the transition to the capillary bed and show neither smooth muscle cells nor elastic fibers [45]. Similar as in the papillary dermis, a horizontal net plexus of arterioles and venules can be found in the lower reticular dermis [43]. The two plexuses are connected by ascending arterioles and descending venules which together unsystematically occur at intervals of 1.5 - 7 mm [45]. The blood vessels in the reticuar dermis differ from those in the papillary dermis, generally by being thicker (about 50 µm) but also by having more cell layers of smooth muscle and a different wall structure [44]. In the hypodermis, the arterioles and venules show the same morphology and size like those of the lower plexus [43]. However, also larger arterioles holding diameters up to 100 µm exist which, by definition, already could be considered small arteries [46, 398]. Table 3 surveys the arterial vasculature in the skin and states whether the respective vessel type is pulsatile.

When describing vascular characteristics of the skin, vasomotion should be mentioned. Vasomotion is the spontaneous but rhythmical contraction of arterioles and precapillary sphincters [107, 291]. The maximum cutaneous vasomotion of 0.10 - 0.17 Hz is present at the ascending arterioles in the reticular dermis [45].

Table 3: Arterial vasculature in different skin layers with respect to the occurring vessel types and important characteristics. The pulsatile character (compliance) was determined based on the existence of elastin in the vessel walls. (information retrieved from [46, p. 300], [43, p. 4S], [45, pp. 4-5])

		Occurring vessel type	Vessel diameter	Pulsatile character
Papillary dermis	Capillary loop	Ascending limb	8 - 12 µm	No
		Intrapapillary loop	7.5 - 10 µm	No
		Descending limb	10 - 17 µm	No
	Upper plexus	Terminal arteriole (with elastin)	17 - 26 µm	Yes
		Terminal arteriole (without elastin)	10 - 15 µm	No
		Arterial capillary	10 - 12 µm	No
		Venous capillary	10 - 12 µm	No
Reticular dermis	Mid-dermis	Ascending arteriole	40 - 50 µm	Yes
	Lower plexus	Arteriole	40 - 50 µm	Yes
Hypodermis		Arteriole	50 - 100 µm	Yes

2.3.2 *Optical Properties*

Light is part of the electromagnetic radiation, and it divides into non-visible light, which comprises ultraviolet (100 - 400 nm) and infrared (770 nm - 1 mm) radiation, and into visible light (400 - 770 nm) [284]. A comprehensive understanding of the light's interaction with the cutaneous tissue is crucial for the proper application of optical measurement techniques. Therefore, this section summarizes important facts for the visible and near-infrared (NIR) range.

When light falls onto and into the skin, different optical effects take place, namely reflection, refraction, absorption and scattering [20]. Figure 7 depicts the principles of these effects for a skin model. The paths of the photons within the skin tissue can only be described stochastically and the distribution is considered to be diffuse [174]. The remitted light, which eventually can be detected, consists of a reflective fraction from the surface and back-scattered fraction from inside the tissue.

Refraction occurs when light passes through mediums where the refractive indices changes, and it is the stronger the larger this change is [284]. Consequently, significant refraction arises between the air and the epidermis (indices: 1.00 vs. 1.41 - 1.49) but also between the epidermis and the dermis (1.36 - 1.41) and in general, within the skin layers since their structure is not homogeneous [188]. The notable index change at the air-skin boundary causes 4 - 7 % of the incident light to be specularly reflected [20]. Besides specular reflection, total reflection emerges at the same boundary if the back-scattered light

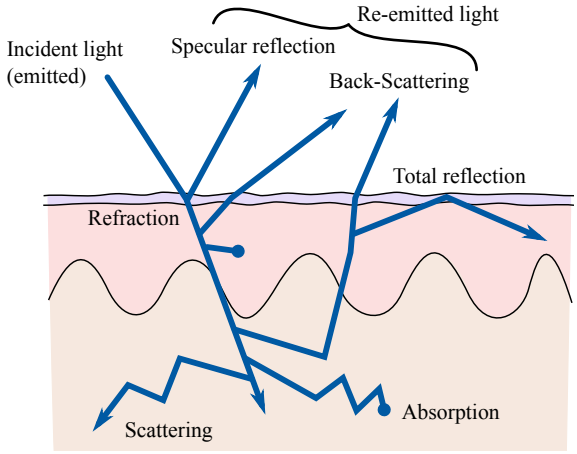

Figure 7: Optical effects that take place in and on the skin. The depiction examplarily shows possible path ways of photons. In reality, a lot more optical processes occur. (The figure is based on the figure in [20, p. 14].)

from the tissue incides at a critical angle $\gtrsim 42\,^\circ$ [94, 284]. In fact, 55 % of the outgoing light theoretically undergoes this back-reflectance [94].

A soon as photons penetrate the skin, absorption, which can be described as a reduction in light energy, occurs [188]. Figure 8 (b) depicts the absorption characteristic for the epidermis and dermis in the visible and NIR range showing a gradual decrease with longer wavelengths. However, the substances that actually define this characteristic vary with the skin layer as well as the wavelength [20, 174, 287]. In the visible range, melanin is the dominant absorber for the epidermis whereas for the dermis, hemoglobin dominates the absorption despite the fact that blood only occupies 0.2 - 0.6 % of the physical dermal volume [188]. While melanin involves a continuous decline in absorption across the wavelengths, hemoglobin features a unique behavior holding maxima in the blue and green light region (see Fig. 8 (a)). Further important absorbers are bilirubin and carotene [20]. In the infrared range, the absorption in the epidermis is mainly attributed to lipids and in the dermis, it is mostly determined by water [27]. The impact of water increases with longer wavelengths and, therefore, can hinder any optical blood-related analyses in such ranges. The absorption properties of the hypodermis are similar to those of the dermis [27, 285]. In the visible range, a significant absorber is hemoglobin whereas in the NIR range, water and lipids define the absorption. The degree of absorption can be mathematically expressed by the coefficient μ_a (in cm^{-1}) [174]. The value describes the mean number of absorption events per centimeter of photon travel [27].

Besides absorption, scattering is the optical effect which is essential to fully explain the optical characteristics of skin tissue [94]. Scattering can be attributed to inhomogeneities in the skin layer's refractive index [20]. When photons are scattered, changes in their direction, polarization and phase occur [188]. In the visible and NIR range, however, scattering does not lead to changes in the wavelength [174]. The scattering properties of the skin layers are mainly determined by fibrous structures being keratin in the epidermis and collagen in the dermis [27, 188]. Additional important scatterers are melanosomes and melanin (in

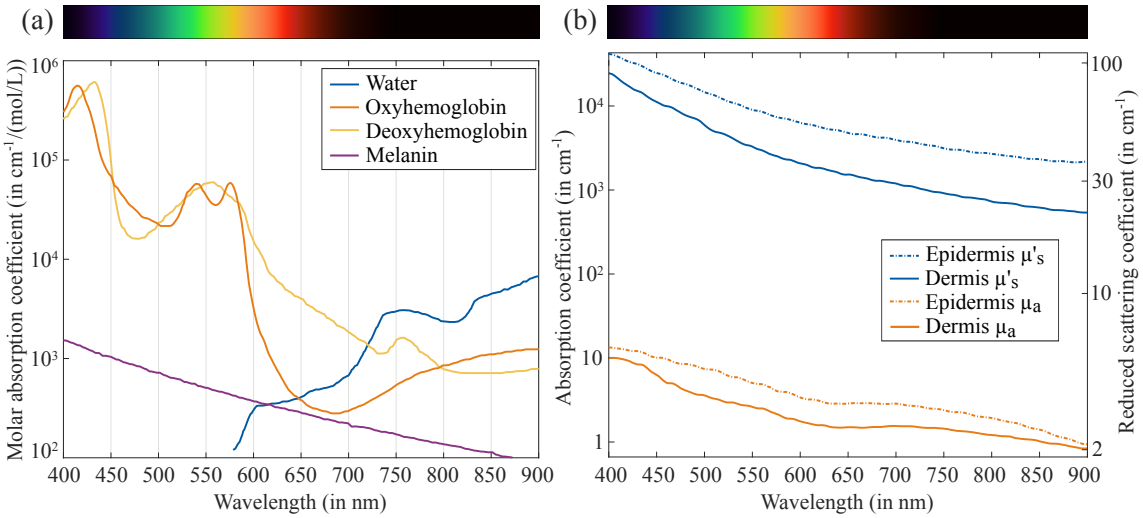

Figure 8: Absorption and scattering characteristics of the skin in dependence of the wavelength: (a) Absorption behavior of important chromophores quantified by the molar absorption coefficient, (b) Absorption and scattering behavior in the epidermis and dermis (*in vitro*) quantified by the absorption and reduced scattering coefficient. (Fig. (a): based on figure/ data in [287, p. 16], Fig. (b): based on figure/ data in [285, pp. 4–5])

epidermis), cell walls and nuclei, and many other substances [188]. As for absorption, the degree of scattering gradually decreases with longer wavelengths in the visible and NIR light spectrum (see Fig. 8 (b)). The trend is associated with a change in the refractive indices as well as a change in differences between the indices of various structures [20]. These characteristics lead, among other things, to greater scattering at vessel walls for shorter visible wavelengths [188]. In relation to the surrounding skin, blood causes generally minor scattering [188]. There are several scattering mechanisms that take place in the skin depending on the size of the interacting particles [174]. For small sizes, scattering is weak and almost isotropic while for higher sizes, scattering is stronger and forward directed [20]. In general, the epidermis and the dermis mostly have a forward scattering behavior implying that photons, which come back to the surface, underwent a great number of scattering events [94, 188]. The degree of scattering is usually quantified by the coefficient μ_s (in cm^{-1}) describing the mean number of scattering events per centimeter of photon travel [27]. However, the reduced scattering coefficient μ_s' is of higher interest since it additionally considers the anisotropy of the photons' path way ($\mu_s' < \mu_s$) [20].

An important parameter, which results from the optical properties of the skin, is the penetration depth[4] of light. The parameter is inversely proportional to μ_a and μ_s' meaning that the more absorption and scattering events occur, the lower the penetration depth is. Consequently, the penetration depth also depends on the wavelength. It gradually increases up to about 1000 nm from where it declines again due to the high absorption by

4 The penetration depth δ of light is defined as the distance, in the direction orthogonally aligned to the skin surface, where the fluence rate of the incident light decreases to $1/e$ (37 %) of its original value [20, 94]. The characteristic can be described by the Beer-Lambert law leaving the penetration depth as reciprocal of the effective attenuation coefficient [174]. In this work, the formula $\delta = (3\mu_a(\mu_a + \mu_s'))^{-0.5}$ was used [274].

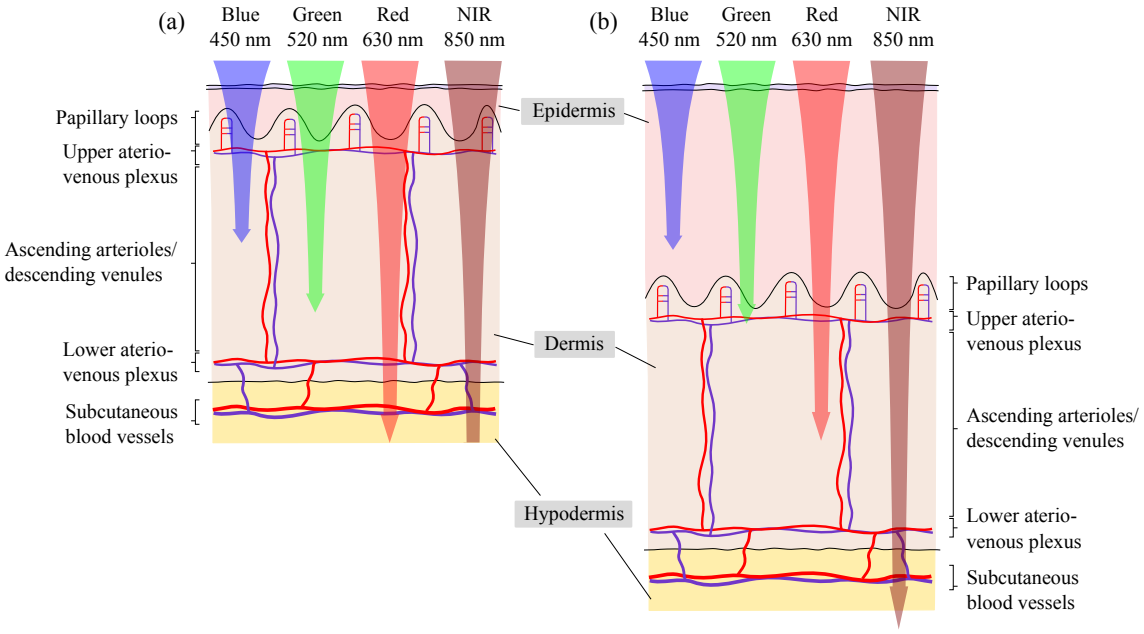

Figure 9: Penetration depth of light into the skin for different wavelengths: (a) Face/ forearm, (b) Palm. The depicted depths represent an average value of calculated depths values based on absorption and scattering coefficients from different authors [27, 285, 325, 399] (see also A.1, Table 14).

water [174]. In the literature, the provided depth values vary strongly as factors like the experimental setup, anatomical differences, and the skin type highly affect the outcome [20, 27, 174, 287]. Based on selected absorption and scattering coefficients for the epidermis and dermis, the penetration depths for different body sites and wavelengths were calculated (see Appendix A.1, Table 14). The general consensus is depicted in in Fig. 9. For the face, only red and NIR light likely reaches down to the deeper net plexus and even to small subcutaneous arteries. In contrast, blue and green light does not travel further than to the reticular dermis. For the palm, green light barely reaches the papillary dermis and only NIR light likely travels down to the deep plexus and smaller arteries.

2.4 PHOTOPLETHYSMOGRAPHY

2.4.1 *Functional Principle*

Photoplethysmography (PPG) is an optical measuring technique which allows the assessment of blood volume changes in the cutaneous vasculature [9, 144]. The technique was firstly described by Hertzman [113] in 1937 and gradually became widely accepted. Nowadays, it can be considered a simple and low-cost way for vital sign monitoring that shows a broad field of application such as in clinical environments [9].

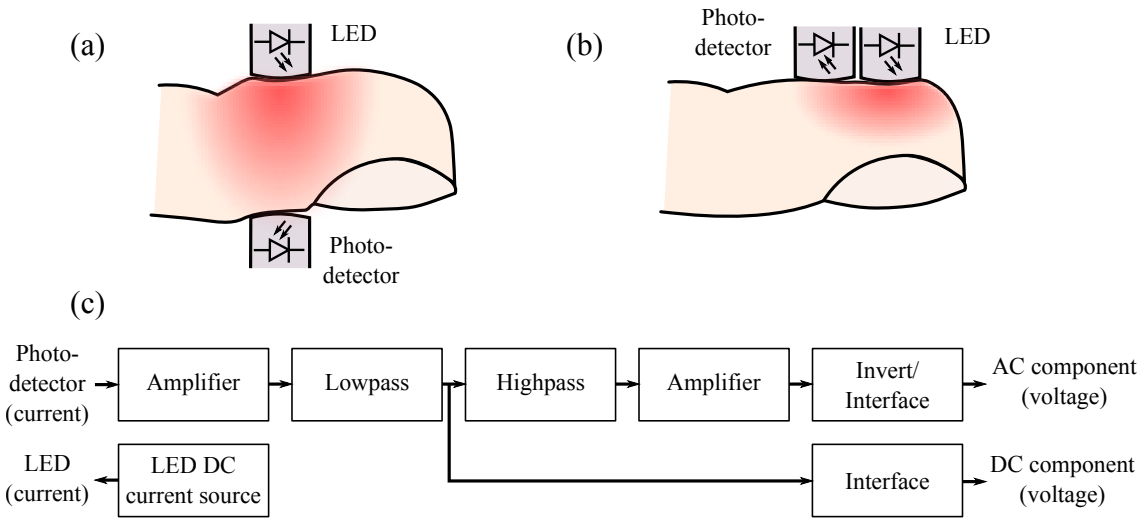

Figure 10: Functional principle of a PPG system: (a) PPG sensor on transmission mode, (b) PPG sensor in reflective mode, (c) Common signal processing steps in the circuit unit of the sensor. For the two modes, the diffuse light distribution within the skin tissue is illustrated (red). (Fig. (c): based on figure in [9, p. R5])

Instrumentation and Signal Acquisition

The main elements of a modern PPG sensor are a light emitting diode (LED), which radiates light in a narrow bandwidth usually in the red and NIR range, and a photodetector, which captures the remitted light from the skin [369]. The sensor is attached to the skin surface, and due to the size of the two units, its measurement area is limited to only a few square millimeters. In order to make the recorded detector output accessible, the temporal signal (also called plethysmogram) undergoes varies processing steps [9] (see Fig. 10 (c)). Initially, the signal is amplified and lowpass filtered to remove high-frequency noise. Then, the alternating component is normally separated from the static component using a highpass filter and amplified again before it is eventually inverted. There are two operation modes for PPG, the reflective mode, where detector and sensor are placed next to each other, and the transmission mode where detector and sensor are positioned on the opposite side of a body part [144]. Figure 10 (a) and (b) illustrate the principles. While the transmission mode restricts the application to finger, toes and ear lobes, the reflective mode permits an application to any body site [9]. Although the differences in plethysmograms of the modes supposed to be minor, certain factors like the photon path way affect the outcome nonetheless [272]. Whereas in the transmission mode, the mean path way between sensor and detector can be described by a line, in the reflective mode, analyses suggest a banana-shape path. Furthermore, probes of the reflective mode often apply less pressure on the skin tissue which causes venous vessels to be less collapsed and oscillations from this vasculature to be more prominent to some extent in the respective plethysmograms [302].

Signal Origin

As presented in the previous Section 2.3, light undergoes reflection, refraction, scattering and absorption when it penetrates the skin. The light, which is captured by the detector, is attenuated due to scattering and absorption. The modulation of this attenuation by physiological processes plays the essential role for achieving a valid PPG signal [144]. As will be explained later in more detail, the raw plethysmogram consists of two main components, a static part (DC - direct current) and an alternating part (AC - alternating current) that can be further subdivided into a high and low frequency component AC_{HF} and AC_{LF}. Since blood's hemoglobin shows a significantly higher absorption than the surrounding bloodless tissue[5], changes in the blood volume represent the key factor for the modulation of the AC component [35]. When the BP changes within the cutaneous and subcutaneous vasculature, compliant vessels will expand or contract in accordance with the pressure (see Section 2.1 and Table 3). The change in the cross-section also changes the blood volume within the considered measurement region and, therefore, leads to the modulation of the incoming light [35, 272]. Especially the cardiac cycle imposes such changes [9]. Since respective cyclic variations are prominent in the arterial vasculature (see Fig. 3 (c)), arterial pulsations play the major role for the AC signal [272]. Figure 15 (a) and (b) illustrate the principle. Besides blood volume changes, two further factors might influence the pulsatile component in the plethysmogram. The first one is the blood flow velocity [237, 275]. The velocity also periodically changes with the cardiac cycle (see Fig. 3 (d)) and is related to erythrocytes' orientation which affects the attenuation of the incident light. Challoner [57] demonstrated the presence of this effect in PPG signals when using a rigid glass tube. The second factor is blood vessel wall movement as shown by Weinman et al. [372]. For this effect, scattering is most likely the dominant modulating property. However, since the group investigated bigger arteries, Nijboer et al. [237] later doubted that the effect would apply to the smaller vasculature.

Signal Characteristics

Figure 11 (a) and (b) examplarily depict a raw plethysmogram and its amplitude spectrum for a 10 s time period. The main frequency component AC_{HF} (0.5 - 2 Hz) is related to the cardiac cycle and only represents about 0.1 % of the full signal's intensity [120]. In fact, around 90 % of the incident light is attenuated by bloodless tissue and another approximate 10 % is either absorbed by static blood fractions or modulated by a varying blood volume in the arterial and venous vasculature [9, 120]. By convention, the displayed signal is inverted[6] so that the systole of the heart beat also corresponds to a maximum [272]. The low frequency variations AC_{LF} (0.01 - 0.5 Hz) in the plethysmogram are caused by respiration, BP control mechanisms (Mayer waves), thermoregulation, and general vasomotor activity like vasomotion [50, 108, 241, 257, 304]. Consequently, changes of the vasomotor vessel tone

5 The absorption coefficients of blood (80 % oxygenation) and the dermis (*in vitro*) are [285, 325]: 450 nm: 300 vs. 6.0 cm^{-1}, 520 nm: 200 vs. 3.0 cm^{-1}, 630 nm: 80 vs. 1.4 cm^{-1}, 850 nm: 74 vs. 1.0 cm^{-1}.

6 Note: If the DC component is not removed from the signal, the component is displayed inversely as well.

plays an important role for these variations, but also the control of precapillary sphincter muscles is partly relevant [9, 144]. Alterations in the venous vasculature, due to oscillations in the intra-thoracic pressure, form the primary factor for induced respiration variations [239]. Eventually, all mechanisms affect the blood volume inside the measurement region. Their manifestations, however, differ between the body sites [8]. It is important to note that changes in the DC and AC_{LF} component might also impact the AC_{HF} component since the amount of blood proportionally influences both fractions [272].

In addition to specific frequency features, the plethysmogram can be characterized by features in the time domain such as beat-related attributes (see Fig. 11 (c)). The PPG beat consists of the anacrotic phase, which holds a rising edge and ends in a systolic maximum, and the prolonged catacrotic phase which ends in a minimum that corresponds to the diastole [11]. The latter phase usually shows a dicrotic notch resulting from the superposition of the forward travelling pulse wave and the reflective wave [9]. The beat's pulsatility including the manifestation of the notch generally increases with a higher compliance and lower peripheral resistance [247]. There are numerous beat features that hold a high diagnostic value, which either concern the pulse shape contour and amplitude, or are derived from temporal assignments to other physiological measures (e.g. PTT - pulse transit time) [79].

Signal-Pressure Dependence

The relation between the BP and the plethysmogram is worth studying as it provides a better understanding of the signal's origin and enables new applications of the technique (see Section 2.4.2). Formula 1 states that for a steady compliance, a higher transmural pressure involves a higher vascular blood volume. However, since the compliance is not steady, the relation is not linear and, in fact, even depends on the pressure itself [272]. Langewouters et al. [175, 176] showed that the vessel diameter and cross-sectional area bear a sigmoid relationship to the intravascular pressure (see Fig. 12 (a)). Reisner et al. [272] confirmed this finding regarding the PPG output. They also noted that intra-beat pressure changes impose hystereses on the relation and that vessels are generally less compliant during these changes than during inter-beat variations.

In a similar way as the physiological BP affects the outcome of the plethysmogram, the external pressure (e.g. by cuff or probe) plays a role [21]. With an increasing contact force, the magnitude of the DC component gradually increases while the magnitude of the AC_{HF} component first increases and then gradually decreases [333] (see Fig. 12 (b)). When the external pressure rises, the arterial wall is compressed which allows the vessel to become more compliant (AC_{HF} magnitude's maximum) up to the state in which the transmural pressure reaches zero ($P_i = P_e$) [272, 333]. When $P_e > P_i$, the static external pressure dominates the behavior of the arterial vessel. It involves a decline in the magnitude of the AC_{HF} component up to the point where the vessel is eventually occluded.

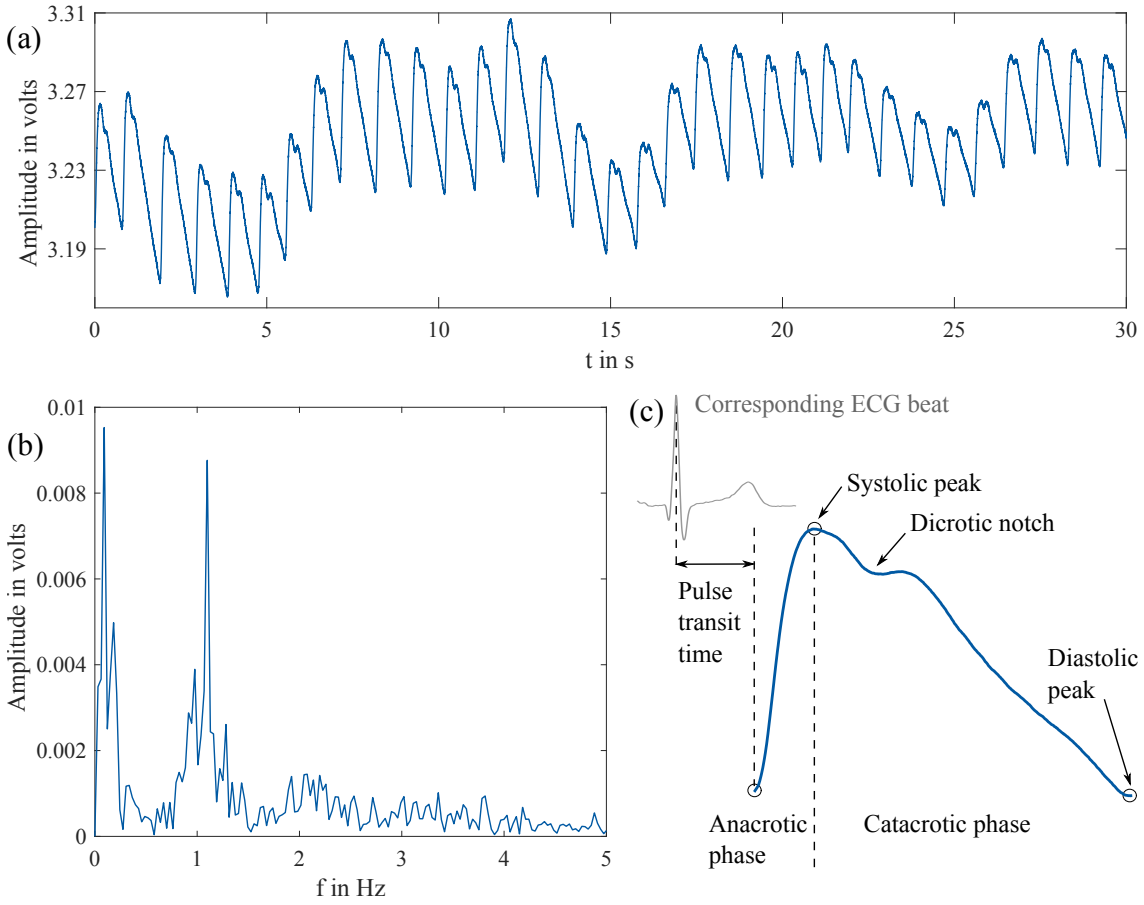

Figure 11: PPG signal characteristics: (a) Raw reflective PPG signal from finger (inverted and with DC component), (b) Amplitude spectrum for the signal, (c) Single PPG beat (smoothed) with typical features.

Signal-Wavelength Dependence

The wavelength of the emitting LED in PPG is chosen based on three factors [9]: (1) the penetration depth of light, (2) the high absorption of melanin and water in the ultraviolet and NIR range, respectively, and (3) the absorption characteristics of oxyhemoglobin and deoxyhemoglobin (see Fig. 8 (a)). Common choices are red and NIR wavelengths which usually represent a compromise between the factors [369]. As explained in Section 2.3.2, light of longer wavelengths in the visible and NIR range reaches deeper and larger vessels permitting those vessels to contribute information to the blood volume signal. Giltvedt et al. [98] compared green (560 nm) and NIR light (950 nm) using a reflective PPG setting. They monitored BP changes by applying an occlusion test and concluded that green light carries information from arterioles and NIR light already from small arteries. However, for increasing wavelengths, the absorption by water increases approaching similar values like the important attenuator hemoglobin [27]. Since hemoglobin is essential for obtaining a pulsating blood volume component (see above), its absorption behavior should be taken into consideration. Cui et al. [71] investigated wavelengths between 420 and 940 nm with a reflective PPG probe and determined the the signals' pulsation strength (AC_{HF} component).

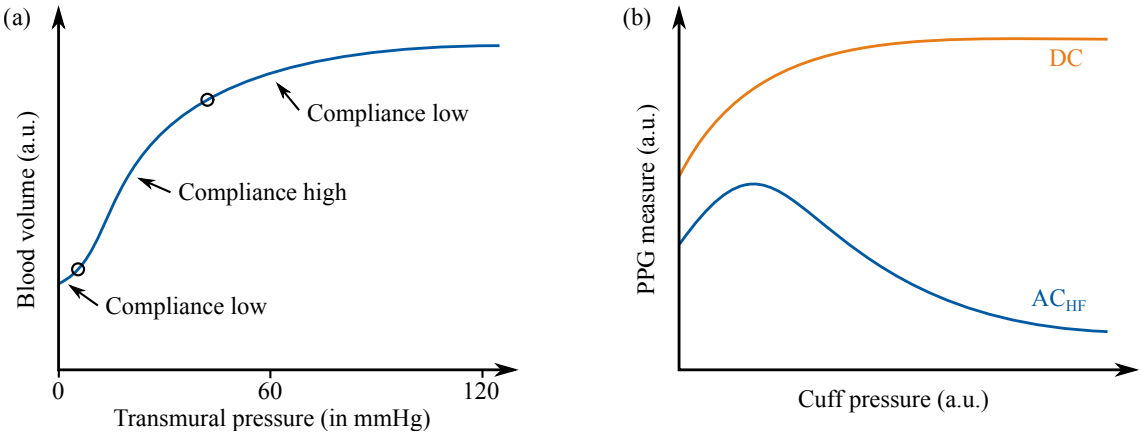

Figure 12: Impact of the transmural and extravascular pressure on PPG related measures: (a) Vascular blood volume in relation to transmural pressure in a finger artery, (b) Behavior of PPG signal components DC and AC_{HF} when applying an external cuff pressure. Note: For (a), intra-beat changes impose hystereses on the curve. (Fig. (a): based on figure in [176, p. 47], Fig. (b): based on figures in [333, pp. 1329-30])

The author observed maximal values between 510 and 590 nm which coincides with local maximums in the hemoglobin's absorption spectra (see Fig. 8 (a)). Although hemoglobin has a similar strong characteristic for blue wavelengths, the pulsation was small in this range. This outcome can be attributed to the low penetration depth since the vessels' pulsatile character is low in superficial dermal layers [27, 43] (see Table 3 and 14).

Further Signal Dependencies

Besides the mentioned factors (body site, operation mode, pressure, wavelength), there are numerous further elements that affect the shape, size, and frequency components of the PPG signal [144, 272]. Figure 17 gives an overview of technical, anatomical and physiological elements which are relevant. Apart from the general impact of BP changes, the ANS plays an important role as it controls the vessel compliance and the blood volume in the vasculature of interest.

2.4.2 *Applications*

Since the invention of PPG, the technique has been applied and validated in various settings and environments [7]. Applications of PPG involve the determination of physiological measures such as the HR, respiration, BP, blood flow, oxygen saturation, and cardiac output, as well as the assessment of the arterio-venous vasculature and of autonomic functions [9, 57, 144, 272].

As stated above, the plethysmogram's AC_{HF} component is related to the cardiac cycle. Therefore, the HR information can be extracted straightforwardly using methods in the time domain like zero-crossing, frequency domain techniques or approaches which utilize both domains [232, 385, 396]. The reliability of such procedures is generally affected by

movement and cardiac arrhythmia [9]. Nevertheless, proper signal processing methods allow PPG-based HR monitoring to be applied successfully during activities, for diseased subjects, in clinical environments, and in sleep studies [89, 138, 377, 389, 396].

The physiological dependence of the blood volume on the BP and the visual resemblance of respective signals led researchers to model transfer systems between the plethysmogram and the BP signal [10, 218]. Moreover, selected features of the PPG pulse contour can be exploited to build a predictor for the DBP and SBP [169, 324, 332]. Despite the convenience of only requiring PPG to determine the BP, other approaches have been developed that combine the technique with additional instruments. Peñáz [256] introduced the volume clamp method which estimates the continuous BP from a pressure controlled finger cuff which is set to flatten the pulsation in a simultaneously captured plethysmogram. The technique was commercialized by Finapres® (Finapres Medical Systems BV, Enschede, The Netherlands) in the 1980s and extensively tested and studied in numerous settings and situations [9, 130]. An established non-invasive way to determine the SBP on a PPG basis exploits the surrogate measure PTT [235, 240]. The PTT is normally calculated as the temporal shift between the R-peak in the electrocardiogram and the diastolic point in the plethysmogram [9] (see Fig. 11 (c)). It is set to represent the travelling time of the pulse wave from the heart to a distal point and, therefore, highly correlates with the pulse wave velocity which itself correlates with the BP [192, 272]. However, the PTT approach has limits since the R-peak is not a good marker for the actual mechanical systole and since the PTT is strongly affected by the arterial compliance where variations are not properly considered in the typically applied calibration schemes. [242, 255, 272, 397].

As mentioned in section 2.4.1, the frequency components of the plethysmogram are influenced by activities of the ANS. Applications concerning the AC_{HF} component, for example, assess the HR variability which provides information about autonomic functions that can be linked to the cardiovascular health [144, 330]. PPG is also applicable to analyze the microvascular circulation when reactions in the ANS are induced by external stimuli like temperature changes, inspiratory gasp challenges or simply by medication [9]. The strength of the AC_{HF} and DC components is controllable through the vasomotor tone [243, 244]. Kamal et al. [144] demonstrated that an increase of the ambient temperature from 15 °C to 25 °C within 10 min leads to an gradual increase in the strengths of both components (DC inverted) caused by vasodilation. In the same way, the thermoregulatory vasoconstriction can be induced by a cold stimulus [155]. Medication-induced changes were studied with respect to anaesthesia [177, 236]. A reduced variability in the lower frequency components (0.01 - 0.15 Hz) of the PPG signal suggests that the sympathetic activity as inhibited during anaesthesia and that blood volume changes are mainly a result of PP changes.

PPG provides an easy way to assess age and disease-related variations in the vasculature [9]. With increasing age, vessels become stiffer which involves an elongation of the anacrotic phase and an attenuation of the dicrotic notch [11]. Similarly, the severity of vascular diseases is determinable as it comes with the damping, delay and diminishment of the peripheral pulse [66, 170, 308].

Other applications of PPG include monitoring of the respiration and the arterial oxygen saturation [153, 172, 238]. The latter one can be accomplished by capturing plethysmograms at two separate wavelengths where the absorption characteristic of hemoglobin and deoxyhemoglobin differ significantly (e.g. red and NIR) [9]. The ratio of the respective two AC_{HF}/DC ratios is correlated to the oxygen saturation and can be used for calibrating PPG-based oximeters.

2.5 CAMERA-BASED PHOTOPLETHYSMOGRAPHY

2.5.1 *Functional Principle*

Camera-based photoplethysmography (cbPPG) is an optical measurement technique that allows the assessment of blood volume changes in the (sub-)cutaneous vasculature by utilizing video cameras [35, 381]. Figure 13 depicts the functional principle. As can be seen, the technique bases on the key ideas of the classical PPG where incident light is modulated by physiological processes in the skin and a re-emitted fraction is captured by a detector (see also Fig. 10). For cbPPG, the detector is a digital camera sensor combined with a lens. Three major advantages evolve from this instrumentation [326, 376, 381]:

- *Remote setting*: No contact is required between the skin and the camera/ light source.
- *Ambient light*: No dedicated light source is required; ambient light is sufficient.
- *Spatial assessment*: The camera sensor provides spatially resolved information about the skin area of interest enabling the acquisition of locally distributed cbPPG signals.

Instrumentation and Signal Acquisition

The camera sensor can be described as a two-dimensional array of photodetectors in which incoming photons induce an electrical charge [199]. For each detector element (or pixel), the charge is repetitively readout and reset with a specific frequency [233]. This frequency determines the number of images that are obtained in one second by the camera and is called frame rate. The pixel-related charges are converted into voltages which are then amplified and digitized with a certain precision (referred to as color depth) [74, 199]. Figure 13 (b) visualizes the procedure. As a result, digital images can be formed. They are defined as pixel arrays of values that are proportional to the occurring light intensity and the exposure time of the sensor [74]. It is important to note, depending on the setting, an image pixel may contain the information of several sensor pixels [233]. In certain camera models, optical color filters are attached to the pixels in an alternating manner (see Fig. 13 (b)) [74]. For a red, green, and blue (RGB) color configuration, each image is describable by three separate channels. The respective cameras are referred to as RGB cameras and are widely used since additive mixing of red, green, and blue intensities reproduces any appearing color in the visible spectrum [277]. In contrast, cameras with no or only one type of filter are called monochrome cameras.

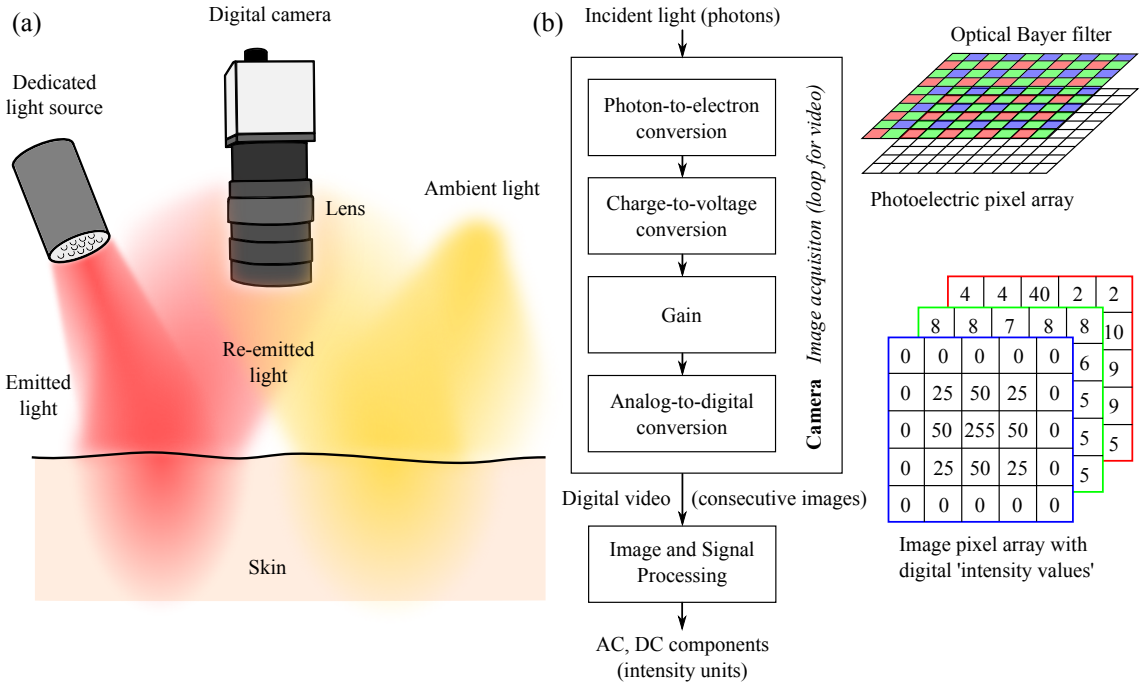

Figure 13: Functional principle of a cbPPG system: (a) System in reflective mode operating with ambient light and a dedicated light source, (b) Simplified processing structure comprising the main steps inside and outside the camera. Here, an RGB camera is depicted where an optical filter allows to create a three-channel digital image which contains information of the red, green and blue light ranges. (Fig. (b): based on figures in [199, pp. 200,204])

After image acquisition, the emerging video stream has to be further processed to yield suitable cbPPG signals[7]. For a fixed exposure time and stable environment conditions, in theory, the temporal value of each image pixel represents the unfiltered output of a single PPG sensor. In practice, a single pixel track usually does not bear much physiological information due to degradation by noise [348]. There are numerous kinds of noises (e.g. photon shot noise, dark current shot noise, thermal noise, reset noise, quantization noise) which arise during the operation of the camera and eventually affect the image [74, 125]. Although the noise is not always fixed, as it can be dependent on time, temperature, and signal (intensity value), spatial averaging in the image generally decreases the noise's impact [125, 185]. For cbPPG, the averaging of several pixels[8] values significantly enhances the quality of the resulting temporal mean, i.e. the plethysmogram (see Fig. 14). To a certain degree, an increasing number of pixels also leads to a stronger manifestation of the physiological signal components [150, 348]. Figure 14 (b) shows that larger sizes of a so-called region of interest (ROI) involve a better noise cancellation as well as a higher stationarity in the cbPPG signal. However, larger sizes also cause the inclusion of local skin areas that provide signals which might differ in phase and amplitude [147, 348]. In this

7 Note: In this work, the term "cbPPG signal" and "(camera-based) plethysmogram" are used interchangeably for the output of a cbPPG measurement system.
8 In the following chapters, the term "pixel" usually refers to the image pixel, not the physical sensor pixel.

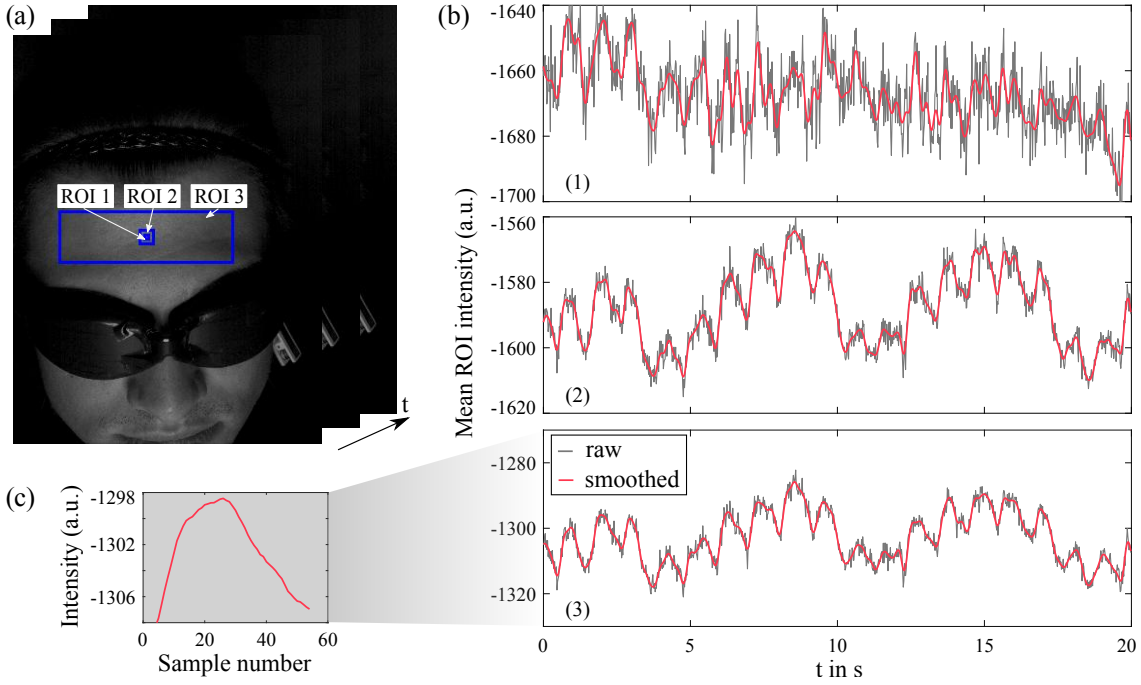

Figure 14: Signal extraction in cbPPG: (a) Video stream (images) with the selected ROI 1 (5×5 pixels), ROI 2 (15×15 pixels), and ROI 3 (180×55 pixels), (b) Extracted cbPPG signals (inverted) for the three ROIs, (c) Averaged beat (smoothed) of the single beats from signal (3). For recording, a monochrome camera and a dedicated light source at a peak wavelength of 518 nm was used.

case, averaging over the whole ROI can diminish the pulsation strength in the resulting plethysmogram [148] (see Fig. 14 (b)-(2) vs. (3)).

Two major advantages in cbPPG, the remote application and the spatial assessment, arise from the possibility to obtain focused images which permit the local assignment of pixels to skin areas in the field of view. In 1998, Blazek [34] was the first to propose a cbPPG system realizing these two advantages. Based on the invention, Blazek and Wu et al. [35, 381] demonstrated how arterial and venous blood volume changes can be measured using a monochrome camera and an NIR light source. Early works primarily followed the instrumental principle of PPG as dedicated LED lighting in the the red and NIR color ranges were adopted [119, 121, 123, 376]. Later studies also employed light sources in the blue, green, and orange range [120, 147, 299, 339]. A milestone was set by Takano and Ohta [326] in 2007 who revealed cbPPG to function exclusively with broadband ambient light. In 2008, Verkruysse et al. [348] corroborated the sufficiency of ambient light (daylight with artificial fluorescent light) and additionally proved that cbPPG is applicable with a consumer RGB camera. Two years later, Poh et al. [262] showed that even a simple RGB webcam can be utilized. These findings established the convenience of camera-based vital sign monitoring. Nowadays, most cbPPG systems operate with common RGB cameras and ambient light [209]. The fact that the camera does not have to be in close proximity to the subject plays an important role in those systems. However, various studies demonstrated maximal distances to be between 100 and 150 m resulting from the performance of lenses

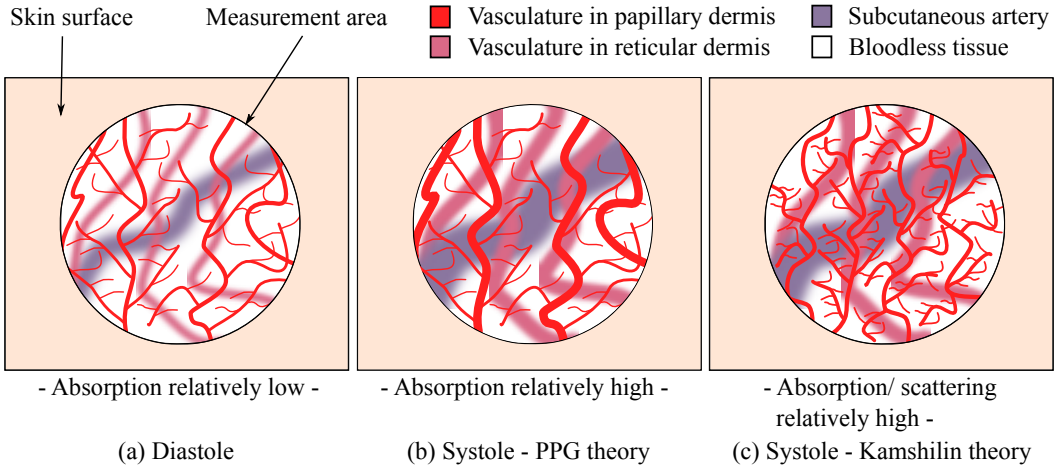

Figure 15: Measurement principle in PPG and cbPPG for the arterial skin vasculature: (a) Vasculature during the diastolic phase in cardiac cycle, (b) Vasculature during the systolic phase according to the conventional PPG theory, (c) Vasculature during the systolic phase according to the theory by Kamshilin et al. [145, 149]. The effect of vessel expansion is amplified for the sake of visualization.

and atmospheric conditions (outdoors) [29, 81, 347]. Despite the similarities between PPG and cbPPG, cbPPG is rarely employed in the transmission mode since directed light sources are necessary and a respective application is mainly restricted to the finger [15, 119, 121, 202, 228, 381].

Signal Origin

Although the functional principle of cbPPG strongly resembles the one of PPG, the origin of the captured physiological information is not completely clarified yet [339]. The most obvious theory supports the model of the conventional PPG in which blood volume changes are the key factor for affecting the back-scattered light from the skin [9] (see Section 2.4.1). In this case, the camera-based plethysmogram can also be divided into a DC, AC_{LF} and AC_{HF} component. The model bases on the fact that compliant vessels in the cutaneous and subcutaneous vasculature change their diameter in accordance with BP changes and fluctuations in the vasomotor tone (see Section 2.1, Table 3). These variations involve changes in the blood volume which lead to the eventual modulation of the incoming light since the blood's hemoglobin has a significant higher absorption coefficient (visible and NIR range) than bloodless tissue [120, 272]. As mentioned in the previous section, arterial pulsations play the major role in shaping the AC components where especially the cardiac cycle imposes high power fractions. Figure 15 (a) and (b) illustrate the model's principle for the diastole and systole of one cycle. Early works in cbPPG adopted the blood volume theory demonstrating the acquired waveforms[9] to have high resemblance to the conventional plethysmogram in terms of its shape, signal power and modulation of the AC components by respiration and heart activity [119, 123, 202, 348, 381]. Verkruysse et al.

9 Like the PPG signal, the cbPPG signal is often displayed inversely where high values reflect a high blood volume.

[348] confirmed the theory by revealing that the green channel of an RGB camera provides the strongest AC_{HF} signal. This outcome coincides with the absorption characteristic of hemoglobin (see Fig. 8) and proves the blood volume to be a defining factor. Other works contributed to the theory by showing that externally induced changes in the arterial and venous blood volume reflect in the captured cbPPG signal [35, 148, 234, 381]. Based on waveform analyses, simulations and pulse oximetry investigations, more recent studies also reached the conclusion that the classic PPG model applied to cbPPG [228, 229, 349].

Challenging the blood volume theory, Volkov et al. [356, 357] attempted to shed more light on the origin of cbPPG signals utilizing nail fold video-capillaroscopy. They demonstrated that the velocity signal of erythrocytes in capillaries strongly resembles the cbPPG signal within an adjacent region. While the authors ruled out the velocity itself to be a modulating factor in cbPPG, the associated change of the blood cell's orientation was considered to play a role (see Section 2.4.1). However, they settled with another theory in which the capillary density emerges as the determining factor (described in next paragraph). Moço et al. [229] also analyzed the nail fold via video-capillaroscopy. Contradicting the study by Volkov et al., it was found that the occurrence of strong cbPPG signal amplitudes is independent of the prevailing capillary density.

Kamshilin et al. [149] were the first group who doubted that high AC_{HF} values in the green light range actually arise from a varying blood volume due to pulsating vessels. They claimed, there is a low probability of green light to interact with such vessels which supposedly are rather located in subcutaneous layers. Furthermore, it was argued that the conventional PPG model cannot explain why nearby skin regions may provide counterphase cbPPG signals as observed by Teplov et al. [334]. The group proposed a new model which presumes solely deep-lying arteries to show relevant oscillations of the transmural pressure. These oscillations periodically deform the adjacent tissue in the dermis where resulting stresses reach up to the stratum corneum. The deformation also synchronously changes the density of capillaries in the papillary dermis. According to the model, scattering and absorption will increase with a higher degree of deformation what eventually causes the modulation of the light intensity. The authors demonstrated that the compression of the skin by an external force enhances the modulation as a consequence of this effect. While Kamshilin et al. initially did not address the role of blood in their theory, later, they acknowledged the blood volume to be a modulating factor stemming from the density variation of the capillary bed [145]. However, only Volkov et al. [357] clearly defined absorption as the dominant attenuator in this context based on the influence of hemoglobin. Figure 15 (c) illustrates the idea. Sidorov et al. [306] further applied the new model to the results of experiments in which NIR light was used. As also stated in [145, 149], they suggested that for longer wavelengths, the effect of dermis deformation is diminished in favor of the classic blood volume effect (see above).

Another mechanism which can add physiological information to the cbPPG signal is called ballistocardiographic (BCG) effect [225]. It leads to a cyclic body motion caused by the forces of blood movement in the heart and arteries, as well as the heart movement itself

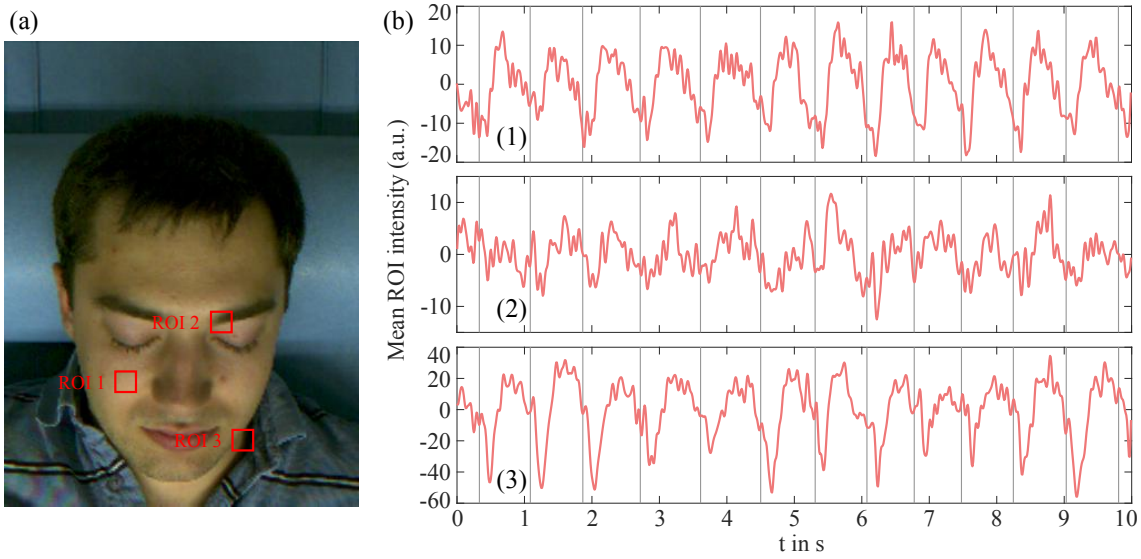

Figure 16: Different physiological signals extracted from the video recording: (a) Video image with selected ROIs, (b) Averaged ROI intensity values from the green channel (inverted and bandpass filtered between 0.5 and 15 Hz). Signal (1) represents a true cbPPG signal, (2) a signal degraded by global BCG artifacts, and (3) a signal degraded by local BCG artifacts from the carotid artery. The gray vertical lines depict the R-peaks' position of the reference electrocardiogram. Note: The amplitudes of the three signals differ substantially.

[99]. In this work, that mechanism is declared as *global BCG effect*. Additionally, the term *local BCG effect* is introduced describing a regional displacement of a skin area due to the pulsation force of subjacent vessels [226]. Both type of effects can be exploited to extract the HR from videos [24, 93, 297, 301] but are considered artifacts when true plethysmographic signals are demanded [32, 225, 226]. Moço et al. [225] quantified the impact of global BCG effects for the face area in cbPPG videos. The impact was found to become stronger when the incident light angle was not orthogonal with respect to the skin surface. In this case, especially high-contrast regions like skin edges and facial features contribute to the motion-based intensity modulation. Such regions provide BCG signals (or artifacts) which might superimpose with wanted plethysmograms. The group demonstrated that homogeneous and orthogonal illumination generally minimizes the problem although non-uniform face regions remain as potential BCG signal source. Figure 16 depicts an example where those kind of regions led to the degradation of the cbPPG signal. It should be noted that global and local BCG waveforms are wavelength independent, might hold high energies at the HR's harmonics and can prevail the power of corresponding plethysmograms [225, 226, 228]. By focusing on the wrist area, Moço et al. [226] also studied local BCG effects. The effects' influence increased in the vicinity of large arteries if inhomogeneous and lateral illumination was applied. The group illustrated that different orientations of the skin surface towards the light source could cause complete phase shifts in resulting BCG signals. Again, homogeneous lighting diminished the effects. Nevertheless, some BCG patterns remained present, particularly at high-contrast regions (skin texture, edges, wrin-

kles). Figure 16 depicts a degraded cbPPG signal at the carotid artery. This area was often found to provide strong physiological signals where the underlying effect was not always understood by the authors [13, 16, 181, 348].

As in PPG, the wavelengths of the used light range play an important role for the outcome in cbPPG due the skin's optical properties (see Section 2.3.2). Whereas for PPG, dedicated light sources with selected spectral ranges are employed, for cbPPG, these ranges can be simply determined by the camera's RGB filters which separate the incoming broadband light. Corral et al. [67, 203] investigated what light spectrums within 380 and 980 nm are optimal for the application of non-contact PPG. Regarding the AC_{HF} component, the strongest signal-to-noise ratio (SNR) was found for wavelengths between 480 and 610 nm as well as 800 and 925 nm. However, the first band provided about three times higher SNR values than the latter one. More recently, Blackford et al. [30] conducted a similar experiment and achieved essentially the same SNR response across the spectrum. These results coincide with prior findings for contact PPG [71] and are largely in accordance with the absorption characteristic of hemoglobin (see Fig. 8 (a)) defining the blood volume as dominant modulation effect. Interestingly, the absorption in the blue range is high while the SNR was reported to be low there. This behavior can be attributed to the shallow penetration depth of blue light (see Fig. 9). To that end, various researchers argued the penetration depth to be generally smaller in cbPPG than in PPG caused by the different emitter-sensor geometry/ setup [120, 348]. The missing sensor contact, for example, was indeed shown to affect the cbPPG signal as external pressure on the skin significantly increased the strength of the AC_{HF} component [149, 228, 306]. Kamshilin et al. [149] rejected the known idea of a changing vessel compliance to be the reason for this phenomena (see Section 2.4.1 and Fig. 12) and promoted their deformation theory. Moço et al. [228] claimed that an external force occludes the superficial vasculature and leads to the light's interaction with deeper vessels which are supposedly dilated because of the force's stimulation. This concept of superficial occlusion was backed by a later study where spectroscopic measurements and cbPPG simulations showed that, in case of tissue compression, the blue-green wavelength range is strongly affected while in the red-NIR range, only minor changes were observed [229].

Signal Characteristics

In the previous section, it was described how emitted light in PPG is attenuated and modulated by the different constituents of the skin. Although the exact model is hard to transfer to cbPPG, one can assume a similar characteristic where most of the light is attenuated by bloodless tissue and only a smaller portion is either absorbed by a static blood volume fraction or modulated by varying fractions in the arterial and venous vasculature [35, 120, 381]. Despite the resemblance, caution is advised when interpreting the captured cbPPG signal. Changes in the DC component are not solely of physiological origin but are also affected by variations in the ambient light, movements, ROI fluctuations, and adjustments in the camera parameters [167, 252, 321, 348, 383]. Moreover, these changes have impact

on the AC components [269]. Liu et al. [189] analyzed the relation between the AC_{HF} (linked to cardiac cycle) and the DC component by varying the light source's intensity for steady camera settings. The group revealed a linear dependence as more emitted light also increases the re-emitted alternating fractions. Accordingly, Verkruysse et al. [348] reported that lighter appearing skin areas yield higher magnitudes in the AC_{HF} component. In order to avoid the dependence, relative amplitudes can be considered by using the ratio AC_{HF}/DC [149, 228, 367]. In this way, respective oscillations are quantifiable independent of the absolute light intensity. Hülsbusch [120] estimated possible values for the relative AC_{HF} component with regards to the (reflective) cbPPG application. The results amounted to approximately 1.5 % for the blue wavelength range, 2 % for green and 0.1 % for red and NIR.

Similar to the PPG signal, the low frequency part AC_{LF} of the cbPPG signal contains information about different mechanisms in the body [32, 348]. Observed variations ≤ 0.1 Hz were claimed to be associated with vasomotion and Mayer waves [122, 123, 202]. Blanik et al. [32] actually proved the presence of the vasomotor rhythm (around 0.1 Hz) based on the outcome of allergic reactions at the skin. Variations above 0.1 Hz and below the HR were shown to be related to the respiratory cycle [41, 328, 376]. Besides the modulation of the blood volume[10], the respiration also induces signal oscillations through the breathing-synchronous motion of body parts [142, 403]. Tarassenko et al. [328] argued this motion to be a dominant factor as smaller ROIs provided stronger magnitudes in the respiratory frequency range. Verkruysse et al. [348] acknowledged the impact of motion as non-plausible phase shifts between respiration signals of adjacent skin regions occurred. In contrast to findings in the PPG field (see Section 2.4.1), no cbPPG studies were found that analyzed whether thermoregulatory functions reflect in the AC_{LF} component.

Further Signal Dependencies

As mentioned in the previous paragraphs, there are many factors which directly and indirectly shape or impair the cbPPG signal. Figure 17 gives an general overview on technical, anatomical and physiological determinants. The following list further discusses aspects that are particularly relevant in cbPPG:

- *Sensor noise*: The camera introduces broadband noise to the cbPPG signal [120]. The impact of certain noise sources increases with a decreasing light density (darker image) which might compromise the manifestation of the plethysmographic waveform [82, 233].
- *Color depth*: The color depth (given in Bit) defines the intensity resolution. A strong pulsation at the AC_{HF} component would cause oscillations of about 40 units for 12 Bit, 10 units for 10 Bit and only 2 to 3 units for 8 Bit (based on values in [120]). Therefore, spatial averaging is especially important to overcome this resolution limitation including the quantization noise [116, 209, 362].

10 The (camera-based) blood volume signal is modulated by the respiration in three ways: (i) Oscillation of the baseline, (ii) variation of the pulsation strength in AC_{HF}, (iii) HR variability [403].

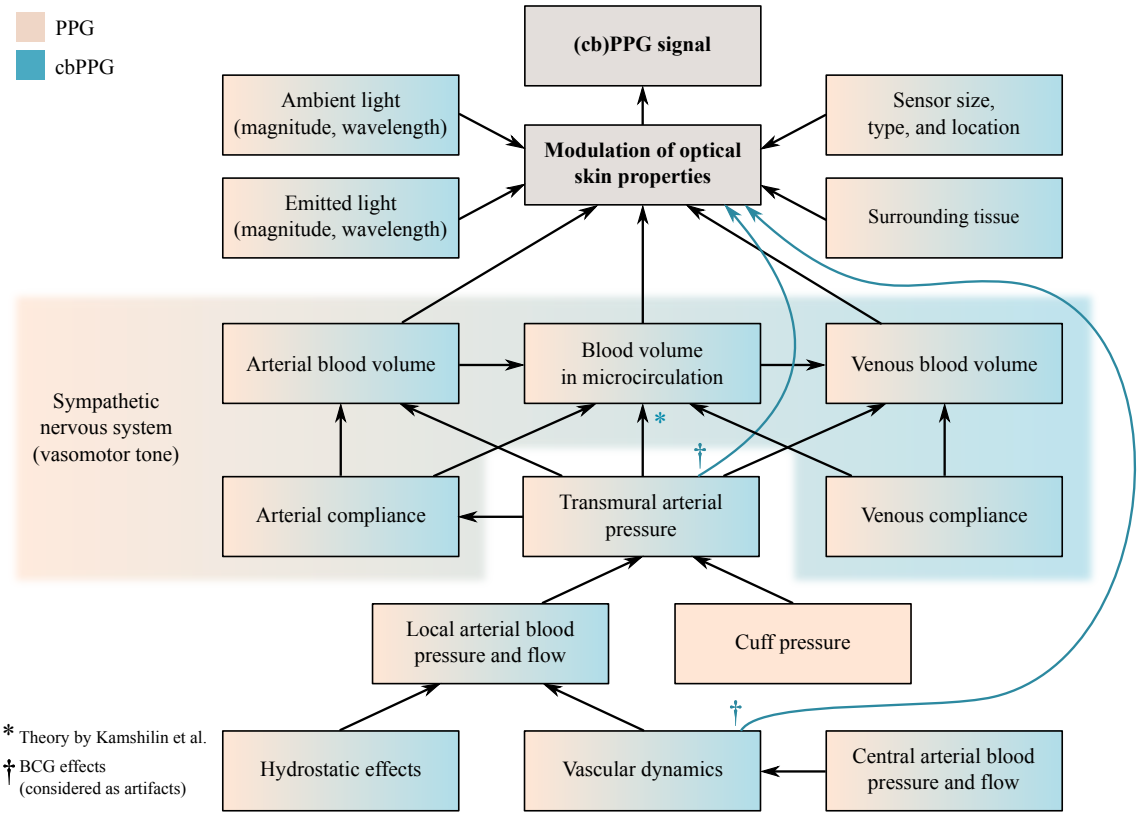

Figure 17: Factors that directly and indirectly influence the outcome of the (cb)PPG signal. Effects by skin temperature changes can be attributed the sympathetic nervous system and are, therefore, implied as well. (based on figure in [272, p. 951])

- *Frame rate*: Frame rates of cameras used in cbPPG are often ≤ 30 fps (e.g. [41, 148, 262, 328, 362]). Such rates lead to a low temporal resolution of the cbPPG signal hindering a correct mapping of distinct characteristics like the dicrotic notch or systolic peak [323].
- *Optical filter*: The filters in an RGB camera allow the simultaneous detection of light from different wavelength bands [233]. However these bands usually overlap causing cross-sensitivities between the three color channels [189].
- *Body site*: The cutaneous physiology and anatomy make certain body areas more applicable for optical assessment than others [344] (see Section 2.3.1). In cbPPG, face and hand regions proved to be suitable measurement sites (e.g. [137, 147, 322, 328, 348]).
- *Artifacts*: Due to the general low signal strength (AC_{HF}/DC) and the nature of the sensor-detector geometry, cbPPG is very susceptible to movements and light fluctuations [116].

2.5.2 *Applications*

Heart Rate, Respiration, and Oxygen Saturation

The HR[11] is the primarily investigated parameter for cbPPG applications [209, 280]. Numerous approaches have been proposed for the extraction of the HR from obtained cbPPG signals [109, 280]. In addition to the concept of peak detection in the time domain, such approaches make use of the Fourier transform [2, 262, 269, 395, 402], wavelet transform [23, 41, 84, 110, 323], auto-regressive models [326, 328], and learning-based methods [117, 118, 154, 380] to achieve a reliable HR estimation. As mentioned in the previous section, the cbPPG signal is modulated by the respiration in various ways. Applications often exploit this effect and extract the breathing rate in combination with the HR [5]. It has been demonstrated that the respiration can be precisely assessed, either from baseline oscillations [6, 323, 328, 353, 395], or from the inter-beat variability [41, 213, 263]. Besides the respiration and HR, the arterial oxygen saturation proved to be of high interest in cbPPG [403]. While some systems work with complicated setups including triggered illumination, switching filters or dual-camera arrangements to derive the parameter [84, 162, 299, 349], others simply operate with ambient light using the red and blue channel of RGB cameras [23, 83, 104, 328, 353]. At the end, all of those approaches predict the oxygen saturation by calculating the conventional ratio-of-ratios (see Section 2.4.2). Van Gastel et al. [403] were the first to propose another concept in which cbPPG signals of three different NIR wavelengths are considered concurrently.

Artifact Handling

In order to create realistic and everyday cbPPG applications, it is inevitable not to deal with disturbances concerning subject movements, light variations, and noise in general. The main goal of studies, which address those problems, is either the separation of the physiological signal component or at least the suppression of artifacts [109, 209, 280]. One way to achieve those goals is the transformation of the RGB video data into another color space since the cardiac pulsation, illumination changes and motion manifest differently there [341]. In particular the HSV, YCbCr, CIE *XYZ*, CIE *YUV*, CIE *L*a*b**, and CIE *L*u*v** spaces could be utilized successfully [41, 63, 320, 341, 386]. Another way is the employment of blind source separation techniques that allow the derivation of the undistorted plethysmographic content from a number of mixed cbPPG signals [370]. Concretely, the principal and independent component analyses are usually applied where the input signals can be extracted out of different color channels [116, 182, 194, 196, 213, 262, 342] as well as ROI locations [362, 370]. Besides the more common approaches, there are numerous customized methods which were developed to increase the robustness of cbPPG [209, 280, 366]. The ones most noteworthy will be briefly explained. De Haan et al. [400,

11 As the HR quantifies the actual pumping rate of the heart, in theory, cbPPG is only able to measure a derived quantity at the periphery called *pulse rate* [361]. For reasons of simplicity, the term HR is used here.

401] proposed model-based techniques in which optical skin characteristics in the RGB space are exploited to decompose the RGB signals into distortions and the blood volume component. Wang et al. [366] further refined those ideas by determining the pulse signal in a defined RGB plane orthogonal to the skin tone. The group also presented a data-driven approach where individual skin color spaces are created for signal extraction [364]. More recently, Wang et al. designed methods that achieve robustness by selectively filtering in the frequency domain [367, 368]. In addition to proper signal processing, the ROI selection plays an important role for the cbPPG's reliability. This subject will be discussed in Chapter 5.

Blood Pressure

Similar as in PPG, the relationship between the plethysmogram and the BP is of special interest in cbPPG [337]. In this context, the PTT may represent a simple surrogate for BP derivatives (see Section 2.4.2). It has been shown that plausible PTT estimates can be acquired when using cbPPG signals from suitable palm or face areas [150, 295, 358]. Such measurements all require the electrocardiogram's R-peak as reference. To overcome this inconvenience, studies attempted to determine transit times solely from the temporal shift between cbPPG signals of distant body sites [152, 298]. Furthermore, camera-based BCG signals were considered to substitute the electrocardiogram for calculation [227, 300]. Several investigations revealed moderate to high correlations between respective shift values and the SBP as well as the traditional PTT [137, 231, 295, 300, 318]. Some researches were even capable to predict the DBP and SBP out of single cbPPG signals utilizing specific waveform features [134, 254]. Sugita et al. [319] demonstrated how just one feature is applicable to potentially estimate the SBP. Recently, Yoshizawa et al. [387] combined different approaches in a multivariate regression model where the HR, the shift value and the pulsation amplitude were used as predictors.

Autonomic Functions

As cbPPG evolves, the remote assessment of autonomic functions also gains attention [263, 336]. On the one hand, changes in the cutaneous vasculature were analyzed when provoked by external stimuli (see Chapter 6). On the other hand, more conventional measures like HR variability parameters were obtained [209]: While some works just prove the feasibility of determining those parameters [167, 210, 216, 263, 323], others actually examined variations that were extrinsically induced [92, 131, 152, 213].

Spatial Perfusion

One of the biggest advantages of cbPPG is the possibility to spatially image physiological quantities. Numerous researches have constructed so-called perfusion maps depicting local amplitude or phase information (e.g. [147, 328, 376]). However, only a few studies exist where their clinical or diagnostic value was demonstrated. Verkruysse et al. [348] showed

that peculiarities can be exposed for malign skin treated by laser therapy. Hülsbusch [120] revealed the maps' benefit for wound assessment and Blanik et al. [32] for allergic testing. Zaproudina et al. [392] were able to image the disparities in the facial perfusion of migraine patients. Furthermore, it was reported how the maps' pattern behaves in case of temperature changes, vascular occlusion and local anesthesia [91, 148, 166, 283].

Further Applications

Besides the mentioned applications, there are several other scenarios in which cbPPG has been considered an asset. One example is the classification of living skin in video scenes [365]. The basic idea of utilizing the cardiac pulse for differentiation was also adopted to create real-life security systems where masks or pictures of faces could be correctly rejected [112, 173, 190, 245]. Another example is the employment of cbPPG for the contactless stress detection. Various investigations have described that mental stress, which was induced by cognitive tasks or visual stimuli, can be identified using parameters like the HR or HR variability [40, 92, 152, 195, 211, 213]. Dingli and Giordimaina [76] proved the camera-based HR to be a predictor of emotional states while playing computer games. Giannakakis et al. [97] were able to classify affective states by jointly assessing the HR and facial cues in videos. Furthermore, cbPPG may serve as a convenient technique (i) to examine the vasculature [35, 146, 201], (ii) to measure the jugular venous pulse [16], (iii) to monitor neuro-electrostimulation procedures [165], (iv) to estimate the skin temperature [62], and (v) to rate responses to gustatory stimuli [101].

Test Data and Environments

To a high degree, the eventual benefit of cbPPG is defined by the data for which the technique was assessed and the environments in which it was applied. Most works evaluated their methodical ideas in small groups of healthy and young subjects under controlled test conditions [109, 209, 280]. The studies that considered larger, non-laboratory, and more heterogeneous data sets are rather rare. Blazek et al. [35] were the first to employ cbPPG in a clinical environment in order to assess the dermal perfusion of patients. Scalise et al. [288] demonstrated how cbPPG can be used to monitor the HR of neonates in an intensive care unit. This idea was expanded in later investigations where not only motion, different illumination settings, and health states were taken into account but also other parameters like the infants' respiration and oxygen saturation were determined [2, 31, 159, 353, 403]. Tarassenko et al. [328, 352] presented a new cbPPG approach which allowed a reliable vital sign measurement for patients during dialysis sessions. Couderc et al. [68, 69] analyzed subjects undergoing cardioversion and could prove atrial fibrillation to be detectable by cameras. Yan et al. [384] were also able to remotely identify atrial fibrillation when simply utilizing a smartphone camera. Other clinical studies include the application of cbPPG in a pediatric intensive care unit [23], in the course of hand surgery [201, 282, 283], and for allergic testing [32]. Within this thesis and corresponding publications, the

cbPPG's capability to function in challenging clinical settings was assessed as well (see Chapter 3). Despite the clinical employment, the main focus remains on using cbPPG in everyday situations. During and after physical exercises, for example, the technique proved to be applicable determining the HR [321, 322, 364, 366, 368, 400], the BP [137, 295] and the activity of the ANS [39, 136]. Several works have shown that cbPPG can be deployed in an automotive environment for driver monitoring [37, 168, 179, 380, 395]. Even the measurement from a drone was considered [6]. Further demanding scenarios for cbPPG involve its application throughout hypoxic episodes [3, 104, 349] and in the course of magnetic resonance imaging [312].

CHAPTER SUMMARY

The first part of this chapter intended to show how a photoplethysmographic signal is affected by optical properties, anatomical characteristics, physiological processes and autonomic activities. The pulsatility of the blood wave alters throughout the vascular system and can be detected in the cutaneous microvasculature. When light penetrates the skin, scattering and absorption are the defining processes for modulation which also determine the penetration depth. For PPG, the relatively high absorption of hemoglobin plays the major role in the optical acquisition of the mentioned pulsatility based on blood volume changes. For cbPPG, the modulating elements are not completely clarified yet. The main advantages of cbPPG are the remote application, its operability with ambient light and the possibility of spatial assessment. Especially the first two add more degrees of freedom to the measurement technique but also compromise the robustness. Both, PPG and cbPPG have been tested in different environments and settings. However, cbPPG still lacks the evidence to be applied reliably for broad variety of scenarios and individuals.

3

TECHNICAL SETUP AND DATA

This chapter describes the data material, which was analyzed in the thesis, and technical aspects of cbPPG measurement setups which were applied to acquire the associated video recordings. In this context, the first section introduces an entirely novel measuring system that was employed in the majority of the experiments. The next two sections present the studies in which the actual data was obtained. Firstly, details about two studies from clinical environments are delineated. Secondly, three studies from laboratory environments, which attempted to investigate specific technical or physiological issues, are described. Information is generally provided based on relevance for cbPPG and importance for subsequent analyses.

3.1 NOVEL MEASUREMENT SYSTEM

In order to enable an easy and convenient application of cbPPG in different environments, a novel measurement stand was designed and built. Figure 18 shows the system's main components including the (i) constructional framework, (ii) recording computer, (iii) power supply, and (iv) the sensing component with the cameras and an active illumination. The framework was set up using a modular system by the item Industrietechnik GmbH (Solingen, Germany). The company provided support during the design phase, conducted stress analyses, and manufactured the aluminum profiles. Safety and flexibility were chosen to be important construction requirements. A solid and heavy basis prevents the stand to tip over when loaded unevenly. Wheels on the bottom allow a mobile employment and an adjustable arm on the top the accurate positioning of the installed cameras over the considered skin area (see Fig. 18 (a)). The cameras are part of the so-called sensing component which was mounted on the end of the arm. Figure 18 (d) depicts the setup.

To enable the cbPPG measurement at different wavelengths, an RGB as well as a NIR camera were utilized. Two high-end industrial models by the IDS Imaging Development Systems GmbH (Obersulm, Germany) were selected for that purpose. In Table 4, the main characteristics are summarized. The frame rate of both cameras was set to 100 fps to ensure a high temporal resolution in the eventually obtained plethysmograms. Similarly, a high resolution in the intensity range was guaranteed by using color depths of 12 Bit. With respect to the frame rate, an additional advantage emerged. Common illumination

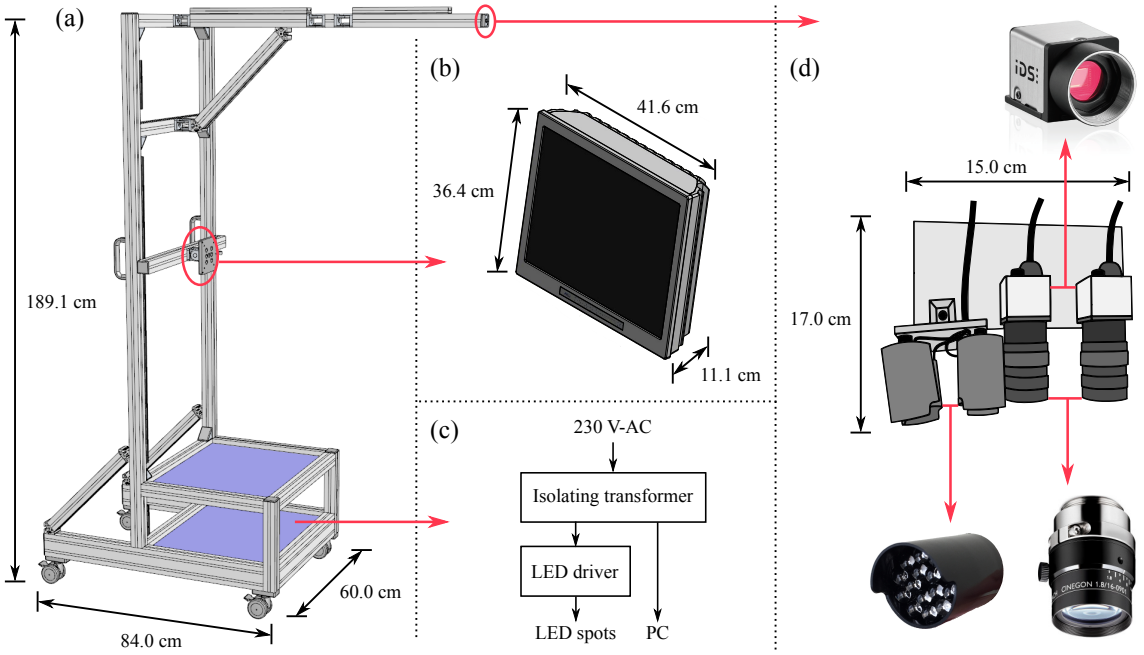

Figure 18: The main parts of the developed cbPPG measurement stand: (a) Constructional framework, (b) Recording computer, (c) Power supply, (d) Sensing component including the cameras, lenses, and the LED spots. (Fig. (a): provided by item Industrietechnik GmbH, Fig. (b): provided by ACL GmbH, Fig. (d) camera: from [126, p. 1], lens: from [292, p. 1])

sources that are driven by alternating current of 50 Hz may cause light flickering in low sampled videos [346]. This effect could be prevented with the chosen rate as it is high enough and a multiple of the supply frequency. The image sizes of the two cameras were set to 320×420 pixels or to 420×320 pixels depending on whether the field of view was desired to be higher or wider. In either setting, the exposure time was held constant at its maximum resulting in values of 9.84 ms and 9.82 ms, respectively[1]. Since the defined image sizes would normally decrease the field of view as they would only cover a small sensor region, subsampling with a factor of 4 was applied so that three rows and columns were always skipped in the readout process. The automatic control of any kind of camera parameter was turned off, and the gain was set to zero. For both cameras, the same lens model (Cinegon 1.8/16) by Schneider-Kreuznach, Jos. Schneider Optische Werke GmbH (Bad Kreuznach, Germany) was employed. It features a focal length of 16.4 mm, an entrance pupil diameter of 9.1 mm, and a broadband transmission spectrum of 400 - 1000 nm [292]. Aperture and focus were always adjusted manually. At the aforementioned spatial resolution and a working distance between 50 and 100 cm, which was used in the cbPPG setup, the image plane eventually mapped an area ranging from about 21×28 cm to 43×57 cm. Besides of providing a cbPPG measurement with deeper penetrating wavelengths, the NIR

1 The readout speed of the sensor cells, which is determined by the so-called pixel clock, restricts the exposure time [128]. It was recommended by the manufacturer to set the clock to the lowest possible value. Due to the sensor's architecture and the different number of addressed rows in the two size settings, different clock frequencies were used eventually causing varying exposure times.

Table 4: Specifications of the used cameras and the NIR light source. The information was retrieved from the data sheets and the uEye camera handbook [126–128, 157]. Note: For the RGB camera, one pixel is described by four separated sensor units due to the Bayer filter.

	RGB CAMERA	NIR CAMERA		LED SPOT
Name	UI-3370CP-C-HQ	UI-3370CP-NIR-GL	Name	BL0106-15-29
Sensor type	CMOS		Diameter	26 mm
Shutter	Global shutter		Number of LEDs	15
Resolution	2048×2048 pixels		Viewing angle	40 °
Color depth	12 Bit		Peak wavelength	880 nm
Sensor size	11.264 mm×11.264 mm		Spectral bandwidth*	50 nm
Pixel size	5.5 µm		Electrical power	580 mW
Sensor filter	Bayer	–	Radiant intensity	350 mW/sr
Camera filter	NIR cut-off (650 nm)	glass (ultraviolet cut-off)		

* The bandwidth is defined as the width of the spectral response curve at half height.

camera can also be exploited to compensate poor ambient light conditions. To do so, four LED spots by the Kingbright Electronic Europe GmbH (Issum, Germany) were added to the sensing component (see Fig. 18 (d)). They operate at non-visible wavelengths around 880 nm and, therefore, do not disturb the the subject of interest. Table 4 lists more details. Since the NIR camera originally comes with a broad spectral sensitivity, an optical band-pass filter by MidOpt - Midwest Optical Systems, Inc. (Palatine IL, USA) was mounted to the camera. The filter limits the measuring range to the emission range of the LED light source. Figure 19 shows the respective response characteristics. The figure also depicts the corresponding curves of the RGB camera.

Both cameras were connected via USB 3.0 to a personal computer (see Fig. 18 (b)), i.e. the OR-PC® 19 by the ACL GmbH (Leipzig, Germany). The model is compact, fanless, complies with the DIN standard EN 60601 for medical devices, and is approved to be applied in various clinical environments. Technical specifications were customized as follows: Intel® Core™ i7 processor with 3.4 GHz, working memory of 8 GB, internal hard disk storage of 1 TB. Additionally, a 1 TB solid-state drive was built in solely for the purpose of video recording as it supports high writing speeds. The display was selected to be a touch screen to allow easy user interactions without the need of a keyboard or mouse. The computer was run under Microsoft Windows® 7 for which a personalized software was programmed to initiate and terminate the actual cbPPG measurement. The software visualized the cameras' imaging planes, enabled the input of individual information, provided instant feedback on camera and recording settings, and saved the video streams uncompressed into binary files. Further installed programs, e.g. for the communication to patient monitors or other reference sensor systems, are described in detail in the following sections.

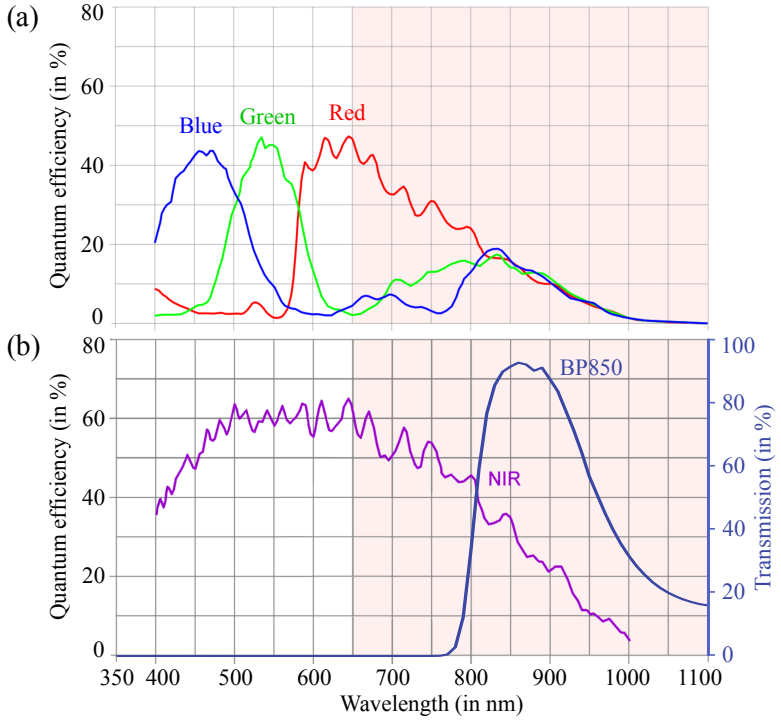

Figure 19: The quantum efficiency of the used camera sensors: (a) RGB camera IDS UI-3370CP-C-HQ, (b) NIR camera IDS UI-3370CP-NIR-GL. For the latter one, the transmission characteristic of the applied bandpass filter (MidOpt BP850) is depicted as well. (Fig. (a): from [126, p. 1] - modified, Fig. (b): from [127, p. 1] - modified/ filter data from [217])

To ensure electrical safety, an isolating transformer (ERT 230/230/2G) by the Thalheimer Transformatorenwerke GmbH (Thalheim, Germany) was added to the stand. It galvanically isolated the outlet power from the devices, i.e the computer and the LED driver. The driver (model 66000164) by the Josef Barthelme GmbH & Co. KG (Nürnberg, Germany) was used to supply the NIR light source. The cameras were supplied via USB 3.0 directly through the computer.

The novel measurement setup was successfully applied in major studies comprising different clinical trials and laboratory experiments. A total of 133 volunteers were recorded failure-free with the system leading to video data of over 76 hours. It proved to yield reliable results in challenging environments and to be easily adaptable to varying surrounding conditions. Due to the comprehensible layout and the intuitive user interface, the system could be operated by persons with different technical understanding such as students, engineers, and medical staff. To the best of my knowledge, it is the only cbPPG system that was able to gather large amounts of heterogeneous data and still remained flexible, integrable, mobile, and user-friendly at the same time.

3.2 STUDIES FROM CLINICAL ENVIRONMENTS

3.2.1 *Intraoperative Study*

One of the studies, which was conducted with the novel measurement system, involved the remote monitoring of patients during surgery at the Department of Anesthesiology and Intensive Care Medicine, University Hospital, TU Dresden. Each patient who took part in the experiment was informed about the procedure, gave written consent, and permitted the scientific use of the acquired data. The study was in accordance with with the Helsinki Declaration and approved beforehand by the Institutional Review Board at TU Dresden (EK168052013).

In total, 83 subjects were enrolled in the study. However, due to technical issues regarding the cbPPG system and the communication to the patient monitor, only 41 subject-related recordings could be further used for evaluation. The residual group comprised patients of older age with mostly light skin tones who underwent surgery, either on the extremities or the stomach area. About half of the group was rated to have cardiovascular problems that were relevant for the planed intervention. Pre-existing vascular diseases were of high interest in the study (e.g. hypovolemia, stenosis, thrombosis, varicosis, artery occlusive disease). Perioperative care followed clinical standards. General anesthesia was induced and maintained for all individuals where the anaesthetics were administered almost exclusively by inhalation and only for one subject by intravenous infusion. During the operation, the patients were mechanically ventilated, and a warming blanket was applied to prevent hypothermia. Medication including vasopressors and opioids was given via a syringe pump counteractively to occurring events. Additional and more detailed information about the patients and the surgery is listed in Table 5.

For the actual experiment, the measurement stand was stationed at the head end of the operating table and the sensing component was aligned towards the face of the patient who was in a supine position (see Fig. 20). Depending on the table's height, the distance between the cameras and the face varied in a range from about 0.5 to 1 m. A large part of the image plane covered the frontal head area which was to some extent occluded by the surgical cap, drape, and occasionally tape in the eye section. The video recording was performed within the surgery and lasted approximately 30 min. It was initiated at a convenient time by the anesthetists who also supervised the measurement. Before each recording, they adjusted the lenses' focus as well as the aperture in order to adapt the cameras' exposure to the prevailing illumination conditions. The latter adjustment was especially important because the lighting could alter as it was defined by the surgical light and the fluorescent lamps which were not always turned on. An overview of the different lighting situations can be found in the Appendix A.3 (Fig. 61).

Besides storing the video data, the stand's computer was also used to capture information about momentary measures such as the application of medication, settings in support systems, or the acquisition of certain clinical values. For this purpose, a customized input

Table 5: Information about the intraoperative study regarding the patient group, surgery, and video recordings. Selected details are given based on availability and relevance for the output of the cbPPG measurement. If no count value is given, always the mean and standard deviation are depicted for the 41 patients. The symbol # indicates the number of subjects where the data was existent (if not stated, no data was missing).

	Characteristic	Value
Body-related parameters	Female : Male (number)	17 : 24
	Age (in years)	65.2 ± 12.0
	Body mass index (in kg/m^2)	26.1 ± 4.6
	Fitzpatrick skin type (number)*	
	Type I	2
	Type II	38
	Type III	1
	Body temperature (in °C)$^{\#35}$	35.9 ± 0.5
	Hemoglobin concentration (in mmol/L)$^{\#38}$	8.4 ± 1.0
Medical history	NYHA (number)†	
	0 - not examined	4
	1 - no problems	35
	2 - irrelevant problems	0
	3 - relevant problems	2
	Vascular system (number)†	
	0 - not examined	0
	1 - no problems	20
	2 - irrelevant problems	2
	3 - relevant problems	19
Surgery-related parameters	Duration anesthesia (in min)	238.2 ± 120.3
	Duration surgery (in min)	157.3 ± 99.9
	Blood loss (in ml)$^{\#38}$	414.6 ± 348.3
	Noradrenalin/ Akrinor infusion (number)	20
	Sufentanil infusion (number)	13
Video recording	Duration (in min)	32.0 ± 7.2
	Mean intensity value (in %)‡	
	Blue channel	39.3 ± 12.7
	Green channel	50.8 ± 13.9
	Red channel	46.1 ± 10.0
	NIR channel	29.2 ± 7.6

* The Fitzpatrick scale allows the classification of skin color types [87]. Nowadays, six types are used where 'I' refers to very light skin and 'VI' to very dark [88]. Here, only the first three were present.

† The categories stem from the ANDOK^{live} protocol [72]. They are set by the anesthetists and assess the respective physiological system (heart, vasculature) based on the risk of narcotization. The NYHA numbers refer to the NYHA (New York Heart Association) classification which is a standardized way to state the degree of heart failure [18].

‡ $0 \mathrel{\widehat{=}} 0\,\%$ and $4095 \mathrel{\widehat{=}} 100\,\%$ (12 Bit)

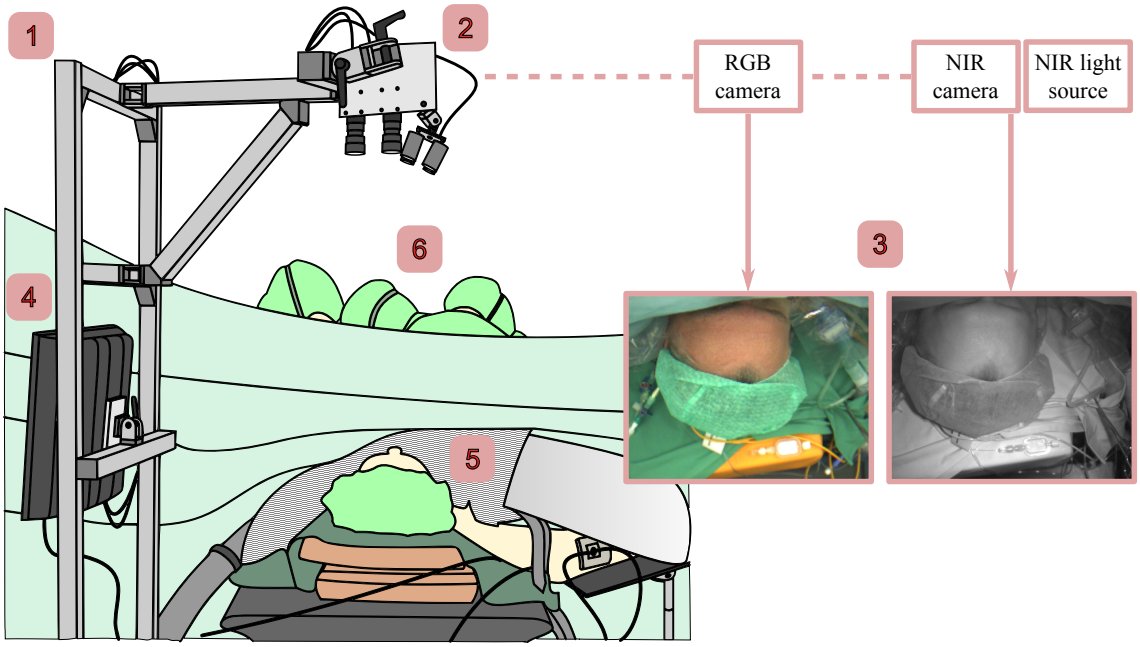

Figure 20: Measurement stand in the intraoperative setting: (1) Constructional framework, (2) Sensing component, (3) Imaging plane of the two cameras, (4) Recording computer, (5) Patient, (6) Surgeons. In this application, the wider camera view (420×320 pixels) was used. (from [340, p. 4] used under the Creative Commons Attribution 4.0 International License - modified in image depiction)

mask was provided. Furthermore, the computer was employed to gather biomedical reference signals from the patient monitor (type IntelliVue by the Philips GmbH in Hamburg, Germany). The signals could be accessed online via the software ixTrend Express 2.0 (ixellence GmbH in Wildau, Germany) and were synchronized to the video streams with an accuracy of about 1 ms. On the one hand, continuous signals, i.e. the electrocardiogram (three Einthoven and Goldberger leads), photoplethysmogram, and in some cases the invasive BP, were obtained with a sampling frequency of 250 Hz. On the other hand, trend signals (1 Hz) for the arterial oxygen saturation, HR, DBP, SBP, and MBP were collected.

3.2.2 *Postoperative Study*

Another study, which was conducted with the new measurement system, involved the remote monitoring of patients after cardiac surgery in the intensive care unit at the Herzzentrum Dresden, Department of Cardiac Surgery, University Hospital, TU Dresden. Each patient who took part in the experiment was informed about the procedure, gave written consent, and permitted the scientific use of the acquired data. The study was in accordance with with the Helsinki Declaration and approved beforehand by the Institutional Review Board at TU Dresden (EK168052013).

A cohort of 160 subjects was enrolled and recorded in the study. Again, different technical issues led to the exclusion of several measurements leaving 70 individuals where the data sets could be used for further analyses. The residual group comprised elderly

patients with lighter skin tones who underwent elective cardiac surgery (e.g. aortic valve replacement, coronary artery bypass graft surgery, mitral valve surgery). Besides the heart problems, a considerable number of them also suffered from hypertension, diabetes, and various vascular diseases. The actual experiment took place in the intensive care unit, after the surgical intervention, and as soon as the admission process was completed. Postoperative procedures followed clinical standards. Most of the subjects were mechanically ventilated and externally paced at a rate of 90 bpm. Administered medication, such as inotropes, vasodilators, and vasoconstrictors, were prescribed in agreement with the respective guidelines [56]. Additional and more detailed information about the patients and the treatment is listed in Table 6.

In order to meet imposed conditions regarding the postoperative cbPPG application, the following modifications were made to the measurement stand: (i) Lowering of the constructional base, (ii) installation of an additional display for instant feedback, (ii) extension of the arm, (iv) installation of a keyboard holder. For the cbPPG experiment, the modified stand was stationed next to the bed and its sensing component was positioned over the participant's head at a distance of between 0.5 and 1 m (see Fig. 21). Due to the supine posture of the patients, the image planes of the cameras mainly covered the frontal face area which was partly occluded by nasogastric and orotracheal tubes, as well as their fixation tape. The video recording was started when the patients were still unconscious from the ongoing effects of anesthetics that were given during surgery. However, towards the end, some individuals woke up and moved slightly. The measurement lasted about 30 min. It was overseen by medical staff who also conducted the initial adjustment of the lenses' focus and aperture. Again, the latter adjustment was especially important because the illumination altered as it was defined by varying natural light and fluorescent lamps (not always on). In general, considerable changes in the light intensity, homogeneity and color could be observed (see Appendix A.3, Fig. 63).

As in the previously described study, the recording computer was utilized to (i) store biomedical reference signals and (ii) capture information about momentary measures such as the application of medication, settings in support systems, or the acquisition of certain clinical values. The first point was achieved by accessing the patient monitor CARESCAPE^{TM} B850 (GE Healthcare GmbH in Little Chalfont, UK) via the software Datex-Ohmeda S/5^{TM} Collect (Datex-Ohmeda, Inc. in Madison WI, USA). On the one hand, continuous signals, i.e. the electrocardiogram (modified Einthoven lead II), photoplethysmogram and the invasive BP (radial artery) could be obtained with a sampling frequency of 300 Hz. On the other hand, trend signals (1 Hz) for the arterial oxygen saturation, central venous pressure, HR, DBP, SBP, and MBP were collected. Synchronization between the monitor data and the video streams could be realized with an accuracy of about 100 ms.

Table 6: Information about the postoperative study regarding the patient group, treatment, and video recordings. Selected details are given based on availability and relevance for the output of the cbPPG measurement. In case no count value is given, always the mean and standard deviation are depicted for the 70 patients.

	Characteristic	Value
Body-related parameters	Female : Male (number)	20 : 50
	Age (in years)	70.3 ± 11.4
	Body mass index (in kg/m^2)	28.8 ± 4.1
	Fitzpatrick skin type (number)*	
	Type I	4
	Type II	58
	Type III	8
	Body core temperature (in °C)	36.2 ± 0.5
	Hemoglobin concentration (in mmol/L)	6.8 ± 0.8
Medical history	NYHA class ≥ II (number)†	32
	Arterial hypertension (number)	61
	Diabetes mellitus (number)	33
	Coronary heart disease (number)	50
	Peripheral arterial occlusive disease (number)	9
	Carotid stenosis (number)	7
Treatment	Cardiac pacing (number)	50
	Mechanical ventilation (number)	67
	Noradrenaline infusion (number)	23
	Nitroglycerine infusion (number)	40
	Dobutamine infusion (number)	7
Video recording	Duration (in min)	30.2 ± 2.3
	Past time after surgery (in min)	99.1 ± 42.19
	- one was patient excluded who was recorded after two days -	
	Mean intensity value (in %)‡	
	Blue channel	32.4 ± 11.6
	Green channel	37.6 ± 11.4
	Red channel	42.2 ± 14.5
	NIR channel	33.4 ± 8.1

* The Fitzpatrick scale allows the classification of skin color types [87]. Nowadays, six types are used where 'I' refers to very light skin and 'VI' to very dark [88]. Here, only the first three were present.

† The NYHA (New York Heart Association) classification is a standardized way to assess the degree of heart failure [18]. A distinction is made between four classes where class II-IV are associated with evident limitations (cardiovascular diseases).

‡ $0 \mathrel{\widehat{=}} 0\,\%$ and $4095 \mathrel{\widehat{=}} 100\,\%$ (12 Bit)

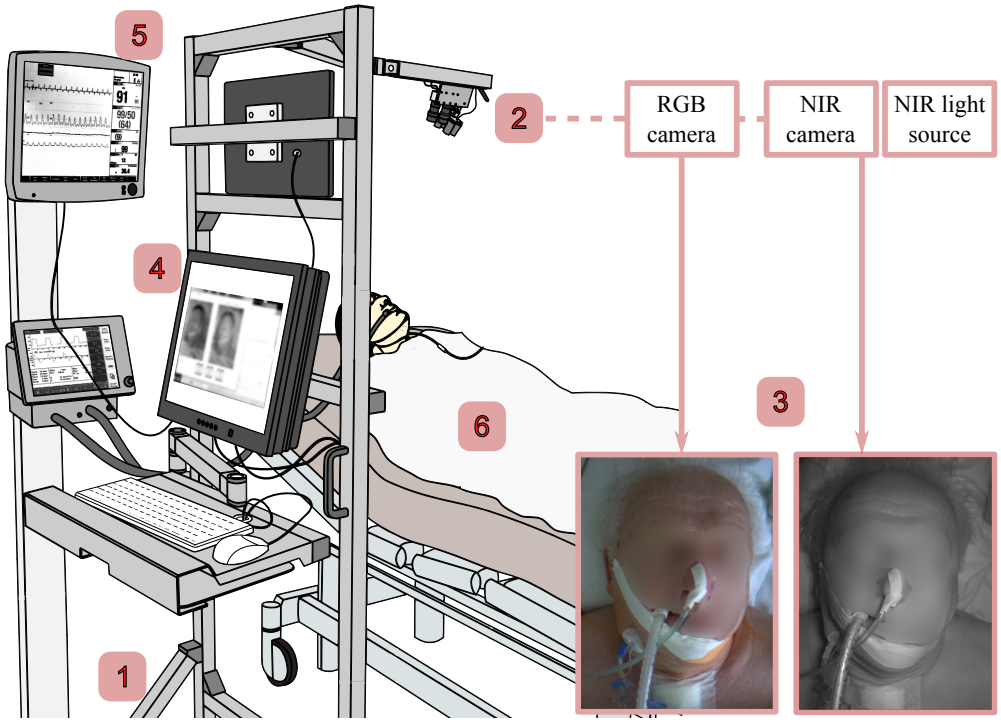

Figure 21: Measurement stand in the postoperative setting: (1) Constructional framework, (2) Sensing component, (3) Imaging plane of the two cameras, (4) Recording computer, (5) Patient monitor, (6) Patient. In this application, the higher camera view (320×420 pixels) was used.
The figure is reprinted and changed with the publisher's permission from: A. Trumpp, S. Rasche, D. Wedekind, M. Rudolf, H. Malberg, K. Matschke, and S. Zaunseder, "Relation between pulse pressure and the pulsation strength in camera-based photoplethysmograms", in: *Current Directions in Biomedical Engineering,* 3(2), Berlin: De Gruyter, 2017, pp. 489–492, Fig. 1.

3.3 STUDIES FROM LABORATORY ENVIRONMENTS

3.3.1 *Cold Pressor Test*

A third study, which was conducted with the novel measurement system, involved the remote monitoring of volunteers performing the cold pressor test (CPT). It was carried out at the Institute of Biomedical Engineering, TU Dresden. Each individual who took part in the experiment was informed about the procedure, gave written consent, and permitted the scientific use of the acquired data. The study was in accordance with with the Helsinki Declaration and approved beforehand by the Institutional Review Board at TU Dresden (EK119032016).

The CPT is an experimental method where participants immerse a limb into cold water to evoke stress and pain reactions [114, 223]. In this study, 22 subjects were recruited to perform the CPT twice with their right hand, once in the sitting position and once in the supine position. Each posture-related test took place on a separate day. As a consequence, 44 measurements were obtained of which one had to be disregarded due to technical issues. The measurement process comprised a baseline phase of 5 min, the actual CPT with

Table 7: Information about the CPT study regarding the subjects, experiment, and video recordings. Details are given based on availability and relevance for the output of the cbPPG measurement. If no count value is given, always the mean and standard deviation are depicted, either for the 22 subjects or for all 43 experiments (last two sections).

	CHARACTERISTIC	VALUE
Body-related parameters	Female : Male (number)	10 : 12
	Age (in years)	25.5 ± 3.7
	Body mass index (in kg/m^2)	21.7 ± 2.1
	Fitzpatrick skin type (number)*	
	Type I	3
	Type II	16
	Type III	3
Test-related parameters	Experiments (number)	43
	... in sitting position (number)	22
	... in supine position (number)	21
	Duration CPT (in s)	116.1 ± 70.8
	Early termination CPT (number)	20
Video recording	Duration (in min)	27.2 ± 2.1
	Mean intensity value (in %)†	
	Blue channel	44.3 ± 12.8
	Green channel	47.6 ± 12.8
	Red channel	56.3 ± 12.2
	NIR channel	43.8 ± 9.0

* The Fitzpatrick scale allows the classification of skin color types [87]. Nowadays, six types are used where 'I' refers to very light skin and 'VI' to very dark [88]. Here, only the first three were present.

† $0 \mathrel{\widehat{=}} 0\,\%$ and $4095 \mathrel{\widehat{=}} 100\,\%$ (12 Bit)

3 min, a recovery phase of 15 min, and three different periods of 3 min where saliva samples were collected. Although the subjects were asked to remain the hand in the water for the whole 3 min, some of them could not bear the pain and terminated early. Regardless of the outcome, everyone was instructed to keep calm and breathe normally. The participating group consisted of healthy and young individuals with mostly lighter skin tones. Cardiovascular diseases, neurological, endocrinological, and psychological disorders, acute allergies, overweight, and the intake of medication or drugs led to the exclusion of potential volunteers from the very start. Additional and more information about the subjects and the experimental procedure can be found in Table 7 and in Section 6.2.1.

In order to realize cbPPG measurements in the different postures, the arm of the stand was extended and equipped with an additional joint. Thus, the sensing component could be easily positioned, either in front of the head when the participant was sitting, or above the head when lying. Figure 22 shows the setup for the first scenario. For the second scenario, the tilt table was used in a similar way as it is depicted in Fig. 23. In both cases, the

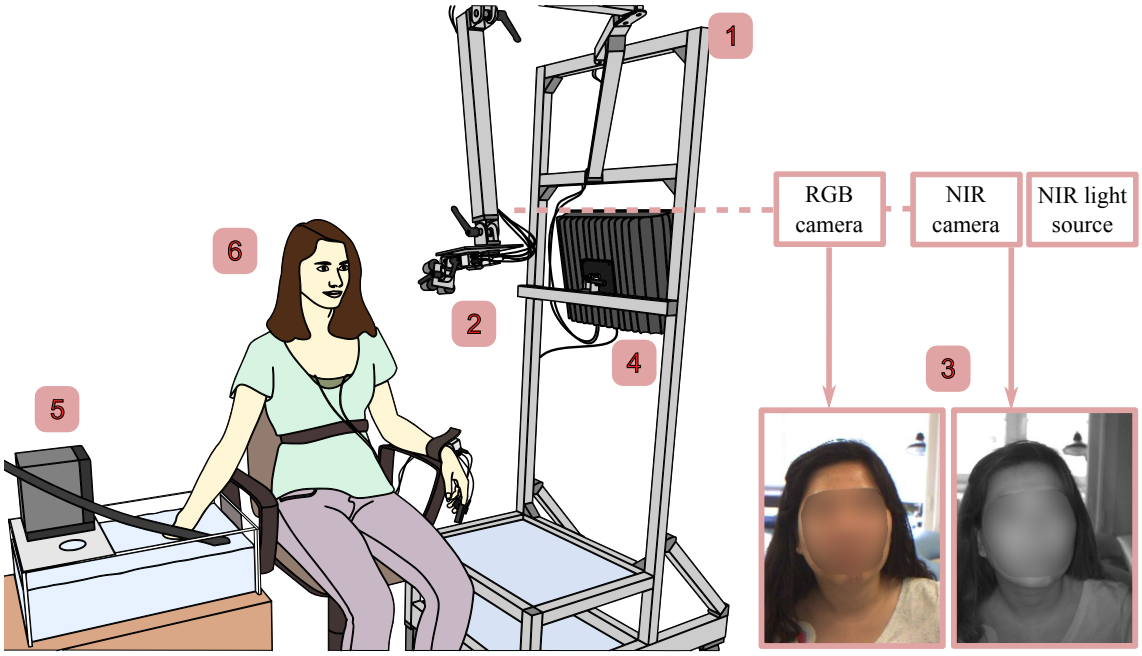

Figure 22: Camera-based measurement setup for the CPT in the sitting position: (1) Constructional framework, (2) Sensing component, (3) Imaging plane of the two cameras, (4) Recording computer, (5) Water tank with cooling system, (6) Study participant. In this application, the higher camera view (320×420 pixels) was used.

cameras were rather close to the subject (0.5 m) so that the image planes mainly mapped the frontal face area and the upper part of the body. The video recordings were conducted over the course of the aforementioned experimental phases and lasted about 27 min. During the measurement, the participants occasionally talked and moved. Motion often occurred while submitting saliva samples and within the CPT as a result of pain or the body's re-alignment towards the water tank. Before each recording, the cameras' aperture was adapted to the prevailing illumination conditions which were defined by changing natural light and the room's fluorescent lamps.

As in the other studies, biomedical reference signals were obtained. The acquisition unit PowerLab® 16/35 by ADInstruments Ltd. (Dunedin, New Zealand) was used to simultaneously collect signals from different sensors with a sampling rate of 1000 Hz. The dedicated software LabChart® allowed to visualize and store the respective data on a separate computer. The following signals were recorded:

- Finger plethysmogram (captured via ADInstruments' IR Plethysmograph MLT1020FC)
- Electrocardiogram, modified Einthoven lead II (amplified with ADInstruments' Bio Amp FE132)
- Respiration signal (captured via ADInstruments' respiratory belt MLT1132)
- Non-invasive continuous BP signal (determined using the Finometer® MIDI by Finapress Medical Systems B.V. in Enschede, Netherlands)

The BP was derived from the left middle finger but the system also provided an estimation for the brachial pressure. In order to synchronize the video streams with the reference

signals, the trigger outputs of the cameras were connected with the PowerLab as well. Hence, a uniform timestamp basis could be realized. In addition to the listed devices, the Eintauchkühler TC45-F by the Peter Huber Kältemaschinenbau AG (Offenburg, Germany) was employed which controlled the temperature of the CPT's water tank (3 °C). Furthermore, the laboratory's air conditioning was exploited to ensure a constant ambient temperature of 21 °C.

3.3.2 *Skin Heating and Cold Face Test*

The second laboratory study involved the remote monitoring of volunteers which were exposed to cold and warm stimuli. It was carried out at the Institute of Biomedical Engineering, TU Dresden. Each individual who took part in the experiment was informed about the procedure, gave written consent, and permitted the scientific use of the acquired data. The study was in accordance with with the Helsinki Declaration and approved beforehand by the Institutional Review Board at TU Dresden (EK168052013). It should be noted that some of the following content already appeared in one of my publications [336].

A cohort of ten volunteers was recruited for the study. The group featured young and generally healthy subjects who were fair-skinned. One participant suffered from hypertension and was treated with the appropriate medication. The experiment consisted of six consecutive measurement cycles with 90 s each. Two different physiological tests were performed over the course of those cycles while the subjects were resting motionless on a tilt table in the supine position. In the first test, the skin of the inner left arm was heated with the objective of evoking local vasodilation [61, 139]. The warm stimulus was induced at the beginning of the experiment and persisted to its end. The second test was the cold face test (CFT) which is a method to concurrently activate the SNS and the PSNS by applying a cold stimulus to the face [111, 273, 373]. In this study, a gel ice pack ($\approx 0\,^{\circ}\mathrm{C}$) was placed on the forehead for 30 s within the last three measurement cycles. The pack also covered the temples but excluded the eyes to avoid the ocular reflex [273]. More information about the subjects and the experimental procedure can be found in Table 8 and in Section 6.2.1, respectively.

Camera-based monitoring was conducted using a single industrial RGB camera. It was the same model that was chosen for the developed measurement stand, and it was also equipped with the same lens by Schneider-Kreuznach (see section 3.1). However, the camera's settings were configured differently. The frame rate was set to 300 fps, the exposure time to 3.21 ms, the spatial resolution to 1024×200 pixels (subsampling factor of 2), and the color depth to 12 Bit. The automatic control of any kind of camera parameter was turned off, and the gain was set to zero. The high frame rate was defined with the objective of capturing local hemodynamics, and the wide image size was necessary to map the whole left arm. For the experiment, the camera was mounted on the tilt table above the subject at a distance of about 90 cm (see Fig. 23). The alignment resulted in a recording area with the size of approximately 65×12.5 cm. During the measurement, the room was completely

Table 8: Information about the participants and the video recordings regarding the skin heating and CFT experiments. Details are given based on availability and relevance for the output of the cbPPG measurement. If no count value is given, always the mean and standard deviation are depicted for the ten subejcts.

	Characteristic	Value
Body-related parameters	Female : Male (number)	1 : 9
	Age (in years)	24.9 ± 3.4
	Body mass index (in kg/m^2)	23.6 ± 4.1
	Fitzpatrick skin type (number)*	
	Type I	2
	Type II	8
Video recording	Mean intensity value (in %)†	
	Blue channel	26.1 ± 3.7
	Green channel	33.8 ± 4.2
	Red channel	57.7 ± 5.2

* The Fitzpatrick scale allows the classification of skin color types [87]. Nowadays, six types are used where 'I' refers to very light skin and 'VI' to very dark [88]. Here, only the first two were present.

† 0 $\widehat{=}$ 0 % and 4095 $\widehat{=}$ 100 % (12 Bit)

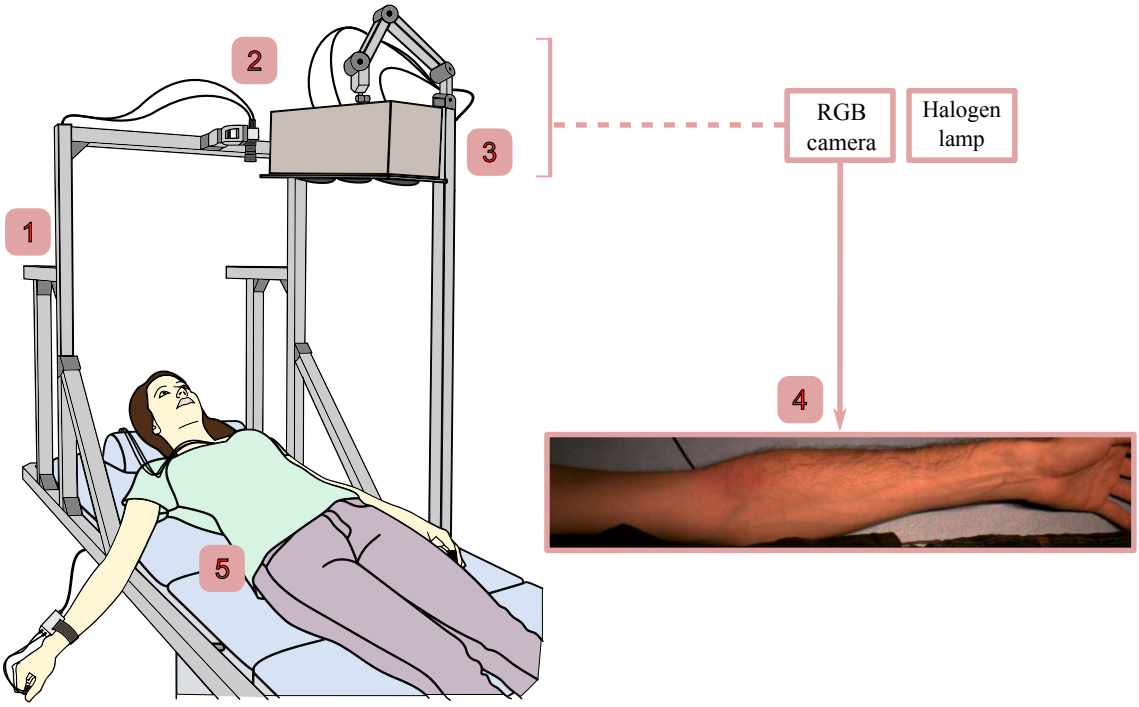

Figure 23: Camera-based measurement setup for the assessment of temperature stimuli: (1) Tilt table with constructional framework, (2) Camera, (3) Halogen illumination, (4) Imaging plane of the camera, (5) Study participant.

darkened. The only light source was a customized illumination unit which also served as heat source for the warming test. It consisted of three halogen lamps by the Osram GmbH (München, Germany), each with an electrical power of 75 W (operating voltage: 12 V, diameter: 111 mm, viewing angle: 40 °). The lamps were supplied by three DC power adapters that ensured a flicker-free lighting (model STD-12090 by Adapter Technology Co., Ltd. in New Taipei City, Taiwan).

For evaluation purposes, biomedical reference signals were obtained. These signals included a plethysmogram from the left index finger, an electrocardiogram (Einthoven lead II), and a non-invasive continuous BP signal from the right middle finger. The same devices and sensors were used as employed in the CPT study (see Section 3.3.1). The videos and the reference signals were stored on a separate computer. Synchronization between the two data sources was realized, again, utilizing the trigger output of the camera.

3.3.3 *Optical Polarization Experiment*

The third laboratory study aimed at investigating the value of optical polarization filtration for cbPPG. It was carried out at the Institute of Biomedical Engineering, TU Dresden. Each individual who took part in the experiment was informed about the procedure, gave written consent, and permitted the scientific use of the acquired data. The study was in accordance with with the Helsinki Declaration and approved beforehand by the Institutional Review Board at TU Dresden (EK168052013). It should be noted that the following descriptions are partly adopted from my corresponding publication [339].

A cohort of 24 volunteers was recruited for the study. Due to technical problems, the recordings of only 18 could be further used. The residual group comprised one female and 17 males who were all young and healthy (age: 25.7 ± 2.4 years, body mass index: 23.4 ± 3.1 kg/m^2). According to the Fitzpatrick scale [88], most of them showed light skin tones (type I: 1, II: 14, III: 3). For the actual experiment, the subjects were asked to sit down and comfortably rest their head on a soft pillow, which was placed on a desk, and remain relaxed and steady. A hair circlet was put on at the frontal hair line in order to maximize the visibility of the forehead. This step was important since this area served as ROI. Furthermore, the participants had to wear safety goggles to prevent a potential eye irritation caused by the applied illumination (see below).

Camera-based monitoring was conducted using a single industrial NIR camera. It was the same model that was chosen for the developed measurement stand, and it was also equipped with the same lens by Schneider-Kreuznach (see Section 3.1). Here, however, the camera was operated without the NIR bandpass filter, and the settings also differed slightly. The frame rate was set to 50 fps, the exposure time to 19.73 ms, the spatial resolution to 320×420 pixels (subsampling factor of 4), and the color depth to 12 Bit. The automatic control of any kind of camera parameter was turned off, and the gain was set to zero. During the experiment, the room was completely darkened. A customized illumination unit, which held a 6×9 array of LED clusters, was the only light source [178]. Each cluster

Table 9: Technical specifications of the RGB LEDs and optical filters used for the polarization experiment. The information was retrieved from the respective data sheets [293, 296]. (Reprinted and adapted with permission from [339], The Optical Society (OSA).)

		Blue	Green	Red
LED	Peak wavelength	453 nm	518 nm	632 nm
	Spectral bandwidth*	23 nm	33 nm	14 nm
	Viewing angle	120 °	120 °	120 °
	Electrical power	5.2 W	5.2 W	3.4 W
	Luminous intensity	0.2 cd	1.2 cd	0.7 cd
Polarization filter	Transmission glass	59 %	59 %	56 %
	Transmission film	74 %	80 %	75 %
	Extinction ratio† glass	300	7000	100000
	Extinction ratio film	1000	8000	70000

* The bandwidth is defined as the width of the spectral response curve at half height.

† The extinction ratio is defined as the transmittance of parallel aligned polarization filters divided by the transmittance of perpendicularly aligned filters [36].

contained three different types of LEDs, one of them being the RGB LED model SFT722N-S (Seoul Semiconductor Co., Ltd. in Danwon-gu, South Korea). All diodes were driven by a constant current to avoid unwanted flickering in the videos. The light colors could be adjusted separately to the desired intensity. Further technical specifications are listed in Table 9. The illumination unit and the camera were placed in front of the participants at a distance of about 450 mm resulting in a recording area with the size of 19×25 cm which mostly covered the face (see Fig. 24).

As mentioned at the beginning, the objective of this study was to assess the value of polarization filtration for cbPPG. Polarization in the context of electromagnetic waves refers to the vibration direction of the electric field component [100]. Interestingly, a specific polarization of incident light changes when it penetrates the skin [19]. Based on this knowledge, different scenarios were tested using two linear polarization filters by Schneider-Kreuznach, Jos. Schneider Optische Werke GmbH (Bad Kreuznach, Germany). The first filter, a plastic film (model P-W 76 0.8), was attached to the illumination unit with the polarization direction being oriented vertically. The second filter, a glass pane (model IF AUF), was mounted in front of the camera and could be changed in its orientation. Table 9 provides further technical information. In the experiment, the parallel and the perpendicular alignment of the polarizers was investigated (denoted by '||' and '+', respectively). For comparison, the application without filters was tested as well (denoted by 'o'). Those settings were combined with different lighting situations. Overall, 16 measurements of 20 s had to be made; of which only the blue, green, and red light scenario was further considered for evaluation (see Fig. 24 for an example). At the beginning of every test, the camera's aperture was adjusted with the attempt to obtain a similar exposure across all video recordings. As reference, a plethysmogram was obtained from the left ear (ADIn-

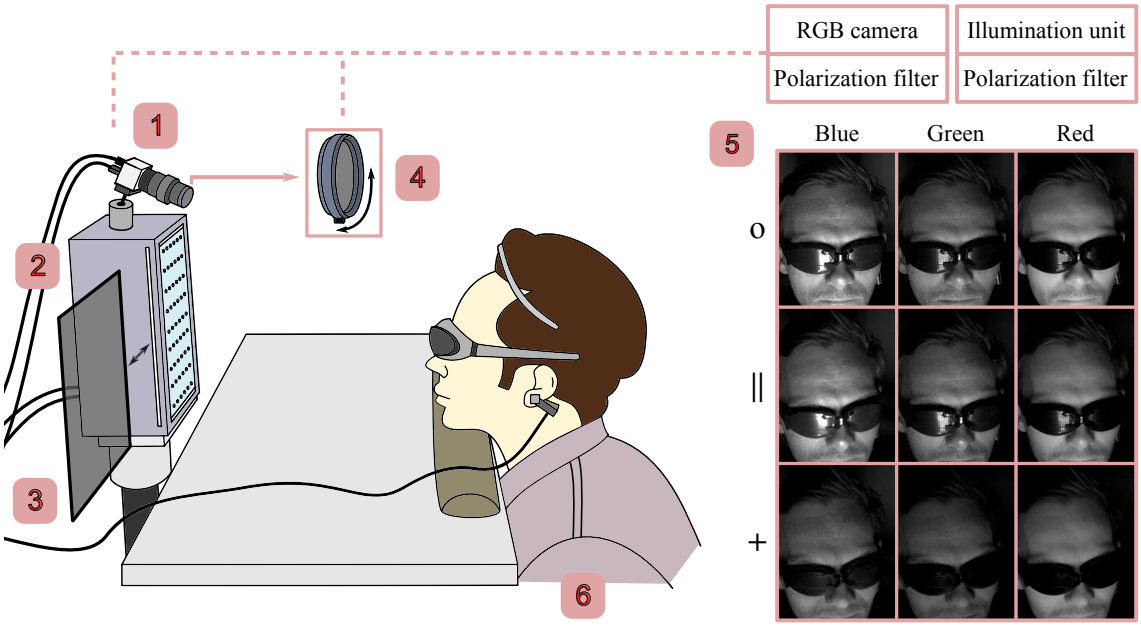

Figure 24: Camera-based measurement setup for the assessment of the value of polarization filtration: (1) Camera, (2) Multi-wavelength illumination unit, (3) Polarization filter (film), (4) Polarization filter (glass), (5) Image plane of the camera at different wavelength and filter settings, (6) Test subject with hairband and protection goggles. The parallel filter setting is denoted by '||', the perpendicular one by '+', and the setting without filters by 'o'. (Reprinted and adapted with permission from [339], The Optical Society (OSA).)

struments, ear clip MLT1020EC). The acquisition of the signal and its synchronization to the video stream was realized in the same way as done in the other laboratory studies. All data was eventually stored on a separate computer.

CHAPTER SUMMARY

In the first part of this chapter, a novel measuring system for cbPPG was presented. The system allowed multispectral recordings to be conducted, was mobile, adaptable, and generally easy to use. It was successfully applied in numerous experiments that involved the monitoring of healthy, diseased, young, and old volunteers. The second part of the chapter described the studies from which the data material for this thesis was obtained. On the one hand, the data was derived from two clinical studies where 111 patients were recorded who either were recovering from cardiac surgery, or were undergoing a surgical intervention. On the other hand, three laboratory studies provided material. Two of them intended to investigate how cbPPG is able to capture physiological reactions which were induced by the cold pressor test, the cold face test, and a local skin heating test. The third study aimed at finding the beneficial value of optical polarization filtration when employed in cbPPG.

4

VALUE OF POLARIZATION FILTRATION

This chapter addresses an important hardware aspect in cbPPG, i.e. the application of optical polarization filters. On the one hand, it is investigated which particular filter setting leads to the highest increase in signal quality. On the other hand, systematic variations in different settings are evaluated to shed more light on the origin of cbPPG signals. The first section briefly explains how optical polarization works and surveys cbPPG studies which have already employed polarizers. The second section describes the methods that were used to acquire and assess the plethysmograms from the data. The third section presents the results. The last section discusses the outcome with respect to the formulated goals. It should be noted that the following descriptions are partly adopted from my corresponding publication [339].

4.1 STATE OF THE ART

Light is part of the electromagnetic radiation [284]. For isotropic mediums, the electromagnetic waves are transverse meaning that the vectors of the electric and magnetic fields are orthogonal to the direction of travel [187]. When speaking of optical polarization, one refers to a characteristic oscillation of the electric component [100]. In order to properly describe this oscillation, the propagating wave can be considered as a superposition of two orthogonal basis waves for which amplitude changes only occur in one direction of the electric field (E_x and E_y) [187, 309]. There are two main states or extremums of polarization, the linear and the circular polarization [100]. In the first state, the two basis waves may differ in their amplitude but a have a defined phase shift of 0 or $\pm\pi$. In the second state, they hold the same amplitude but have a phase shift of $\pm\pi/2$ that leads to a helix-like shape [78]. Figure 25 visualizes the theory. If light has no prominent polarization state, it is called unpolarized [1]. Polarization can be created by various optical processes, such as scattering, reflection, and absorption [100, 187]. However, the mechanism of polarization generally refers to the extraction of a polarized light beam from an unpolarized beam, for example by means of a dedicated optical filter (see Section 3.3.3) [187]. Consequently, it also involves a loss in intensity. Two peculiarities are especially of interest when it comes to the light's interaction with skin [19, 132]:

- Light that is specularly reflected does not lose its polarization state.

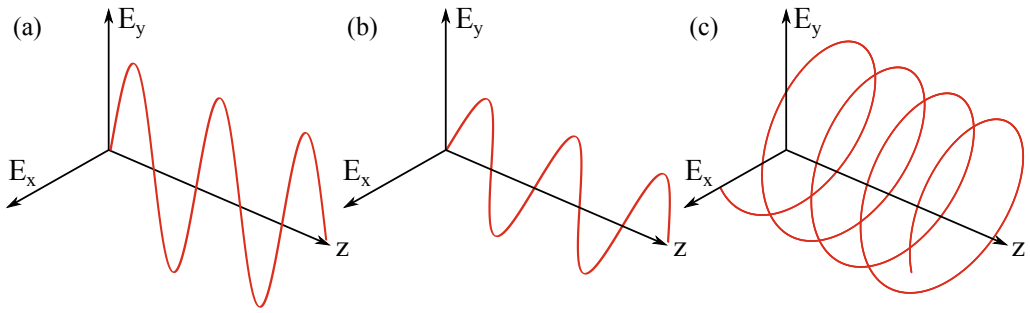

Figure 25: Propagating waves in z-direction with different polarization states: (a) Linearly polarized wave with no x component in the electric field $\mathbf{E}$, (b) Linearly polarized wave with an x and y-component, (c) Circularly polarized wave. (based on information in [100])

- As polarized light propagates within biological tissue, its polarization state changes due to scattering.

As a result, if the polarization direction of a filter at a light source is aligned with the one of another filter at a corresponding sensor, a skin measurement mostly provides information from the surface. In contrast, a perpendicular alignment would favor information from beneath the surface. There are several established imaging techniques which already exploit those characteristics for their skin-related analyses [28, 75, 103, 132, 133, 246]. Recently, Mishra et al. [220–222] demonstrated how the degree of (de)polarization could be utilized to estimate the HR and the oxygen saturation from the index finger.

In the field of cbPPG, polarizers seem to be applied rather sporadically. A mentionable number of works used the perpendicular filter alignment to suppress specular reflection from the skin surface[1]. However, investigations that systematically assess the benefit of polarization filtration for cbPPG are rare. Hülsbusch [120] tested linear polarization in a perpenidcular setting but could not show any improvements in the signal quality. Sidorov et al. [305] compared the perpendicular setting versus a setting without filters for the palm which was compressed against a glass plate. They reported a reduction of noise and artifacts but no significant increase in the blood pulsation amplitude when using polarizers.

Goal

In this chapter, the value of polarization for cbPPG is determined. The parallel filter alignment (denoted by '||') and the perpendicular alignment (denoted by '+') were assessed in relation to a scenario where no filters were employed (denoted by 'o'). Moreover, three illumination situations, i.e. blue, green, and red lighting, were considered for each scenario. The ultimate goals are to (i) to analyze which filter setting leads to the highest increase in signals' pulsation strength, and (ii) to draw conclusions about the origin of cbPPG signals based on characteristic responses in the different filter and color settings. Except of the corresponding publication [339], to the best of my knowledge, there are no equivalent investigations in the field.

1 References: [92, 148–150, 201, 225, 226, 228, 229, 283, 306, 358, 383, 392]

4.2 METHODS

Experimental Procedure

Figure 26 depicts the procedure of the polarization experiment. For each subject, 16 subsequent measurements of 20 s were conducted. Due to reasons of relevance, only nine of them were further used for evaluation. The first three measurements were performed with the polarizers being aligned perpendicularly. As described in Section 3.3.3, one filter was mounted to the camera while the other one was placed in front of the illumination unit. In the next three measurements, the parallel alignment was applied, and in the last three measurements, no filters were installed at all [2]. Each group-related measurement involved a different light color configuration of the illumination unit: i) Blue, ii) green and iii) red. Across the experiment, the LEDs were always operated at their maximum output.

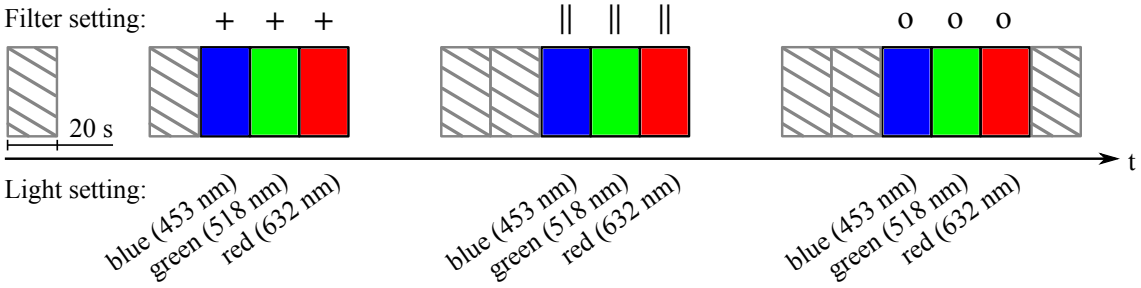

Figure 26: Procedure of the polarization experiment. Each box denotes one measurement. The gray boxes illustrate measurements which were not considered for evaluation. As a result, nine measurements with different illumination and filter settings remained for the analyses. The symbol 'o' represents the setting without polarizers, '||' the parallel setting and '+' the perpendicular setting.

Image and Signal Processing

For each subject, one large ROI for the forehead was defined in the first frame of the first measurement. The ROI was then held statically throughout the recording. Moreover, the same ROI was used for the following measurements but repositioned in the corresponding first frame if necessary. During the annotation, the attempt was made not to include high-contrast areas like skin edges. Figure 27 (a) shows an example. In further descriptions, the forehead ROI will be denoted by $\mathrm{ROI}_{\mathrm{full}}$. In order to take regional differences into account, spatially distributed ROIs (size of 15×15 pixels) were defined and automatically fitted in $\mathrm{ROI}_{\mathrm{full}}$ of each subject. An example can be found in Fig. 27 (b). Across all 18 subjects, between 49 and 133 (90 ± 24.6) blocks were built. Those blocks will be referred to as $\mathrm{ROI}_{\mathrm{i,small}}$ (i is the ROI number). By comparing the quality of the block signals, the aim was to find systematic characteristics which are worth to look into and which should be considered for a substantial analysis. Based on the results (see Fig. 28, red wavelength)

2 Note: In this chapter, the term "filter setting" will be used which also refers to the setting without polarizers.

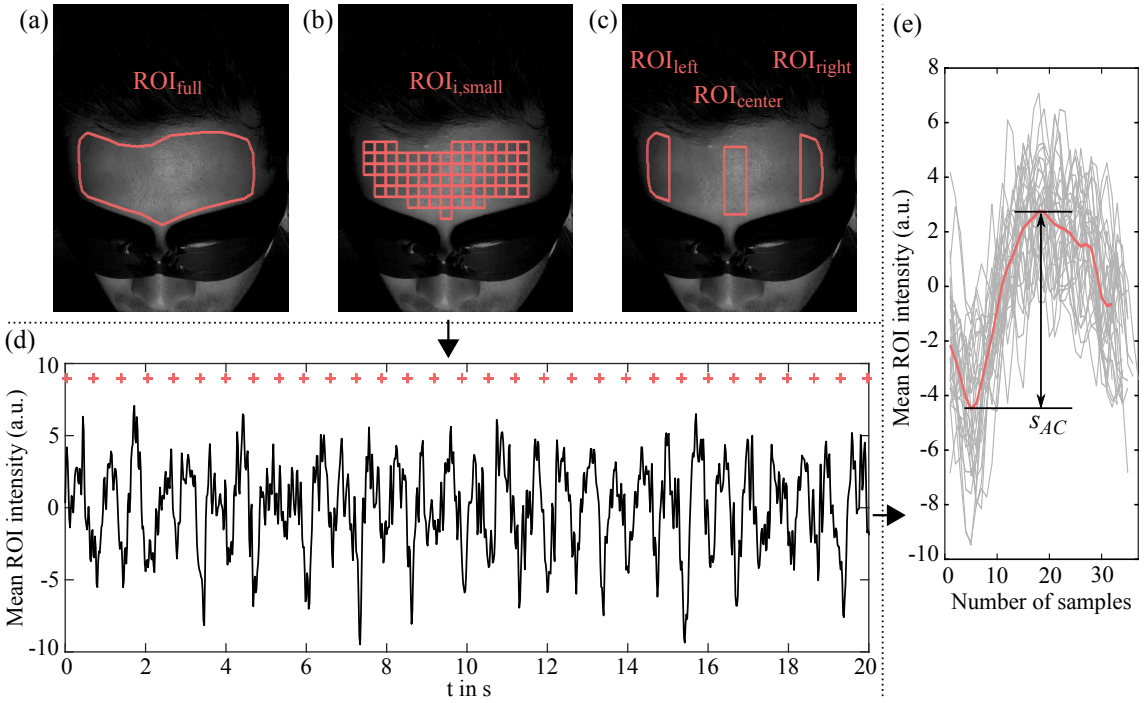

Figure 27: Main processing steps for the evaluation of the polarization experiment: (a) Selection of the forehead ROI, (b) Selection of equally sized sub-ROIs, (c) Selection of ROI strips, (d) Beat detection in the extracted cbPPG signal (red crosses: diastolic positions from reference plethysmogram), (e) Calculation of the parameter s_{AC} in the mean beat (red). (Reprinted and adapted with permission from [339], The Optical Society (OSA).)

and prior knowledge about BCG influences at lateral areas [225], three additional ROIs were determined and set to be evaluated in depth along with $\mathrm{ROI}_{\mathrm{full}}$. Two regions $\mathrm{ROI}_{\mathrm{left}}$ and $\mathrm{ROI}_{\mathrm{right}}$ were positioned at the left and right side of the forehead holding a width of 30 pixels (empirically chosen). The third region $\mathrm{ROI}_{\mathrm{center}}$ was defined as a reference with the same width and aligned in the middle of $\mathrm{ROI}_{\mathrm{left}}$ and $\mathrm{ROI}_{\mathrm{right}}$. The three ROIs were confined by $\mathrm{ROI}_{\mathrm{full}}$, and they all had similar sizes ensuring a better comparability between the results (see Fig. 27 (c) for an example).

After annotation, the cbPPG signals were extracted by averaging the pixel values inside the respective ROI for every video frame. Consequently, for each measurement and ROI, one signal was obtained. To assess the quality of the acquired signals, an appropriate index had to be selected. Hülsbusch [120], who also investigated polarization filtration for cbPPG, did not clarify what kind of quality parameter he used. Sidorov et al. [305] took the strength of the $\mathrm{AC}_{\mathrm{HF}}$ component and normalized it with the magnitude of the steady signal component. In general, such a normalization makes sense to avoid the dependency of this strength on the absolute light intensity [189]. For the pulse-based calculation of the arterial oxygen saturation, for example, the step is carried out for the same reason [104]. However, the (quasi-)steady components (DC, $\mathrm{AC}_{\mathrm{LF}}$) in plethysmograms are also influenced by factors that do not necessarily affect the $\mathrm{AC}_{\mathrm{HF}}$ component (see Paragraph *Signal Characteristics* in 2.5.1). Stated another way, an actual stronger oscillation of the blood volume might not always reflect in the normalized parameter. Therefore, it was decided to solely declare the

pulsation strength of the AC_{HF} component (denoted by s_{AC}) as quality index. For the determination of s_{AC}, firstly, the signals were bandpass filtered using a Butterworth filter (order 5, cutoff 0.5 and 15 Hz) to suppress low-frequency variations and high-frequency noise. Next, the signals were inverted and its beats were detected. To prevent any false detections, the plethysmograms from the ear clip were utilized. The plethysmograms' minima positions, which were extracted by applying the OSET MaxSearch algorithm [286], were used to cut out the single beats of the cbPPG signals. Beats were omitted if their height was bigger than 30 intensity units[3]. The remaining beats were averaged to one mean beat. Eventually, the pulse strength s_{AC} was set as the distance between the absolute minimum and maximum of the mean beat resulting in one s_{AC} value for each measurement and ROI. Figure 27 exemplarily depicts the procedure for one signal. Since the reference-guided detection does not consider if the pulsation component is related to the cardiac cycle, a noise level estimate n_{AC} was calculated for comparison[4]. Two different ROIs with similar size and illumination as ROI_{full} and $ROI_{left/right/center}$, respectively, were applied to the background in a reference measurement. It should be noted that this step was based on an analogous approach from Kamshilin et al. [148]. In the same way as s_{AC}, n_{AC} was determined for the extracted signals leaving two noise values, one for the full forehead ROI and one for the ROI strips. The values are visualized as magenta lines in Fig. 29.

Evaluation and Statistics

Across all 18 subjects and nine measurements, the behavior of the s_{AC} values was statistically analyzed in each of the four ROIs (full, left, center, right). In order to assess whether the polarization filtration causes a significant change in s_{AC}, a Friedman test was applied separately for each light color setting and ROI. If the Friedman test showed significance, post-hoc tests were performed using the Wilcoxon signed-rank test (two-sided) where p-values were adjusted by the Bonferroni correction. Note that always three groups ('o','||','+') with 18 values were considered. In a second analysis, the differences between the three wavelength configurations were evaluated for each ROI and filter setting. Statistical testing was done over the respective three groups (blue, green, red) in the same way as in the first analysis. Eventually, a third analysis was performed to compare the results of the three ROI strips since they were built due to local differences. For this purpose, three groups (left, middle, right) were taken into account for each light color and filter setting and statistically tested as described above.

The Friedman and the Wilcoxon signed rank test were chosen based on the recommendations in [33]. The following reasons led to the decision: (i) A general dependency exists between the analysis-related groups, (ii) the s_{AC} values show no normal distribution.

3 The thresholds stems from the analyses of Hülsbusch [120] who reported a maximum relative pulsation strength of about 2 %. In the polarization study, the mean ROI intensity was approximately 1500 units (normalization value). Thus, the threshold could be calculated: $2\,\%/100\,\% \cdot 1500 = 30$.

4 The idea behind the approach is that an s_{AC} value can be rightly found invalid if it approximates the respective n_{AC} value. In this way, false conclusions are avoided.

Implementation

The described processing and evaluation steps were all implemented in MATLAB R2016a (The MathWorks, Inc. in Natick MA, USA). For certain steps, such as the ROI annotation, bandpass filtering or statistical testing, available functions from the software's toolboxes were used.

4.3 RESULTS

The results for the full forehead ROI are depicted in Fig. 29 (a). The Friedman test shows that the polarization filtration leads to a significant change in the signals' pulsation strength for all three light color configurations (see Table 10, first column). The strongest differences can be found for blue and green light, the lowest for red. As the post-hoc tests prove, the '+' setting yields signals with significant higher pulsations s_{AC} than the '||' setting does. The same holds true for the '+' and 'o' setting with the exception of the red wavelength range. It should be noted that for red light, the s_{AC} values accumulate around the noise level which makes their validity questionable. Blue is the only light color to provide statistical differences between the 'o' and '||' setting although the trend within each color configuration implies the 'o' setting to perform generally better. When comparing the effects of the illumination wavelengths, substantial differences can be found (see Table 11, first three rows). The strongest ones occur with respect to red light. The application of the green light provides the best outcome for s_{AC}. The values for blue are similarly high while the ones for red yield poor results.

Figure 28 illustrates the locally determined pulsation strengths in $\mathrm{ROI_{i,small}}$ at the forehead of three subjects. This illustration can be found for all individuals in the Appendix A.2 in Fig. 59. Mainly for red lighting, a strong pulsation seems to occur for the left and right area when comparing them against the center area. This effect caused the decision to investigate these regions separately by applying and assessing $\mathrm{ROI_{left}}$ and $\mathrm{ROI_{right}}$, as well as $\mathrm{ROI_{center}}$ for reference purposes (see also Section 4.2).

For the three ROI strips, the results generally show larger s_{AC} values than for the full ROI (see Fig. 29 (b) - (d)). The characteristic of s_{AC} in the center ROI, with respect to the different light color and filter settings, highly resembles the one in the full ROI. Apart from the red light configuration, the polarization filtration proves again to have a significant impact on the outcome (see Table 10, column 3). The results of the post-hoc tests show minor irregularities. However, the two lateral ROIs provide a more contradictory outcome. Whereas for the right ROI, polarization seems to affect the signal's pulsation strength, for the left ROI, there are barely any differences between the filter settings (see Table 10, column 2 and 4). The applied post-hoc tests confirm this assessment. For the right ROI, the '+' setting is consistently better than the '||' setting and, except for red lighting, also better than the 'o' setting. When comparing the effects of the illumination wavelengths (Table 11), no differences can be found on the left and the right side. The pulsation strength values for

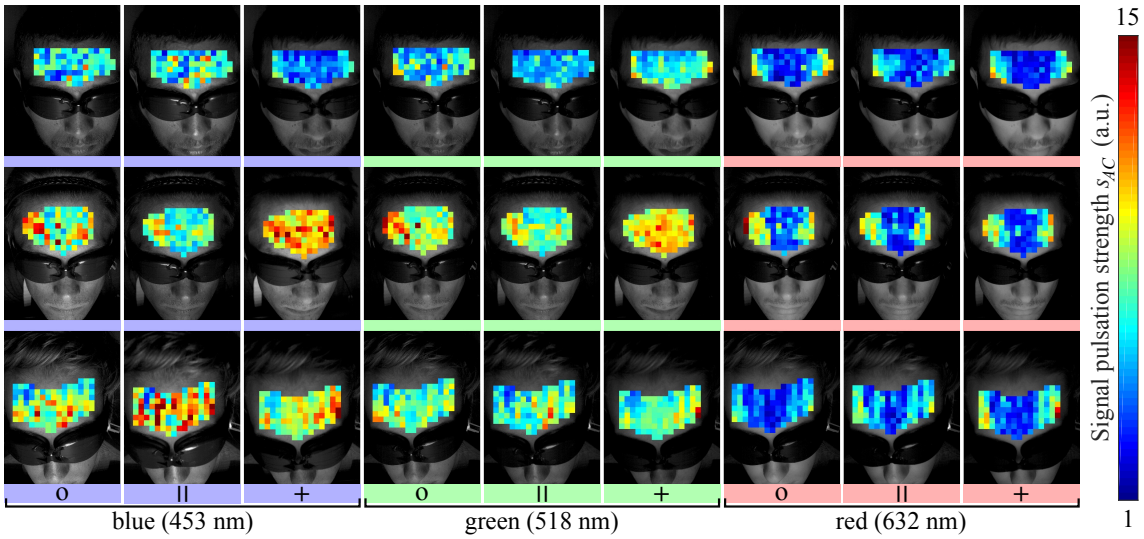

Figure 28: Depiction of the local pulsation strength s_{AC} in $\text{ROI}_{\text{i,small}}$ (three subjects are depicted exemplarily). The respective values are false-color coded (see color map). The symbol 'o' represents the setting without polarization filters, '||' the parallel setting and '+' the perpendicular setting. The chosen light color setting is represented by lines below the images and is specified with the peak wavelengths. (Reprinted and adapted with permission from [339], The Optical Society (OSA).)

red light are substantially higher in these ROIs and reach the same level as can be achieved for blue and green light. Only for the center ROI, the results significantly differ between the color configurations, which is mainly caused by the poor performance at red light. When comparing the three ROI locations (Table 12), one comes to a similar conclusion. Exclusively for red light, the left, as well as the right region prove to provide significantly different results for all filter settings with respect to the center region. However, according to the tests, the lateral regions do not differ from each other. For green and blue light, the results imply that there are no differences between the locations regardless of which filter setting was employed. Note: The factors 'filter setting', 'color setting' and 'ROI location' were considered separately, and conclusions were drawn with regard to those factors.

Table 10: Impact of polarization filtration on the signal pulsation strength s_{AC}: Results of the Friedman tests that were applied to analyze the differences between groups of the same color but varying filter settings. The values are given separately for all tested ROIs (full forehead, left, center and right region). The corresponding post-hoc tests are depicted in Fig. 29. (Reprinted with permission from [339], The Optical Society (OSA).)

	ROI			
	FULL	LEFT	CENTER	RIGHT
Blue	***	**	***	***
Green	***	n.s.	***	***
Red	*	n.s.	n.s.	*

n.s. $p > 0.05$, * $p \leq 0.05$, ** $p \leq 0.01$, *** $p \leq 0.001$

Table 11: Impact of the light configuration on s_{AC}: Results of the i) Friedman tests that were applied to analyze the differences between groups of the same filter setting but varying light color configurations (column 1), and ii) post-hoc tests for the comparison of the configurations (column 2-4). The results are listed for each ROI. The symbol 'o' represents the setting without polarization filters, '||' the parallel setting and '+' the perpendicular setting. (Reprinted and adapted with permission from [339], The Optical Society (OSA).)

		Light Color			
		All	Blue - Green	Blue - Red	Green - Red
Full	o	***	*	***	***
	||	***	**	***	***
	+	***	*	***	***
Left	o	n.s.	n.a.	n.a.	n.a.
	||	*	n.s.	n.s.	n.s.
	+	n.s.	n.a.	n.a.	n.a.
Center	o	***	n.s.	***	***
	||	***	**	***	***
	+	***	*	***	***
Right	o	n.s.	n.a.	n.a.	n.a.
	||	n.s.	n.a.	n.a.	n.a.
	+	n.s.	n.a.	n.a.	n.a.

n.a. post-hoc test not applied, n.s. $p > 0.05$, * $p \leq 0.05$, ** $p \leq 0.01$, *** $p \leq 0.001$

Table 12: Impact of the ROI location on s_{AC}: Results of the i) Friedman tests that were applied to analyze the differences between groups of the same filter setting but varying ROI locations (column 1), and ii) post-hoc tests for the comparison of the three ROI locations (column 2-4). The results are listed separately for each light configuration. The symbol 'o' represents the setting without polarization filters, '||' the parallel setting and '+' the perpendicular setting. (Reprinted with permission from [339], The Optical Society (OSA).)

		ROI			
		All	Left - Right	Left - Center	Right - Center
Blue	o	n.s.	n.a.	n.a.	n.a.
	||	n.s.	n.a.	n.a.	n.a.
	+	n.s.	n.a.	n.a.	n.a.
Green	o	n.s.	n.a.	n.a.	n.a.
	||	n.s.	n.a.	n.a.	n.a.
	+	n.s.	n.a.	n.a.	n.a.
Red	o	***	n.s.	***	***
	||	***	n.s.	***	***
	+	***	n.s.	***	***

n.a. post-hoc test not applied, n.s. $p > 0.05$, * $p \leq 0.05$, ** $p \leq 0.01$, *** $p \leq 0.001$

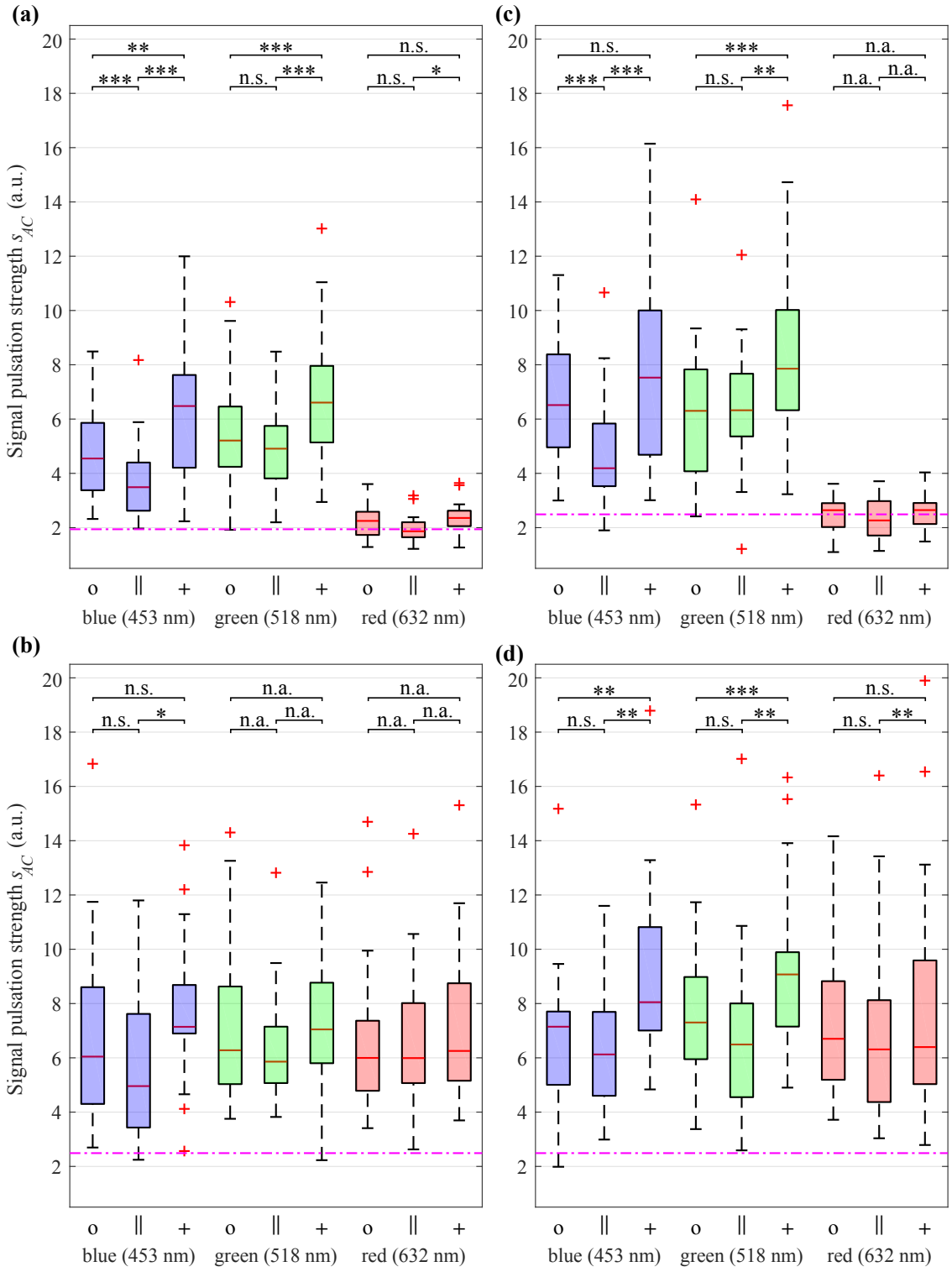

Figure 29: Boxplots of the pulsation strength values depicted for the different light color and filter settings: (a) Full forehead ROI, (b) Left ROI, (c) Center ROI, (d) Right ROI. The results of post-hoc tests (filtration) are also given (n.s. $p > 0.05$, * $p \leq 0.05$, ** $p \leq 0.01$, *** $p \leq 0.001$). If the post-hoc test was not applied 'n.a.' is used. The symbol 'o' represents the setting without polarization filters, '||' the parallel setting and '+' the perpendicular setting. The chosen color setting is represented by the boxes' coloration and is specified with the peak wavelengths. The magenta lines depict the noise level n_{AC}. (Reprinted and adapted with permission from [339], The Optical Society (OSA).)

4.4 DISCUSSION

4.4.1 *Impact of Polarization Filtration*

Apart from the red light configuration and the left ROI location, the '+' filter setting proved to provide signals with the highest pulsation strengths, while the '||' setting consistently led to the lowest values. This outcome suggests that cbPPG signals hold higher qualities when the received light from the skin surface is eliminated. With respect to the performance of the 'o' setting, it can be similarly concluded that effects from the surface suppress the cardiac information in signals from deeper skin layers. Theses results deviate from the outcome of Hülsbusch's study [120] who found no improvements in the signal quality when using the '+' filter setting. The findings also fundamentally disagree with the ones of Sidorov et al. [305]. They reported that the application of the '+' setting leads to no significant increase in the relative pulsation strength for the green wavelength range. Interestingly, in their setup, the palm region was compressed against a glass plate, and only suitable ROIs (so-called hot spots) were taken into account. The tissue pressure might be a defining factor since it substantially changes the optical characteristics of the (sub-) cutaneous measurement site (see Paragraph *Signal Origin* in Section 2.5.1). It should be also mentioned that the glass plate alters the light coupling into the skin due to the higher refractive index of glass [271]. Moreover, specular reflection will mainly occur on the glass surface as it is much smoother than the skin surface [284]. Present reflections, however, were most likely avoided anyway by the applied ROI selection. In other words, the group's setup is hard to compare to the contactless scenario in this study.

In order to make sure that conflicting findings are not caused by the employed quality parameters, an additional investigation was performed where the pulsation strength was normalized on the steady signal component (denoted by s_{DC}), analogously to Sidorov et al. [305]. The results for the relative strength values ($100\,\% \cdot s_{AC} / s_{DC}$) can be found in the Appendix A.2 in Fig. 60. The outcome for the filter, light color and ROI setting strongly resembles the one of the s_{AC}-based analyses (see Fig. 29) proving the validity of the chosen parameter. The resemblance was expected since the camera's aperture was repeatedly adjusted to keep the mean image intensity[5] constant across the measurements. A consistent intensity decrease in the '+' setting could be observed nevertheless (see Fig. 24 (5) - last row). As this setting usually provides a larger pulsation strength, the normalization with s_{DC} only leads to an even better differentiation and does not compromise the fundamental consensus.

The influence of polarization filtration evidently depends on the ROI location and appears to almost vanish at the left lateral region (see Fig. 29 (b) - (d)). However, the similarities between the full and the center ROI imply that the influence remains dominant in larger regions regardless of local differences. It should be noted, the effect of achieving

5 Note: The mean image intensity is proportional to s_{DC} meaning that if the mean intensity stays unchanged, a normalization does not affect the characteristic behavior of the parameter.

higher pulsations in smaller ROIs originates from the fact that averaging over larger regions causes a suppression of local variations in the signal's morphology (see Paragraph *Instrumentation and Signal Acquisition* in Section 2.5.1).

4.4.2 *Signal Origin*

Light Color Setting

Classic blood volume theory For the full and the center ROI, blue and green light provide the highest signal pulsation strengths whereas red light yields the lowest strengths (see Fig. 29 (a) and (c)). This behavior coincides with the absorption characteristic of hemoglobin [188] and, therefore, supports the theory that the cbPPG signal arises from blood volume changes. However, compared to other experimental investigations [30, 67, 71, 203], which multispectrally analyzed the cardiac strength of photoplethysmographic signals, the blue wavelength range shows a surprisingly high response. In general, many factors can play a role for the varying performance of certain light ranges. The application of external pressure on the examined skin tissue, for example, might cause such variations (see Section 2.4.1 and 2.5.1). Previous cbPPG works showed that the compression of superficial tissue leads to a significant change in the morphology and amplitude of the received signal [149, 228]. Moço et al. [228, 229] argued that in this case, the cbPPG signal mostly arises from the deeper-lying vasculature due to the occlusion of superficial vessels. This theory could explain the outcome for the blue light. While common PPG sensors always apply pressure on the skin, setups for cbPPG usually do not [9, 393]. Therefore, in a contactless setting, superficial vessels have a stronger impact on the signal, especially for blue light where the penetration depth is low and the absorption by hemoglobin high (see Fig. 8 and 9). However, Corral et al. [67, 203] who also conducted remote measurements on the forehead did not report particular good signal qualities in the blue wavelength range. When applying the classic PPG theory to such results, the limited performance for blue light can be attributed to the penetration depth as photons interacts less with pulsating vessels than they would do for longer wavelengths (see Table 3 and Fig. 9).

Theory by Kamshilin et al. Since the results of this study show better qualities for blue light, the theory by Kamshilin et al. [145, 149, 357] might pertain. As described in Section 2.5.1, the theory presumes that the oscillation of the transmural pressure in arteries periodically deforms the adjacent tissue including the papillary dermis. The deformation causes the density of shallow capillaries to oscillate as well. Consequently, incoming light can be modulated by even superficial blood volume changes and does not have to reach the pulsatile vasculature (see Fig. 15). If true, according to the absorption characteristic of hemoglobin [188], one would expect a high pulsation strength in the blue wavelength range. It should be pointed out, the theory was proposed based on experiments at the inner hand where short-wavelength light indeed barely reaches any blood vessels due to

the thickness of the epidermis (see Fig. 9 (b) and Table 2). At the forehead, however, it is very likely for blue light to interact with compliant arterioles (see Fig. 9 (a)).

ROI Location

Based on the deviating results which were obtained for the lateral ROIs (see Table 12), one may argue that the cardiac signals in these regions (partly) arise from sources other than those in the center ROI. In Section 2.5.1 (Paragraph *Signal Origin*), it was described how BCG effects degrade the photoplethysmographic signal in videos recordings. Moço et al. [225] studied the impact of global[6] BCG effects in facial areas and found that they are most prominent in case of inhomogeneous and non-orthogonal illumination. Since the forehead has a characteristic horizontal curvature [398], it is save to say that in this experiment, a lateral ROI placement causes the respective skin surfaces to not be aligned orthogonally towards the direction of the incoming light. Therefore, cbPPG signals in the left and right ROI are certainly to some extent influenced BCG interference. Moreover, different investigations have reported a general wavelength independence of BCG effects [225, 226]. This insight further proves the significant impact of those effects in $\mathrm{ROI}_{\mathrm{left}}$ and $\mathrm{ROI}_{\mathrm{right}}$ as the pulsation strength values for red light reach the same level as for blue and green light. Such a characteristic can not be found if blood volume changes are defining for the signal's modulation (see Fig. 29 (c)). Moço et al. [225] also discovered that remnants of the BCG interference were still present in the blue channel despite applying homogeneous and orthogonal illumination. Although this finding could represent an alternative to clarify the high signal response for blue light in $\mathrm{ROI}_{\mathrm{center}}$ and $\mathrm{ROI}_{\mathrm{full}}$, it is uncertain why BCG effects would not have a similar influence in all three lighting settings.

In general, the left and right ROI provide qualitatively comparable results. Nevertheless, differences in the filter setting between the regions are noteworthy. In the following, it is established why these differences presumably reflect the impact of BCG effects. Moço et al. [225] claimed that subsurface scattering is the main mechanisms which is responsible for the light's modulation by BCG effects. Specular reflectance at the skin surface was declared to be a minor contributor. In fact, in their experiments, perpendicularly oriented polarizers were employed to suppress specular reflection [225, 226]. However, when considering the outcome for the relative pulsation strength (see Fig. 60), especially for blue light, cardiac information appears to emerge more distinctively from the direct surface ('||' setting for $\mathrm{ROI}_{\mathrm{left}}$ and $\mathrm{ROI}_{\mathrm{right}}$). Known characteristics of optical processes in the skin actually support this theory (see Section 2.3.2). Light inside the tissue undergoes total reflection if it hits the surface with an angle $\gtrsim 42\,^{\circ}$. As a consequence, the more the camera is aligned with that angle, the more light from the surface and the less light from inside the skin is received. Furthermore, if the angle is exceeded, exclusively surface information is obtained by the camera. In other words, in case of non-orthogonality, specular reflection is probably the main modulating mechanism for BCG effects. Based on those insights, pure BCG sig-

6 Global BCG effects originate from the forces of blood movement in the heart and arteries, as well as the heart movement itself, and they cause the body to oscillate in accordance with the cardiac cycle [99].

nals should show a high response in the '||' setting. Pure photoplethysmographic signals, in contrast, should manifest the best in the '+' setting (e.g. in $\mathrm{ROI}_{\mathrm{center}}$) as the light's interaction with the vasculature is necessary. Hence, regarding the outcome for the filter settings, the impact of BCG effects must be the strongest in the left ROI (filtration differences marginal) whereas, in the right ROI (filtration differences notable), BCG and blood volume effects contribute more equally to the measured signal. The disparity between the left and right ROI most likely originates from a systematic dislocation in the system setup. The initial arrangement of the light source might have led minimally to a non-symmetrical illumination of the face. Consequently, the right forehead area was illuminated more orthogonally causing a suppression of the BCG effects' influence. Nevertheless, the results' tendency in both regions is still very similar when comparing it to the center ROI.

Filter Setting

Polarization filtration provides additional value to the investigation of establishing the signal's origin. The generally good performance of the '+' setting for the full and center ROI (blue and green light) proves that cbPPG signals from those regions are mainly modulated by variations in the vasculature (i.e. beneath the surface). However, the cardiac signal component in the '||' setting is still existent as corresponding s_{AC} values lie considerably above the noise level (see Fig. 29 (a) and (c)). The outcome could imply that the cbPPG signals in $\mathrm{ROI}_{\mathrm{full}}$ and $\mathrm{ROI}_{\mathrm{center}}$ also arise from the skin surface. The following listing discusses this hypothesis:

a) *BCG effect* If BCG interference is effective in homogeneously and orthogonally illuminated areas, the receivable information about blood volume changes will be superimposed by BCG information. In this case, cardiac surface signals would be detectable and exclusively caused by BCG effects. However, for homogeneous illumination, Moço et al. [225] only found a remnant BCG interference to occur in the blue wavelength range which would not explain the results for the green light configuration.

b) *Depolarization* As polarized light penetrates the skin, its polarization state changes due to scattering (depolarization) [75, 132]. The deeper the light travels, the stronger the degree of depolarization is [222]. However, unpolarized light is simply a superposition of linearly polarized waves with a random phase in the polarization plane [187]. This fact implies that there will be always a fraction of backscattered light which holds the same polarization state as the incoming light. The fraction can be captured by the camera in the '||' setting and carries information from skin layers other than the surface. It would also be affected by hemoglobin's absorption, and one would predict a lower pulsation strength for red light.

c) *Filter's extinction ratio* The extinction ratio of polarizers is a quality index [36]. Finite ratio values, as existent in this experiment (see Table 9), show that light can not be polarized perfectly. Therefore, unpolarized and polarized fractions from beneath the skin surface might enter the camera sensor in the '||' setting (similar to b)). However, due to the high extinction ratios, this effect is assumed to be negligible.

In conclusion, the performance of the '||' setting is mostly explainable by point b).

Morphology Analysis

The contour analysis of the pulse waveform is an additional approach to draw conclusions about the cbPPG signal's origin [225, 226]. In particular, the assessment of morphology changes which result from a different ROI placement, light color and filter setting might provide a benefit in this study. The quantification of such changes across all subjects turned out to be complicated as certain shape characteristics vary strongly among individuals. Hence, for discussion, only one participant was considered where the waveforms show specific peculiarities that were also found for other subjects. The mean beats of the chosen subject are visualized in Fig. 30, depicted for the different ROI strips, filter settings, and light configurations. The beats were determined as described in Section 4.2.

Middle ROI For blue and green light, the shape of the waveforms in the center ROI resemble the classic PPG waveform (see Fig. 11) which backs the previously stated claim that the respective signals are modulated by blood volume changes. The filter setting has more impact on the beats' height as on the shape. For red light, the contour is hard to characterize due to the low pulsation strength.

Left ROI In the left ROI, the waveforms are substantially different from those in the center ROI which mainly reflects in changes of phase and frequency (Fig. 30, first row). Such shifts in phase and frequency generally point to the presence of BCG effects [225, 226]. It should be pointed out that camera-based BCG signals do not show a definite characteristic since their manifestation highly depends on the ROI location and the orientation of the light source [225, 226]. Similar to s_{AC}, the waveform only varies slightly in the different light configurations. This outcome further supports the theory of BCG interference to be prominent in $\mathrm{ROI}_{\mathrm{left}}$ (see Paragraph *ROI Location*).

Right ROI Based on the results for the pulsation strength in the right ROI, it was concluded earlier that BCG and blood volume effects contribute more equally to the measured signal there. When considering the waveforms (Fig. 30, third row), this conclusion can be corroborated since they appear to be a mixture of the waveforms from the center and left ROI. For red light, BCG interference seems to be dominant which not only reflects in the shape but also in the pulsation strength (see center ROI for comparison). For blue and green light, polarization filtration still causes an attenuation and augmentation of the waveforms, in a way, as one would expect it to occur for blood volume signals.

CHAPTER SUMMARY

The objective of this chapter was to assess the value of polarization filtration for cbPPG. To do so, a data set of 18 subjects, which were recorded with different polarizer and light settings, was analyzed. The evaluation was performed based on a quality parameter, the cardiac pulsation strength s_{AC}, which was determined for cbPPG signals from the individ-

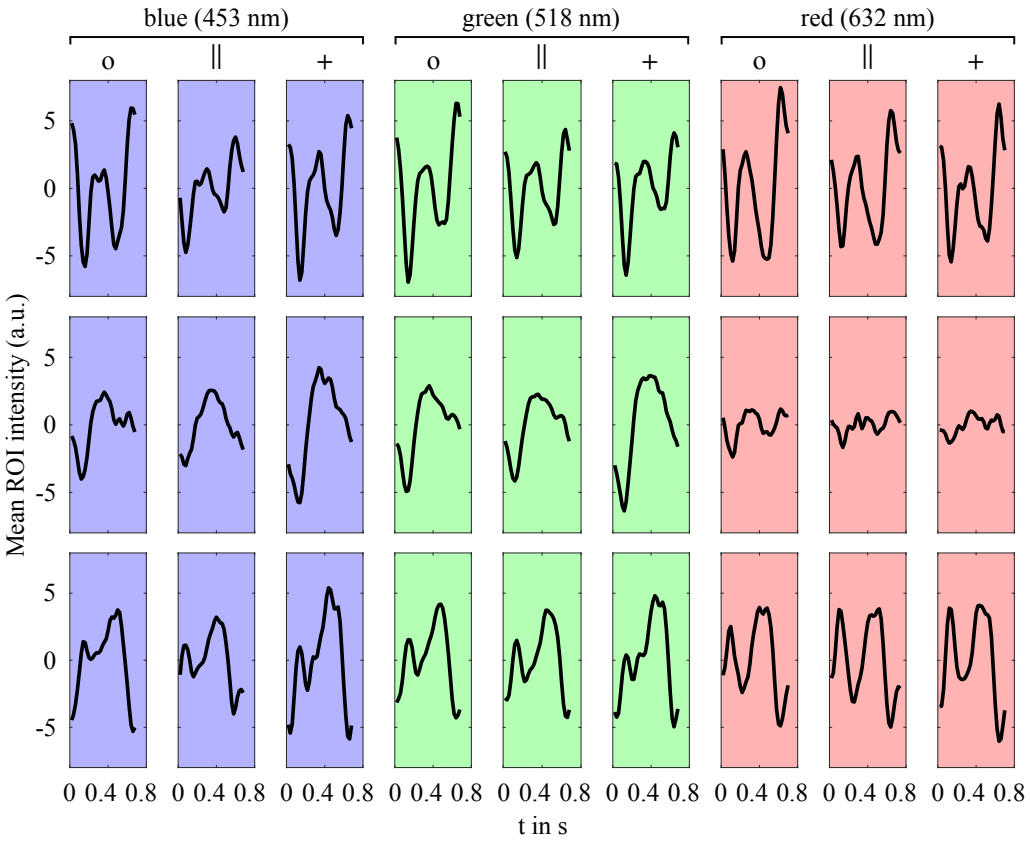

Figure 30: Calculated mean beats of one subject for different ROIs, filter and light color settings. The first row shows the results of the left ROI, the second row for the center ROI and the third row for the right ROI. The symbol 'o' represents the setting without polarizers, '||' the parallel setting and '+' the perpendicular setting. The chosen light configuration is represented by the boxes' coloration and is specified with the peak wavelengths. (Reprinted and adapted with permission from [339], The Optical Society (OSA).)

uals' forehead. The results show that in case of orthogonal illumination, a perpendicular filter alignment provides a significant benefit for cbPPG in the blue and green wavelength range. Furthermore, the outcome supports the theory that blood volume variations are the defining element for the signals' modulation. A strong pulsation for blue light, however, led to the suspicion that the classic PPG model does not hold for cbPPG. Instead, it might be evidence for an alternative model to apply, the *deformation model by Kamshilin*. In case of non-orthogonal illumination, polarization filtration has a smaller impact on the quality of cbPPG signals. This outcome can be associated with BCG interference which is prominent in the lateral regions and affects all wavelength ranges equally. Considering the filter-dependent behavior of another quality parameter, i.e. the relative pulsation strength s_{AC}/s_{DC}, it was found that specular reflections contribute strongly to the modulation of the BCG signal component. In conclusion, the cbPPG's response to specific polarizer and light settings is potentially a useful marker to distinguish between camera-based BCG signals and blood volume signals.

5

NOVEL APPROACH FOR ROI SELECTION

In this chapter, a novel method for ROI selection in cbPPG is introduced. The proposed approach tackles the problem of BCG interference, which was discussed in the last chapter, as it attempts to automatically reject affected skin areas. Furthermore, the method is designed not to be restricted to a specific body site or to rely on the presumption that blood volume variations can always be detected. The first section gives a brief overview on available ROI selection techniques, points out their drawbacks, and formulates the research gap. The next section delineates the different steps of the novel method. The third section describes how the method's performance was evaluated. Three large and challenging data sets were chosen for that purpose. The fourth section presents the results which are then discussed in the last section with respect to other approaches. It should be noted that the following descriptions are partly adopted from my corresponding publication [340][1].

5.1 STATE OF THE ART

One of the biggest advantages of cbPPG is that no contact is required between the sensor and the skin site. The camera can be set up remotely not disturbing the subject at all. As a result, the considered person has not only to be located for the measurement, but potentially suitable skin areas have to be isolated as well. In addition, it is necessary to track a detected region (ROI) as relative movements might occur. To sustain the cbPPG's convenient applicability, those steps should also be conducted automatically. The efficiency of ROI selection eventually determines the quality and validity of the extracted plethysmograms [171, 181, 393] and is, therefore, crucial.

In general, facial regions are preferred ROI candidates since they are most often accessible and because the cutaneous perfusion is relatively high at these sites [344, 393]. There are three main approaches of how to select such regions for cbPPG (see Fig. 31). The most common approach is to utilize established detection algorithms that provide the position of the whole face[2] or of specific facial landmarks[3]. The found locations are then used to define one or several ROIs (e.g. cheeks and forehead) which are usually adjusted over time

1 The original work is licensed under the Creative Commons Attribution 4.0 International License. Some descriptions were adopted and modified.
2 References: [5, 6, 64, 83, 85, 90, 93, 110, 112, 131, 173, 216, 254, 262, 279, 329, 371, 375, 391]
3 References: [37, 92, 105, 117, 179, 183, 210, 213, 245, 264, 265, 328, 331, 343, 390]

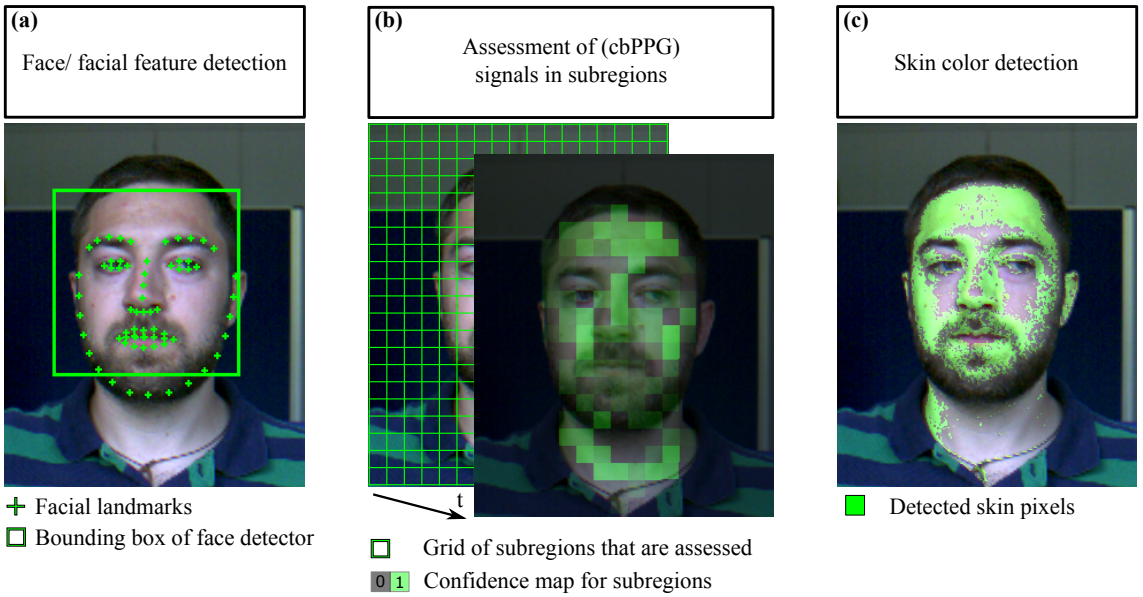

Figure 31: Three main approaches for facial ROI selection in cbPPG: (a) Detection of the face or facial features, (b) Assessment of local signals over time with respect to their physiological content, (c) Skin color detection. Please note, the pictures illustrate the principle ideas. Actual implementations may vary. (The figure was created based on descriptions in [393] and the research presented in Section 5.1. The examples were built with methods proposed in [184, 354] – bounding box, [25] – landmarks, [200, 259] – skin detection.)

by means of tracking techniques or by simply carrying out the initial detection repeatedly [393]. This approach, however, relies on the visibility of certain anatomical areas and might consequently fail if the face is partly occluded or rotated [115]. Even if the detection succeeds, a selected ROI could still be blocked, for example by hair. These problems may not be relevant in controlled environments, like the laboratory, but have to be considered for clinical settings and realistic everyday scenarios [269, 368] (see Section 5.3.1). One way to avoid any dependence on the detectability of facial features is to select ROIs based on the presence and prominence of physiological information in local time signals [13, 14, 38, 104, 311, 355, 363, 365] (see Fig. 31 (b)). For that approach, the images are firstly blurred, downsampled or divided into small subregions. The extracted signals from the pixels/ subregions are then assessed in terms of their variations related to the cardiac or respiratory cycle. Utilizing the assessment, a regional selection or weighting can be performed. Although the approach seems convenient, two major drawbacks arise. First, it relies on a distinct manifestation of the cardiac pulsation in the plethysmograms. This manifestation is most likely strong in young and healthy subjects, but certainly diminished in older and vascular diseased subjects [9, 66, 170, 388]. Consequently, the pulsation may be hard to identify for the latter group. Second, small image regions often hold low-quality cbPPG signals (see Section 2.5.1, Fig. 14) predisposing the approach to failure. Another way to find suitable face ROIs is to apply skin classifiers which detect proper pixels or patches solely based on the characteristic appearance of skin in a set color space [65, 186, 212, 260, 327, 367, 368, 395] (see Fig. 31 (c)). Such an approach is often pursued by works

that focus on signal processing and accept potential insufficiencies in the classification result. In fact, skin classifiers were found to be rather employed in combination with face or facial landmark detection in order to enhances the overall robustness of the ROI selection process[4]. To that end, it should be noted, many methods actually combine the described approaches somehow: (i) skin detection & local signal assessment [362, 402], (ii) skin detection & local signal assessment & face/ facial landmark detection [106], (iii) local signal assessment & face/ facial landmark detection [42, 86, 167, 198, 261, 352].

Besides the general goal of reliably localizing ROIs, identifying homogeneous regions should be also of high concern. As explained in Section 2.5.1 (Paragraph *Signal Origin*) and subsequently proven in the last chapter, heterogeneously illuminated skin areas provide BCG signals which substantially degrade the wanted blood volume signals. Although relevant, only some studies address the issue of homogeneity for ROI selection [14, 42, 106, 215, 253, 331, 386]. To do so, the usual attempt is to exclude or weight non-suitable pixels or pixel clusters based on local intensity values, lightness values and image gradients. However, for the eventual application, all those methods either still require an initial face/ facial landmark detection or depend on well-manifested cbPPG signals from small subregions.

Goal

In this chapter, a novel and fully automated ROI selection method is proposed that utilizes level set segmentation to minimize the influence of BCG artifacts. The method (i) does not rely on the detectability of anatomical features, (ii) chooses and tracks visible skin regions which are homogeneously illuminated, and (iii) solely operates on the image plane without being dependent on the presence of temporal variations related to the cardiac cycle. Except of the corresponding publication [340], to the best of my knowledge, there are no works that offer equivalent methods in the field of cbPPG. The wide-ranging applicability of the new method is demonstrated on the video data from the intraoperative, postoperative and CPT studies. The performance is evaluated with respect to the quality of extracted cbPPG signals and correctly detected HRs. Furthermore, the ROI homogeneity is assessed.

5.2 NOVEL METHOD

5.2.1 *Skin Classification*

The initial detection in the presented ROI selection approach was carried out with a skin classifier by Jones and Rehg [140, 141]. By doing so, potentially suitable regions can be found without being dependent on the visibility of anatomical features. The classifier was chosen because several survey papers on skin segmentation techniques declared it to be

4 References: [12, 23, 41, 135, 154, 164, 196, 252, 253, 267, 380, 382, 400]

one of the best performing method available [143, 258, 351]. It must only be constructed once and is then generally applicable. The construction was based on the descriptions in [141]. First, two RGB histograms $H_{skin}(\mathbf{c})$ and $H_{\neg skin}(\mathbf{c})$ were built, one for the class *skin* and one for the class $\neg skin$. To do so, a provided database by Jones and Rehg was used which contained over 4000 images where skin was apparent and labeled, and over 8000 images where no skin was apparent. For each of the two image groups, the occurrence frequency of every RGB color $\mathbf{c}$ was counted across the pixels and entered into the bins of the respective histogram. The images' color depth of 3×8 Bit led to a histogram size of 256^3 bins. Second, the conditional probability density functions $p(\mathbf{c}|skin)$ and $p(\mathbf{c}|\neg skin)$ were calculated by normalizing the histograms on the total number of counts[5] n_{skin} and $n_{\neg skin}$ [143]:

$$p(\mathbf{c}|skin) = \frac{H_{skin}(\mathbf{c})}{n_{skin}} \ , \quad p(\mathbf{c}|\neg skin) = \frac{H_{\neg skin}(\mathbf{c})}{n_{\neg skin}} \ . \tag{2}$$

These functions allow to state how likely it is that a given color $\mathbf{c}$ in the RGB space represents skin or not skin. Third, the eventual classifier was derived utilizing the Bayesian decision rule [77]. The classifier labels a particular image pixel with the color $\mathbf{c}$ as skin if [140]:

$$\frac{p(\mathbf{c}|skin)}{p(\mathbf{c}|\neg skin)} \geq \theta \ , \tag{3}$$

where θ is a threshold which determines the ratio between the true positive and false positive classification rate. A once defined threshold does not usually have to be adapted to achieve a similar result for different skin tones and lighting conditions. This robustness arises from the large and heterogeneous training data set that included images of persons with different skin types captured in various environments and illumination situations [141]. An example for the classification performance is depicted in Fig. 32. As can be seen, the choice of θ is always a trade-off between assigning too less pixels correctly to the skin class and assigning too many pixels falsely.

5.2.2 *Level Set Segmentation*

Since the classifier operates on a pixel level and does not take any local distributions into account, the outcome is usually insufficient and may not meet the requirement of obtaining homogeneously illuminated skin regions. To deal with this issue, a segmentation approach by Brox et al. [49] that utilizes the level set method was subsequently applied.

5 For the skin color histogram, a total of 79,194,520 skin pixels were counted. For the non-skin color histogram, 841,862,409 pixels were counted.

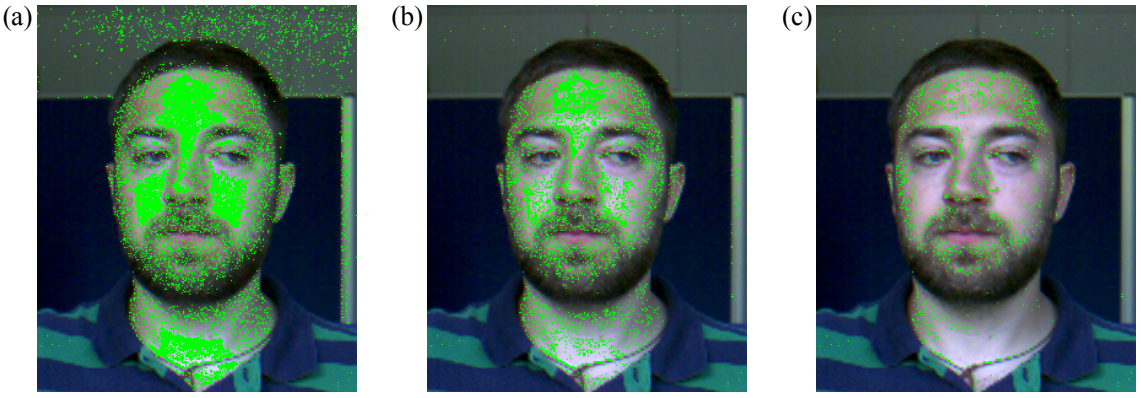

Figure 32: Outcome of a Bayesian skin classifier [140, 141] depicted at an example for three different thresholds θ. Please note, before classification, the images' intensity values were adjusted (see Section 5.2.5).

Established segmentation techniques often formulate their goal as an optimization problem in which an energy functional E is minimized such as [70]:

$$\frac{\partial C_s}{\partial t} = -\frac{\partial E(C_s)}{\partial C_s} \ , \tag{4}$$

where C_s represents the separating image contour that evolves from an initialization point at t_0 to an optimum state at t_E. The level set method allows to describe this propagation of C_s in an implicit manner using the time-dependent function $\Phi(\mathbf{x}, t)$ (also called level set function) [248]. In doing so, the contour is represented by a level line in Φ, usually at zero [70]:

$$C_s = \{\mathbf{x} \in \Omega \mid \Phi(\mathbf{x}) = 0\} \ , \tag{5}$$

with Ω being the image plane that is segmented by C_s in the space $\mathbf{x} = (x, y)$. For a two-phase segmentation approach, the inside region Ω_1 and the outside region Ω_2 are then defined as follows[6] [248]:

$$\Omega_1 = \{\mathbf{x} \in \Omega \mid \Phi(\mathbf{x}) > 0\} \ , \quad \Omega_2 = \{\mathbf{x} \in \Omega \mid \Phi(\mathbf{x}) < 0\} \ , \tag{6}$$

given that Φ is a surface which is convex upwards. Figure 33 illustrates the idea for an example. With the level set function as new descriptor, the optimization problem from equation 4 can be reformulated [70]:

$$\frac{\partial \Phi}{\partial t} = -\frac{\partial E(\Phi)}{\partial \Phi} \ . \tag{7}$$

By minimizing E, the surface Φ is dynamically changed until an optimum is reached. The question may arise why it is necessary to use a level-set-based implicit representation

6 The regions clearly define the image plane: $\Omega = \Omega_1 \cup \Omega_2$

for the evolving segmentation contour. In fact, there are several advantages which are associated with such an approach [47, 49, 70]:

- The contour does not have to be tested for self-intersection since it will not occur due to the characteristics of Φ.
- Unconnected areas, which belong to the same region Ω_i (i: number of phase), can be simply described by the same level set function. Furthermore, a directed alteration of Φ permits to easily split, merge or exclude these areas.
- The optimization process is simplified which potentially prevents the contour to get stuck at undesired boundaries during the minimization.

Aside from the fact that the level set method generally facilitates the segmentation procedure, choosing an appropriate functional E remains a challenge. To tackle this issue, here, the works by Brox et al. [48, 49] were considered who introduced a statistical region-based framework which proved to have great success for different kinds of segmentation tasks. The respective energy functional for the two-phase case reads [48]:

$$E = -\sum_{j=1}^{M} \int_{\Omega} \Big(H(\Phi) \cdot \log\, p_{1j} + (1 - H(\Phi)) \cdot \log\, p_{2j} \Big)\, d\mathbf{x} + \nu \int_{\Omega} |\nabla H(\Phi)|\, d\mathbf{x}\ , \tag{8}$$

where p_{1j} and p_{2j} are the regional statistics, ν the smoothness factor, and H the Heaviside function that is defined as [49]:

$$H(\Phi) = \begin{cases} 1 & \Phi > 0 \\ 0.5 & \Phi = 0 \\ 0 & \Phi < 0 \end{cases}\ . \tag{9}$$

Let $F(\mathbf{x})$ be a feature vector with M channels. Each channel F_j describes a certain characteristic of the input image for every location in $\mathbf{x}$. Thus, regarding the values of F_j, the quantity p_{ij} represents the probability that an image location belongs to the region Ω_i ($i = \{1, 2\}$) [49, 70]. In accordance with equation 7, the energy functional is minimized by means of the gradient descent in order to obtain the evolution equation [48]:

$$\frac{\partial \Phi}{\partial t} = H'(\Phi) \left[\sum_{j=1}^{M} \underbrace{\log \frac{p_{1j}(F_j)}{p_{2j}(F_j)}}_{\text{homogeneity term}} + \underbrace{\nu \cdot \mathrm{div} \frac{\nabla \Phi}{|\nabla \Phi|}}_{\text{curvature term}} \right], \tag{10}$$

with H' being the derivative of H and 'div' denoting the divergence of the normalized vector field[7]. The equation implicitly describes the segmentation contour's propagation from an initialization state $\Phi(\mathbf{x}, t_0)$ to an optimum $\Phi(\mathbf{x}, t_E)$. In the course of this process, the first term allows to separate Ω_1 and Ω_2 based on the similarity of the F_j values in those regions. An optimum is reached when at least one region holds a high homogeneity

7 $\nabla\Phi = (\partial\Phi/\partial x,\ \partial\Phi/\partial y)^T$ is the vector field and $|\nabla\Phi|$ are the corresponding magnitudes that are used for normalization.

with respect to the selected features in F [49]. The second term is the curvature term which pushes the level set function and, by implication, also the contour to become smoother [248]. The degree of smoothness is controlled by ν. It should be pointed out that the regional separation is very exact due to the implicit representation by Φ. In practice, the contour can be mapped onto the subpixel grid of the image.

Adaption and Contribution

When analyzing the structure of equation 10, it is evident why the framework by Brox et al. [48, 49] is well-suited for ROI selection in cbPPG. As mentioned several times before, homogeneously illuminated skin areas are the most promising regions for providing pure plethysmographic signals that are not affected by BCG interference. By means of the equation's first term, the homogeneity problem can be included in the selection process. However, there are two important issues which must be addressed to make the level-set-based approach applicable to cbPPG videos: (i) The definition of an appropriate feature vector F, and (ii) the correct initialization of the segmentation. For the feature vector, the image's intensity values were taken into account as they reflect the prevailing illumination situation. Since the majority of the recordings for this thesis encompass an RGB and a monochrome NIR video stream (see Chapter 3) and since the novel method is supposed to be able to process both streams, two different vectors emerge. In case of the RGB video, all three color channels $I_R(\mathbf{x})$, $I_G(\mathbf{x})$, $I_B(\mathbf{x})$ were added to F. In case of the NIR video, only one channel $I_N(\mathbf{x})$ could be added. In addition to the image intensity, the texture was considered as a feature [49]. The idea behind this step originates from the findings of Butler et al. [52] who showed that heterogeneities in the skin's surface topology cause artifacts if motion occurs. By integrating a texture measure J into F, homogeneous skin structures can be favored during the segmentation. For the NIR video, the measure $J_N(\mathbf{x})$ was determined by calculating the local standard deviations for $I_N(\mathbf{x})$ in neighborhoods of 5×5 pixels. For the RGB video, the measure $J_{RGB}(\mathbf{x})$ was obtained in the same way although each color channel was processed separately, and the values were then averaged to a single image. It should be pointed out, different texture quantities [49, 205] were tested with regard to the discussed application; the standard deviation proved to be the most effective one. The feature vectors for the RGB and NIR case eventually read:

$$F(\mathbf{x}) := \Big(I_R(\mathbf{x}),\, I_G(\mathbf{x}),\, I_B(\mathbf{x}),\, J_{RGB}(\mathbf{x})\Big) \quad \text{and} \quad F(\mathbf{x}) := \Big(I_N(\mathbf{x}),\, J_N(\mathbf{x})\Big)\,. \tag{11}$$

The density functions, which assess the probability for the pixels' belonging to Ω_1 and Ω_2 in the course of the segmentation, were modelled by Gaussian distributions [48]:

$$p_{ij} = \frac{1}{\sqrt{2\pi\sigma_{ij}^2}} \exp\left(-\frac{(F_j - \mu_{ij})^2}{2\sigma_{ij}^2}\right), \tag{12}$$

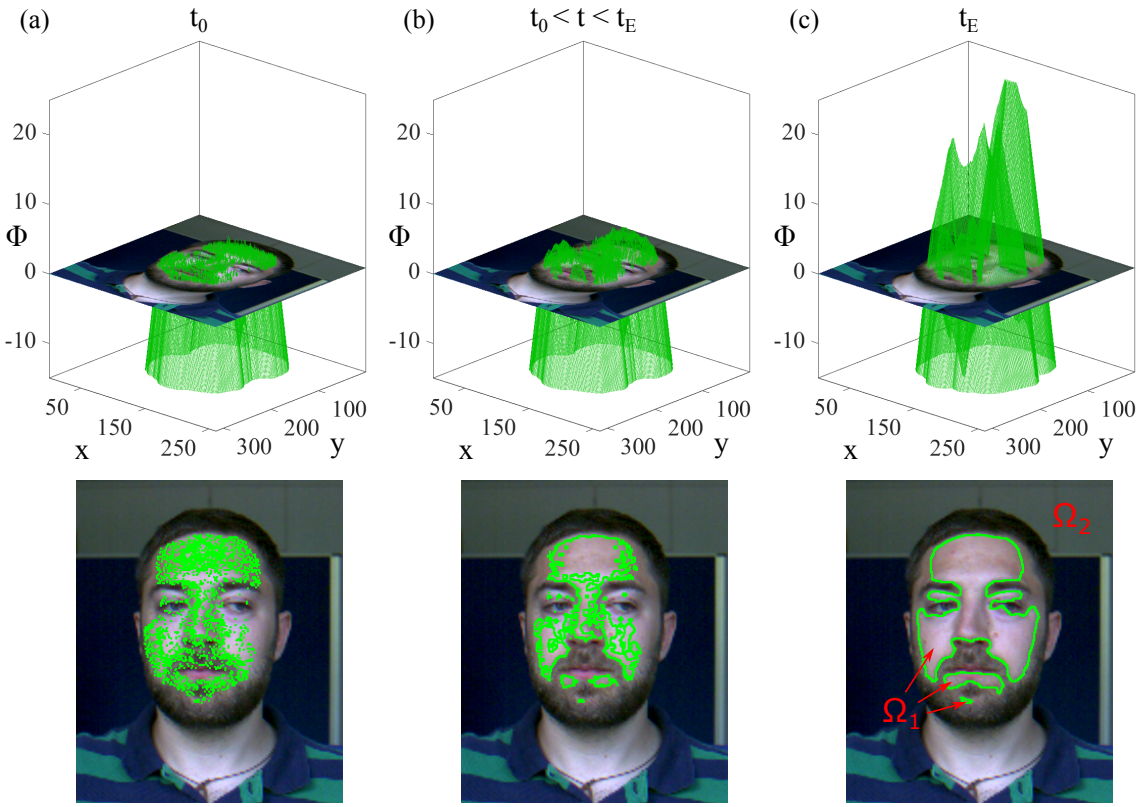

Figure 33: Example for a segmentation process using the presented level-set-based approach: (a) Initialization point defined by the skin classifier, (b) Point during segmentation, (c) Point when process has converged. The two regions which are separated, the inside region Ω_1 and the outside region Ω_2, are implicitly described and changed by the level set function Φ. The corresponding contour ($\Phi = 0$) is depicted in the images below the graphs. Note: t represents the segmentation time for an image and does not refer to the time component in the videos.

where μ_{ij} and σ_{ij} are the mean and standard deviation of the values in $F_j(\mathbf{x})$ given that $\mathbf{x} \in \Omega_i$, with $j = [1, 4]$ for the RGB case and $j = [1, 2]$ for the NIR case.

The initialization of the segmentation process defines if or how well the desired skin areas can be selected. As stated before, the presented skin classifier was employed in combination with the level-set-based approach. The detected skin region Ω_{SKN}^{RGB} was used to initialize the surface Φ through the assignment $\Omega_1(t_0) := \Omega_{SKN}^{RGB}$. By doing so, it was ensured that during the contour's propagation, Ω_1 evolved into a skin region with the maximum homogeneity. The final ROI consequently emerges to $\Omega_{ROI}^{RGB} := \Omega_1(t_E)$. For this procedure, it was found that an underrepresentation of the skin by the classifier led to a better outcome as missing skin areas could easily be compensated by the segmentation whereas falsely detected skin pixels rather led to a misperformance. Therefore, the classifier's threshold was set to $\theta = 5$. Figure 33 depicts the segmentation process for an example. However, this particular initialization approach only works if RGB images are present since the skin classifier was trained for the respective color space. In order to also enable the handling of NIR images, a different solution had to be established as explained in the following section.

5.2.3 *Image Registration*

For the video data, which was obtained with the cbPPG measurement stand (see Section 3.1), a frame-wise assignment between the RGB and NIR stream was possible due to simultaneous control of the cameras. In fact, the same frame number k was used for both streams as temporal descriptor. As a result, to a certain instant k, a selected ROI in an RGB image can be directly transferred to the corresponding NIR image.

In a first attempt, a common registration scheme was tested to map Ω_{ROI}^{RGB} onto the plane of I_N. Such a scheme normally comprises [102]: (i) Feature detection and selection in both images ($I_{R,G,B}$ and I_N), (ii) feature matching (search for correspondences), (iii) calculation of transformation between the two images. However, because of the different modalities in the RGB and NIR recordings, i.e. illumination and wavelength range, the matching was usually unsuccessful regardless of which kind of features were used[8]. Moreover, a conventional global transformation (projection) would not correctly map the ROI for the considered setup. Due to those insufficiencies, it has been decided to apply an intensity-based block-matching method to transfer Ω_{ROI}^{RGB} [185]. The method firstly divides the green channel I_G of the RGB image[9] into overlapping blocks of 5×5 pixels at the ROI. The overlap was maximized meaning that the shift between the blocks was only one pixel wide. Secondly, for each block Ω_b, the best matching block in I_N was determined within a search area (d_x, d_y) around the location of Ω_b. The mean squared error e_{mse} was chosen as the matching score [185]. In order to suppress the dependency on the absolute image intensity, the blocks were always mean adjusted before the comparison. The matching score eventually read:

$$e_{mse} = \int_{\mathbf{x}\in\Omega_b} \Big[\Big(I_G - \mu_G\Big) - \Big(I_N(x+d_x, y+d_y) - \mu_N\Big)\Big]^2 \, d\mathbf{x} \;, \tag{13}$$

where μ_G and μ_N are the blocks' mean values. Prior knowledge about the cameras' field of view at the measurement stand (see Fig. 18) allowed the estimation of possible displacements and the search area to be limited to $d_x = [-60, 0]$ and $d_y = [0, 10]$ pixels. The restriction not only sped up the registration process but also increased the performance.

The derived ROI for I_N (denoted by Ω_{REG}^N), however, did not map Ω_{ROI}^{RGB} well enough. Even if it had been perfectly mapped, Ω_{REG}^N would usually not be as homogeneous as Ω_{ROI}^{RGB} with respect to the image intensity. This effect is the result of the applied NIR spotlight which caused the illumination situation in the NIR recording to be considerably different from the one in the RGB recording (see Fig. 21). To overcome these drawbacks, the level-set-based segmentation was employed for I_N where the registered ROI was used to initialize the process such as $\Omega_1(t_0) := \Omega_{REG}^N$. The final ROI for the NIR image therefore was defined by $\Omega_{ROI}^N := \Omega_1(t_E)$. Figure 35 (a) summarizes the whole procedure.

8 All types of features, which were available in MATLAB R2016a (e.g. SURF, FAST, Harris corners, BRISK) [204], were tested for the registration task.

9 The green channel was chosen because it was less noisy than the red and the blue channel.

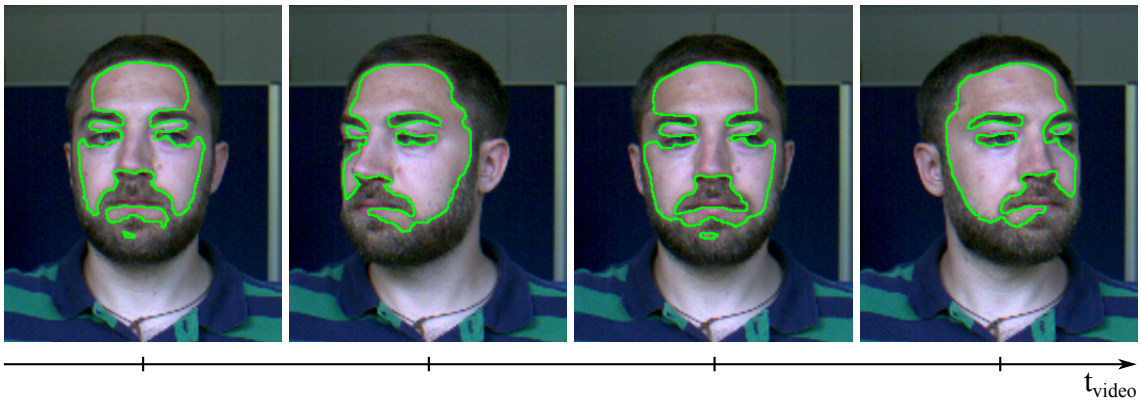

Figure 34: Example for a level-set-based tracking of facial skin regions. Four non-consecutive images from a processed video are depicted with their ROIs (only contour is visualized). The initial ROI was detected using the described skin classifier and the level set segmentation approach (see Sections 5.2.1 and 5.2.2).

5.2.4 *Processing Framework*

In Figure 35 (b), the processing structure of the presented ROI selection method is depicted. An essential part is the *ROI detector* (see Fig. 35 (a)) for which the principle components were explained in the last three sections. The *ROI detector* provides an ROI for the RGB and the corresponding NIR image at a certain instant k in the recording. In theory, it could be executed repeatedly for the images in the two video streams. However, this approach would be computationally expensive. Therefore, a once detected ROI, e.g. at the beginning ($k = 1$), was tracked instead of being redetected. The tracking was also realized by means of the level-set-based algorithm and performed separately for the RGB and NIR video. The procedure entailed a frame-wise segmentation where each process for an image frame I was initialized by the ROI of the preceding frame: $\Omega_1(t_0, k) := \Omega_{ROI}(k-1)$; $\Omega_{ROI}(k) := \Omega_1(t_E, k)$ is then the updated ROI[10]. The processes reached their optimums quickly since possible changes between two consecutive video frames and its ROIs are generally minor. As a consequence, the computational cost was much lower than it would be for redetection. The key idea behind the tracking approach was to maintain the homogeneity in intensity and texture inside the skin regions regardless of which anatomical areas are included or excluded. This idea differs from the conventional tracking concept where specific local points are traced [393]. The advantage of the proposed approach over the conventional one is that abrupt changes in the light intensity can be avoided within the ROI. Figure 34 shows an example for the homogeneity-based tracking.

Despite the convenience of also using the level-set-based algorithm for tracking, problems may emerge when artifacts are present. Two major issues have to be addressed in that context. First, the ROI might disappear if the considered skin region is temporarily occluded or completely left the recording area. Second, non-suitable regions could be

10 The symbol I generally denotes an image which could be a three-channel RGB image or an NIR image. Similarly, Ω_{ROI} denotes an ROI, either for an RGB or for an NIR image.

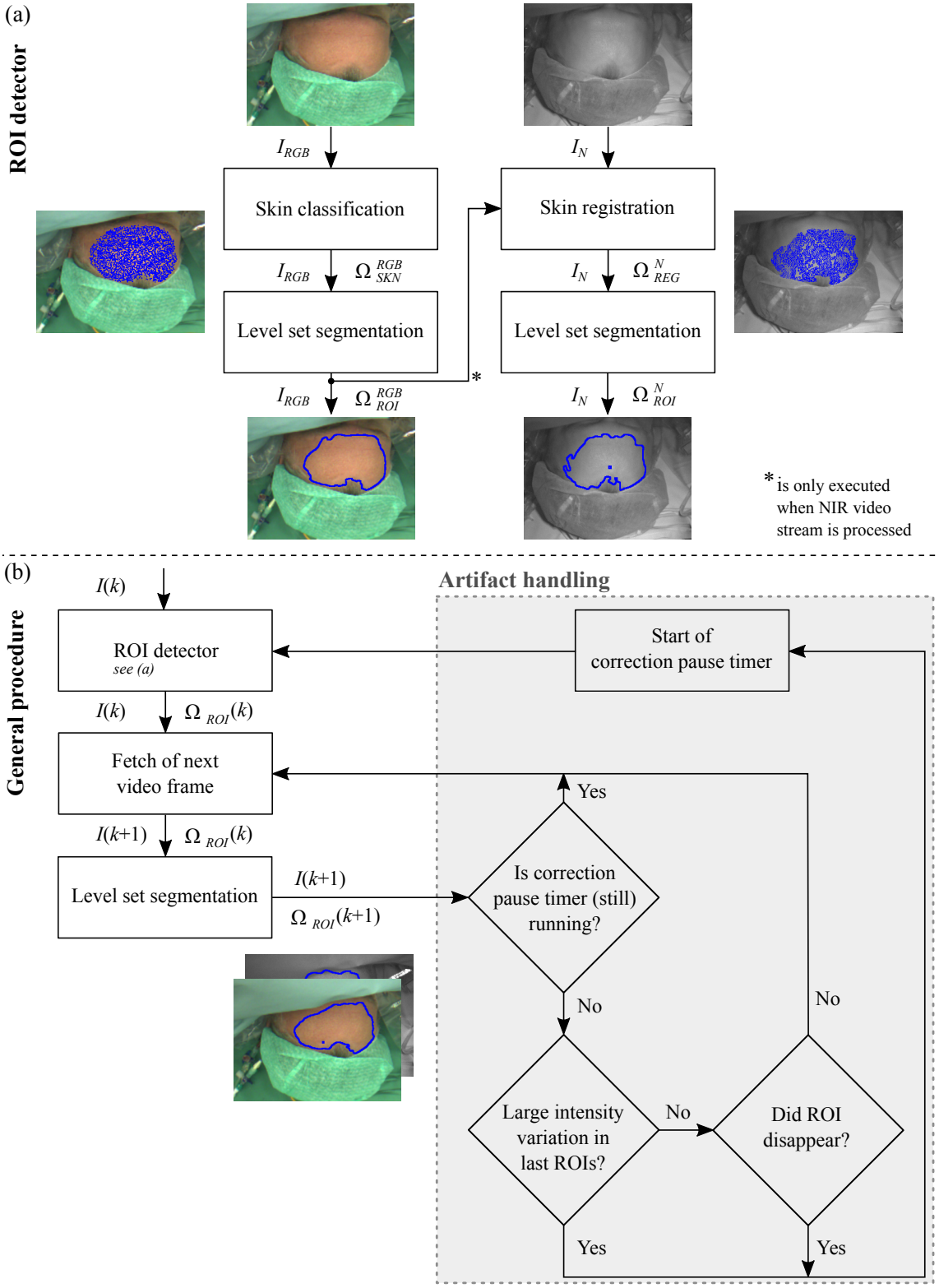

Figure 35: Program structure of the presented ROI selection algorithm: (a) *ROI detector* which (initially) detects the ROI in an RGB image and adapts it to a corresponding NIR image. (b) Flowchart of the whole program (detection and tracking) which runs separately for the RGB and NIR video. For some transitions between the program blocks, the data types are given (I: image, Ω: image region, k: frame number). (from [340] - modified in text and depiction) –

assigned to the ROI if an exposed body part, such as an arm or hand, abruptly enters the area of interest (e.g. in clinical environments). The first problem was easy to identify and was handled by executing the *ROI detector* repeatedly until skin regions were found again. To deal with the second problem, it was continuously tested whether the standard deviation of the mean ROI intensity in the last 10 s exceeded 50 units[11]. If true, the *ROI detector* was executed. This particular procedure bases on the assumption that a sudden ROI reassignment also involves a significant change in the ROI's average intensity. However, by re-executing the detector, similar unwanted changes might be created. To avoid a dead-end process, after each redetection, the artifact monitoring was paused for 15 s. Figure 35 (b) illustrates the principles in a flowchart.

5.2.5 *Implementation*

The implementation of the presented method was carried out in MATLAB R2016a (The MathWorks, Inc. in Natick MA, USA). For standard processing steps, available functions from the software's toolboxes were applied. In this way, the skin classifier as well as the image registration technique could be programmed straightforwardly. The level-set-based segmentation approach, however, entailed more problems. The suggestions by Osher and Fedkiw [248] turned out to be valuable for implementing the algorithm. In the following, important aspects will be explained. The reader, nevertheless, is referred to the book of the two authors for detailed descriptions.

The evolution equation in (10) was solved numerically (forward Euler method) by an iterative procedure. For the segmentation task in the *ROI detector*, 300 (RGB image) and 100 (NIR image) iteration steps[12] were used to obtain Ω_{ROI}^{RGB} and Ω_{ROI}^{N}, respectively. These counts were determined empirically by selecting a broad variety of images and examining how many steps are at least necessary to achieve a stabilized segmentation contour. The largest occurring step counts were rounded up and chosen for the considered data sets. The same strategy was pursued to derive the number of iteration steps for the segmentation task in the course of tracking. Here, a maximum of 50 steps proved to be sufficient. However, since less steps were usually required to reach an optimum, a query was implemented which terminated the process early when the size of Ω_1 between two steps changed insignificantly (< 50 pixels).

The level set function Φ was initialized through $\Omega_1(t_0)$ as a signed distance function using the Euclidean distance [59, 207]. The function represents a surface that is convex upwards where the zero level describes the image contour (see Fig. 33 (a)). After each iteration step, it was newly defined by means of a reinitialization equation as proposed

11 The mean ROI intensity over time is the equivalent of a cbPPG signal. The threshold of 50 units was determined empirically for the color depth of 12 Bit and is distinctly higher than possible physiological variations in that signal (see Section 2.5.1). Therefore, it indicates the occurrence of artifacts.

12 Note: For an NIR image, less iteration steps were needed because the segmentation process was started with the registered ROI which already covered more suitable areas than the skin classifier's result in case of the RGB image.

in [248]. A further important implementation aspect concerned the Heaviside function's derivative H'. Based on the recommendations of Chan and Vese [58], H' was approximated with a smooth Dirac delta function δ_ϵ. The function reads [350]:

$$\delta_\epsilon(\Phi) = \frac{\epsilon}{\pi(\epsilon^2 + \Phi^2)} \ , \tag{14}$$

with ϵ being a tunable parameter which was set to 1.5 [248]. As explained in Section 5.2.2, the smoothness of the segmentation contour can be controlled by the factor ν. For the approach in this work, the suggestion by Brox [48] was taken into account leading to the configuration of $\nu = 0.001 \cdot |\Omega|^{0.7}$ with $|\Omega|$ denoting the image size (in number of pixels).

Although the presented ROI selection algorithm generally turned out to run as expected, some additional methods were found to strongly boost its performance. These methods are briefly delineated in the following listing:

- *Image adjustment* Before applying the skin classifier, the RGB images were processed by the MATLAB's function `imadjust()` [206]. By doing so, the intensity values of each color channel could be remapped so that the whole intensity range (0 - 4095) was used.
- *Outlier removal of skin pixels* False detections of the skin classifier were often single pixels which lay outside of the main detection area. To identify them, it was checked whether skin pixels were located in neighborhoods (50×50 pixels) where more than 90 % of pixels were labeled as non-skin. If so, the pixels were also assigned to the non-skin class.
- *Removal of small regions* The segmentation steps in the *ROI detector* occasionally provided ROIs with small subregions that appeared to have no contribution to the quality of the eventually extracted cbPPG signals. Therefore, unconnected regions which size fell below $0.01 \cdot |\Omega|$ (1 % of image size) were deleted from the ROIs.
- *Outlier removal in image registration* Since the used registration technique attempts to match each ROI pixel separately, failures occur, especially in low-contrast areas. Those failures could be compensated by locally correcting the determined displacement direction between the ROI pixels in $I_G(\mathbf{x})$ and $I_N(\mathbf{x})$. For this purpose, a median filter with an order of 21×21 pixels was applied.
- *Frame skip* Instead of processing each video frame, only every tenth was considered. The ROIs for the intermediate frames were extrapolated from the ROI which was determined last.

Note: All mentioned filter sizes and thresholds were chosen empirically.

5.3 EVALUATION

5.3.1 *Data – Intraoperative, Postoperative, and CPT Study*

For the evaluation of the novel ROI selection method, three data sets were used. On the one hand, the clinical recordings from the intraoperative and postoperative study were

considered (see Section 3.2.1 and 3.2.2). On the other hand, the lab recordings from the CPT study were taken into account (see Section 3.3.1). The recordings were all acquired by the same camera setup, captured the face of the participants, and lasted about 30 min on average. A cbPPG measurement always comprised two recordings, an RGB and a synchronized NIR video stream. It should be noted that in the CPT study, measurements were repeated for each subject. However, for the assessment of the proposed method, all measurements were assumed to be independent since the repetitions were conducted on different days and for different body positions.

The three study environments challenged the ROI selection process in various ways. The following listings state the respective issues.

Intraoperative study (41 measurements):

- face was often partly occluded by surgical drape
- patient was moved by clinical staff
- measuring stand was relocated
- staff reached into recording area
- operation table was readjusted in height
- illumination situation varied due to moving staff
- patient moved due to surgical procedure

Postoperative study (70 measurements):

- face was partly occluded by nasogastric tubes, orotracheal tubes and fixation tape
- head was occasionally turned sideways
- cameras were not always orthogonally aligned towards face
- staff reached into recording area
- illumination situation varied due to interference by natural lighting
- patient moved severely when waking up

CPT study (43 measurements):

- head occasionally left the recording area
- head was occasionally turned sideways
- participant continuously moved slightly due to its general alertness for test
- participant moved strongly during CPT and saliva sampling

Evaluating the points, it is apparent that a classical face detector would not have worked for the clinical data sets because essential facial features were only visible to a limited extent. Furthermore, an ROI selection approach which relies on the presence of local plethysmographic oscillations would have failed since existent vascular diseases in the patient groups compromise the manifestation of these oscillations (see Section 5.1). Those problems justify the use of the developed method. However, they not necessarily hold for the CPT data set. In fact, the recordings of CPT study were primarily assessed for reference purposes.

5.3.2 *Reference Method*

In order to better demonstrate the strength of the novel ROI selection method, it was compared to a conventional selection method which was applied to the data sets as well. A considerable number of works in cbPPG employ a detector by Viola and Jones in combination with the Kanade-Lucas-Tomasi tracker to find and trace suitable face ROIs[13]. Since this approach has proven to lead to a reliable outcome, it was pursued to construct the "reference method". In the following, the main steps are briefly outlined. First, the face was detected by means of the Viola-Jones algorithm which returned a bounding box for the identified location [184, 354]. Because the detector usually performed poorly in the clinical recordings, the initial box was defined manually there. Second, distinctive corner points were selected as viable features within the bounding box [303]. Third, over the course of the video, those points were tracked using the Kanade-Lucas-Tomasi algorithm [193, 335]. In the fourth and last step, the features could then be utilized to re-align the box in consecutive frames (affine transformation). The box eventually represented the ROI of the reference method. Figure 36 illustrates the described procedure for an example. It should be pointed out that the corresponding RGB and NIR videos were processed separately. Due to the relatively strong movements of the subjects who participated in the CPT study, the tracking occasionally did not function as wanted there. To prevent failures for this data set, the Viola-Jones detector was re-executed and the tracker re-initialized if the area of the traced bounding box deviated more than 20 % from the one of a newly detected box.

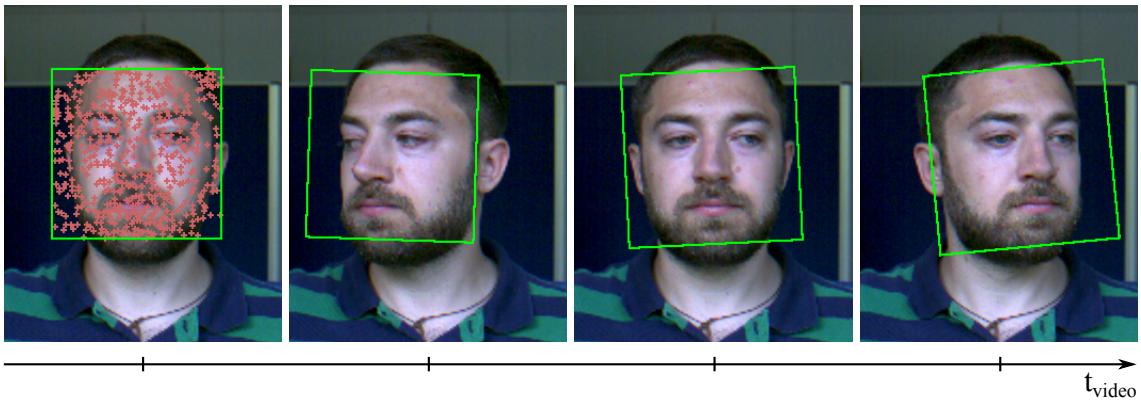

Figure 36: Example for a conventional face detection and tracking approach that is often used for ROI selection in cbPPG. The ROI (bounding box) was identified with the Viola-Jones algorithm [184, 354] and then traced by means of the Kanade-Lucas-Tomasi tracker [193, 335]. The red crosses visualize viable features [303] which were utilized for tracking. Note: For the clinical data sets in this thesis, the initial box (left) had to be defined manually.

13 References: [83, 85, 90, 93, 110, 112, 131, 216, 254, 279, 329, 375]

5.3.3 *Quality Parameter*

In order to quantify the effectiveness of the novel method, three different quality parameters were used. The first parameter was the ROI homogeneity (RIH) which assesses how strong the pixel values fluctuate within an ROI. The idea behind this choice was that a more homogeneous region is better for the acquisition of plethysmograms as it is less prone to BCG interference (see Section 2.5.1). The RIH was calculated for each frame and video channel (blue, green, red, NIR) as follows:

$$q_{RIH} = 1 - \frac{\sigma_{ROI}}{2048} \ , \tag{15}$$

where σ_{ROI} denotes the standard deviation of the ROI pixel's intensity values. In the formula, σ_{ROI} is normalized to the maximum possible deviation[14] leaving a quality measure that ranges between 0 and 1. The second and third parameters were chosen to be indices which assess how well the found ROIs are suited for the extraction of cbPPG signals. The indices were employed under the assumption that a better ROI selection also leads to better quality signals. For calculation, at first, the videos were divided into consecutive segments of 10 s. Next, for each segment and color channel, a plethysmogram was acquired by averaging the values of the pixels inside the corresponding ROI. The obtained signals were removed from its linear trend and further filtered using an FIR highpass (order: 250, cutoff frequency: 0.5 Hz). They were then zero-padded to 2^{13} points and transferred into the frequency domain by means of a Fast Fourier transform. The amplitude spectrum $|X(f)|$ of the transformed signals was utilized to determine the camera-based HR f_{cam} by detecting the maximum peak between 30 and 200 bpm (see Fig. 37). The search limits stem from the regulations defined in the American standard for HR meters in [55]. To eventually construct one of the quality measure, i.e. the HR detection rate (HDR), the reference HR f_{ref} had to be determined as well. For the data sets of the CPT and postoperative study, segment-wise f_{ref} values were derived from the electrocardiogram[15]. For the data set of the intraoperative study, those values were derived from the finger plethysmogram, in the same way as it was done for the cbPPG signals. The plethysmogram was favored in this data set because, in general, it was barely degraded by artifacts. Having the reference HR, the HDR parameter could be calculated [269]:

$$q_{HDR} = 100\,\% \cdot \frac{n_{cor}}{n_{tot}} \ , \tag{16}$$

with n_{tot} being the total number of segments within a measurement and n_{cor} the number of segments in which f_{cam} deviated less than 5 bpm from f_{ref}. The limit for correct detection (± 5 bpm), again, was inferred from the regulations in [55]. The third quality measure, the

14 Since the considered videos have a color depth of 12 Bit, the pixel values range between 0 and 4095. The maximum possible standard deviation for this range is 2048.

15 The electrocardiogram was divided into 10 s segments, and the R-peaks were selected using the QRS detector from the BioSig toolbox [290]. For each segment, one HR value was obtained by calculating the reciprocal of the median peak-to-peak interval.

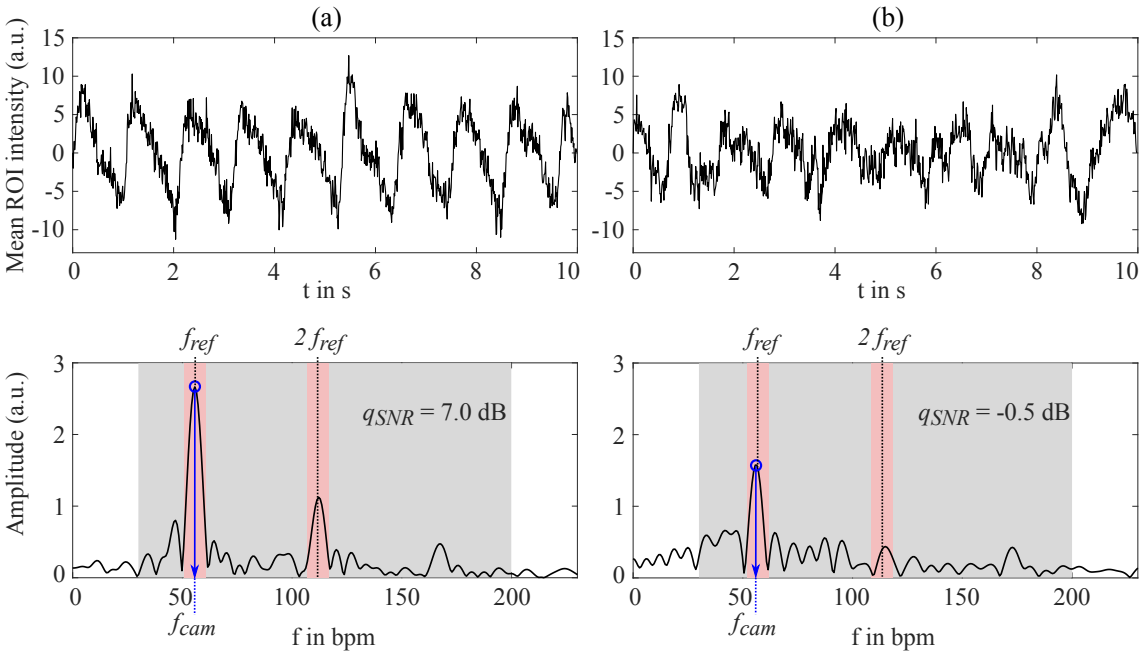

Figure 37: Illustration of how cbPPG signals can be assessed. First row: Detrended, filtered, and inverted cbPPG signals of different qualities. Second row: Derived amplitude spectrums of the signals. The camera-based HR f_{cam} was determined by detecting the maximum peak (blue circle) between 30 and 200 bpm. The SNR parameter q_{SNR} was calculated by normalizing the squared amplitudes around the reference HR and its first harmonic (red area) to the residual squared amplitudes between 30 and 200 bpm (gray area).

SNR, was determined directly in the amplitude spectrum. Based on the work of de Haan and Jeanne [400], the respective parameter was computed in the following manner:

$$q_{SNR} = 10 \cdot \log_{10} \left(\frac{\int_{f=30\ \text{bpm}}^{200\ \text{bpm}} \Pi(f)\, |X(f)|^2\ df}{\int_{f=30\ \text{bpm}}^{200\ \text{bpm}} (1 - \Pi(f))\, |X(f)|^2\ df} \right) , \tag{17}$$

where Π is defined as:

$$\Pi(f) = \begin{cases} 1 & \text{if } |f_{ref} - f| \leq 5 \text{ bpm} \\ 1 & \text{if } |2f_{ref} - f| \leq 5 \text{ bpm} \\ 0 & \text{otherwise} \end{cases} . \tag{18}$$

Taking the prevalent noise into account, the SNR assesses how well the cardiac pulsation is manifested in the cbPPG signals. In order to achieve a better understanding, Fig. 37 illustrates the SNR calculation for two signal examples.

Comparing the three quality parameters, it is apparent that they are calculated at different time levels. While q_{HDR} takes a whole measurement into account, q_{SNR} is determined for each segment and q_{RIH} even for each channel image. To standardize the evaluation, the two latter parameters were adjusted: The SNR values were averaged across the segments,

and the RIH values across the frames and segments[16]. As a result, each video channel of a measurement was equally describable by three quality values.

Note: All parameters had to be computed twice, once for the case when the the ROI selection method was applied to the data sets and once for the case when the reference method was employed.

5.3.4 *Statistics*

The statistical assessment was carried out separately for the three data sets. For each color channel and quality parameter, two groups existed, one with the results of the novel method and one with the results of the reference method. The groups contained as many data points as measurements were available , i.e. (i) 41 for the data set of the intraoperative study, (ii) 70 for the data set of the postoperative study, and (iii) 43 for the data set of the CPT study. To analyze whether significant differences emerge when the novel method is applied with respect to the reference method, the corresponding group pairs were tested using a Wilcoxon signed-rank test (two-sided). This particular test was chosen based on the recommendations in [33]. The following reasons led to the decision: (i) A general dependency exists between the analysis-related groups, (ii) the values of the quality indices show overall no normal distribution.

5.4 RESULTS

5.4.1 *ROI Selection*

For all videos of the test data sets, the proposed algorithm automatically detected and tracked appropriate ROIs. In some rare cases, however, the method was not able to select any region. Table 13 lists the average number of segments for which single ROIs could not be determined. As can be seen, only for the measurements of the intraoperative and postoperative studies, the issue occurred at all. More importantly, the actual counts are rather low with the NIR videos being affected slightly stronger by the misperformance than the RGB videos.

Table 13: Mean number of video segments ($\pm$ standard deviation) in which single ROIs could not be determined. Depiction: *New method* (*Reference method*).

	Intraoperative study	Postoperative study	CPT study
RGB videos	0.7 ± 1.6 (0.2 ± 0.6)	1.7 ± 10.7 (0 ± 0)	0 ± 0 (0.1 ± 0.3)
NIR videos	1.4 ± 5.0 (0.2 ± 0.6)	1.7 ± 12.0 (0 ± 0)	0 ± 0 (0.1 ± 0.3)

16 The average number of measurement segments per color channel was: (i) 192.2 ± 43.5 for the data set of the intraoperative study, (ii) 181.0 ± 13.8 for the data set of the postoperative study, and (iii) 163.0 ± 12.4 for the data set of the CPT study.

Figure 38: Examples of selected ROIs in the videos of the intraoperative study. The ROIs were determined using the proposed level-set-based method. Each row represents a separate measurement. The first two columns show the results for the RGB and NIR image at the beginning of the recording, the last two columns at a later point in time. Note: Only the ROIs' contour is illustrated (blue). Facial features were blurred to preserve anonymity.

The Figures 38, 39, 40 show the selected ROIs of several study participants at different states in the videos. The examples reflect the strength of the level-set-based approach which proves to be robust against illumination changes, limitations in the face's visibility, and against variations in scale and rotation. The new method demonstrates its ability to precisely identify skin pixels that describe homogeneously illuminated areas. Non-suitable regions depicting hair, tubes, tape, clothes etc. were rejected successfully in the majority of the images (see Fig. 39 (a) and (b), Fig. 40 (b)). Furthermore, skin regions which deviated considerably from the brightness of the favoured area and which were not orthogonally aligned towards the camera could be reliably omitted as well (see Fig. 38 (a) and (b), Fig. 39 (b) and (c)). Analyzing the examples, it is also apparent that, in order to fulfill the requirement of homogeneity, a determined ROI may have holes and can consist of several unconnected regions. The advantage of using a separate segmentation step for the NIR images (in the *ROI detector*) is evident when looking at the results in Fig. 38 (a) and Fig. 40 (b) and (c). A homogeneous area in the RGB video might appear much more heterogeneous in the corresponding NIR video because a different illumination situation was prevalent during the recording. The chosen procedure leads to a independent adjustment of the ROIs and allows the varying modalities to be considered in the selection process. Despite the general satisfying outcome, minor problems emerged. First, non-facial regions from the upper part of body were often assigned to the ROI if skin was visible there (see Fig. 39 (a) and (c), Fig. 40 (a) and (c)). Second, non-skin areas became sometimes a target

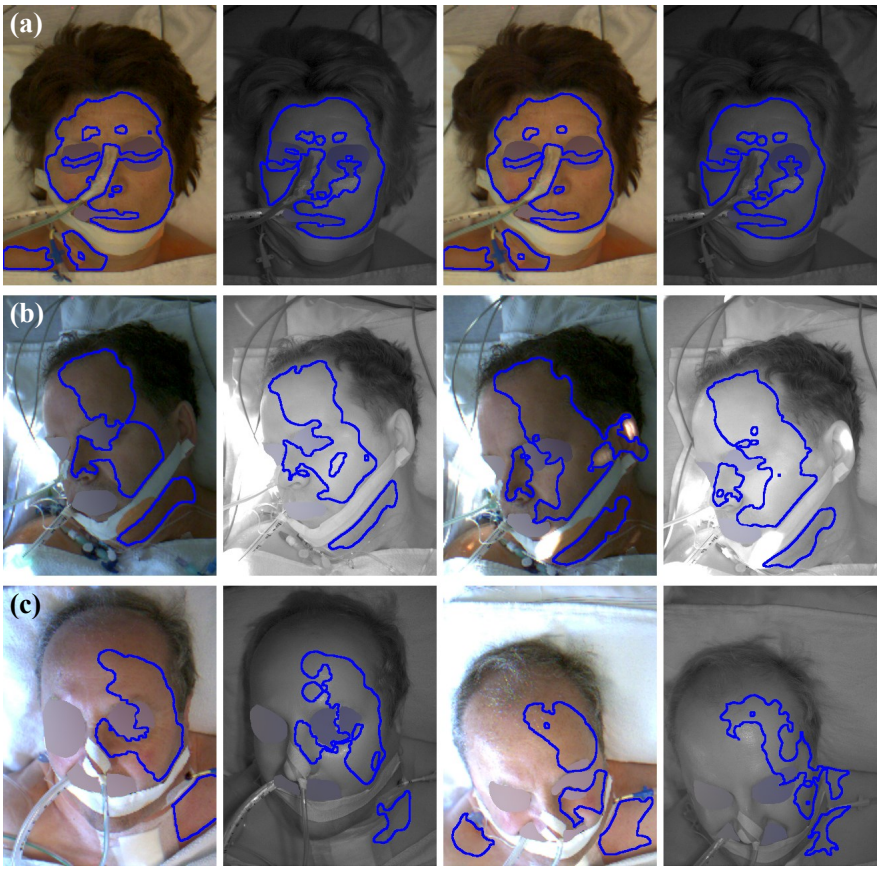

Figure 39: Examples of selected ROIs in the videos of the postoperative study. The ROIs were determined using the proposed level-set-based method. Each row represents a separate measurement. The first two columns show the results for the RGB and NIR image at the beginning of the recording, the last two columns at a later point in time. Note: Only the ROIs' contour is illustrated (blue). Facial features were blurred to preserve anonymity.

as well in case they were close to the ROI's location and held similar intensity values (see Fig. 38 (b), Fig. 40 (a)). In the Appendix A.3, on overview of the selected ROIs can be found for each data set.

As explained in Section 5.3.3, the quality parameter q_{RIH} was employed to quantify the homogeneity in the determined ROIs. The Figures 41, 42, and 43 show the results for the parameter individually for the cases (i) when the level-set-based method was used and (ii) when the reference method was applied. Throughout the data sets and in every video channel, the new method yielded significantly higher RIH values than the reference method did. Especially in the blue and green channels, high homogeneities were achieved. A comparison between the results of the three data sets reveals that the new ROI selection procedure provides the most homogeneous regions for the videos of the postoperative study. In contrast, for the videos of the CPT study, the least homogeneous ROIs were obtained. This data-depended characteristic could also be observed in the outcome of the reference method. In order to assess the reproducibility of the methods' performance with respect to the RIH, the variation of q_{RIH} across the measurements (interquartile range of boxplots) was analyzed. The lowest variation occurred when using the new method

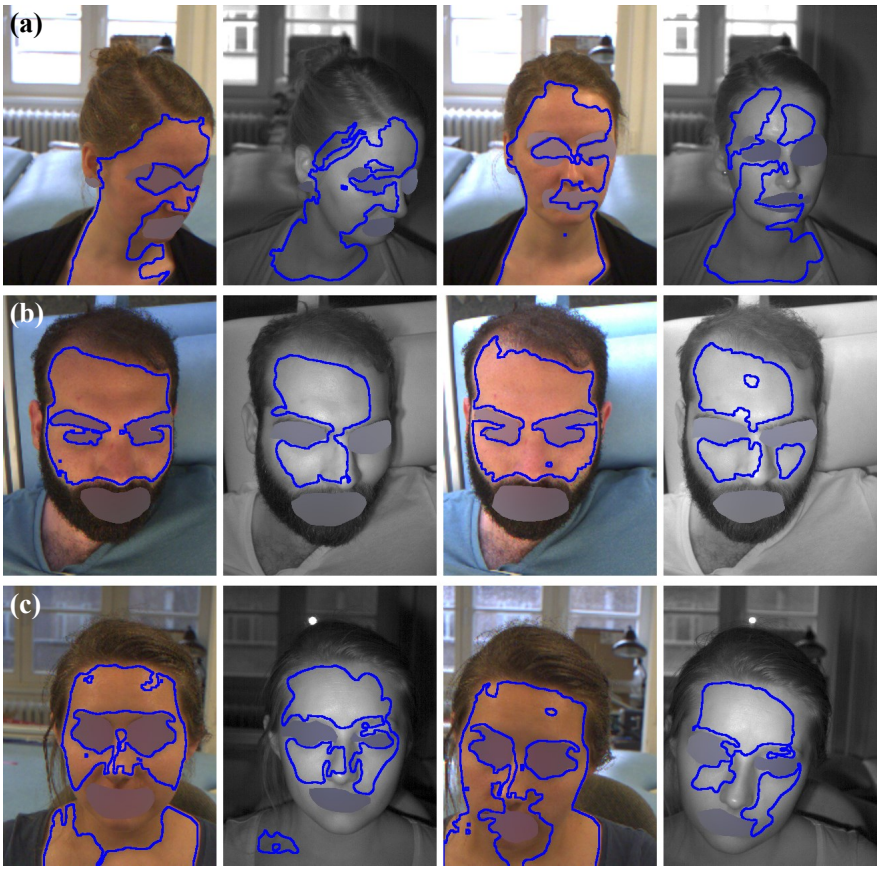

Figure 40: Examples of selected ROIs in the videos of the CPT study. The ROIs were determined using the proposed level-set-based method. Each row represents a separate measurement. The first two columns show the results for the RGB and NIR image at the beginning of the recording, the last two columns at a later point in time. Note: Only the ROIs' contour is illustrated (blue). Facial features were blurred to preserve anonymity.

while the strongest variation was associated with the application of the reference method. Another peculiarity in the results concerns the RIH median values of the method-related groups. Interestingly, the smallest differences of between 0.04 and 0.1 were found in the NIR channel. In the other channels, differences around 0.15 were more usual.

Although this chapter focuses on the methodical advantages of the level-set-based approach, the eventual usability was also evaluated. To do so, the real-time capability was rated on a Windows® computer in MATLAB R2016a (i5-4590 @ 3.3 GHz - single core). The rating showed that only the tracking can be performed in real-time ($< 10\,\text{ms}$). However, an implementation of the algorithm in C++ would most likely be sufficient to run detection task in real-time as well.

5.4.2 *Photoplethysmographic Monitoring*

The Figures 44, 45, and 46 depict the results for the parameters q_{HDR} and q_{SNR} which assess the quality of the extracted cbPPG signals. Again, it is discriminated between the

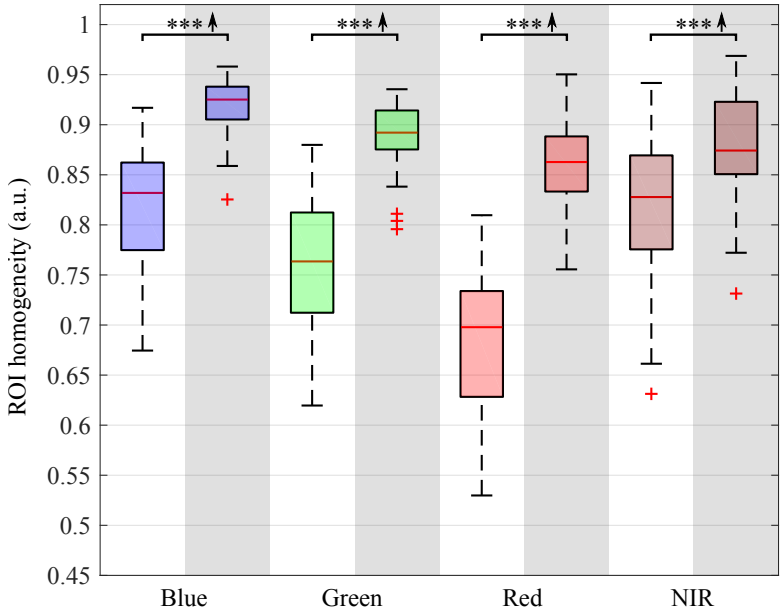

Figure 41: Results of the ROI homogeneity assessment for the videos of the intraoperative study. The outcome is shown separately for each color channel. The highlighted boxplots (gray) depict the homogeneity values that arise when the level-set-based method is used, whereas the other plots are associated with the reference method. Above the boxes, the results of the statistical tests are also given (*** $p < 0.001$). The arrows denote whether the new method performed significantly better or not.

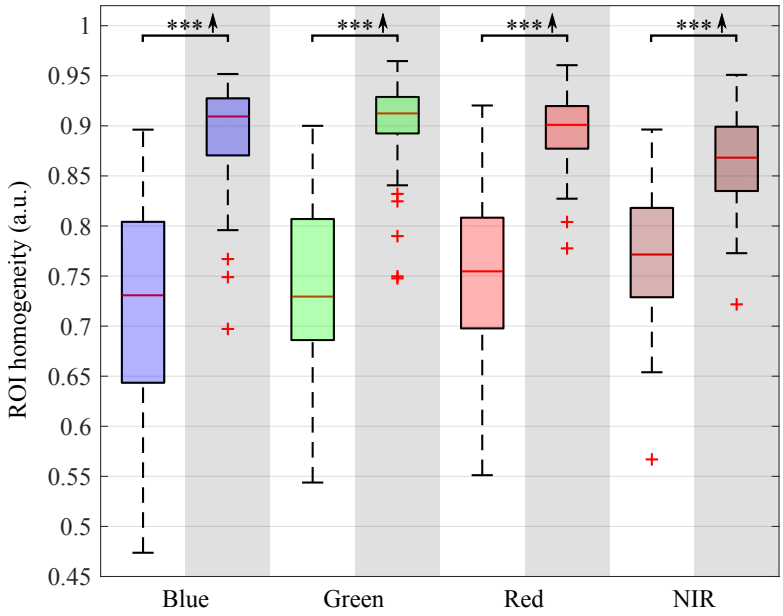

Figure 42: Results of the ROI homogeneity assessment for the videos of the postoperative study. The outcome is shown separately for each color channel. The highlighted boxplots (gray) depict the homogeneity values that arise when the level-set-based method is used, whereas the other plots are associated with the reference method. Above the boxes, the results of the statistical tests are also given (*** $p < 0.001$). The arrows denote whether the new method performed significantly better or not.

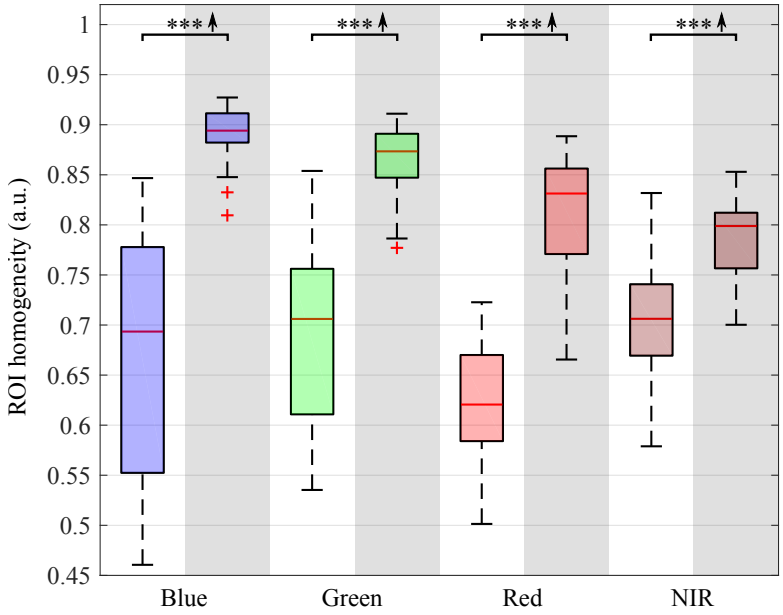

Figure 43: Results of the ROI homogeneity assessment for the videos of the CPT study. The outcome is shown separately for each color channel. The highlighted boxplots (gray) depict the homogeneity values that arise when the level-set-based method is used, whereas the other plots are associated with the reference method. Above the boxes, the results of the statistical tests are also given (*** $p < 0.001$). The arrows denote whether the new method performed significantly better or not.

cases when the new method and when the reference method was used for ROI selection. With the exception of one instance (postoperative study: HDR outcome in NIR channel), the new method provided significantly higher detection rates as well as SNR values than the reference method did. Throughout the data sets, those quality values proved to be maximal in the green channel. Furthermore, the NIR channel turned out to be a good candidate for acquiring physiological information. In contrast, the lowest signal qualities were consistently found in the blue channel. As can be seen in the figures, the parameters q_{HDR} and q_{SNR} manifested in the same way across the channels. This effect indicates the measures to have a similar explanatory power.

The three considered studies entailed various challenges for the developed method where occurring problems eventually also reflected in the quality of the plethysmograms. The highest HDR and SNR values were reached for the videos of the intraoperative study while the lowest ones were obtained for the videos of the postoperative study. However, an analysis of the method-related differences in the two quantities (reference vs. new) revealed another pattern. In the green channel, the largest median enhancement of the HDR was observed for the data of the postoperative study: 72.4 vs. 76.5 % (intraoperative study: 94.2 vs. 95.6 %, CPT study: 86.0 vs. 89.2 %). Interestingly, in the same channel, the biggest enhancement of the SNR was found for the data of the intraoperative study: 0.9 vs. 2.9 dB (postoperative study: -3.6 vs. -2.7 dB, CPT study: -0.8 vs. 0.5 dB). In the other color channels, especially in the red and NIR one, the the most mentionable improvements were achieved for the videos of the intraoperative and CPT study.

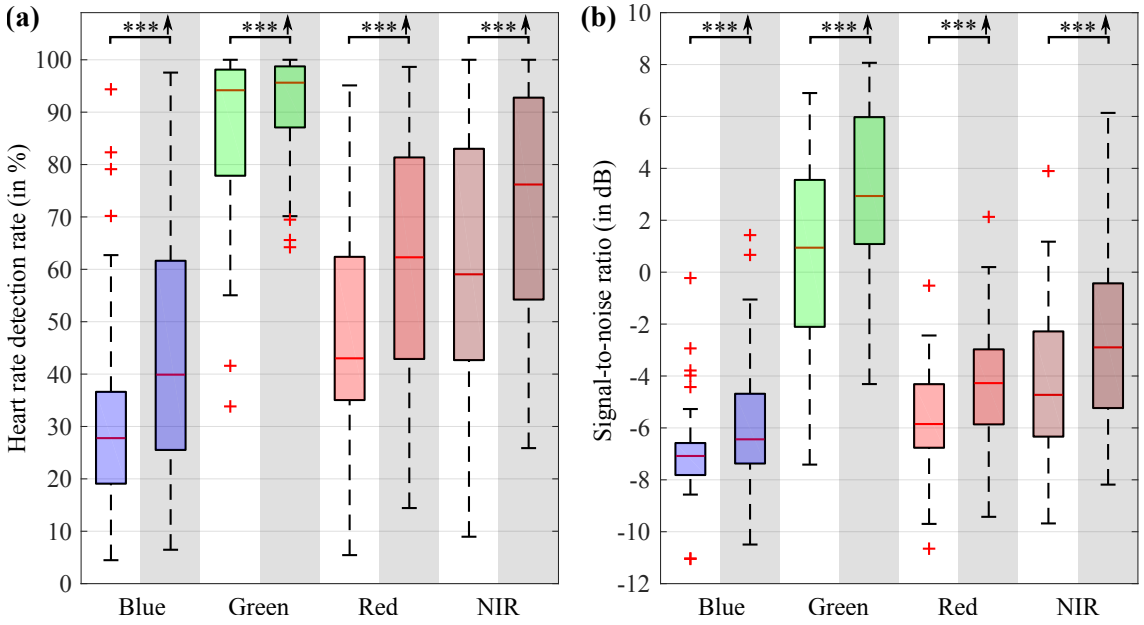

Figure 44: Results of the signal quality assessment for the videos of the intraoperative study: (a) HDR, (b) SNR. The outcome is shown separately for each color channel. The highlighted boxplots (gray) depict the quality values that arise when the level-set-based method is used, whereas the other plots are associated with the reference method. Above the boxes, the results of the statistical tests are also given (*** $p < 0.001$). The arrows denote whether the new method performed significantly better or worse.

As already described in the previous section, the variation of the quality values across the measurements (interquartile range of boxplots) is a good indicator for the reproducibility of the methods' performance. For q_{HDR} and q_{SNR}, the developed method did not cause a systematically lower variation. At least in the green channel of the videos from the intraoperative and CPT study, the parameters' fluctuation within the measurements decreased. For the data of the postoperative study, a consistent increase was observed in all color channels.

An important goal of this chapter is to show how suitable the proposed ROI selection approach is for clinical and laboratory environments. The work did not focus on specific postprocessing steps, such as source separation techniques, to achieve the best possible signal qualities. For example, an appropriate combination of the information in the different color channels could significantly enhance the quality of the plethysmograms [393]. To get an idea of the potential benefit nonetheless, it was tested which contribution the blue, red, and NIR channel can make to maximizing the HDR in the green channel. For the calculation of the respective HDR values, the assumption was made that in each segment, always the correct HR (if available) is selectable between the two considered channels. The results reveal the NIR channel to contribute the strongest by far: (i) intraoperative study: 95.6 % (green) vs. 97.3 % (green & NIR), (ii) postoperative study: 76.5 % (green) vs. 81.3 % (green & NIR), (iii) CPT study: 89.2 % (green) vs. 91.3 % (green & NIR).

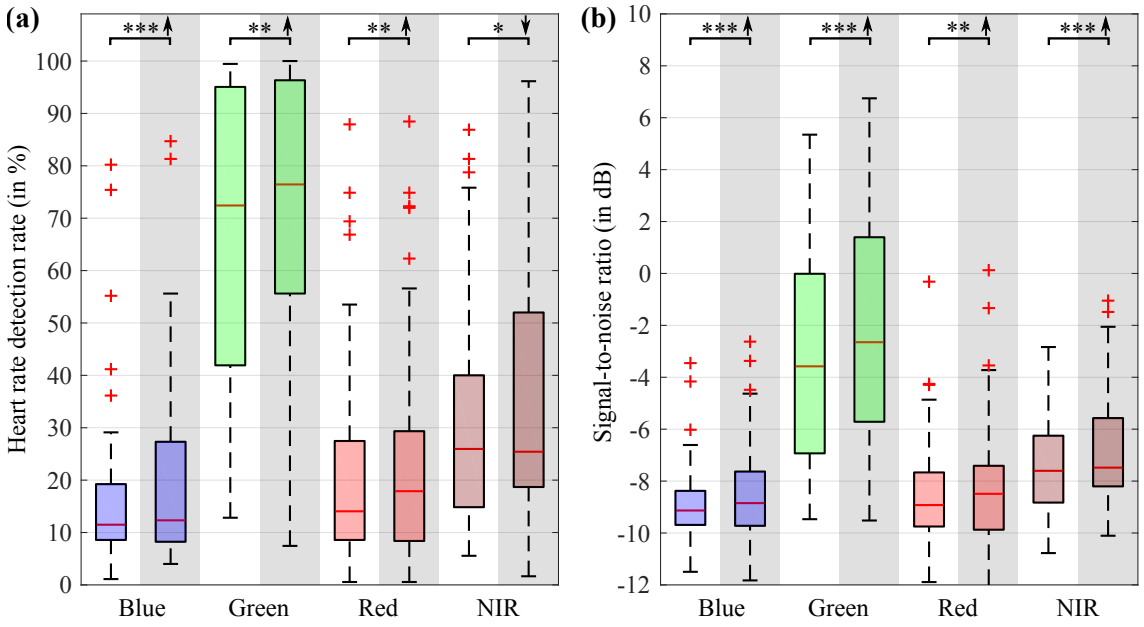

Figure 45: Results of the signal quality assessment for the videos of the postoperative study: (a) HDR, (b) SNR. The outcome is shown separately for each color channel. The highlighted boxplots (gray) depict the quality values that arise when the level-set-based method is used, whereas the other plots are associated with the reference method. Above the boxes, the results of the statistical tests are also given (* $p \leq 0.05$, ** $p < 0.01$, *** $p < 0.001$). The arrows denote whether the new method performed significantly better or worse.

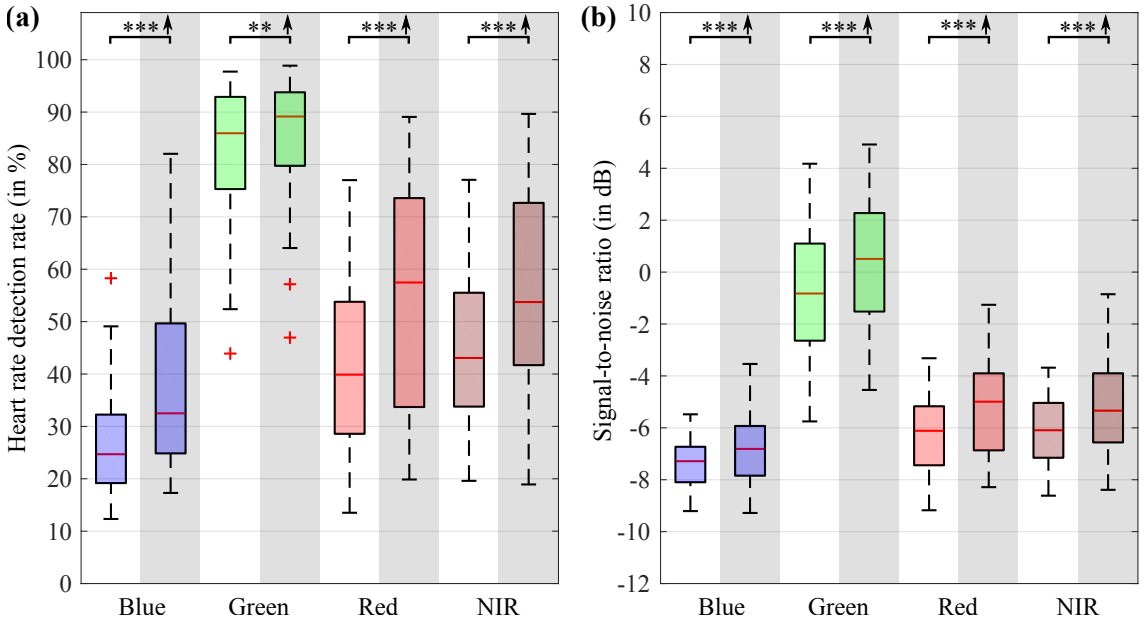

Figure 46: Results of the signal quality assessment for the videos of the CPT study: (a) HDR, (b) SNR. The outcome is shown separately for each color channel. The highlighted boxplots (gray) depict the quality values that arise when the level-set-based method is used, whereas the other plots are associated with the reference method. Above the boxes, the results of the statistical tests are also given (** $p < 0.01$, *** $p < 0.001$). The arrows denote whether the new method performed significantly better or worse.

5.5 DISCUSSION

5.5.1 *ROI Selection*

Skin classification is an easy way to locate potential ROIs without being reliant on the visibility a specific anatomical features. In this thesis, it was decided early on to employ a skin classifier as initial detection step (see Section 5.2.1). Works in cbPPG that follow the same approach most often apply a threshold-based classifier in the YCbCr color space [212, 260, 367, 368, 395]. To get an impression about the performance, the classifier was briefly tested as a replacement for the Bayesian method in the presented processing framework. The standard thresholds proved to entail a general overrepresentation of the skin areas. They were also hard to adjust to changing conditions on a large scale of data. The Bayesian classifier, in contrast, was found to provide a reliable outcome for various skin tones and in different environment and illumination situations. By adjusting θ, the detection sensitivity could be easily controlled, a feature which was very important to correctly initialize the level set segmentation (see Paragraph *Adaption and Contribution* in 5.2.2). Despite those advantages, the Bayesian classifier was barely used for the cbPPG application so far [267, 338].

As explained before, the level-set-based algorithm involves an iterative process where the evolving segmentation contour has to reach a stable state. If the contour does not stabilize at the desired ROI borders, it will move forward until a local optimum is found. In the best-case scenario, only further skin regions, which may not fulfill the requirement of homogeneity, will be included (see e.g. Fig. 63 row 7, column 5, Fig. 64 row 9, column 1, Fig. 65 row 6, column 2). In the worst-case scenario, non-skin regions will be assigned to the ROI (see e.g. Fig. 62 row 3, column 5, Fig. 64 row 7, column 5, Fig. 66 row 1, column 7). The results showed that the issue of destabilization rather occurred for the NIR images. For the RGB images, the information of three different color channels was entered into the feature vector F which significantly helped the segmentation process to run more consistently. The analyses also revealed that oversaturated areas can cause stabilization problems. Such areas are highly homogeneous and, therefore, are regarded as wanted regions by the algorithm although they do not carry useful information. Furthermore, heavy movements by the subjects, as apparent in the videos of the CPT study, contributed to segmentation errors. In the following, various approaches are discussed which could solve the described issues:

- *Face detection* The combination of a standard face detection method with the level-set-based method would allow to define limits for the evolution of the segmentation contour. Moreover, skin areas that lie outside of the face (see Fig. 40) could be omitted in this way. However, as facial features have to be clearly visible for the approach, the eventual application in a broad variety of environments is questionable.
- *Limitation for regional means* Under ideal conditions, the mean intensity value of an ROI should not change abruptly over time. The uncontrollable expansion of the seg-

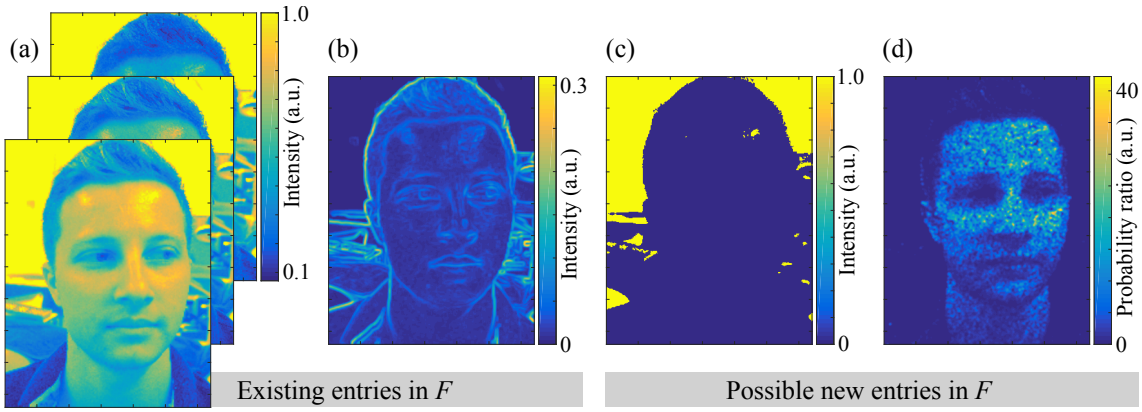

Figure 47: Depiction of the entries in the feature vector F for an RGB image: (a) Color channels I_R, I_G, I_B, (b) Texture map J_{RGB}, (c) Oversaturation map (the pixels that are oversaturated in the RGB image are denoted by the value 1), (d) Map of the skin probability ratio (for each pixel, the value $p(\mathbf{c}|skin)/p(\mathbf{c}|\neg skin)$ was calculated as done in the Bayesian classifier). While (a) and (b) depict the entries for the current implementation, (c) and (d) represent proposals for future works. The displayed subject authorized the usage of the footage.

mentation contour, for example, may lead to such changes. To resolve the problem, the variation range of the regional means μ_{1j} in Ω_1 could be restricted for the segmentation process.

- *Extension of feature vector* The elements (or maps) of the feature vector F determine which areas will be favored during the segmentation. Therefore, the issue of oversaturation could be tackled by adding a map to the vector where pixels with excessive values are explicitly marked-off (see Fig. 47 (c)). Furthermore, the issue of non-skin selection could be addressed by adding a skin map where for each pixel, the skin probability ratio $p(\mathbf{c}|skin)/p(\mathbf{c}|\neg skin)$ is calculated (see Fig. 47 (d)). However, the latter approach would only work for RGB images.

A further source of error in the processing framework is the image registration step. The accurate mapping of the ROI from the RGB to the NIR image proved to be challenging. Registration failures not only affected one video frame but also the following frames as a once falsely matched region was tracked until redetection was performed. An easy solution would involve the installation of a beam splitter which enables both cameras to map exactly the same scene [224]. In doing so, the registration step could be completely avoided.

As already delineated in the introduction, there are only a few works which offer ROI selection methods that neither rely on the visibility of anatomical features, nor on the distinct manifestation of local plethysmograms. Moreover, many of those works used rather simple and insufficient methods as they focused on signal processing [260, 367, 368]. To the best of my knowledge, solely Stricker et al. [317] presented a more complex approach very similar to the one proposed here. The group also combined a skin classifier with a segmentation method, namely *GrabCut* [278]. Due to the resemblance, it was decided to test the approach for a number of images. In comparison to the level-set-based method,

GrabCut performed significantly worse as high-contrast non-skin and more heterogeneous skin areas were selected.

5.5.2 *Homogeneity*

The results for the RIH measure prove that the level set segmentation approach is most suitable for identifying homogeneous regions. The relatively low variation of q_{RIH} across the measurements further shows how stable the new method operates when surrounding conditions and individual characteristics alter. Differences between the data sets can be attributed to the impact of motion artifacts which generally compromised the performance of the method. In the postoperative study, where overall high RIH values were achieved, the patient movement was minor. In contrast, in the CPT study, where the lowest values were obtained, movement occurred much more often and stronger. As explained in the previous section, stabilization problems in the segmentation process predominantly arose for the NIR videos. The homogeneity parameter also reflects these problems. The improvement, which could be realized by the developed method, for example, was the lowest in the NIR channel.

In the past, several works have already attempted to consider local homogeneity when selecting ROIs. Melchor Rodríguez and Ramos-Castro [215, 216], as well as Tasli et al. [331] used simple thresholding approaches the exclude darker face regions. Amelard et al. [14] suppressed the contribution of pixels at high image gradients. Similarly, Park et al. [253] downgraded areas in the vicinity of edges, and Gupta et al. [106] actively removed edges from the ROI. Yang et al. [386] built a roughness measure which was employed to only select the smoothest regions. Bousefsaf et al. [42] utilized the lightness component of the CIE $L^*u^*v^*$ color space to create cluster with different uniformity attributes. Using a flood-field algorithm, Addison et al. [3] generated ROIs that exclusively held pixels with similar intensity values. Despite the variety of concepts, none of those methods allows a continuous (time and space) and pixel-wise selection of ROIs where the degree of homogeneity is not statically set but automatically adapts to the prevalent situation. To the best of my knowledge, solely the proposed level-set-based method is able to meet all these criteria.

5.5.3 *Photoplethysmographic Monitoring*

The outcome of the SNR and HDR assessment proves the new method to select proper ROIs that provide high-quality cbPPG signals. The method's application allows a reliable HR detection (green channel: 76.5 % - 95.6 %) elevating cbPPG to a suitable monitoring technique for clinical and non-clinical environments. As delineated in Section 5.4.2, the result for the three data sets differ considerably. The reasons for those differences, however, are not always associated with the performance of the developed algorithm. In the videos of the postoperative study, for example, the patient movement was low and the ROI selection

worked rather well. Yet, the signal qualities appear to be moderate there. A closer look at the plethysmograms reveals that the cardiac pulsation was often weak. On the one hand, cardiovascular diseases, which were strongly present in the patient group (see Table 6), can cause such a suppression of the pulsation [9]. On the other hand, the pathophysiological state after surgery may involve the blood flow to bypass superficial skin layers in response to autonomous control and thermoregulation [269, 337] and, therefore, may eventually impair the detection of cbPPG signals. A further factor could be the illumination which proved to be inadequate in the study (see Fig. 63, Table 6). Bad lighting leads to a low image intensity and, consequently, to a low pulsation strength [189, 269]. For the videos of the intraoperative study, a different pattern manifested in the results. Interestingly, the achieved signal qualities were very high although cardiovascular diseases were present in the patients (see Table 5). This positive effect can be attributed to the administered general anesthetics which caused the peripheral blood vessels to dilate [4]. It was already shown by Rubins et al. [282, 283] that in case of anesthesia, the amplitude of camera-based plethysmograms enhances significantly. For the videos of the CPT study, lower SNR and HDR values are most likely linked to the misperformance of the new method. Especially movements turned out to be a problem. The strong variation in the results could reflect instabilities in the ROI selection process (see Fig. 45). Since all participants were young and healthy, it is save to assume that there are no physiological or anatomical reasons why blood volume variations should not be well-detectable [9, 11, 51]. The only exception in the experiment would be the time period where the CPT was conducted. The CPT leads to peripheral vasoconstriction which actually may compromise the manifestation of the cbPPG signals [307, 394].

In general, a potential source of error in the processing framework evolves from the way artifacts are handled (see Fig. 35). The key idea behind the tracking approach was to retain the regions' homogeneity over time and avoid abrupt light changes in the ROI. However, when an artifact is found and the *ROI detector* is re-executed, the intensity values of the prior ROI will not be considered for the new selection. As a consequence, the eventually acquired cbPPG signal may hold edge-like characteristics which hinder a valid HR extraction. It is worth noting that, in fact, the mean re-execution count of the *ROI detector* was quite low throughout the data sets (intraoperative study, RGB: 9, NIR: 3/ postoperative study, RGB: 10, NIR: 4/ CPT study, RGB: 10, NIR: 6). Moreover, redetection had to be less often carried out for the NIR videos. This outcome is most likely related to the lighting configuration. While the illumination in the RGB recordings was defined by ambient light, the illumination in the NIR recordings was mainly defined by the installed LED spot lights. Therefore, in moments where the ambient light was insufficient or altered strongly (e.g. due to movements, changing weather), the LED spots could still provide stable illumination conditions for the NIR recordings. As a result, the NIR videos were normally less degraded by artifacts than the RGB videos which also explains why the NIR channel made the highest contribution to maximizing the HDR in the green channel (see

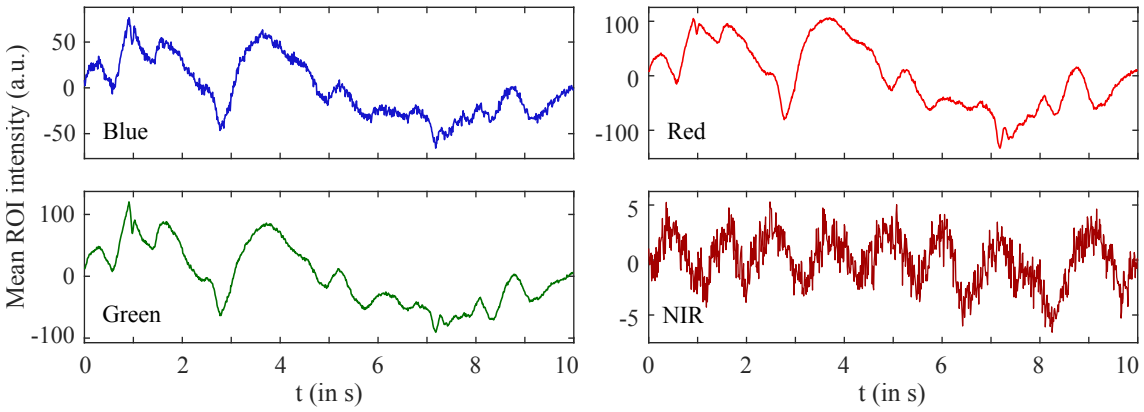

Figure 48: Example of cbPPG signals extracted from the blue, green, red and NIR channel. Variations in the ambient light caused artifacts to occur in the RGB video while the NIR video remained unaffected (cardiac pulse is visible). The ROIs were well-defined in both videos. The signals were solely detrended for the depiction. Note: Different scales were used for the plots.

Section 5.4.2). Figure 48 shows an example that illustrates the benefit added by the NIR recording.

The SNR assesses the cbPPG signal's quality based on the strength of the cardiac pulsation. The found parameter characteristic in the different color channels coincides with the outcome of prior investigations which also evaluated the quality of multispectral photoplethysmograms [30, 67, 203]. As shown, the green wavelength range usually provides the largest SNR values. Since the absorption coefficient of hemoglobin is relatively high in this range (see Fig. 8), it can be concluded again that blood volume variations are a defining factor for the modulation of cbPPG signals. However, in comparison to the results of the polarization experiment, a surprisingly low SNR was achieved in the blue channel (see Fig. 29). This inconsistency might be hardware-related. While at the measurement stand, the blue wavelength range is indirectly defined by the optical filters on the camera sensor, in the polarization experiment, the range is directly set by the dedicated illumination with blue light. An analysis of the spectral bandwidths revealed that a much wider range of light enters the sensor when the filters are in use than when the active LED lighting is employed (120 nm vs. 23 nm, see Fig. 19 and Table 9). The unfavorable superposition of information from a broad wavelength range could eventually be the reason why the signal qualities in the blue channel turned out to be low here.

Moço et al. [225, 226] showed how homogeneously illuminated regions provide purer photoplethysmograms which are less corrupted by BCG artifacts. The group proposed a method that was able to suppress the impact of BCG interference at the measurement site. Unfortunately, the method had to be calibrated beforehand, and it relied on a distinct manifestation of the cardiac pulsation in local cbPPG signals. The level-set-based approach does not have those drawbacks and, at the end, yields a similar outcome as only the most homogeneous skin areas are selected for signal extraction. It should be noted, the determined ROIs of the reference method, i.e. bounding boxes, most likely caused BCG

effects to strongly modulate the acquired signals since high-contrast areas were usually included in the boxes. These effects can ultimately increase the HDR and SNR because the two quantities only assess the strength of the cardiac component but not its origin (blood volume variations vs. movements). This peculiarity could explain why the improvement by the new method seemed to be rather minor (see Fig. 44, 45, and 46). A better HR detection is not necessarily associated with a higher purity of the plethysmograms.

5.5.4 *Clinical Application*

As delineated in Section 2.5.2, there are numerous studies in which the applicability of cbPPG was tested for clinical environments. The convenience, flexibility and degree of automation that is provided by the newly developed measurement stand as well as the presented ROI selection method, however, were normally not given in those studies. Only Tarassenko et al. [328] and Bal [23] proposed similar systems, in their cases for a dialysis facility and a pediatric intensive care unit, respectively. To the best of my knowledge, this thesis and the corresponding publications [269, 338, 340] are the first works to prove that cbPPG is a valid monitoring technique in intra-surgical (general anesthetic) and post-surgical situations. Moreover, the level-set-based algorithms allows the monitoring to be carried out fully automatically.

CHAPTER SUMMARY

In this chapter, a novel and fully automated method for ROI selection in cbPPG was proposed. The method overcomes the drawbacks of previous approaches as it does not rely on the detectability of anatomical features and solely operates on the image plane without being dependent on the presence of temporal variations related to the cardiac cycle. Furthermore, it only detects and tracks the most homogeneous skin regions which eventually prevent the plethysmograms to become degraded by BCG artifacts (see Chapter 4). Three challenging data sets obtained from laboratory and clinical studies were tested to prove how efficient the method performs in different situations. For more than 152 hours of video data, it was shown that proper ROIs can be determined reliably. Moreover, they were found to be well-suited for the extraction of high-quality cbPPG signals. In combination with the developed measurement stand (see Chapter 3), the new method paves the way for a remote, autonomous and automated monitoring system which is independent of the application environment.

6

ASSESSMENT OF AUTONOMIC FUNCTIONS

While the last chapters addressed fundamental questions regarding the technical setup and processing structure in cbPPG, this chapter focuses more on the actual application of the technique. The primary goal here is to reveal how autonomic reactions, which are triggered by certain external stimuli and affect the vascular tone, can be detected by cbPPG. Additionally, the chapter intends to shed further light on the origin of the camera-based signals. The first section provides an overview of works that investigated the capability of cbPPG to capture vasomotor activity. The second section delineates the experimental tests, formulates the hypotheses, and describes the methods as well as the evaluation process. The third section presents the results. The last section discusses the outcome with respect to the defined goals. It should be noted that parts of the following content already appeared in two of my publications [336, 394].

6.1 STATE OF THE ART

Despite the numerous advantages that cbPPG has over other measurement techniques, the most evaluated physiological parameter is still the HR [209, 280]. There is general lack of studies which investigate further application fields – the assessment of autonomic functions being one of them [393]. The easiest way to assess such functions is to analyze the HR variability which, to some extent, acts as surrogate for the ANS's activity (see Section 2.2.2 and 2.5.2). More interesting, however, is how responses of the ANS in the cutaneous vasculature reflect in certain cbPPG measures. Only few works have addressed this question so far. In the following, a brief overview is given.

In order to evoke a controlled and classifiable reaction of the ANS, external stimuli are needed. The anticipated changes in the vasomotor tone can then be captured by the cameras, and attempts can be made to identify them in the video recordings. In 2011, Rubins et al. [281] were the first to follow this procedure for their analysis. They found that a vasodilatory effect due to local skin heating significantly increases the cbPPG signal's pulsation strength. Marcinkevics et al. [201] later performed a similar test and came to the same conclusion regarding the relative pulsation strength. Frassineti et al. [91] induced reactions by regional heat and cold stimulations. The group demonstrated that the spatial distribution of the signal amplitude is considerably more homogeneous in case of heating.

Besides local temperature changes, gradual changes in the ambient temperature have been utilized to assess thermoregulatory responses in the skin. Verkruysse et al. [349] put subjects in a climate chamber and exposed them to a temperature drop of 17 °C. The resulting peripheral vasoconstriction manifested in the cbPPG signals as a decrease of the pulsatile amplitude. Another way to trigger the vasoconstrictory effect is to temporally obstruct breathing such as was done by Amelard et al. [17]. In accordance with the outcome of the aforementioned study, they observed a decline in the pulsation strength. Bousefsaf et al. [39] elicited vasoconstriction by means of physical exercises. The group recorded the participants after the exercises when the peripheral vasculature started to dilate again. The recovering vessel tone was found to reflect in the pulsatile signal component. It should be noted, in addition to the presented research, there are further works where the vasomotor activity was assessed in the course of stimulation (e.g. through vascular occlusion, application of skin liniment, local anesthesia) [148, 201, 282, 283]. However, those works were not taken into account here since actual autonomous functions played no or only a minor role in their experiments.

Goal

In this chapter, it is further investigated how cbPPG can be used to assess autonomic reactions in the cutaneous vasculature. Three established (psycho-)physiological tests, the CFT, the CPT, and a local skin heating test [139, 223, 273], were performed with the purpose of activating the ANS and evoking quantifiable responses in the skin. Except of my own publications [336, 394], to the best of my knowledge, there are no cbPPG-related works that conducted such a variety of ANS-stimulating experiments. In addition to the assessment of autonomic functions, this chapter also attempts to shed more light on the origin of camera-based signals. For both analyses, the pulsation strength s_{AC} was chosen as evaluation parameter.

6.2 METHODS

6.2.1 *Data – Heating, Cold Face, and Cold Pressor Test*

In order to acquire a data basis for the set investigation, two different studies were conducted. In the first study, the inner arm of ten volunteers was recorded while a local heating test and a CFT were performed (see Section 3.3.2). For each participant, six consecutive measurements of 90 s were carried out where the heat stimulus was continuously applied and the respective cold stimulus only temporarily during the last three measurements. The full experimental procedure is depicted in Fig. 49. For the eventual analyses, every measurement was divided into 30 s windows $W_{i,j}$ ($i = [1, 6]$ and $j = [1, 3]$) with i being the measurement number and j the window number. In the second study, the face

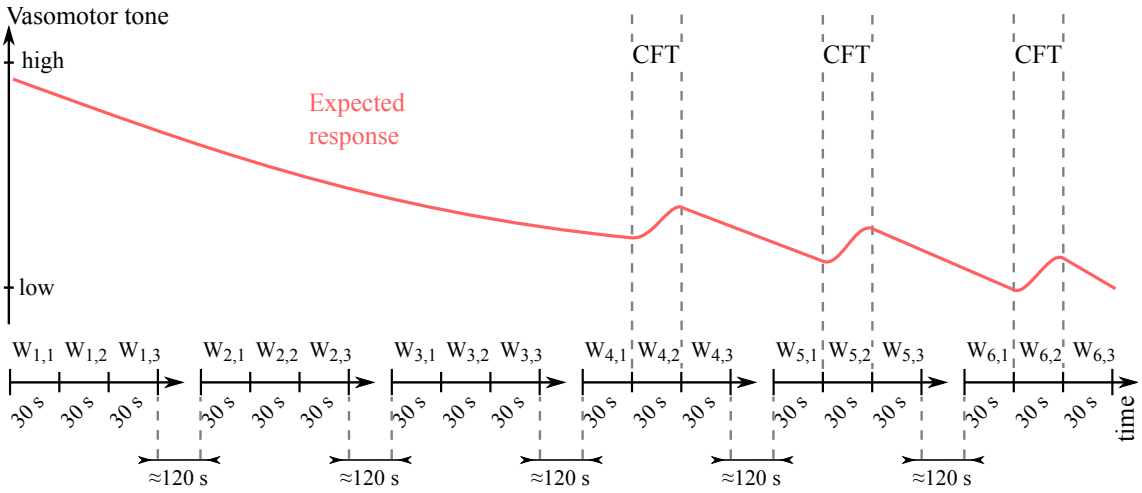

Figure 49: Experimental procedure for the local skin heating test and the CFT. The experiment comprised six consecutive measurements. The heat stimulus for the first test was applied over the course of the whole experiment. The cold stimulus for the second test was only applied in the last three measurements. For evaluation, 18 windows $W_{i,j}$ were constructed. Above the time line, the expected response of the vasomotor tone in the cutaneous vasculature is depicted. This estimate was derived based on the results presented in [61, 273, 315].

of 22 volunteers was recorded while a CPT was performed (see Section 3.3.1). Each subject participated twice so that overall, 44 measurements were obtained. One measurement had to be excluded due to technical errors and another six due to strong subject movement[1]. As a result, 37 measurements were left for evaluation. The whole experiment lasted approximately 30 min and comprised several phases (see Fig. 50). The CPT phase occupied about 3 min and was carried out after the first 8 min of measurement. For the eventual analyses, five different time windows with a length of 10 s were constructed[2]. Three windows $W_{BL1\text{-}3}$ were placed in the baseline phase and two ($W_{T1\text{-}2}$) in the CPT phase. While the first CPT window covered the beginning of the test, the latter one encompassed the moment where the individual SBP was the highest. This approach was chosen because the test procedure was not as reproducible as in the other study. The participants themselves had to immerse their hands into the water which led to the uncertainty of when the maximum stress was present. The placement of the last window ensured that episodes with physiological responses are included in the analysis. It is important to note, no window was constructed for the phase succeeding the CPT as too much movement occurred during the saliva sampling.

1 Note: In this chapter, the ROIs were selected manually (see Section 6.2.2). Subject movement was considered strong when a defined ROI could not be re-allocated to the same anatomical area in one of the following evaluation windows.

2 It should be pointed out that the evaluation windows in the two studies were defined with different lengths (30 s vs. 10 s). For each window, a cbPPG signal was extracted and the pulsation strength s_{AC} was determined. Pretests showed that the signal quality at the arm was low, and a longer segment was needed to obtain a reliable s_{AC} value. For the CPT study, 10 s proved to be sufficient.

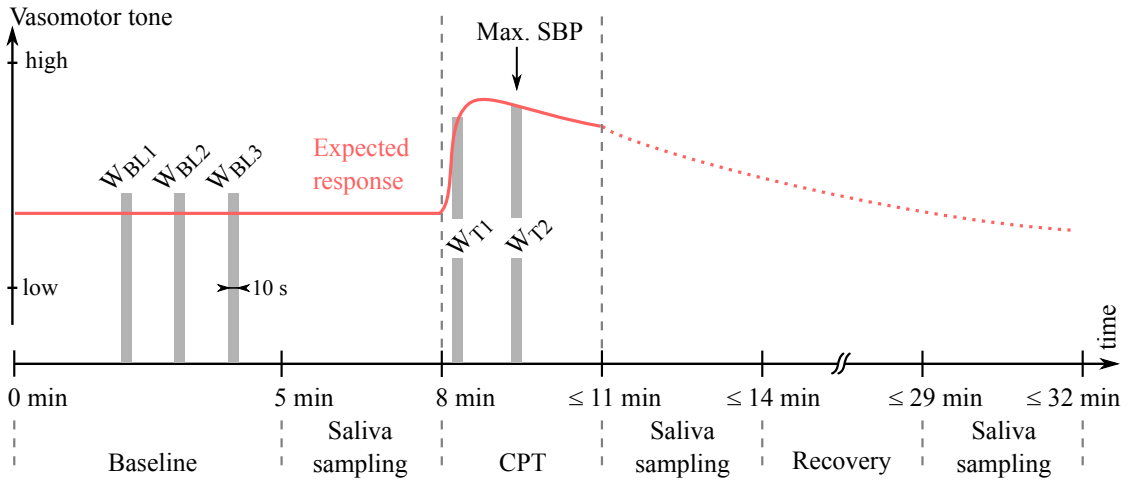

Figure 50: Experimental procedure for the CPT. The stress-stimulating episode lasted for about 3 min and took place within a measurement period of approximately 30 min. For evaluation, five 10 s windows were constructed, three of them in the baseline ($W_{BL1\text{-}3}$), and another two during the actual test ($W_{T1\text{-}2}$). Above the time line, the expected response of the vasomotor tone in the cutaneous vasculature is depicted. This estimate was derived based on the results presented in [151].

The three (psycho-)physiological tests, which were performed in the studies, elicited autonomous reactions. In the following listing, the effects of each test are explained in more detail:

- *Local skin heating* The exposure of a certain body part to heat or cold impacts the (sub-)cutaneous vascular tone in a different way as when the whole body undergoes a gradual change in the ambient temperature [61]. In addition to the described thermoregulatory mechanisms in Section 2.2.2, the regional stimulation also triggers local mechanisms [107]. In case of heating, local vasodilation occurs. The vascular adaption is not only controlled by the SNS through the smooth musculature but also by the release of nitric oxid which activates the endothelial function [61, 139].
- *Cold face test* The CFT has proven to be a simple way to elicit the diving reflex by applying a cold stimulus to the forehead [373]. It is used to assess autonomic functions as the SNS and PSNS are activated concurrently [273]. The reported reactions are peripheral vasoconstriction and bradycardia [111]. Furthermore, an increase in the (systolic) BP has been observed as response to the stimulation [156, 273, 315]. Note: Local temperature effects at the forehead were not considered in this study since the arm was chosen as recording area.
- *Cold pressor test* The CPT is an experimental method where participants immerse a limb into cold water to evoke stress and pain reactions [114, 223]. The stimulus activates the SNS as well as the hypothalamic–pituitary–adrenal axis which is an important hormonal control system [219, 316]. Reported bodily responses include (i) an increase in cortisol, (ii) cutaneous vasoconstriction, (iii) tachycardia, and (iv) and a rise in BP [191, 219, 294, 310]. Note: Local temperature effects at the limb were not considered in this study since the face was chosen as recording area.

In conclusion, all three tests involve changes in the vasomotor tone which are controlled by the ANS. Figure 49 and 50 illustrate the expected behavior across the different experimental phases. Here, it is assumed that an appropriate camera-based quantity is able to reflect the tone changes through the related variations in the blood volume. The signal pulsation strength s_{AC} was chosen for this purpose. Within the described constraints, the parameter is believed to be inversely proportional to the vascular tone.

6.2.2 *Processing and Evaluation*

In order to extract the wanted information from the videos, at first, ROIs had to be defined. It was decided to manually label the regions since an automatic selection may have led to inconsistencies and false assignments. For the videos of the heating and CFT experiment, an ROI was determined at the beginning of each measurement and kept unchanged throughout the measurement. The annotation enclosed the inner arm. Skin edges and the wrist area were omitted because they are known to hold BCG artifacts [226] (see Section 2.5.1). Figure 51 (a) shows an example. For the videos of the CPT experiment, an ROI was defined for each evaluation window and also kept unchanged for the whole length of the window. Here, the center of the forehead was selected as depicted in Fig. 52 (a). This particular face region was chosen due to its proven suitability for acquiring high-quality plethysmograms [171, 181].

After annotation, the cbPPG signals were extracted from the green channel[3] by averaging the respective pixel values inside the ROI. The obtained signals were then assigned to the aforementioned windows ($W_{1\text{-}6,1\text{-}3}$ and $W_{BL1\text{-}3}$, $W_{T1\text{-}2}$). For every window, the pulsation strength s_{AC} was calculated in the same way as it was done for the polarization experiment (see Section 4.2). In the following, a brief description of the procedure is given. First, the signals were filtered with a bandpass (cutoff frequencies: 0 and 15 Hz). Second, the single cbPPG beats were identified and cut out at reference points. For this purpose, the position of the R-peaks in the electrocardiogram were used[4]. Third, the beats that were not corrupted by artifacts were averaged to a mean beat for each window. Finally, s_{AC} was determined as the height of the mean beat. Figure 51 and 52 illustrate the procedure.

As explained in the previous section, besides changes in the vascular tone, the CFT and the CPT also trigger changes in the HR and BP. Therefore, it makes sense to additionally analyze those quantities. To do so, for each evaluation window a HR, SBP, and PP value was estimated from the corresponding reference signals: The HR was calculated as the reciprocal of the median inter-beat interval (R-R duration) in the electrocardiogram, the SBP as the median of the beat-related maximums in the BP signal, and the PP as the median of the minimum-to-maximum distances[5].

3 The green channel was chosen because, in comparison to the other channels, it provides the strongest plethysmographic signals [348].

4 The R-peaks in the electrocardiograms were selected using the QRS detector from the BioSig toolbox [290].

5 Note: The diastolic and systolic points (minimums and maximums) in the BP signal were obtained by applying the OSET MaxSearch algorithm [286].

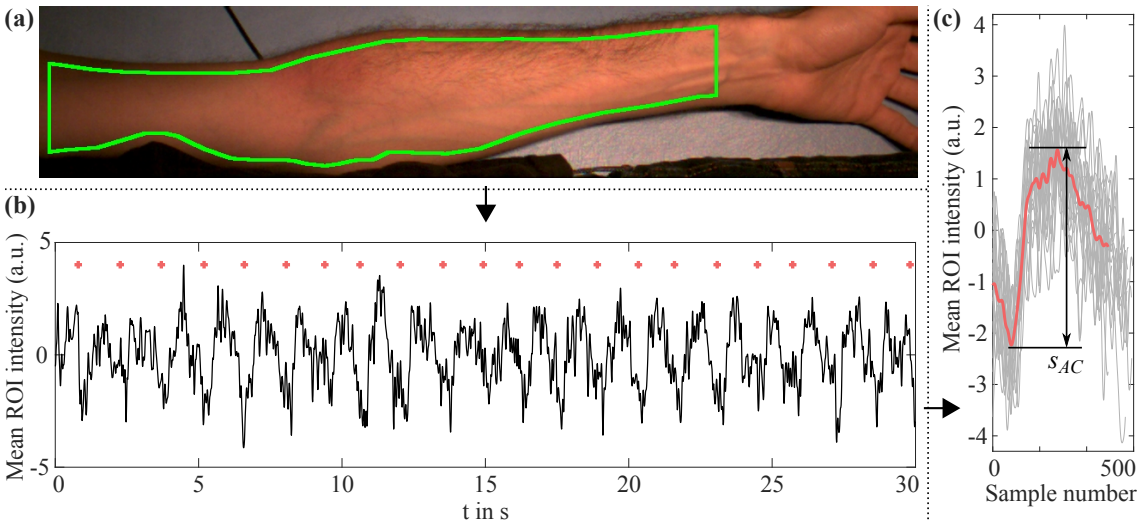

Figure 51: Main processing steps for the evaluation of the videos from the heating and CFT experiment: (a) Selection of the arm ROI (only contour is shown), (b) Beat detection in the extracted cbPPG signal (filtered) using the R-peaks' position from the reference electrocardiogram (red crosses), (c) Calculation of the parameter s_{AC} in the mean beat (red).

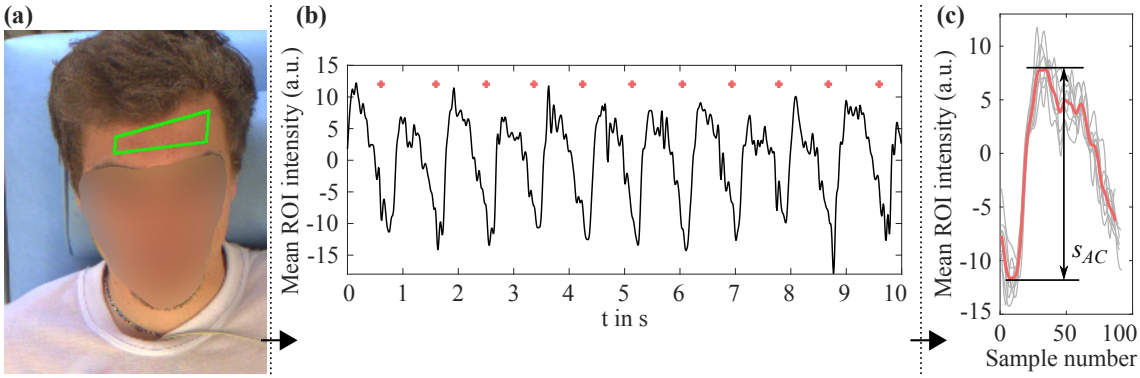

Figure 52: Main processing steps for the evaluation of the videos from the CPT experiment: (a) Selection of the forehead ROI (only contour is shown), (b) Beat detection in the extracted cbPPG signal (filtered) using the R-peaks' position from the reference electrocardiogram (red crosses), (c) Calculation of the parameter s_{AC} in the mean beat (red).

Statistics

In order to analyze whether the three ANS-stimulating experiments involve a significant change in the pulsation strength s_{AC}, statistical testing was utilized. For the skin heating experiment, a gradual increase in s_{AC} was expected. The behavior of the parameter was evaluated across the six measurement cycles in the windows $W_{1\text{-}6,1}$ as they were unaffected by the CFT. The predicted trend was quantified using the the Spearman's rank correlation coefficient ρ which was chosen due to the ordinal time scale [268]. To validate the significance of the trend, the Page test was employed [249]. The test was proven to be well-suited for the prevalent conditions [289]. It applies a test statistic L that can easily be converted into a common p-value.

For the CFT experiment, a decrease in s_{AC} was expected. To quantify the changes, the manifestation of s_{AC} was examined over the course of the corresponding time windows $W_{4\text{-}6,1\text{-}3}$. Since in the last three measurement cycles, the procedure was identical (see Fig. 49), they were considered as separate measurements and it was assumed that they were independent. As a consequence, only three groups (before, during, and after CFT) had to be compared for the analysis. First, the Friedman test was carried out to reveal whether general differences exist between the groups. If the Friedman test showed significance, second, post-hoc tests were performed using the Wilcoxon signed-rank test (two-sided) where the p-values were adjusted by the Bonferroni correction. It should be noted that the testing was done in the same way as in Chapter 4 and was also based the same reasoning.

For the CPT experiment, a decrease in s_{AC} was expected as well. The parameter's behavior was examined across the five evaluation windows. The statistical analyses, however, were only carried out for the last three windows W_{BL3}, W_{T1}, and W_{T2}. Again, all measurements were assumed to be independent so that each window-related group held 38 s_{AC} values. Differences between the groups were assessed by means of the same test methods as used for the CFT experiment.

As mentioned before, besides s_{AC}, it was decided to also take the reference quantities HR, SBP, and PP into account for evaluation. Changes in those quantities were investigated utilizing the analysis procedure that was employed for s_{AC}.

6.3 RESULTS

Skin Heating Test

Figure 53 shows the results of the skin heating experiment regarding the pulsation strength s_{AC}. As can be seen, a gradual increase manifested in the cbPPG parameter over time. The only exception was found in window $W_{4,1}$ where a notable decline was observed. Nevertheless, this inconsistency did not affect the general rising trend which reflected in a moderate correlation of $\rho = 0.57$ and, furthermore, proved to be highly significant ($L = 849, p < 0.001$). The strongest increase in s_{AC} appeared in the transition from window $W_{2,1}$ to $W_{3,1}$ (median: 0.52) and from window $W_{4,1}$ to $W_{5,1}$ (median: 0.51). Besides the analysis of changes in the pulsation strength, it is of interest to find out how comparable the single values are at a given time. To do so, the interquartile range was assessed. Here, the largest ranges arose in window $W_{1,1}$ and $W_{5,1}$.

It was also tested if significant trends existed for the reference quantities HR, SBP, and PP. No clear pattern was apparent however.

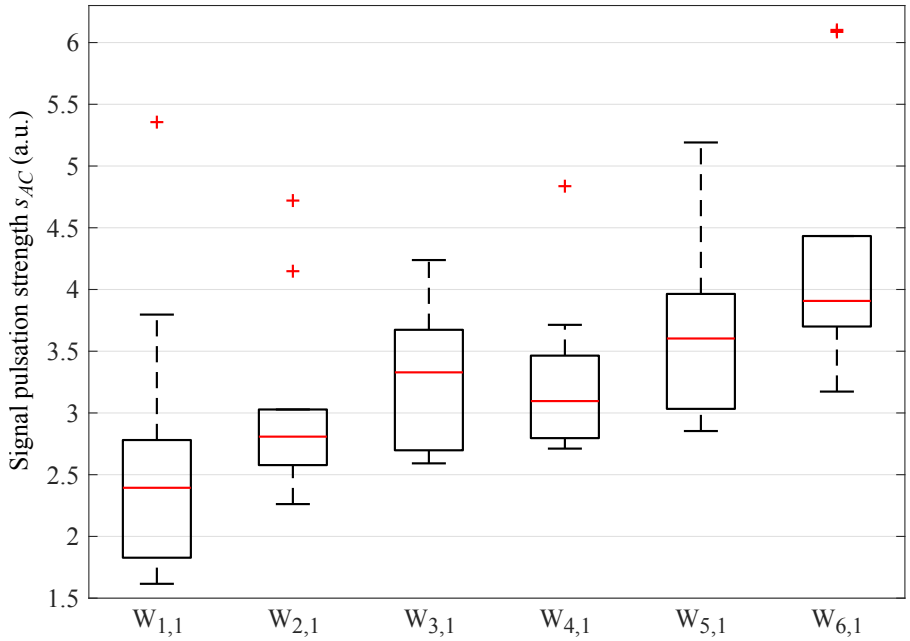

Figure 53: Results of the skin heating experiment regarding the pulsation strength s_{AC}. Each boxplot depicts the distribution of the subject-related values (10 values per group) for the corresponding evaluation window.

Cold Face Test

Figure 54 shows the results of the CFT experiment. For the pulsation strength s_{AC}, the Friedman test revealed that there are no significant differences between the three window-related groups: before, during, and after the CFT. Despite the statistical outcome, a notable decrease in the median value during stimulation was observed nonetheless. The high variation of s_{AC} in the corresponding windows $W_{4\text{-}6,2}$, however, caused this result to be not reliable. For the HR, also no significant differences could be found between the groups although a continuous decline in the median was visible. A closer look at the boxplots in Fig. 54 (a) reveals furthermore that for some subjects, the HR did not decrease at all during stimulation but, in fact, increased. The SBP and PP were the only examined quantities where the Friedman tests showed significance ($p < 0.01$). Moreover, the post-hoc tests proved a significant BP rise to occur when the ice pack is applied to the forehead (see Fig. 54 (b) and (c)). The pressure decreased again after the CFT ($W_{4\text{-}6,3}$). However, this drop was solely significant for the PP measure. Similar to s_{AC}, the interquartile range widened for the SBP in the windows $W_{4\text{-}6,2}$. Interestingly, for the PP, the highest range was found in the last windows.

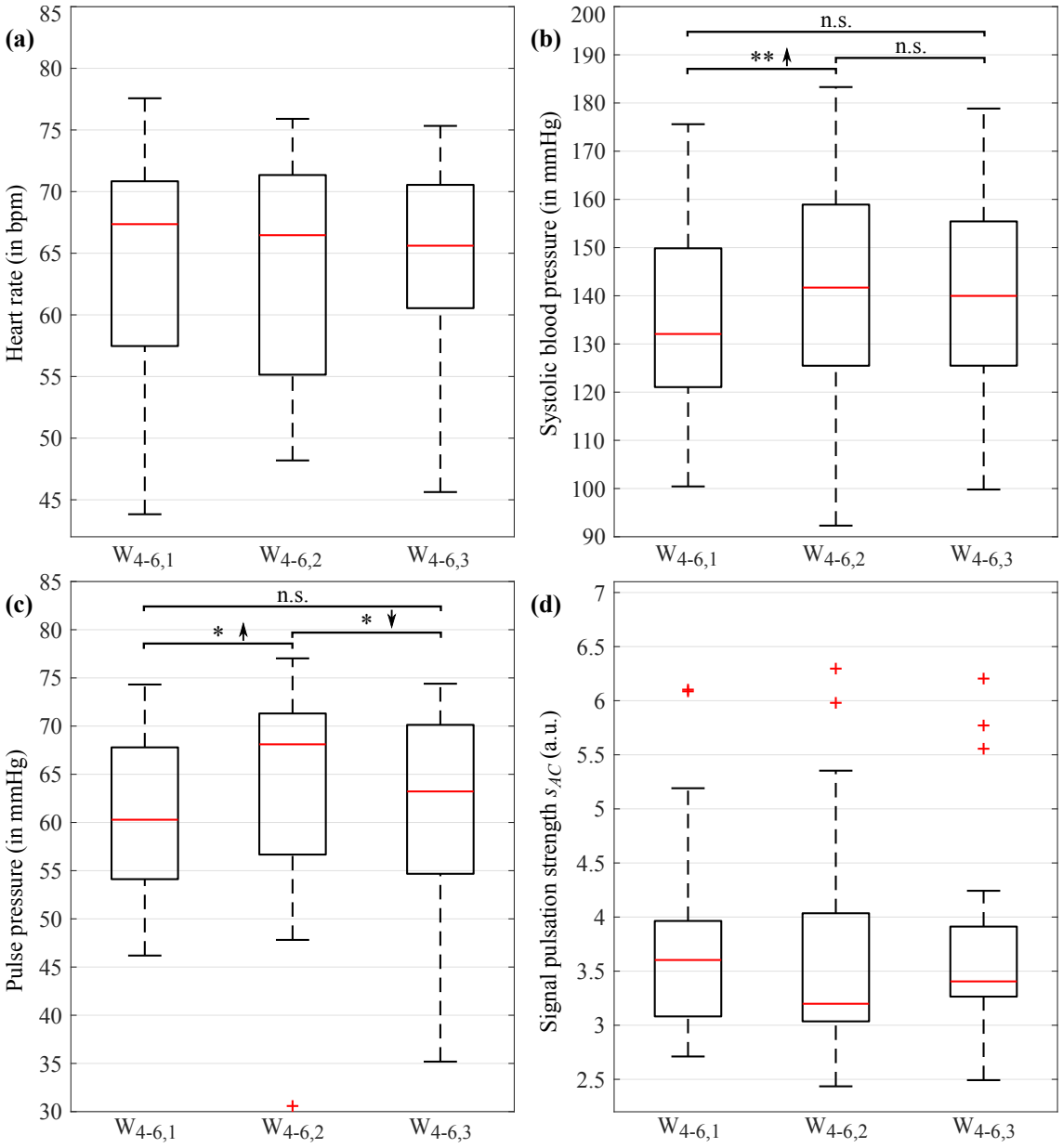

Figure 54: Results of the CFT experiment depicted for the different evaluation windows: (a) HR, (b) SBP, (c) PP, (d) Signal pulsation strength s_{AC}. Each boxplot describes 30 values based on the number of measurements. Above the boxes, the outcome of the statistical post-hoc tests were displayed (n.s. $p > 0.05$, * $p \leq 0.05$, ** $p < 0.01$) if the preceding Friedman tests showed significance. The arrows denote whether an increase or decrease was observed in the respective parameter.

Cold Pressor Test

Figure 55 depicts the results of the CPT experiment. Compared to the other two experiments where the arm was the measurement object, it is apparent that here, the pulsation strength is generally much higher.

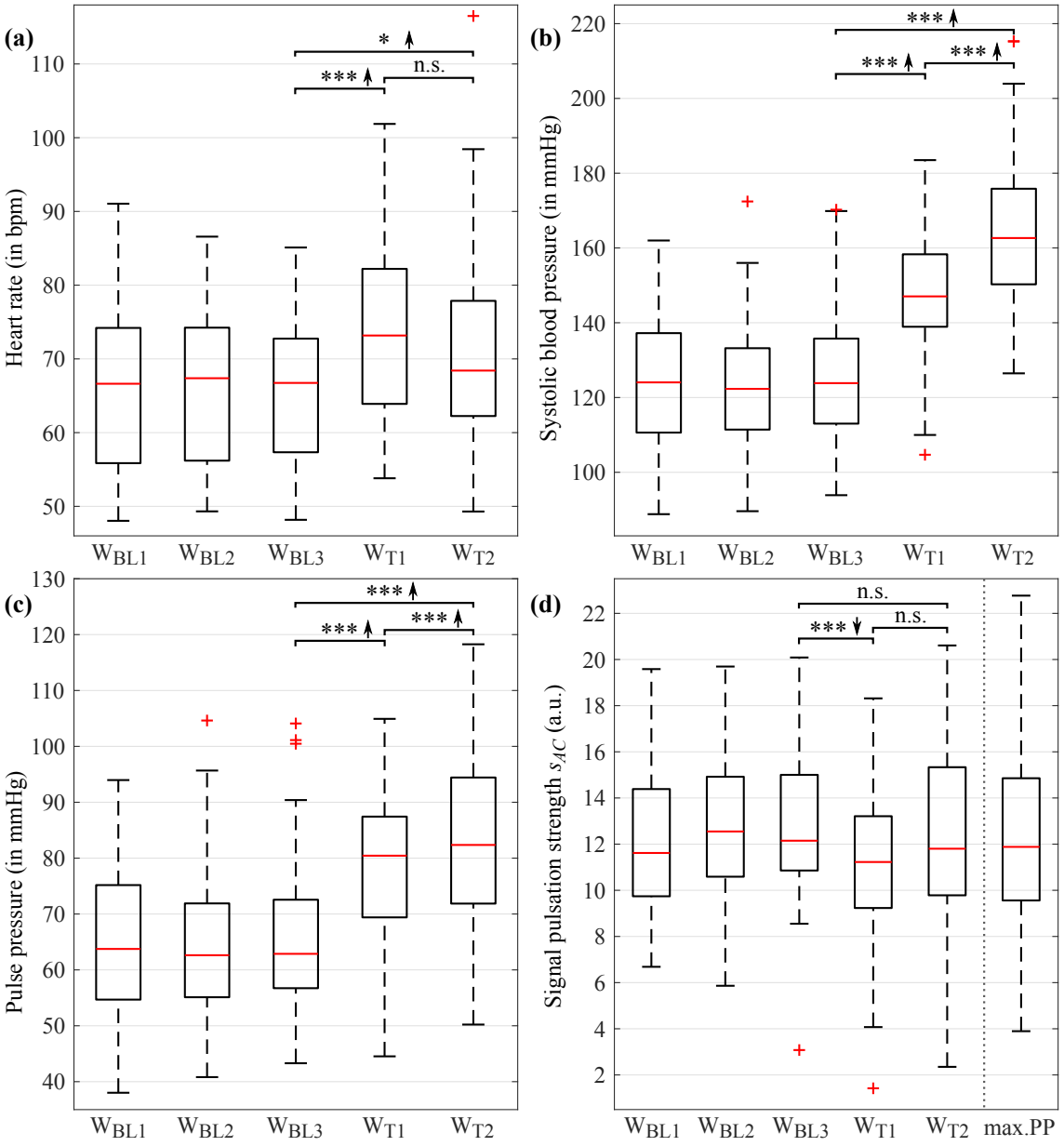

Figure 55: Results of the CPT experiment depicted for the different evaluation windows: (a) HR, (b) SBP, (c) PP, (d) Signal pulsation strength s_{AC}. For the pulsation strength, additionally, the window is shown where the PP was maximal. Each boxplot describes 38 values based on the number of measurements. Above the boxes, the outcome of the statistical post-hoc tests were displayed (n.s. $p > 0.05$, * $p \leq 0.05$, *** $p < 0.001$) if the preceding Friedman tests showed significance. The arrows denote whether an increase or decrease was observed in the respective parameter.

Within the baseline windows $W_{BL1\text{-}3}$, s_{AC} amounted to about 12 units on average (3.6 in the CFT analysis). At beginning of the CPT in window W_{T1}, a significant drop occurred in the parameter (see Fig. 55 (d)). Later in the test, at the time of the highest SBP (W_{T2}), however, s_{AC} seemed to revert to the baseline level again. The individual response strongly varied in W_{T2} as the interquartile range turned out to be relatively wide. The same

holds for the window where the PP was maximal[6]. This variation most likely caused the associated post-hoc analyses to reveal non-significant differences between the groups. In contrast, the Friedman test showed high significance ($p < 0.001$). For the HR measure, the outcome principally differed (see Fig. 55 (a)). Similar to s_{AC}, within the baseline $W_{BL1\text{-}3}$, the parameter remained more or less unchanged. During stimulation, however, a significant increase appeared in both windows W_{T1} and W_{T2} with respect to W_{BL3} (Friedman test: $p < 0.001$). The strongest reaction manifested in the first test window while in the second one, a recovery-like effect became apparent. This result implies that at the time of the maximum SBP, the HR has already reached its peak and is decreasing. In the same way as for s_{AC}, a larger interquartile range was also observed for the HR during the CPT. The clearest response to the cold stimulus was found for the two BP quantities (see Fig. 55 (b) and (c)). For both measures, a highly significant increase emerged over the course of the stimulation. The Friedman test and all post-hoc tests resulted in $p < 0.001$. For the SBP, the increase was rather constant whereas for the PP, it declined towards the last window W_{T2}. Interestingly, associated with this decline was a rise of the individual PP differences (interquartile range). As for the other parameters, the baseline showed no peculiarities in the BP quantities.

6.4 DISCUSSION

6.4.1 *Detection of Autonomic Reactions*

The results prove that autonomic reactions in the human body can generally be captured by cbPPG. To the best of my knowledge, this work and my corresponding publications [336, 394] are the first investigations in the field of cbPPG to assess the technique with respect to the application of the CFT and CPT.

Skin Heating Test

The found increase of the pulsation strength during skin heating is in accordance with the known vasodilatory effects caused by the stimulation [61, 107, 139]. Moreover, it is consistent with the outcome of other cbPPG works [91, 201, 281] and confirms the hypothesis that s_{AC} reflects the vasomotor tone at least to some extent (see Fig. 49). Local warming over a longer period of time (> 20 min) leaves a unique pattern in the cutaneous vascular conductance involving a sharp rise in the beginning followed by a brief decrease which then transitions into a plateau phase [61]. For the most part, those characteristics also manifested in the pulsation strength. The initial increase was found in window $W_{1\text{-}3,1}$ and the the decrease in window $W_{4,1}$. The subsequent plateau phase, however, could not be identified. One reason might be that the experiment simply did not last long enough

6 Note: Across the subjects, the time of the maximum SBP more or less corresponded with the time where the PP was maximal.

(≈ 19 min). Another reason might result from the temporal overlap between the skin heating test and the CFT in the second half of the experiment. The cold stimulus in the CFT led to an activation of the SNS possibly entailing vasoconstriction which would substantially alter the expected behavior of s_{AC}. This theory could furthermore explain why the variation in window $W_{5,1}$ is relatively high. The window represents the first measurement period after the CFT. One would assume that the individual response to the counteractive stimulation strongly differs in this window. In contrast, the large interquartile range in $W_{1,1}$ presumably arises from the varying starting conditions of the subjects (temperature of place they came from, effect on circulation after lying down).

Cold Face Test

Although statistical non-significant, a decrease in the median HR was noticeable for the CFT. The observed drop points to an activation of the PSNS and is in accordance with the reports from the literature [273, 315, 373]. In some participants, during stimulation, the HR increased which indicates that the cardiac SNS was activated (see Table 1). The reaction could have been the consequence of stress caused by: (i) occurring pain as a result of the coldness, (ii) the overall mental state of awaiting an unpleasant feeling [107]. The found rise in SBP also suggests a sympathetic activation. The response is known and can be expected for the CFT [156, 273, 315]. Whereas the pressure changes from the windows $W_{4\text{-}6,1}$ to $W_{4\text{-}6,2}$ were significant, the ones from $W_{4\text{-}6,2}$ to $W_{4\text{-}6,3}$ were not (see Fig. 54 (b)). This peculiarity implies that the subjects did not fully recover in the 30 s after the test, and it proves that the effects of the CFT have a prolonged impact (e.g. on the heating experiment). The high SBP variation in $W_{4\text{-}6,2}$ reflects the individual differences in the reactivity of the ANS upon stimulation. As for the HR, statistical testing resulted in non-significance for s_{AC}. The limited number of measurements or the influence of the warming stimulus might be a reasons for those results. Visibly, the pulsation strength appeared to decrease in $W_{4\text{-}6,2}$ nonetheless. The outcome would confirm the hypothesis of s_{AC} to be a surrogate for the vasomotor tone since the drop is consistent with a CFT-related vasoconstriction (see Fig. 49). The wide interquartile range in $W_{4\text{-}6,2}$ shows, again, how different the individual responses are. As mentioned before, there are no works that analyzed the cbPPG's capability to capture the bodily reactions to the CFT. However, investigations exist which assessed camera-based measures for central and local cooling scenarios [91, 349]. Similar to the results here, Verkruysse et al. [349] found the pulsatile amplitude to decrease when a cold stimulus was applied.

Note: It was also evaluated how the finger plethysmogram changes due to the CFT. As presumed, the pulsation strength significantly declined during stimulation.

Cold Pressor Test

The observed increase in the HR and the SBP is in accordance with the reports from other CPT studies [219, 294, 310]. The high significance in the statistical analyses indicates

that the physiological response was considerably stronger for the CPT than for the CFT. While the two investigated pressure quantities seem to rise continuously over the course of the test, the HR appears to rise only shortly at the beginning. This peculiarity can be attributed to bodily mechanisms for BP regulation. An elevated BP triggers the ANS which attempts to decrease the pressure, e.g. by controlling the HR (see Fig. 5). Therefore, the HR drop in window W_{T2} is most likely associated with the activation of the cardiac PSNS. As in the other two experiments, large individual differences reflect in a stronger variation of the parameters. Especially during stimulation, the variation increases. However, in the CPT experiment, this behavior does not exclusively originate from physiological disparities but is also the result of the used protocol. Whereas for the skin heating test and the CFT, all stimuli were applied by a separate person, for the CPT, the participants had to immerse their hands themselves into the water tank. Such a procedure bears uncontrollable factors (e.g. time, duration and depth of immersion) and, consequently, leads to a higher parameter variation. When comparing the s_{AC} values obtained from the arm area with the ones obtained from the forehead (Fig. 53 and 54 vs. Fig. 55), it is apparent how substantially stronger the signal pulsation in the face is. This observation is in accordance with the findings of Tur et al. [344] who investigated regional differences in the cutaneous perfusion using PPG and laser Doppler velocimetry. In the same way as for the other two experiments, the change in s_{AC} reflects the predicted changes in the vasomotor tone, i.e. vasoconstriction in case of the CPT (see Fig. 50). The strongest vascular reaction apparently occurred right at the beginning of the test (window W_{T1}) as s_{AC} significantly dropped there. The recovery-like behavior in W_{T2} is probably linked to BP regulation effects. As explained with regard to the HR, the respective regulatory mechanisms attempt to decrease the elevated BP. The response includes the resistance vessels' dilation which potentially causes s_{AC} to rise again [107].

6.4.2 *Signal Origin*

For the set conditions of the three experiments, s_{AC} proved to be inversely proportional to the vasomotor tone. This outcome supports the theory that cbPPG signals are modulated by blood volume changes which arise from pulsatile vessels in the cutaneous vasculature (classic PPG theory). When the tone of such vessels alters, the pulsation strength of true photoplethysmograms is expected to alter accordingly [243, 244, 272]. Furthermore, the outcome allows to exclude BCG effects from being a major contributor for the signals' modulation. As rhythmical motion of larger vessels and the heart itself is defined as the cause of those effects, vasodilatory and vasoconstrictory variations in the periphery would not reflect in camera-based BCG signals [99, 225, 226].

Vascular blood volume changes can mathematically be described as the product of the compliance and the change in the transmural pressure (see equation 1):

$$\Delta V = C \cdot \Delta P_{tm} \ , \tag{19}$$

where the second term is approximable by ΔP_i if the surrounding tissue is not compressed [291]. The BP change ΔP_i itself is a surrogate for the PP (symbol: P_{pp}) in case a whole heart cycle is considered for calculation [160, 236]. The compliance is indirectly proportional to the vasomotor tone which is here denoted by T [107, 158]. Based on those concepts and on the presumption that s_{AC} quantifies blood volume changes, the following relation can be derived from equation 19:

$$s_{AC} \propto 1/T \cdot P_{pp} \; . \tag{20}$$

According to the relation, the pulsation strength varies inversely with respect to the tone. As this characteristic was actually found in the presented analyses, the presumption about s_{AC} is evidently true which further proves that the classic PPG origin theory applies for cbPPG as well. However, the relation also exposes the PP to be a defining factor. The question arises to what extent the PP influences alterations in s_{AC}. Figure 54 and 55 provide some answers. On the one hand, a decrease in the pulsation strength appears to be associated with a PP increase. On the other hand, the moment where the PP is maximal seems not to be aligned with the moment where s_{AC} is maximal. Those two peculiarities reveal that, in fact, the PP only plays a minor role in shaping the pulsation strength's behavior[7]. They also show that the origin theory by Kamshilin et al. [145, 149] most likely does not hold for cbPPG. For the green wavelength range, which was considered here as well, the group claimed, a periodic deformation of the papillary dermis defines the pulsatile signal (see Section 2.5.1). This deformation is supposedly caused by deep-lying arteries where the transmural pressure leads to a rhythmical displacement of the vessel walls and subsequently of the adjacent tissue. If true, one would expect a clearer and distinct relationship between the PP and s_{AC}. Moreover, changes in the vasomotor tone would presumably have no impact on s_{AC} since (i) according to the group, mainly non-compliant capillaries modulate the green light signal, and (ii) the deep-lying arteries, the authors speak of, are probably not even part of the tone-controlled resistance vasculature [107].

As mentioned in the previous section, the inner arm area provides substantially lower s_{AC} values than the forehead. These results cannot be attributed to differences in the skin layers' thickness because the two sites feature a comparable anatomy (see Table 2). However, when looking at the density of papillary loops, the face has the highest counts [398]. Based on this fact, one could actually argue in favor of the Kamshilin theory. Interestingly, at the arm, solely the heating experiment elicited a significant change in the pulsation strength. Besides cutaneous vasodilation and sweating, hyperthermia generally causes the number of recruited skin capillaries to be elevated [26, 230]. With regards to the observed

7 Note: The stated relation 20 principally only holds if all parameter values were derived from the same vascular segment. The central PP, for example, should not be used for calculation because s_{AC}, in contrast, is a measure that carries information from a completely different vasculature (skin vessels). However, since in the laboratory experiments, the BP was obtained from the finger (see Section 3.3), it is believed that the corresponding PP values are peripheral enough to be considered for the formulated relation.

increase in s_{AC}, the latter characteristic represents another argument for the Kamshilin theory. A higher temperature would implicate more activated capillaries to periodically move in and out of the measurement area (ROI) due to the alleged deformation process. Consequently, the pulsation strength in the extracted cbPPG signals would increase since a larger amount of blood is involved in the oscillation.

In conclusion, there is stronger evidence for the classic PPG theory to apply for cbPPG as well. However, it cannot be ruled out completely that the theory by Kamshilin et al. also pertains to some extent in certain scenarios, e.g. when shorter light wavelengths are used or when specific skin sites are considered.

CHAPTER SUMMARY

In this chapter, it was shown how cbPPG can be applied to capture the activity of the ANS when stimulated. Three established (psycho-)physiological tests were performed with the purpose of evoking quantifiable responses in the skin vasculature. The results proved that changes in the vasomotor tone, i.e. vasodilation and vasoconstriction, reflect in the pulsation strength of the cbPPG signals. Furthermore, the outcome allowed to shed more light on the signals' origin. The characteristical relationship between s_{AC}, the tone, and the PP led to the conclusion that the classic PPG theory most likely pertains to cbPPG as well. Solely some peculiarities, which occurred in the analysis of the forearm videos, rather support the alternative deformation theory by Kamshilin. In summary, the presented findings do not only open up new application fields for cbPPG but also provide a deeper understanding of the measurement technique.

7

CONCLUSION

7.1 SUMMARY

In this thesis, four major topics in the field of cbPPG were addressed: (i) Technical setup, (ii) ROI selection, (iii) applications, and (iv) signal origin. The main findings and conclusions of the work are summarized in the following paragraphs.

Technical Setup

In Chapter 3, a novel measuring system for cbPPG was introduced. The system features a mobile construction, a medical computer, a power supply unit, two cameras, and an NIR illumination source. It allows video recordings in the visible and non-visible light range to be obtained. Numerous interfaces moreover enable the synchronization of those recordings with data streams from patient monitors or other devices. In the course of three large studies conducted in clinical and laboratory environments, the system's great flexibility, autonomy, user-friendliness, and integrability could be successfully proven. Over 76 hours of video data from 133 volunteers was derived with the setup and evaluated afterwards. Future work should attempt to include preprocessing units into the system so that online analyses can be performed.

In Chapter 4, it was investigated what value optical polarization filtration adds to cbPPG. Different filter settings were compared for different lighting configurations. The results proved that in case of orthogonal illumination, a perpendicular filter alignment leads to a significant increase in signal quality for the blue and green wavelength range. In case of non-orthogonal illumination, the impact of polarization filtration was smaller. This outcome could be associated with a stronger BCG interference. The cbPPG's response to specific polarizer and light settings is potentially a useful marker to identify and rate BCG effects.

ROI Selection

In Chapter 5, a novel and fully automated ROI selection method, which utilizes level set segmentation to minimize the influence of BCG artifacts, was proposed. The method overcomes the drawbacks of previous approaches as it (i) does not rely on the detectability

of anatomical features, (ii) chooses and tracks visible skin regions which are homogeneously illuminated, and (iii) solely operates on the image plane without being dependent on the presence of temporal variations related to the cardiac cycle. Furthermore, it is able to deal with multispectral video recordings from different cameras. Three challenging data sets with more than 152 hours of video were used to evaluate the method's performance. It was shown that proper ROIs could be determined reliably throughout the videos. Moreover, they were found to be well-suited for the extraction of high-quality cbPPG signals. Future work should attempt to implement a real-time capable version of the method and integrate it into the software unit of the aforementioned measuring system.

Application Fields

In Chapter 6, it was demonstrated how cbPPG can be applied to capture the activity of the ANS when stimulated. Three established (psycho-)physiological tests were performed with the purpose of evoking quantifiable responses in the skin vasculature. The results proved that changes in the vasomotor tone, i.e. vasodilation and vasoconstriction, reflect in the pulsation strength of the cbPPG signals. However, substantial differences were found between the arm and forehead measurements. Prospective studies with larger test groups will be necessary to reveal how regional characteristics affect the cbPPG's outcome.

Due to the new and easy-to-use measurement system, cbPPG could be successfully applied in clinical environments. Overall 70 patients in an intensive care unit and 41 patients in the course of surgery were recorded with the system and examined exclusively on the basis of the acquired video data. Despite the challenging recording conditions and the diseases, from which the patients suffered, the employed processing methods (Chapter 5) were able to reliably extract cbPPG signals and robustly determine the HR.

Throughout the work, the conducted analyses were not restricted to small and homogeneous test groups. In total, 161 participants were enrolled in five different studies. The cohort featured people of different ages, health states, genders, and skin tones. Measurements were not only carried out for controlled scenarios but also in realistic situations.

Signal Origin

The majority of the results in this thesis support the theory that cbPPG signals reflect blood volume changes which arise from pulsatile vessels in the cutaneous vasculature. There are three reasons why this conclusion can be drawn. First, the wavelength-dependent behavior of the signal's quality is in accordance with the absorption characteristic of hemoglobin (Chapter 4 and 5). Second, the pulsation strength is significantly higher when signal components from the skin surface are suppressed (Chapter 4). Third, triggered variations in the vasomotor tone affect cbPPG signals in a way as it is expected when blood volume changes are the defining modulation factor (Chapter 6).

However, certain peculiarities exist in the results which suggest that the deformation theory by Kamshilin et al. is correct. First, the pulsation strength in the blue wavelength

range appeared to be rather large (Chapter 4) although the possibility of blue light to interact with pulsatile vessels is generally low. Second, the signal quality at the forehead, which features a high density of papillary loops, is considerably better than at the forearm although the thickness of epidermal and dermal layers is similar at the two skin sites (Chapter 6). Third, cbPPG significantly responses to local heating but not to vasoconstriction at the arm indicating that the recruitment rate of capillaries might play a role.

The polarization experiment revealed how BCG effects influence the manifestation of cbPPG signals. For non-orthogonally illuminated and spatially heterogeneous ROIs, those effects proved to have a major impact. It could be shown, the higher the impact is, the lesser the signals alter within different wavelength ranges. The results furthermore suggest that specular reflection is a main contributor in the modulation process of the BCG signal component.

In conclusion, there is strong evidence for the classic PPG origin theory to also pertain to cbPPG. Nevertheless, an element of uncertainty remains. It cannot be completely ruled out that the deformation theory by Kamshilin et al. at least applies to some extent, e.g. in shorter wavelength ranges or for specific skin sites. The same holds for the influence of BCG effects. Even if spatially homogeneous ROIs are selected, depending on the location and illumination, BCG interference might still be considerably high.

7.2 OUTLOOK

This work paves the way for cbPPG to evolve into a reliable and widely accepted measuring technique. The accomplishments in the hardware and software fields, the findings with respect to the signal origin, and the newly established application scenarios represent important contributions. Those contributions open up the perspective of cbPPG to become part of everyday life situations. The benefit for these situations can be versatile. In the course of my research, three specific situations were investigated. In the following, a brief overview is given.

The first situation involved the cbPPG's application during sleep. The underlying idea was that the technique offers an easy way to monitor the quality of sleep without impairing the comfort of the subject. In this context, cbPPG also bears a high diagnostic value as disorders like apneas could be detected. In cooperation with the Institute of Robotics and Intelligent Systems at the ETH Zürich, a field study was conducted in the sleep laboratory of the university. A two-unit camera system was designed for this purpose. Each unit comprised an NIR camera and an NIR light source which operated in the wavelength range of 880 nm. Using the NIR range, the participants were not disturbed by the illumination. Both units were set up at the head of the bed, one in the left corner and one in the right corner. In doing so, the participants' face could always be recorded even if they were turned sideways. Figure 56 shows the setting. In the study, one subject was recorded over the course of a night. The evaluation proved that the heart and respiration rate could be continuously monitored with the system.

Figure 56: Camera-based measurement setup in the sleep laboratory: (1) Constructional framework, (2) Camera and NIR illumination at the left bed side, (3) Camera and NIR illumination at the right bed side, (4) Test bed, (5) Test subject. The application of cbPPG during sleep was investigated in cooperation with the Institute of Robotics and Intelligent Systems at the ETH Zürich.

The second everyday scenario, which was investigated in regard to the application of cbPPG, was driving. Here, the idea was that the technique can be employed to monitor the attention state and stress level of drivers in order to detect and prevent dangerous situations and, thus, increase the overall safety on roads. As for the bed environment, the subjects' comfort is not impaired by the technology. In cooperation with the Alps Electric Europe GmbH, an extensive study was carried out where a specific test car was equipped with a customized multi-camera system. The system comprised two separate units. Each unit consisted of a daylight camera, which operated in the green wavelength range of 525 nm, and an NIR camera with an NIR light source (for night vision), which operated in the range of 880 nm. The camera units were positioned on the dashboard in front of the driver. The respective image planes covered the subject's face and upper body. Figure 57 shows the whole setup. In the course of the study, participants were recorded while driving through the city, on rough roads and the highway. The tests proved that the camera-based HR can only be reliably estimated when light changes and movements are marginal.

The third everyday scenario, for which the cbPPG's application was investigated, concerned the home environment. Here, the underlying idea was that for older and morbid persons, the technique provides an easy way to monitor the health state without disturbing daily routines. Emergency situations could be detected instantly and automatically where no actions would be required on behalf of the affected subject. Within the pilot project "fast care – Kamerabasiertes Monitoring" (ref. 03ZZ0519C) funded by the Bundesminis-

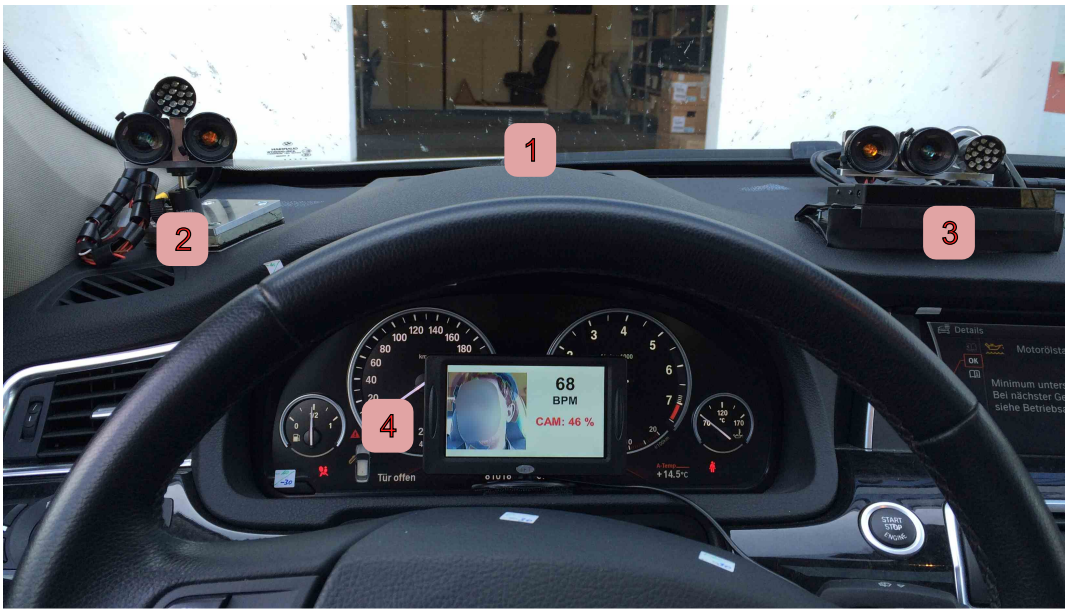

Figure 57: Camera-based measurement setup in the car environment: (1) Dashboard, (2) Daylight and NIR camera with illumination at the A-pillar, (3) Daylight and NIR camera with illumination at the dashboard's center, (4) Display for instant feedback on the HR measurement. The application of cbPPG in the car environment was investigated in cooperation with the Alps Electric Europe GmbH.

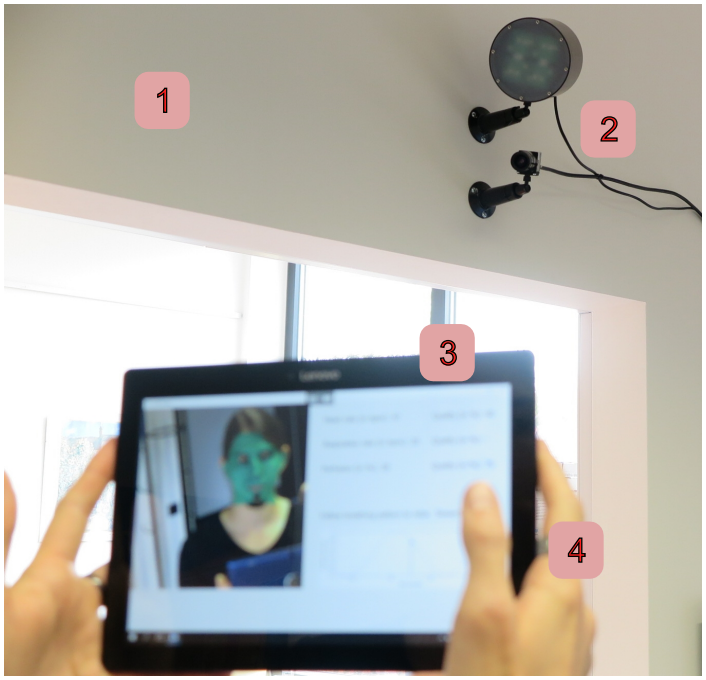

Figure 58: Camera-based measurement setup in the home environment: (1) Apartment wall, (2) RGB camera and light source, (3) Mobile display for instant feedback on the measurement, (4) User. The application of cbPPG in the home environment was investigated within the project "fast care – Kamerabasiertes Monitoring" (ref. 03ZZ0519C) that was funded by the Bundesministerium für Bildung und Forschung.

terium für Bildung und Forschung, a cbPPG system was installed in a small two-room apartment. The system consisted of two identical units of which each encompassed an RGB camera and a controllable RGB light source. The cameras were aligned in a manner that frequently used areas in the apartment were always under surveillance. In order to give users the opportunity to instantly check their vital functions with the system, mobile feedback displays were set up as well. Figure 58 shows the setting. In the course of an experimental study, several volunteers tested the whole setup over a longer period of time. It was found that cbPPG is well-suited to remotely monitor the HR, respiration, and perfusion in the home environment.

A

APPENDIX

A.1 PENETRATION DEPTH OF LIGHT INTO THE SKIN

Table 14: Penetration depth of light into the skin for different wavelengths and body sites. The depths correspond to the incident fluence rate decreasing to $1/e$ (37%) of its original value, and are calculated with the given scattering and absorption coefficients [27, 285, 325, 399] according to the formula presented in [274]. If possible, separate values for the epidermis and dermis were considered. Bashkatov et al. [27] summarized coefficient values of various authors; this data was used as a reference.

Wavelength	Forehead	Cheeks	Palm	Inner forearm
450 nm [325]	0.11 mm	0.11 mm	0.10 mm	0.13 mm
450 nm [285]	0.24 mm	0.23 mm	0.18 mm	0.25 mm
450 nm [27]*		0.7 mm		
450 nm [399]*		0.58 mm		
520/550 nm [325]	0.17/0.20 mm	0.16/0.19 mm	0.13/0.15 mm	0.19/0.22 mm
550 nm [285]	0.53 mm	0.52 mm	0.34 mm	0.54 mm
520 nm [27]*		0.9 mm		
520 nm [399]*		0.99 mm		
630 nm [325]	0.58 mm	0.56 mm	0.28 mm	0.61 mm
630 nm [285]	0.78 mm	0.77 mm	0.50 mm	0.79 mm
630 nm [27]*		1.8 mm		
630 nm [399]*		3.00 mm		
850 nm [285]	1.22 mm	1.21 mm	1.10 mm	1.23 mm
850 nm [27]*		2.4 mm		
850 nm [399]*		4.55 mm		

* No separate coefficients for the epidermis and dermis were given

A.2 RESULTS – POLARIZATION EXPERIMENT

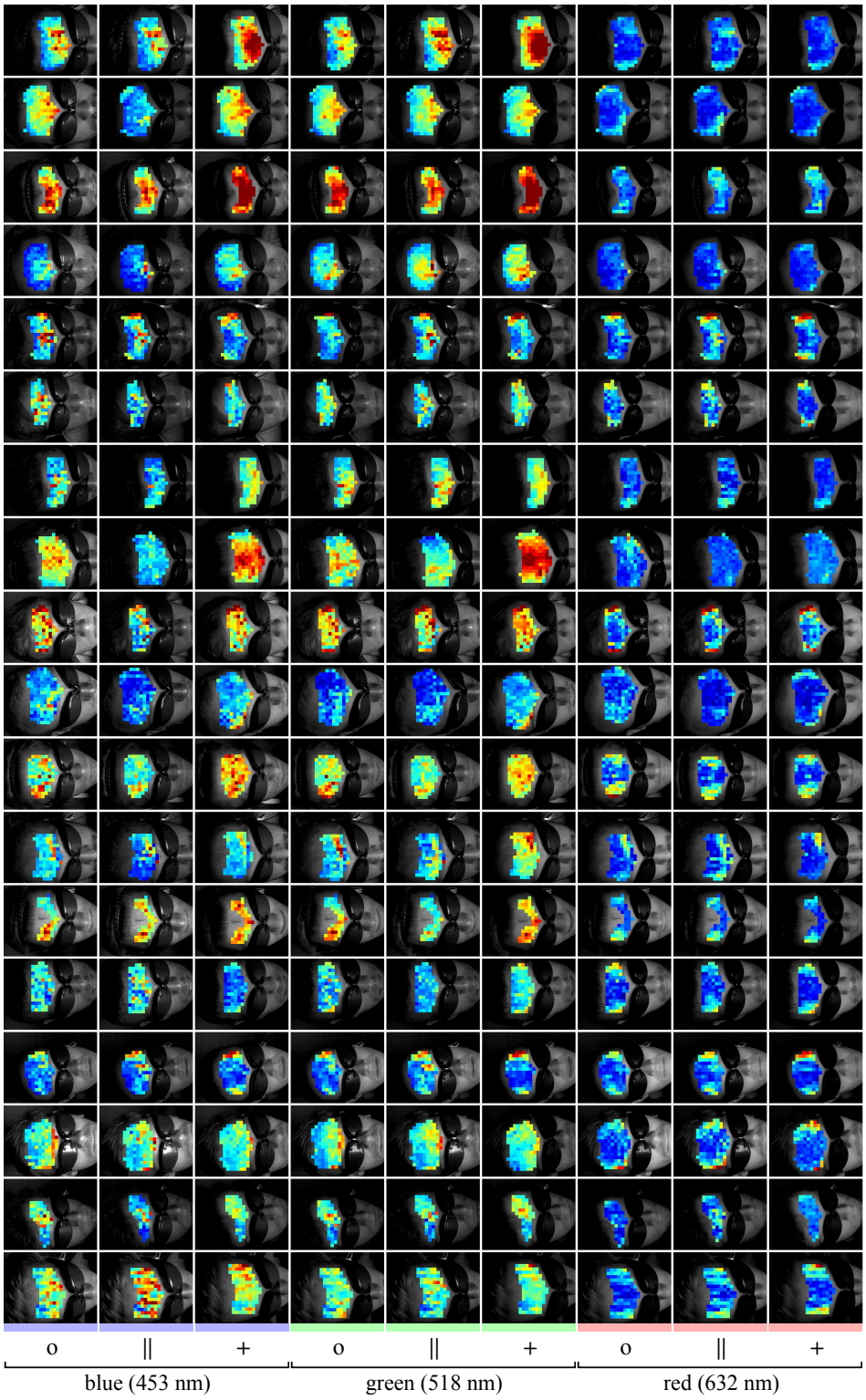

Figure 59: Depiction of the local pulsation strength s_{AC} for all 18 subjects. The respective values are false-color coded where blue refers to a low strength (minimum: $s_{AC} = 1$) and red to a high strength (maximum: $s_{AC} = 15$). The symbol 'o' represents the setting without polarization filters, '||' the parallel setting and '+' the perpendicular setting. The light configurations are illustrated by lines and are specified with their peak wavelengths.

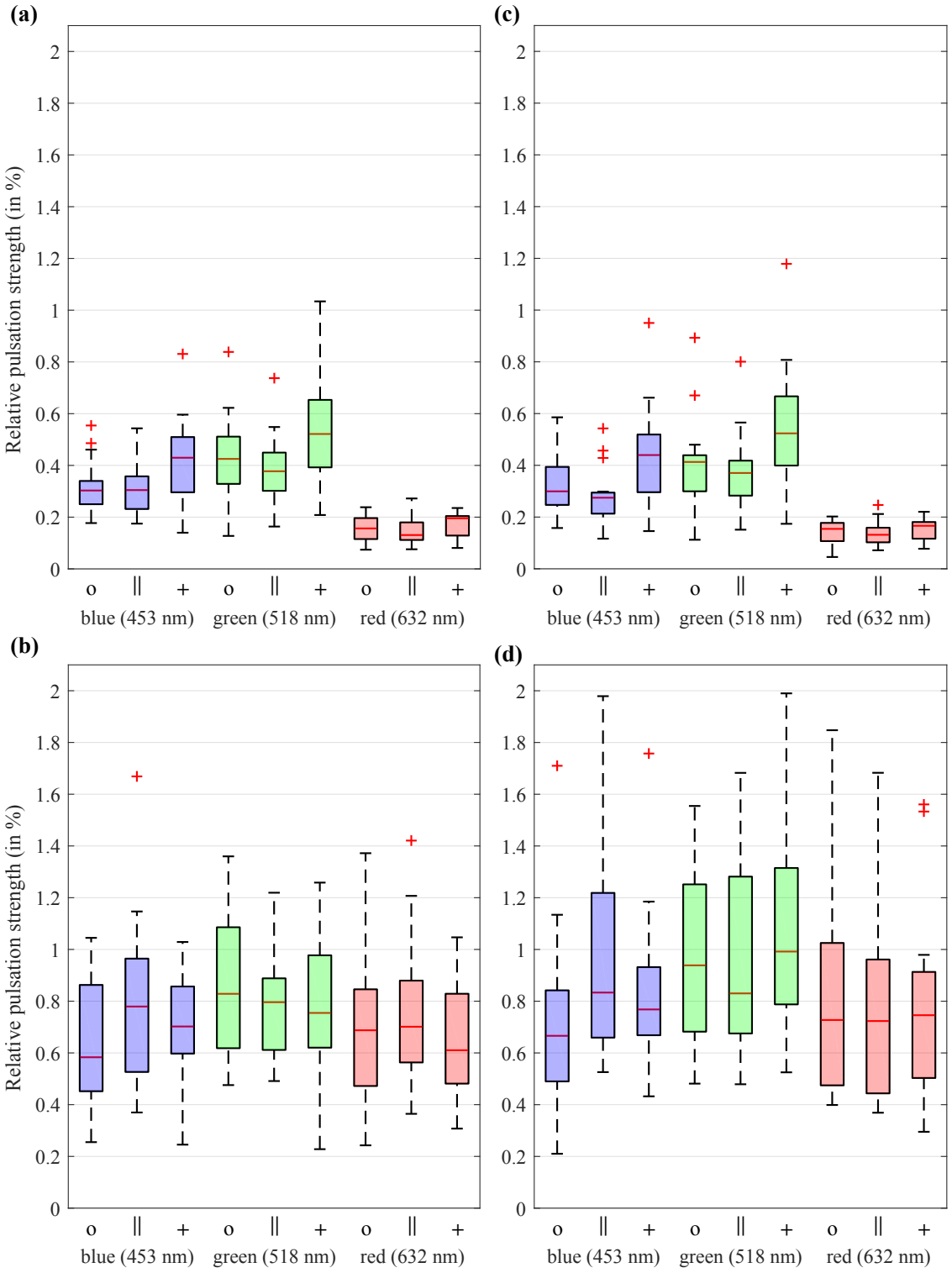

Figure 60: Boxplots of the relative pulsation strength values ($100\,\% \cdot s_{AC}/s_{DC}$) depicted for the different light color and filter settings: (a) Full forehead ROI, (b) Left ROI, (c) Center ROI, (d) Right ROI. The symbol 'o' represents the setting without polarization filters, '||' the parallel setting and '+' the perpendicular setting. The chosen color setting is represented by the boxes' coloration and are specified with their peak wavelengths. Note: The wavelength-dependent values are generally smaller than reported in other studies [120, 229]. This peculiarity occurs because the mean cbPPG beat was used for calculation which is attenuated in comparison to single beats (see Fig. 27).

A.3 RESULTS – NOVEL ROI SELECTION METHOD

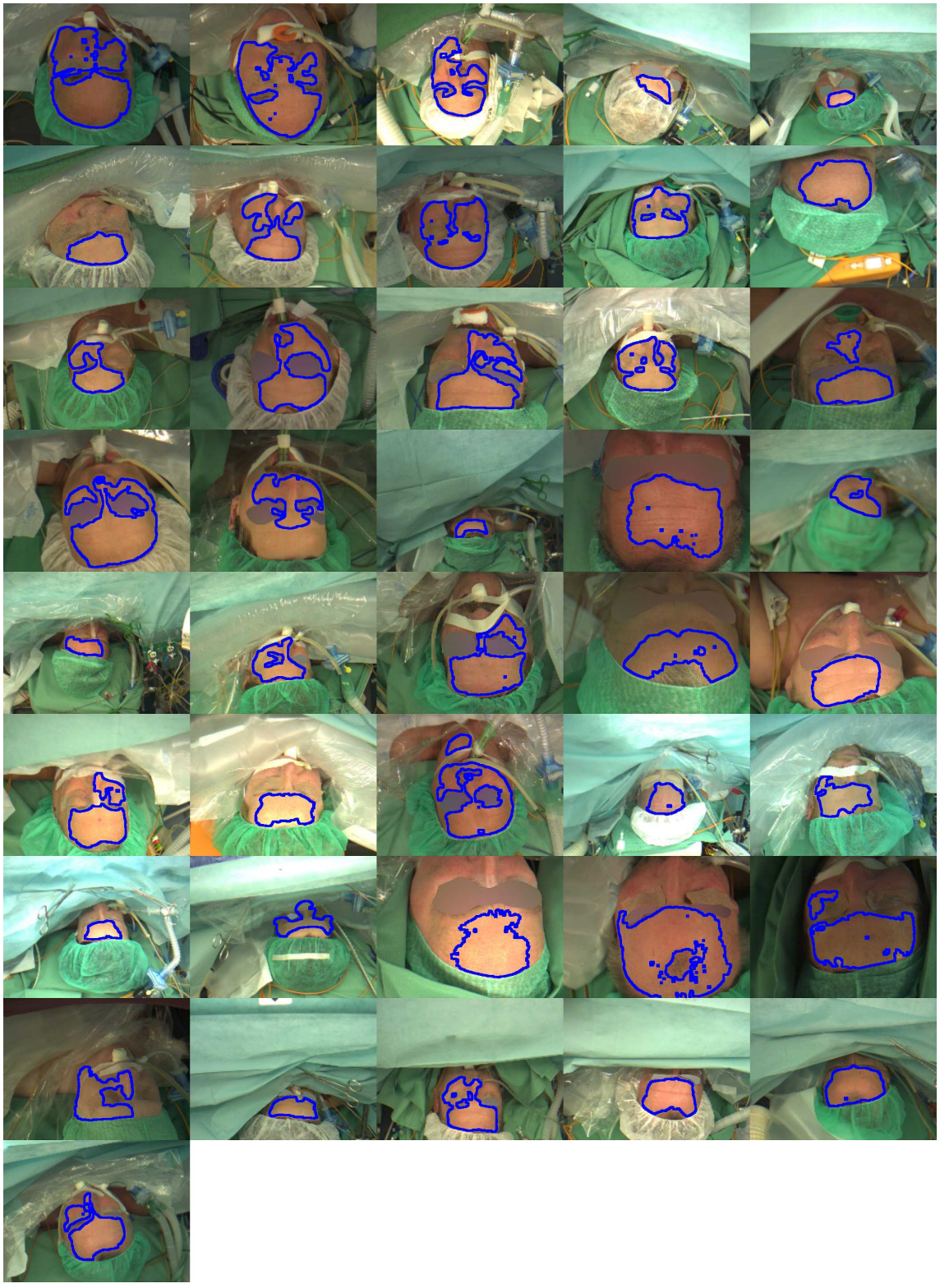

Figure 61: Selected ROIs for the RGB videos of the intraoperative study. The ROIs were determined using the proposed method in Chapter 5. For each patient, the images depict the ROI's contour for the first video frame. If a subject was identifiable, the eye section was blurred.

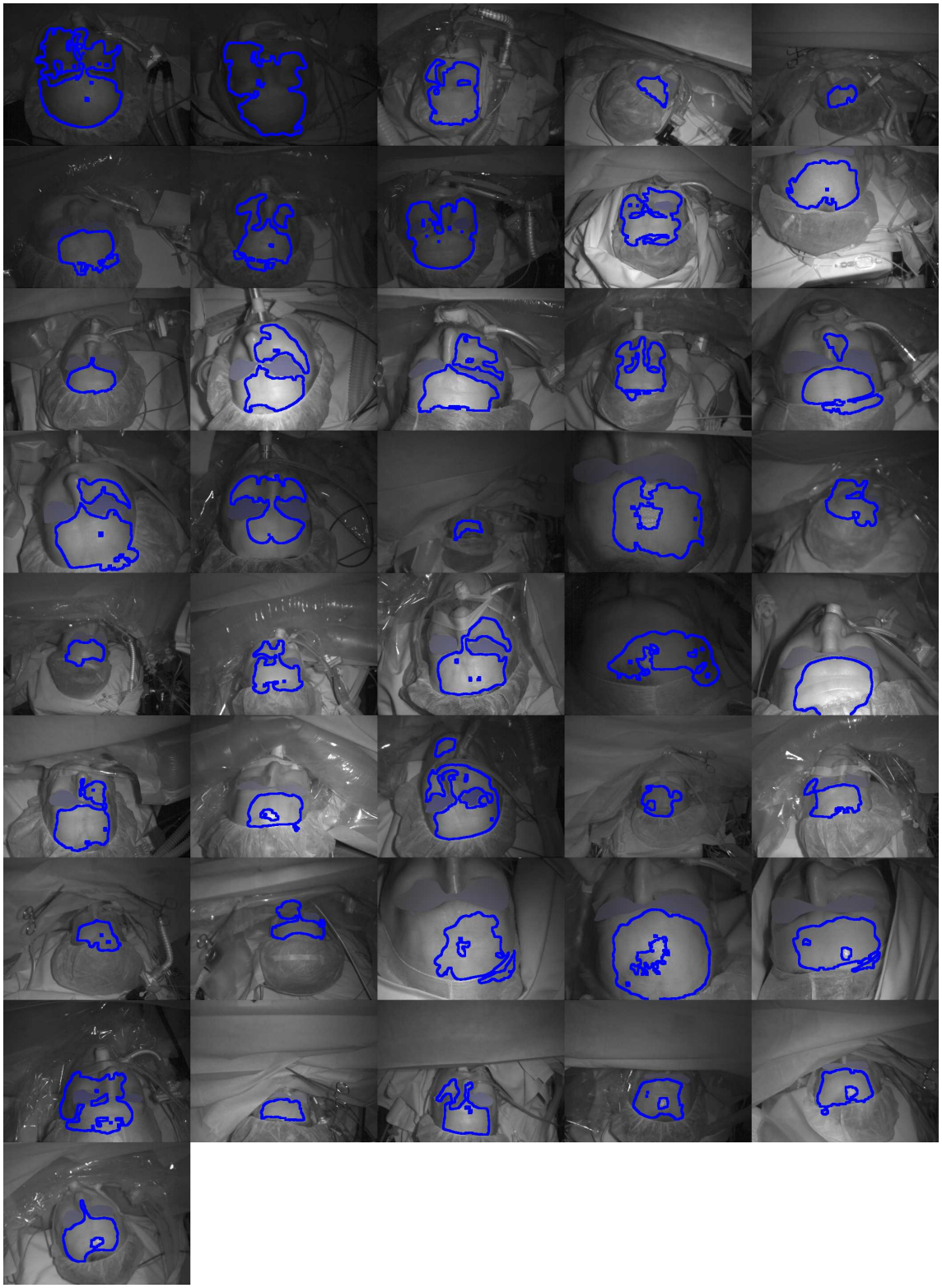

Figure 62: Selected ROIs for the NIR videos of the intraoperative study. The ROIs were determined using the proposed method in Chapter 5. For each patient, the images depict the ROI's contour for the first video frame. If a subject was identifiable, the eye section was blurred.

Figure 63: Selected ROIs for the RGB videos of the postoperative study. The ROIs were determined using the proposed method in Chapter 5. For each patient, the images depict the ROI's contour for the first video frame. Facial features were blurred to preserve anonymity.

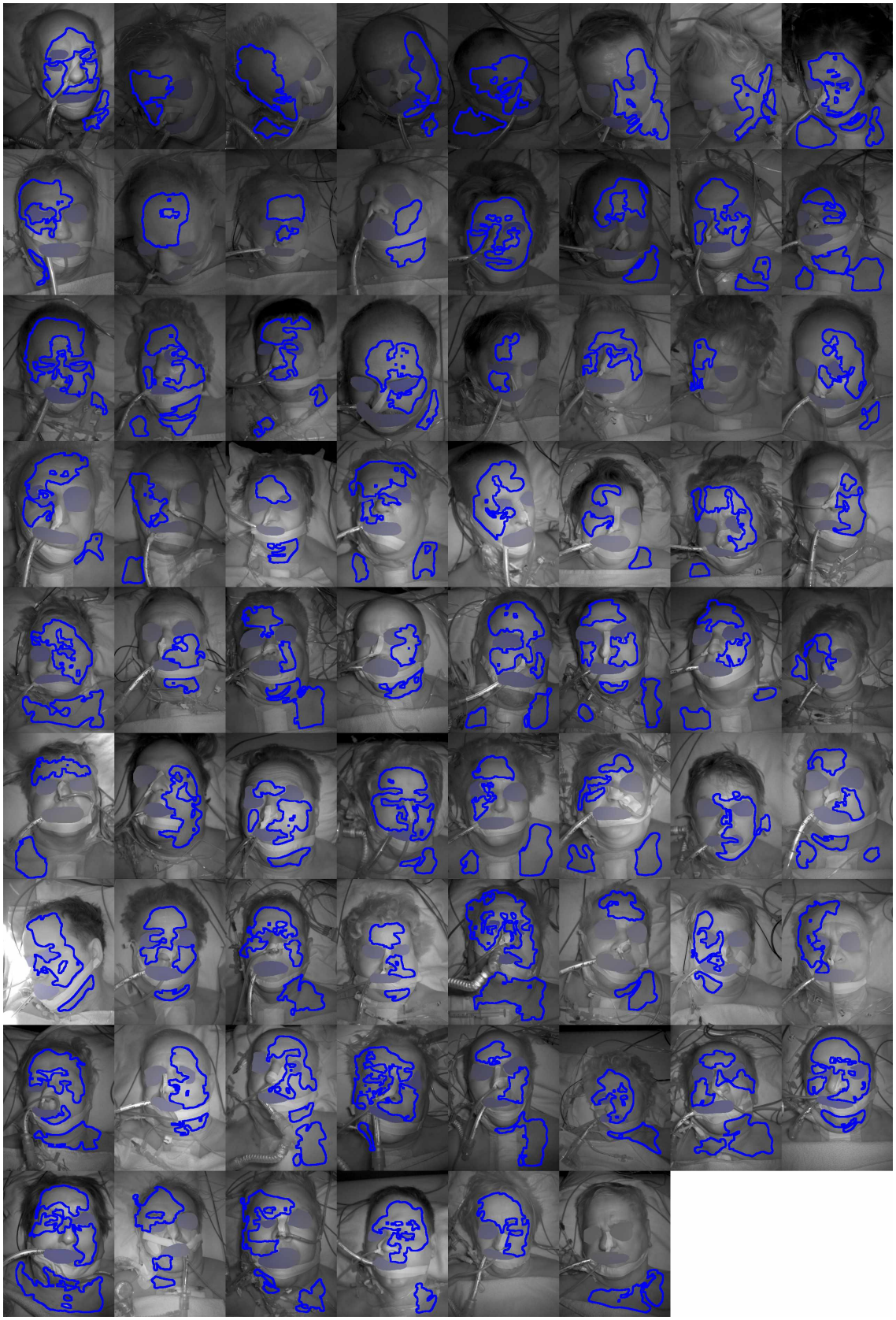

Figure 64: Selected ROIs for the NIR videos of the postoperative study. The ROIs were determined using the proposed method in Chapter 5. For each patient, the images depict the ROI's contour for the first video frame. Facial features were blurred to preserve anonymity.

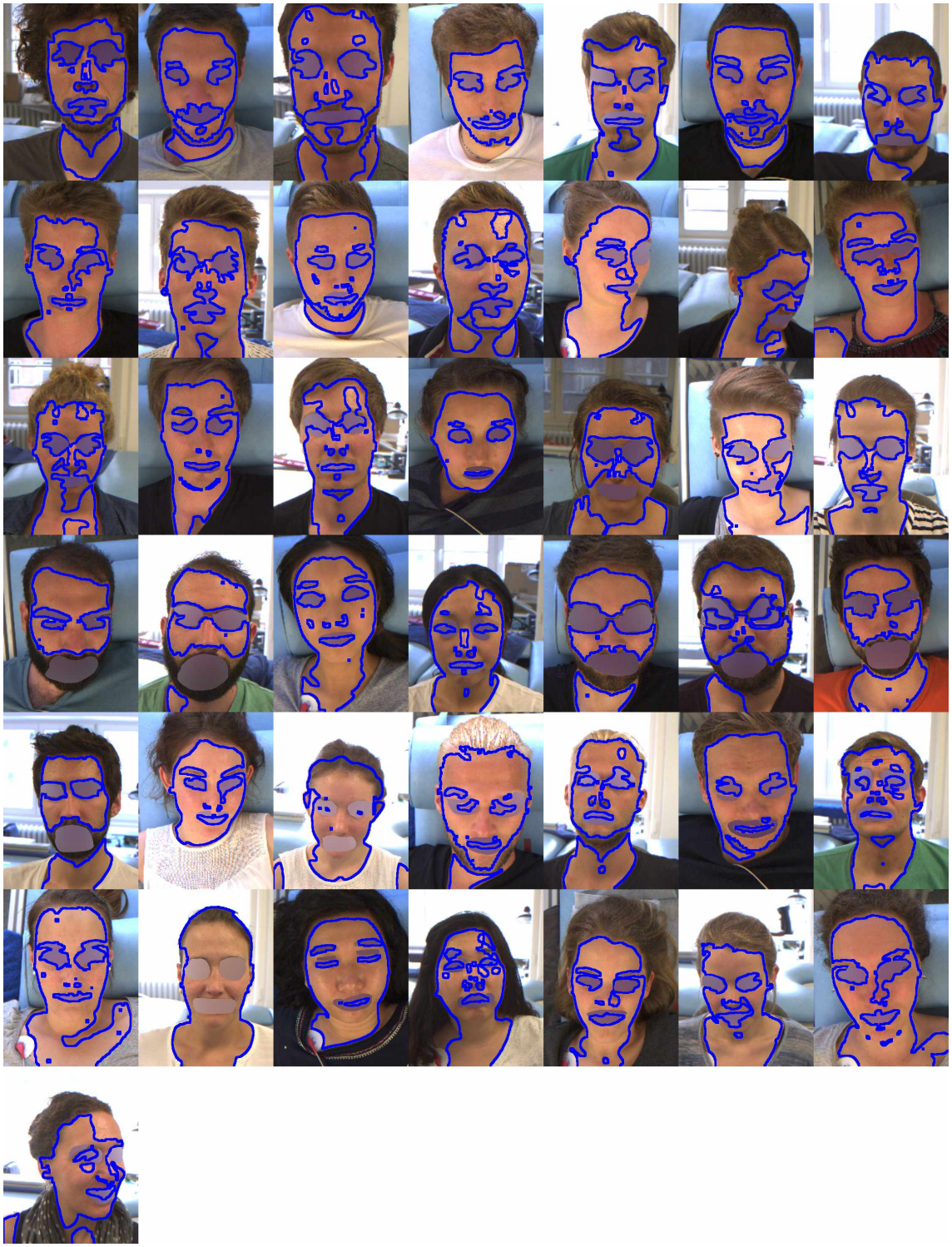

Figure 65: Selected ROIs for the RGB videos of the CPT study. The ROIs were determined using the proposed method in Chapter 5. For each participant, the images depict the ROI's contour for the first video frame. Facial features were blurred to preserve anonymity.

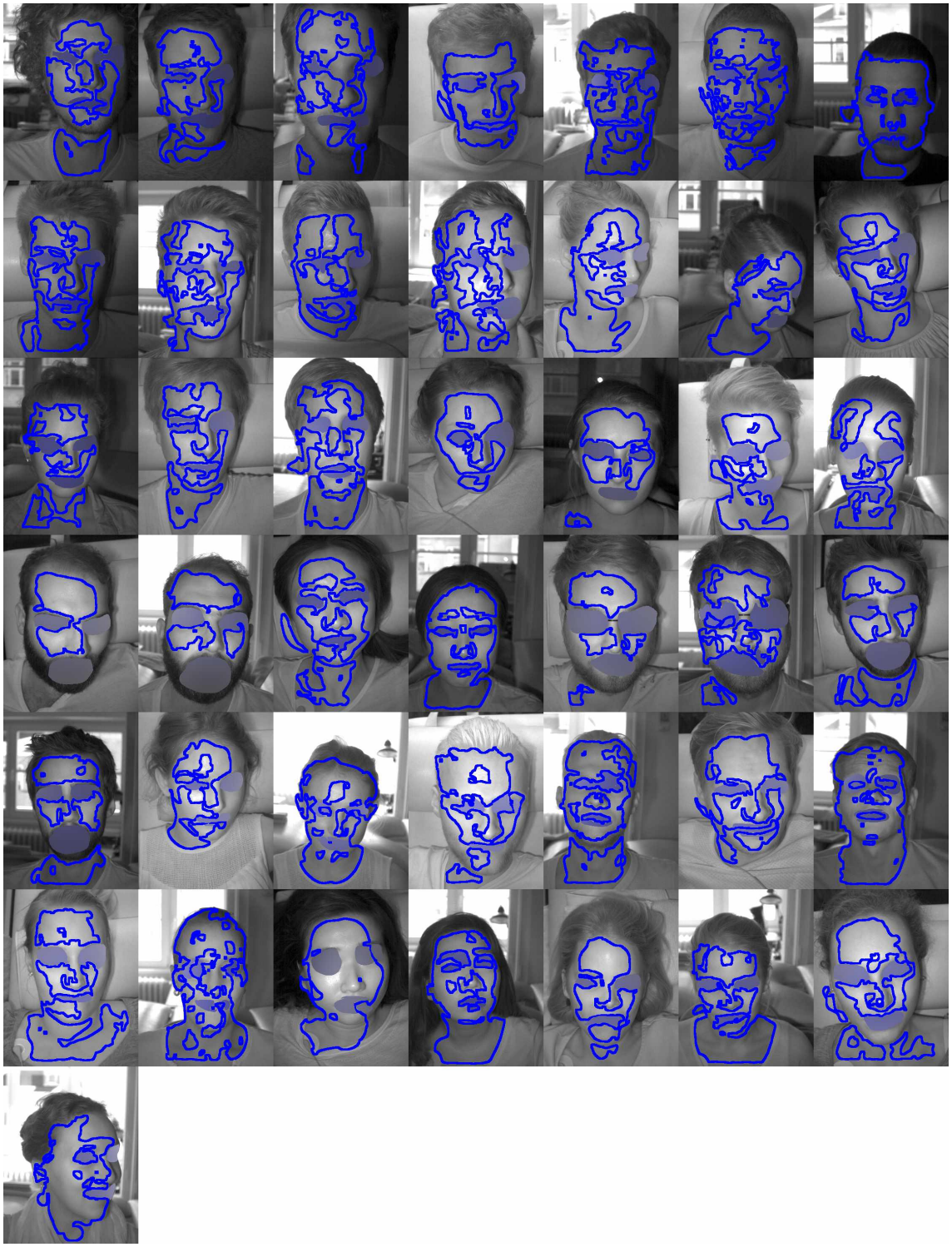

Figure 66: Selected ROIs for the NIR videos of the CPT study. The ROIs were determined using the proposed method in Chapter 5. For each participant, the images depict the ROI's contour for the first video frame. Facial features were blurred to preserve anonymity.

BIBLIOGRAPHY

[1] AZoOptics. *What is Unpolarized Light?* URL: https://www.azooptics.com/Article.aspx?ArticleID=755 (visited on 05/24/2018).

[2] L. A. M. Aarts, V. Jeanne, J. P. Cleary, et al. "Non-contact heart rate monitoring utilizing camera photoplethysmography in the neonatal intensive care unit - a pilot study." In: *Early human development* 89.12 (2013), pp. 943–948. DOI: 10.1016/j.earlhumdev.2013.09.016.

[3] P. S. Addison, D. Jacquel, D. M. H. Foo, and U. R. Borg. "Video-based heart rate monitoring across a range of skin pigmentations during an acute hypoxic challenge." In: *Journal of Clinical Monitoring and Computing* (2017), pp. 1–10. DOI: 10.1007/s10877-017-0076-1.

[4] T. Akata. "General Anesthetics and Vascular Smooth Muscle: Direct Actions of General Anesthetics on Cellular Mechanisms Regulating Vascular Tone." In: *Anesthesiology* 106.2 (2007), pp. 365–391.

[5] A. Al-Naji and J. Chahl. "Simultaneous Tracking of Cardiorespiratory Signals for Multiple Persons Using a Machine Vision System With Noise Artifact Removal." In: *IEEE Journal of Translational Engineering in Health and Medicine* 5 (2017), p. 1900510. DOI: 10.1109/JTEHM.2017.2757485.

[6] A. Al-Naji, A. G. Perera, and J. Chahl. "Remote monitoring of cardiorespiratory signals from a hovering unmanned aerial vehicle." In: *BioMedical Engineering OnLine* 16.101 (2017), pp. 1–20. DOI: 10.1186/s12938-017-0395-y.

[7] A. A. Alian and K. H. Shelley. "Photoplethysmography." In: *Best Practice & Research Clinical Anaesthesiology* 28.4 (2014), pp. 395–406. DOI: 10.1016/j.bpa.2014.08.006.

[8] J. Allen and A. Murray. "Variability of photoplethysmography peripheral pulse measurements at the ears, thumbs and toes." In: *IEE Proceedings - Science, Measurement and Technology* 147.6 (2000), pp. 403–407. DOI: 10.1088/0967-3334/21/3/303.

[9] J. Allen. "Photoplethysmography and its application in clinical physiological measurement." In: *Physiological measurement* 28.3 (2007), R1–39. DOI: 10.1088/0967-3334/28/3/R01.

[10] J. Allen and A. Murray. "Modelling the relationship between peripheral blood pressure and blood volume pulses using linear and neural network system identification techniques." In: *Physiological Measurement* 20.3 (1999), pp. 287–301. DOI: 10.1088/0967-3334/20/3/306.

[11] J. Allen and A. Murray. "Age-related changes in the characteristics of the photoplethysmographic pulse shape at various body sites." In: *Physiological Measurement* 24.2 (2003), pp. 297–307. DOI: 10.1088/0967-3334/24/2/306.

[12] J. L. Alonso-Cuevas and R. E. Sanchez-Yanez. "Simplified Heart Rate Measurement from Video." In: *Proceedings of the 3rd International Workshop on Interactive and Spatial Computing*. 2018, pp. 23–28. DOI: 10.1145/3191801.3191802.

[13] R. Amelard, D. A. Clausi, and A. Wong. "Spatial probabilistic pulsatility model for enhancing photoplethysmographic imaging systems." In: *Journal of Biomedical Optics* 21.11 (2016), pp. 116010–1–7. DOI: 10.1117/1.JBO.21.11.116010.

[14] R. Amelard, D. A. Clausi, and A. Wong. "Spectral-spatial fusion model for robust blood pulse waveform extraction in photoplethysmographic imaging." In: *Biomedical Optics Express* 7.12 (2016), pp. 4874–4885. DOI: 10.1364/BOE.7.004874.

[15] R. Amelard, C. Scharfenberger, F. Kazemzadeh, et al. "Non-contact transmittance photoplethysmographic imaging (PPGI) for long-distance cardiovascular monitoring." In: *arXiv.org* (2015), pp. 1–13. URL: https://arxiv.org/abs/1503.06775.

[16] R. Amelard, R. L. Hughson, D. K. Greaves, et al. "Non-contact hemodynamic imaging reveals the jugular venous pulse waveform." In: *arXiv.org* (2016). URL: http://arxiv.org/abs/1604.05213.

[17] R. Amelard, K. J. Pfisterer, S. Jagani, D. A. Clausi, and A. Wong. "Non-contact assessment of obstructive sleep apnea cardiovascular biomarkers using photoplethysmography imaging." In: *Proc. SPIE, Optical Diagnostics and Sensing XVIII: Toward Point-of-Care Diagnostics*. Vol. 10501. 2018, p. 1050113. DOI: 10.1117/12.2290672.

[18] American Heart Association. *Classes of Heart Failure*. URL: https://www.heart.org/en/health-topics/heart-failure/what-is-heart-failure/classes-of-heart-failure#.WssvRLO2F-0 (visited on 04/09/2018).

[19] R. R. Anderson. "Polarized Light Examination and Photography of the Skin." In: *Archives of Dermatology* 127.7 (1991), pp. 1000–5. DOI: 10.1001/archderm.1991.01680060074007.

[20] R. R. Anderson and J. A. Parrish. "The Optics of Human Skin." In: *Journal of Investigative Dermatology* 77.1 (1981), pp. 13–19. DOI: 10.1111/1523-1747.ep12479191.

[21] J. Ando, A. Kawarda, M. Shibata, K.-I. Yamakoshi, and A. Kamiya. "Pressure-volume relationships of finger arteries in healthy subjects and patients with coronary atherosclerosis measured non-invasively by photoelectric plethysmography." In: *Japanese circulation journal* 55.6 (1991), pp. 567–575. DOI: 10.1253/jcj.55.567.

[22] G. Aumüller, G. Aust, J. Engele, et al. *Anatomie*. 3rd ed. Georg Thieme Verlag, 2014. Chap. 1.3. ISBN: 978-3-13-136043-4.

[23] U. Bal. "Non-contact estimation of heart rate and oxygen saturation using ambient light." In: *Biomedical Optics Express* 6.1 (2015), p. 86. DOI: 10.1364/BOE.6.000086.

[24] G. Balakrishnan, F. Durand, and J. Guttag. "Detecting Pulse from Head Motions in Video." In: *IEEE Conference on Computer Vision and Pattern Recognition*. 2013, pp. 3430–3437. DOI: 10.1109/CVPR.2013.440.

[25] T. Baltrusaitis, P. Robinson, and L. P. Morency. "Constrained Local Neural Fields for Robust Facial Landmark Detection in the Wild." In: *Proceedings of the IEEE International Conference on Computer Vision Workshops, 300 Faces in-the-Wild Challenge*. 2013, pp. 354–361. DOI: 10.1109/ICCVW.2013.54.

[26] K. Barrett, H. Brooks, S. Boitano, and S. Barman. *Ganong's Review of Medical Physiology*. 23rd ed. New Delhi: McGraw Hill, 2010. Chap. 17, 18, 32, 33, 35. ISBN: 978-0-07-160568-7.

[27] A. N. Bashkatov, E. A. Genina, V. I. Kochubey, and V. V. Tuchin. "Optical properties of human skin, subcutaneous and mucous tissues in the wavelength range from 400 to 2000 nm." In: *Journal of Physics D: Applied Physics* 38.15 (2005), pp. 2543–2554. DOI: 10.1088/0022-3727/38/15/004.

[28] B. Baumann, S. O. Baumann, T. Konegger, et al. "Polarization sensitive optical coherence tomography of melanin provides intrinsic contrast based on depolarization." In: *Biomedical Optics Express* 3.7 (2012), pp. 1670–1683. DOI: 10.1364/BOE.3.001670.

[29] E. B. Blackford, A. M. Piasecki, and J. R. Estepp. "Measuring pulse rate variability using long-range, non-contact imaging photoplethysmography." In: *38th Annual International Conference of the IEEE Engineering in Medicine and Biology Society (EMBC)*. 2016, pp. 3930–3936. DOI: 10.1109/EMBC.2016.7591587.

[30] E. B. Blackford, J. R. Estepp, and D. J. McDuff. "Remote spectral measurements of the blood volume pulse with applications for imaging photoplethysmography." In: *Proc. SPIE, Optical Diagnostics and Sensing XVIII: Toward Point-of-Care Diagnostics*. Vol. 10501. 2018, 105010Z. DOI: 10.1117/12.2291073.

[31] N. Blanik, K. Heimann, C. Pereira, et al. "Remote vital parameter monitoring in neonatology – robust, unobtrusive heart rate detection in a realistic clinical scenario." In: *Biomedical Engineering / Biomedizinische Technik* 61.6 (2006), pp. 631–643. DOI: 10.1515/bmt-2016-0025.

[32] N. Blanik, C. Blazek, C. Pereira, V. Blazek, and S. Leonhardt. "Frequency-selective quantification of skin perfusion behavior during allergic testing using photoplethysmography imaging." In: *Proc. SPIE, Medical Imaging 2014: Image Processing*. Vol. 9034. 2014, pp. 1–6. DOI: 10.1117/12.2043567.

[33] S. Blankenberger and D. Vorberg. *Die Auswahl statistischer Tests und Maße*. URL: http://methodenlehre.sowi.uni-mainz.de/download/Lehre/SS2012/SemDA/Persike/Analysebaum.pdf (visited on 05/31/2018).

[34] V. Blazek. "Vorrichtung zur ortsaufgelösten, berührungslosen und funktionellen Visualisierung der dermalen Blutperfusion." Patent DE1,997,141,982 (DE). Oct. 1998.

[35] V. Blazek, T. Wu, and D. Hoelscher. "Near-infrared CCD imaging: possibilities for noninvasive and contactless 2D mapping of dermal venous hemodynamics." In: *Proc. SPIE, Optical Diagnostics of Biological Fluids*. Vol. 3923. 2000, pp. 2–9. DOI: 10.1117/12.387124.

[36] J. Bliedtner, H. Müller, and A. Barz. *Lasermaterialbearbeitung: Grundlagen - Verfahren - Anwendungen - Beispiele*. Taylor & Francis Group, 2013. Chap. 4.3. ISBN: 978-3-446-42168-4.

[37] T. Blöcher, J. Schneider, M. Schinle, and W. Stork. "An online PPGI approach for camera based heart rate monitoring using beat-to-beat detection." In: *IEEE Sensors Applications Symposium*. 2017, pp. 1–6. DOI: 10.1109/SAS.2017.7894052.

[38] S. Bobbia, D. Luguern, Y. Benezeth, et al. "Real-Time Temporal Superpixels for Unsupervised Remote Photoplethysmography." In: *Proceedings of the IEEE Conference on Computer Vision and Pattern Recognition (CVPR) Workshops*. 2018, pp. 1341–1348.

[39] F. Bousefsaf, C. Maaoui, and A. Pruski. "Peripheral vasomotor activity assessment using a continuous wavelet analysis on webcam photoplethysmographic signals." In: *Bio-Medical Materials and Engineering* 27.5 (2016), pp. 527–538. DOI: 10.3233/BME-161606.

[40] F. Bousefsaf, C. Maaoui, and A. Pruski. "Assessment of physiological parameters by non-contact means to quantify mental stress states." In: *AMSE Review* 75 (2014), pp. 19–30.

[41] F. Bousefsaf, C. Maaoui, and A. Pruski. "Continuous wavelet filtering on webcam photoplethysmographic signals to remotely assess the instantaneous heart rate." In: *Biomedical Signal Processing and Control* 8.6 (2013), pp. 568–574. DOI: 10.1016/j.bspc.2013.05.010.

[42] F. Bousefsaf, C. Maaoui, and A. Pruski. "Automatic Selection of Webcam Photoplethysmographic Pixels Based on Lightness Criteria." In: *Journal of Medical and Biological Engineering* 37.3 (2017), pp. 374–385. DOI: 10.1007/s40846-017-0229-1.

[43] I. M. Braverman. "Ultrastructure and organization of the cutaneous microvasculature in normal and pathologic states." In: *The Journal of investigative dermatology* 93.2 (1989), 2S–9S. DOI: 10.1111/1523-1747.ep12580893.

[44] I. M. Braverman. "The Cutaneous Microcirculation: Ultrastructure and Microanatomical Organization." In: *Microcirculation* 4.3 (1997), pp. 329–340. DOI: 10/bnqp2t.

[45] I. M. Braverman. "The Cutaneous Microcirculation." In: *Journal of Investigative Dermatology Symposium Proceedings* 5.1 (2000), pp. 3–9. DOI: 10.1046/j.1087-0024.2000.00010.x.

[46] I. M. Braverman and A. Keh-Yen. "Ultrastructure of the Human Dermal Microcirculation. III. The Vessels in the Mid- and Lower Dermis and Subcutaneous Fat." In: *Journal of Investigative Dermatology* 77.3 (1981), pp. 297–304. DOI: 10.1111/1523-1747.ep12482470.

[47] T. Brox and J. Weickert. "Level Set Segmentation With Multiple Regions." In: *IEEE Transactions on Image Processing* 15.10 (2006), pp. 3213–3218. DOI: 10.1109/TIP.2006.877481.

[48] T. Brox. "From Pixels to Regions: Partial Differential Equations in Image Analysis." PhD Thesis. Saarland University, 2005. Chap. 5.

[49] T. Brox, M. Rousson, R. Deriche, and J. Weickert. "Colour, texture, and motion in level set based segmentation and tracking." In: *Image and Vision Computing* 28.3 (2010), pp. 376–390. DOI: 10.1016/j.imavis.2009.06.009.

[50] A. C. Burton. "The range and variability of the blood flow in the human fingers and the vasomotor regulation of body temperature." In: *American Heart Journal* 127 (1939), pp. 437–453. DOI: 10.1016/S0002-8703(40)90361-1.

[51] A. C. Burton. "On the Physical Equilibrium of Small Blood Vessels." In: *American Journal of Physiology-Legacy Content* 164.2 (1951), pp. 319–329. DOI: 10.1152/ajplegacy.1951.164.2.319.

[52] M. J. Butler, J. A. Crowe, B. R. Hayes-Gill, and P. I. Rodmell. "Motion limitations of non-contact photoplethysmography due to the optical and topological properties of skin." In: *Physiological Measurement* 37.5 (2016), N27–37.

[53] CFCF. *File:2105 Capillary Bed.jpg*. Creative Commons Attribution 3.0 Unported (https://creativecommons.org/licenses/by/3.0/deed.en). URL: https://commons.wikimedia.org/wiki/File:2105_Capillary_Bed.jpg#/ (visited on 08/04/2017).

[54] CFCF. *File:2112 Vessel Blood Pressure Relationships.jpg*. Creative Commons Attribution 3.0 Unported (https://creativecommons.org/licenses/by/3.0/deed.en). URL: https://commons.wikimedia.org/wiki/File:2112_Vessel_Blood_Pressure_Relationships.jpg (visited on 02/07/2019).

[55] *Cardiac monitors, heart rate meters, and alarms*. American National Standard. ANSI/AAMI EC13:2002. Association for the Advancement of Medical Instrumentation, 2002.

[56] M. Carl, A. Alms, J. Braun, et al. "S3-Leitlinie zur intensivmedizinischen Versorgung herzchirurgischer Patienten." In: *Zeitschrift für Herz-,Thorax- und Gefäßchirurgie* 24.5 (2010), pp. 294–310. DOI: 10.1007/s00398-010-0790-1.

[57] A. V. J. Challoner. *Photoelectric plethysmograph, Noninvasive Physiological Measurements*. Ed. by P. Rolfe. London, Academic Press, 1979, pp. 125–151.

[58] T. F. Chan and L. A. Vese. "Active contours without edges." In: *IEEE Transactions on Image Processing* 10.2 (2001), pp. 266–277. DOI: 10.1109/83.902291.

[59] T. Chan and W. Zhu. "Level set based shape prior segmentation." In: *Proceedings of the IEEE Computer Society Conference on Computer Vision and Pattern Recognition*. Vol. 2. 2005, pp. 1164–1170. DOI: 10.1109/CVPR.2005.212.

[60] M. Chappell and S. Payne. *Physiology for Engineers: Applying Engineering Methods to Physiological Systems*. Biosystems & Biorobotics. Springer International Publishing, 2016. Chap. 7, 8, 10. DOI: 10.1007/978-3-319-26197-3.

[61] N. Charkoudian. "Skin Blood Flow in Adult Human Thermoregulation: How It Works, When It Does Not, and Why." In: *Mayo Clinic Proceedings* 78.5 (2011), pp. 603–612. DOI: 10.4065/78.5.603.

[62] X. Cheng, B. Yang, T. Olofsson, G. Liu, and H. Li. "A pilot study of online non-invasive measuring technology based on video magnification to determine skin temperature." In: *Building and Environment* 121 (2017), pp. 1–10. DOI: 10.1016/j.buildenv.2017.05.021.

[63] D. Cho and B. Lee. "Non-contact robust heart rate estimation using HSV color model and matrix-based IIR filter in the face video imaging." In: *38th Annual International Conference of the IEEE Engineering in Medicine and Biology Society (EMBC)*. 2016, pp. 3847–3850. DOI: 10.1109/EMBC.2016.7591567.

[64] J. Choe, D. Chung, A. J. Schwichtenberg, and E. J. Delp. "Improving video-based resting heart rate estimation: A comparison of two methods." In: *Proceedings of the IEEE 58th International Midwest Symposium on Circuits and Systems (MWSCAS)*. 2015, pp. 1–4. DOI: 10.1109/MWSCAS.2015.7282155.

[65] D. W. J. B. Christian Herrmann Jürgen Metzler. "Distant pulse oximetry based on skin region extraction and multi-spectral measurement." In: *Proc. SPIE, Medical Imaging 2018: Image-Guided Procedures, Robotic Interventions, and Modeling*. Vol. 10576. 2018, 105762O. DOI: 10.1117/12.2293623.

[66] E. D. Cooke, S. A. Bowcock, and A. Trevor Smith. "Photoplethysmography of the Distal Pulp in the Assessment of the Vasospastic Hand." In: *Angiology* 36.1 (1985), pp. 33–40. DOI: 10.1177/000331978503600106.

[67] F. Corral, G. Paez, and M. Strojnik. "A photoplethysmographic imaging system with supplementary capabilities." In: *Optica Applicata* XLIV.2 (2014), pp. 191–204. DOI: 10.5277/oa140202.

[68] J.-P. Couderc, S. Kyal, L. K. Mestha, et al. "Pulse Harmonic Strength of facial video signal for the detection of atrial fibrillation." In: *Computing in Cardiology 2014*. 2014, pp. 661–664.

[69] J.-P. Couderc, S. Kyal, L. K. Mestha, et al. “Detection of atrial fibrillation using contactless facial video monitoring.” In: *Heart Rhythm* 12.1 (2015), pp. 195–201. DOI: 10.1016/j.hrthm.2014.08.035.

[70] D. Cremers, M. Rousson, and R. Deriche. “A Review of Statistical Approaches to Level Set Segmentation: Integrating Color, Texture, Motion and Shape.” In: *International Journal of Computer Vision* 72.2 (2007), pp. 195–215. DOI: 10.1007/s11263-006-8711-1.

[71] W. Cui, L. E. Ostrander, and B. Y. Lee. “In vivo reflectance of blood and tissue as a function of light wavelength.” In: *IEEE Transactions on Biomedical Engineering* 37.6 (1990), pp. 632–639. DOI: 10.1109/10.55667.

[72] DATAPEC Medical Solutions. *ANDOK live - Das modulare Anästhesie-Dokumentationssystem*. URL: https://www.datapec.de/produkte/andoklive.html (visited on 04/09/2018).

[73] Y. Dancik, P. L. Bigliardi, and M. Bigliardi-Qi. “What happens in the skin? Integrating skin permeation kinetics into studies of developmental and reproductive toxicity following topical exposure.” In: *Reproductive Toxicology* 58 (2015), pp. 252–281. DOI: 10.1016/j.reprotox.2015.10.001.

[74] *Das Handbuch der Bildverarbeitung*. STEMMER IMAGING GmbH, 2012. Chap. 4. ISBN: 978-3-00-039674-8.

[75] S. G. Demos, A. J. Papadopoulos, H. Savage, et al. “Polarization Filter for Biomedical Tissue Optical Imaging.” In: *Photochemistry and Photobiology* 66.6 (1997), pp. 821–825. DOI: 10.1111/j.1751-1097.1997.tb03231.x.

[76] A. Dingli and A. Giordimaina. “Webcam-based detection of emotional states.” In: *The Visual Computer* 33.4 (2016), pp. 459–469. DOI: 10.1007/s00371-016-1309-x.

[77] R. O. Duda, P. E. Hart, and D. G. Stork. *Pattern classification*. 2nd ed. p. 91. New York: John Wiley & Sons, 2001. Chap. 3. ISBN: 0-471-05669-3.

[78] Edmund Optics. *Introduction to Polarization*. URL: https://www.edmundoptics.de/resources/application-notes/optics/introduction-to-polarization/ (visited on 05/24/2018).

[79] M. Elgendi. “On the Analysis of Fingertip Photoplethysmogram Signals.” In: *Current Cardiology Reviews* 8.1 (2012), pp. 14–25. DOI: 10.2174/157340312801215782.

[80] A. Elmer. “eHealth in Deutschland – Probleme, Projekte, Perspektiven.” In: *Magazin des Wissenschaftlichen Instituts der AOK* 16.3 (2016), pp. 7–13.

[81] J. R. E. Ethan B. Blackford. “Measurements of pulse rate using long-range imaging photoplethysmography and sunlight illumination outdoors.” In: *Proc. SPIE, Optical Diagnostics and Sensing XVII: Toward Point-of-Care Diagnostics*. Vol. 10072. 2017, 100720S–1–13. DOI: 10.1117/12.2253460.

[82] FLIR Machine Vision. *How to Evaluate Camera Sensitivity*. URL: https://www.ptgrey.com/support/downloads/10556 (visited on 12/15/2017).

[83] Q. Fan and K. Li. “Non-contact remote estimation of cardiovascular parameters.” In: *Biomedical Signal Processing and Control* 40 (2017), pp. 192–203. DOI: 10.1016/j.bspc.2017.09.022.

[84] Q. Fan and K. Li. “Noncontact Imaging Plethysmography for Accurate Estimation of Physiological Parameters.” In: *Journal of Medical and Biological Engineering* 37.5 (2017), pp. 675–685. DOI: 10.1007/s40846-017-0272-y.

[85] L. Feng, L. M. Po, X. Xu, and Y. Li. "Motion artifacts suppression for remote imaging photoplethysmography." In: *Proceedings of the 19th International Conference on Digital Signal Processing*. 2014, pp. 18–23. DOI: 10.1109/ICDSP.2014.6900813.

[86] L. Feng, L. M. Po, X. Xu, et al. "Dynamic ROI based on K-means for remote photoplethysmography." In: *Proceedings of the IEEE International Conference on Acoustics, Speech and Signal Processing (ICASSP)*. 2015, pp. 1310–1314. DOI: 10.1109/ICASSP.2015.7178182.

[87] T. B. Fitzpatrick. "Soleil et peau [Sun and skin]." In: *Journal de Médecine Esthétique* 2 (1975), pp. 33–34.

[88] T. B. Fitzpatrick. "The validity and practicality of sun-reactive skin types i through vi." In: *Archives of dermatology* 124.6 (1988), pp. 869–871.

[89] J. Y. A. Foo and S. J. Wilson. "A computational system to optimise noise rejection in photoplethysmography signals during motion or poor perfusion states." In: *Medical and Biological Engineering and Computing* 44.1 (2006), pp. 140–145. DOI: 10.1007/s11517-005-0008-y.

[90] S. H. Fouladi, I. Balasingham, T. A. Ramstad, and K. Kansanen. "Accurate heart rate estimation from camera recording via MUSIC algorithm." In: *Proceedings of the 37th Annual International Conference of the IEEE Engineering in Medicine and Biology Society (EMBC)*. 2015, pp. 7454–7457. DOI: 10.1109/EMBC.2015.7320115.

[91] L. Frassineti, F. Giardini, A. Perrella, et al. "Evaluation of spatial distribution of skin blood flow using optical imaging." In: *Proceedings of the International Conference on Medical and Biological Engineering*. 2017, pp. 74–80. DOI: 10.1007/978-981-10-4166-2_12.

[92] M. Fukunishi, K. Kurita, S. Yamamoto, and N. Tsumura. "Non-contact video-based estimation of heart rate variability spectrogram from hemoglobin composition." In: *Artificial Life and Robotics* 22.4 (2017), pp. 457–463. DOI: 10.1007/s10015-017-0382-1.

[93] E. Gambi, A. Agostinelli, A. Belli, et al. "Heart Rate Detection Using Microsoft Kinect: Validation and Comparison to Wearable Devices." In: *Sensors* 17.8 (2017). DOI: 10.3390/s17081776.

[94] M. J. C. V. Gemert, S. L. Jacques, H. J. C. M. Sterenborg, and W. M. Star. "Skin optics." In: *IEEE Transactions on Biomedical Engineering* 36.12 (1989), pp. 1146–1154. DOI: 10.1109/10.42108.

[95] Georgia Highlands College. *The Nervous System: Organization and Tissue*. URL: http://www2.highlands.edu/academics/divisions/scipe/biology/faculty/harnden/2121/notes/nervous.htm (visited on 05/17/2017).

[96] T. Gerlinger. "Versorgung in ländlichen Regionen." In: *Public Health Forum* 19.1 (2015), pp. 13–14. DOI: 10.1016/j.phf.2010.12.012.

[97] G. Giannakakis, M. Pediaditis, D. Manousos, et al. "Stress and anxiety detection using facial cues from videos." In: *Biomedical Signal Processing and Control* 31 (2017), pp. 89–101. DOI: 10.1016/j.bspc.2016.06.020.

[98] J. Giltvedt, A. Sira, and P. Helme. "Pulsed multifrequency photoplethysmograph." In: *Medical and Biological Engineering and Computing* 22.3 (1984), pp. 212–215. DOI: 10.1007/BF02442745.

[99] L. Giovangrandi, O. T. Inan, R. M. Wiard, M. Etemadi, and G. T. A. Kovacs. "Ballistocardiography – A method worth revisiting." In: *Annual International Conference of the IEEE Engineering in Medicine and Biology Society*. 2011, pp. 4279–4282. DOI: 10.1109/IEMBS.2011.6091062.

[100] D. H. Goldstein. *Polarized Light*. 3rd ed. CRC Press, Taylor & Francis Group, 2011. Chap. 1. ISBN: 978-1-4398-3041-3.

[101] C. Gonzalez Viejo, S. Fuentes, D. D. Torrico, and F. R. Dunshea. "Non-Contact Heart Rate and Blood Pressure Estimations from Video Analysis and Machine Learning Modelling Applied to Food Sensory Responses: A Case Study for Chocolate." In: *Sensors* 18.6 (2018). 1802. DOI: 10.3390/s18061802.

[102] A. A. Goshtasby. *Image Registration - Principles, Tools and Methods*. London: Springer-Verlag, 2012. Chap. 1. DOI: 10.1007/978-1-4471-2458-0.

[103] W. Groner, J. W. Winkelman, A. G. Harris, et al. "Orthogonal polarization spectral imaging: A new method for study of the microcirculation." In: *Nature Medicine* 5.10 (1999), pp. 1209–1212. DOI: 10.1038/13529.

[104] A. R. Guazzi, M. Villarroel, J. Jorge, et al. "Non-contact measurement of oxygen saturation with an RGB camera." In: *Biomedical Optics Express* 6.9 (2015), pp. 3320–3338. DOI: 10.1364/BOE.6.003320.

[105] O. Gupta, D. McDuff, and R. Raskar. "Real-Time Physiological Measurement and Visualization Using a Synchronized Multi-camera System." In: *Proceedings of the IEEE Conference on Computer Vision and Pattern Recognition Workshops (CVPRW)*. 2016, pp. 312–319. DOI: 10.1109/CVPRW.2016.46.

[106] P. Gupta, B. Bhowmick, and A. Pal. "Accurate heart-rate estimation from face videos using quality-based fusion." In: *Proceedings of the IEEE International Conference on Image Processing (ICIP)*, pp. 4132–4136. DOI: 10.1109/ICIP.2017.8297060.

[107] A. C. Guyton and J. E. Hall. *Textbook of Medical Physiology*. 11th ed. Elsevier Saunders, 2006. Chap. 1, 15, 16, 18, 38, 45, 60, 73. ISBN: 0-7216-0240-1.

[108] J. B. Harness and D. Z. Marjanovic. "Low-frequency photoplethysmograph signals." In: *Clinical Physics and Physiological Measurement* 10.4 (1989), pp. 365–367. DOI: 10.1088/0143-0815/10/4/009.

[109] M. A. Hassan, A. S. Malik, D. Fofi, et al. "Heart rate estimation using facial video: A review." In: *Biomedical Signal Processing and Control* 38 (2017), pp. 346–360. DOI: 10.1016/j.bspc.2017.07.004.

[110] M. A. Hassan, A. S. Malik, D. Fofi, N. Saad, and F. Meriaudeau. "Novel health monitoring method using an RGB camera." In: *Biomedical Optics Express* 8.11 (2017), pp. 4838–4854. DOI: 10.1364/BOE.8.004838.

[111] M. E. Heath and J. A. Downey. "The cold face test (diving reflex) in clinical autonomic assessment: methodological considerations and repeatability of responses." In: *Clinical Science* 78.2 (1990), pp. 139–147. DOI: 10.1042/cs0780139.

[112] J. Hernandez-Ortega, J. Fierrez, A. Morales, and P. Tome. "Time Analysis of Pulse-Based Face Anti-Spoofing in Visible and NIR." In: *The IEEE Conference on Computer Vision and Pattern Recognition (CVPR) Workshops*. 2018, pp. 544–552.

[113] A. B. Hertzman. "Photoelectric Plethysmography of the Fingers and Toes in Man." In: *Experimental Biology and Medicine* 37.3 (1937), pp. 529–534. DOI: 10.3181/00379727-37-9630.

[114] E. A. Hines and G. E. Brown. "The cold pressor test for measuring the reactibility of the blood pressure: Data concerning 571 normal and hypertensive subjects." In: *American Heart Journal* 11.1 (1936), pp. 1–9. DOI: 10.1016/S0002-8703(36)90370-8.

[115] E. Hjelmås and B. K. Low. "Face Detection: A Survey." In: *Computer Vision and Image Understanding* 83.3 (2001), pp. 236–274. DOI: 10.1006/cviu.2001.0921.

[116] B. D. Holton, K. Mannapperuma, P. J. Lesniewski, and J. C. Thomas. "Signal recovery in imaging photoplethysmography." In: *Physiological Measurement* 34.11 (2013), pp. 1499–1511.

[117] G. S. Hsu, A. Ambikapathi, and M. S. Chen. "Deep learning with time-frequency representation for pulse estimation from facial videos." In: *Proceesings of the IEEE International Joint Conference on Biometrics (IJCB)*. 2017, pp. 383–389. DOI: 10.1109/BTAS.2017.8272721.

[118] Y. Hsu, Y. L. Lin, and W. Hsu. "Learning-based heart rate detection from remote photoplethysmography features." In: *IEEE International Conference on Acoustics, Speech and Signal Processing*. 2014, pp. 4433–4437. DOI: 10.1109/ICASSP.2014.6854440.

[119] S. Hu, J. Zheng, V. Chouliaras, and R. Summers. "Feasibility of Imaging Photoplethysmography." In: *International Conference on BioMedical Engineering and Informatics*. Vol. 2. 2008, pp. 72–75. DOI: 10.1109/BMEI.2008.365.

[120] M. Hülsbusch. "Ein bildgestütztes, funktionelles Verfahren zur optoelektronischen Erfassung der Hautperfusion." Dissertation. RWTH Aachen, 2008. Chap. 2,3,4,6.

[121] K. Humphreys, T. Ward, and C. Markham. "A CMOS Camera-Based Pulse Oximetry Imaging System." In: *IEEE Engineering in Medicine and Biology 27th Annual Conference*. 2005, pp. 3494–3497. DOI: 10.1109/IEMBS.2005.1617232.

[122] K. Humphreys, C. Markham, and T. E. Ward. "A CMOS camera-based system for clinical photoplethysmographic applications." In: *Proc. SPIE, Opto-Ireland 2005: Imaging and Vision*. Vol. 5823. 2005, pp. 88–95. DOI: 10.1117/12.604822.

[123] K. Humphreys, T. Ward, and C. Markham. "Noncontact simultaneous dual wavelength photoplethysmography: A further step toward noncontact pulse oximetry." In: *Review of Scientific Instruments* 78.4 (2007), p. 044304. DOI: 10.1063/1.2724789.

[124] J. Huppelsberg and K. Walter. *Kurzlehrbuch Physiologie*. 3rd ed. Georg Thieme Verlag KG, 2009. Chap. 2, 4, 14, 32. ISBN: 978-3-13-136433-3.

[125] H. T. Hytti. "Characterization of digital image noise properties based on RAW data." In: *Proc. SPIE, Image Quality and System Performance III*. Vol. 6059. 2006, 60590A–1–12. DOI: 10.1117/12.640500.

[126] IDS Imaging Development Systems GmbH. *UI-3370CP-C-HQ*. (The right of use for the images was obtained). URL: http://www.physimetrics.com/content/PDF_Content/Cameras/IDS/UI-3370CP-C-HQ(1).pdf (visited on 03/21/2018).

[127] IDS Imaging Development Systems GmbH. *UI-3370CP-NIR-GL*. (The right of use for the images was obtained). URL: http://www.physimetrics.com/content/PDF_Content/Cameras/IDS/UI-3370CP-NIR-GL(1).pdf (visited on 03/21/2018).

[128] IDS Imaging Development Systems GmbH. *User Manual uEye Cameras*. Chapter 6, 9. URL: https://www.1stvision.com/cameras/IDS/dataman/uEye_User_Manual.pdf (visited on 03/23/2018).

[129] P. A. Iaizzo (Ed.) *Handbook of Cardiac Anatomy, Physiology, and Devices*. 2nd ed. Springer Science & Business Media, 2009. Chap. 1. DOI: 10.1007/978-1-60327-372-5.

[130] B. P. Imholz, W. Wieling, G. A. van Montfrans, and K. H. Wesseling. "Fifteen years experience with finger arterial pressure monitoring:assessment of the technology." In: *Cardiovascular Research* 38.3 (1998), pp. 605–616. DOI: 10.1016/S0008-6363(98)00067-4.

[131] L. Iozzia, L. Cerina, and L. Mainardi. "Relationships between heart-rate variability and pulse-rate variability obtained from video-PPG signal using ZCA." In: *Physiological Measurement* 37.11 (2016), pp. 1934–1944. DOI: 10.1088/0967-3334/37/11/1934.

[132] S. L. Jacques, J. C. Ramella-Roman, and K. Lee. "Imaging skin pathology with polarized light." In: *Journal of Biomedical Optics* 7.3 (2002), pp. 329–340. DOI: 10.1117/1.1484498.

[133] S. L. Jacques, M. R. Ostermeyer, L. V. Wang, and D. V. Stephens. "Polarized light transmission through skin using video reflectometry: toward optical tomography of superficial tissue layers." In: *Proc. SPIE, Lasers in Surgery: Advanced Characterization, Therapeutics, and Systems VI*. 1996, pp. 199–210. DOI: 10.1117/12.240009.

[134] M. Jain, S. Deb, and A. V. Subramanyam. "Face video based touchless blood pressure and heart rate estimation." In: *IEEE 18th International Workshop on Multimedia Signal Processing (MMSP)*. 2016, pp. 1–5. DOI: 10.1109/MMSP.2016.7813389.

[135] F. Jazizadeh and W. Jung. "Personalized thermal comfort inference using RGB video images for distributed HVAC control." In: *Applied Energy* 220 (2018), pp. 829–841. DOI: 10.1016/j.apenergy.2018.02.049.

[136] I. C. Jeong and J. Finkelstein. "Introducing contactless assessment of heart rate variability using high speed video camera." In: *36th IEEE Sarnoff Symposium*. 2015, pp. 7–11. DOI: 10.1109/SARNOF.2015.7324634.

[137] I. C. Jeong and J. Finkelstein. "Introducing Contactless Blood Pressure Assessment Using a High Speed Video Camera." In: *Journal of Medical Systems* 40.4 (2016), p. 77. DOI: 10.1007/s10916-016-0439-z.

[138] A. Johansson, P. Å. Öberg, and G. Sedin. "Monitoring of Heart and Respiratory Rates in Newborn Infants Using a New Photoplethysmographic Technique." In: *Journal of Clinical Monitoring and Computing* 15.7 (1999), pp. 461–467. DOI: 10.1023/A:1009912831366.

[139] J. M. Johnson and D. L. Kellogg. "Local thermal control of the human cutaneous circulation." In: *Journal of Applied Physiology* 109.4 (2010), pp. 1229–1238. DOI: 10.1152/japplphysiol.00407.2010.

[140] M. J. Jones and J. M. Rehg. "Statistical color models with application to skin detection." In: *Proceedings of the IEEE Computer Society Conference on Computer Vision and Pattern Recognition*. Vol. 1. 1999, pp. 274–280. DOI: 10.1109/CVPR.1999.786951.

[141] M. J. Jones and J. M. Rehg. "Statistical Color Models with Application to Skin Detection." In: *International Journal of Computer Vision* 46.1 (2002), pp. 81–96. DOI: 10.1023/A:1013200319198.

[142] J. Jorge, M. Villarroel, S. Chaichulee, et al. “Non-Contact Monitoring of Respiration in the Neonatal Intensive Care Unit.” In: *12th IEEE International Conference on Automatic Face Gesture Recognition*. 2017, pp. 286–293. DOI: 10.1109/FG.2017.44.

[143] P. Kakumanu, S. Makrogiannis, and N. Bourbakis. “A survey of skin-color modeling and detection methods.” In: *Pattern Recognition* 40.3 (2007), pp. 1106 –1122. ISSN: 0031-3203. DOI: https://doi.org/10.1016/j.patcog.2006.06.010. URL: http://www.sciencedirect.com/science/article/pii/S0031320306002767.

[144] A. A. R. Kamal, J. B. Harness, G. Irving, and A. J. Mearns. “Skin photoplethysmography - a review.” In: *Computer Methods and Programs in Biomedicine* 28.4 (1989), pp. 257–269. DOI: 10.1016/0169-2607(89)90159-4.

[145] A. A. Kamshilin and N. B. Margaryants. “Origin of Photoplethysmographic Waveform at Green Light.” In: *International Conference on Photonics of Nano- and Bio-Structure*. Vol. 86. 2017, pp. 72–80. DOI: 10.1016/j.phpro.2017.01.024.

[146] A. A. Kamshilin, V. V. Zaytsev, and O. V. Mamontov. “Novel contactless approach for assessment of venous occlusion plethysmography by video recordings at the green illumination.” In: *Scientific Reports* 7.1 (2017), p. 464. DOI: 10.1038/s41598-017-00552-7.

[147] A. A. Kamshilin, S. Miridonov, V. Teplov, R. Saarenheimo, and E. Nippolainen. “Photoplethysmographic imaging of high spatial resolution.” In: *Biomedical Optics Express* 2.4 (2011), pp. 996–1006. DOI: 10.1364/BOE.2.000996.

[148] A. A. Kamshilin, V. Teplov, E. Nippolainen, S. Miridonov, and R. Giniatullin. “Variability of Microcirculation Detected by Blood Pulsation Imaging.” In: *PLoS ONE* 8.2 (2013), e57117. DOI: 10.1371/journal.pone.0057117.

[149] A. A. Kamshilin, E. Nippolainen, I. S. Sidorov, et al. “A new look at the essence of the imaging photoplethysmography.” In: *Scientific Reports* 5 (2015), p. 10494. DOI: 10.1038/srep10494.

[150] A. A. Kamshilin, I. S. Sidorov, L. Babayan, et al. “Accurate measurement of the pulse wave delay with imaging photoplethysmography.” In: *Biomedical Optics Express* 7.12 (2016), pp. 5138–5147. DOI: 10.1364/BOE.7.005138.

[151] H. Kashima, T. Ikemura, and N. Hayashi. “Regional differences in facial skin blood flow responses to the cold pressor and static handgrip tests.” In: *European Journal of Applied Physiology* 113.4 (2013), pp. 1035–1041. DOI: 10.1007/s00421-012-2522-6.

[152] B. Kaur, J. A. Hutchinson, and V. N. Ikonomidou. “Visible spectrum-based non-contact HRV and dPTT for stress detection.” In: *Proc. SPIE, Mobile Multimedia/Image Processing, Security, and Applications*. Vol. 10221. 2017, 102210E. DOI: 10.1117/12.2261085.

[153] J. F. Kelleher. “Pulse oximetry.” In: *Journal of Clinical Monitoring* 5.1 (1989), pp. 37–62. DOI: 10.1007/BF01618369.

[154] V. Kessler, M. Kächele, S. Meudt, F. Schwenker, and G. Palm. “Machine Learning Driven Heart Rate Detection with Camera Photoplethysmography in Time Domain.” In: *IAPR Workshop on Artificial Neural Networks in Pattern Recognition*. 2016, pp. 324–334. DOI: 10.1007/978-3-319-46182-3_27.

[155] F. Khan, V. A. Spence, and J. J. F. Belch. “Cutaneous vascular responses and thermoregulation in relation to age.” In: *Clinical Science* 82.5 (1992), pp. 521–528. DOI: 10.1042/cs0820521.

[156] R. K. Khurana. “Cold face test: adrenergic phase.” In: *Clinical Autonomic Research* 17.4 (2007), pp. 211–216. DOI: 10.1007/s10286-007-0422-3.

[157] Kingbright Electronic Co., Ltd. *LED Lamp Cluster BL0106-15-29*. URL: http://www.produktinfo.conrad.com/datenblaetter/125000-149999/149233-da-01-en-IR_Cluster_26mm_BL0106_15_29.pdf (visited on 03/23/2018).

[158] R. E. Klabunde. *Cardiovascular Physiology Concepts*. URL: https://www.cvphysiology.com/Blood%20Pressure/BP004 (visited on 11/05/2018).

[159] J. H. G. M. Klaessens, M. van den Born, A. van der Veen, et al. “Development of a baby friendly non-contact method for measuring vital signs: First results of clinical measurements in an open incubator at a neonatal intensive care unit.” In: *Proc. SPIE, Advanced Biomedical and Clinical Diagnostic Systems XII*. Vol. 8935. 2014, 89351P. DOI: 10.1117/12.2038353.

[160] R. Klinke, H.-C. Pape, and S. Silbernagl. *Physiology*. 5th ed. Georg Thieme Verlag KG, 2005. Chap. 7, 8, 15, 27. ISBN: 3-13-796005-3.

[161] P. A. J. Kolarsick, M. A. Kolarsick, and C. Goodwin. “Anatomy and Physiology of the Skin.” In: *Journal of the Dermatology Nurses’ Association* 3.4 (2011), pp. 203–213. DOI: 10.1097/JDN.0b013e3182274a98.

[162] L. Kong, Y. Zhao, L. Dong, et al. “Non-contact detection of oxygen saturation based on visible light imaging device using ambient light.” In: *Optics express* 21.15 (2013), pp. 17464–17471. DOI: 10.1364/OE.21.017464.

[163] R. Kramme (Ed.) *Medizintechnik*. 4th ed. Springer-Verlag Berlin Heidelberg New York, 2011. Chap. 38. ISBN: 978-3-642-16186-5.

[164] V. S. Kublanov and K. S. Purtov. “Researching the possibilities of remote photoplethysmography application to analysis of time-frequency changes of human heart rate variability.” In: *Proceedings of the International Conference on Biomedical Engineering and Computational Technologies (SIBIRCON)*. 2015, pp. 87–92. DOI: 10.1109/SIBIRCON.2015.7361857.

[165] V. Kublanov, K. Purtov, and D. Belkov. “Remote Photoplethysmography for the Neuroelectrostimulation Procedures Monitoring - The Possibilities of Remote Photoplethysmography Application for the Analysis of High Frequency Parameters of Heart Rate Variability.” In: *Proceedings of the 10th International Joint Conference on Biomedical Engineering Systems and Technologies*. 2017, pp. 307–314. DOI: 10.5220/0006176003070314.

[166] M. Kumar, J. Suliburk, A. Veeraraghavan, and A. Sabharwal. “PulseCam: High-resolution blood perfusion imaging using a camera and a pulse oximeter.” In: *38th Annual International Conference of the IEEE Engineering in Medicine and Biology Society (EMBC)*. 2016, pp. 3904–3909. DOI: 10.1109/EMBC.2016.7591581.

[167] M. Kumar, A. Veeraraghavan, and A. Sabharwal. “DistancePPG: Robust non-contact vital signs monitoring using a camera.” In: *Biomedical Optics Express* 6.5 (2015), pp. 1565–1588. DOI: 10.1364/BOE.6.001565.

[168] J. Kuo, S. Koppel, J. L. Charlton, and C. M. Rudin-Brown. “Evaluation of a video-based measure of driver heart rate.” In: *Journal of Safety Research* 54 (2015), pp. 55–59. DOI: 10.1016/j.jsr.2015.06.009.

[169] Y. Kurylyak, F. Lamonaca, and D. Grimaldi. "A Neural Network-based method for continuous blood pressure estimation from a PPG signal." In: *2013 IEEE International Instrumentation and Measurement Technology Conference (I2MTC)*. 2013, pp. 280–283. DOI: 10.1109/I2MTC.2013.6555424.

[170] K. Kvernebo, J. Megerman, G. Hamilton, and W. M. Abbott. "Response of skin photoplethysmography, laser Doppler flowmetry and transcutaneous oxygen tensiometry to stenosis-induced reductions in limb blood flow." In: *European Journal of Vascular Surgery* 3.2 (1989), pp. 113–120. DOI: 10.1016/S0950-821X(89)80005-2.

[171] S. Kwon, J. Kim, D. Lee, and K. Park. "ROI analysis for remote photoplethysmography on facial video." In: *Proceedings of the 37th Annual International Conference of the IEEE Engineering in Medicine and Biology Society*. 2015, pp. 4938–4941. DOI: 10.1109/EMBC.2015.7319499.

[172] P. A. Kyriacou. "Pulse oximetry in the oesophagus." In: *Physiological Measurement* 27.1 (2006), R1–R35. DOI: 10.1088/0967-3334/27/1/R01.

[173] N. N. Lakshminarayana, N. Narayan, N. Napp, S. Setlur, and V. Govindaraju. "A discriminative spatio-temporal mapping of face for liveness detection." In: *IEEE International Conference on Identity, Security and Behavior Analysis (ISBA)*. 2017, pp. 1–7. DOI: 10.1109/ISBA.2017.7947707.

[174] M. Landthaler and U. Hohenleutner. *Lasertherapie in der Dermatologie: Atlas und Lehrbuch*. 2nd ed. Springer Medizin Verlag, 2006. Chap. 3.

[175] G. J. Langewouters, K. H. Wesseling, and W. J. A. Goedhard. "The static elastic properties of 45 human thoracic and 20 abdominal aortas in vitro and the parameters of a new model." In: *Journal of Biomechanics* 17.6 (1984), pp. 425–435. DOI: 10.1016/0021-9290(84)90034-4.

[176] G. J. Langewouters, A. Zwart, R. Busse, and K. H. Wesseling. "Pressure-diameter relationships of segments of human finger arteries." In: *Clinical Physics and Physiological Measurement* 7.1 (1986), p. 43. DOI: 10.1088/0143-0815/7/1/003.

[177] P. D. Larsen, M. Harty, M. Thiruchelvam, and D. C. Galletly. "Spectral analysis of AC and DC components of the pulse photoplethysmograph at rest and during induction of anaesthesia." In: *International journal of clinical monitoring and computing* 14.2 (1997), pp. 89–95. DOI: 10.1007/BF03356582.

[178] J. Lechner. "Konzeption, Umsetzung und Analyse einer steuerbaren LED Beleuchtungseinheit." Studienarbeit. Germany: TU Dresden, 2015.

[179] K. Lee, D. Park, C. Cho, and H. Ko. "Robust remote heart rate estimation in car driving environment." In: *Proceedings of the IEEE International Conference on Consumer Electronics (ICCE)*. 2018, pp. 1–2. DOI: 10.1109/ICCE.2018.8326130.

[180] Y. Lee and K. Hwang. "Skin thickness of Korean adults." In: *Surgical and Radiologic Anatomy* 24.3 (2002), pp. 183–189. DOI: 10.1007/s00276-002-0034-5.

[181] G. Lempe, S. Zaunseder, T. Wirthgen, S. Zipser, and H. Malberg. "ROI Selection for Remote Photoplethysmography." In: *Bildverarbeitung für die Medizin 2013, Informatik aktuell*. 2013, pp. 99–103. DOI: 10.1007/978-3-642-36480-8_19.

[182] M. Lewandowska, J. Ruminski, T. Kocejko, and J. Nowak. "Measuring pulse rate with a webcam — A non-contact method for evaluating cardiac activity." In: *Federated Conference on Computer Science and Information Systems (FedCSIS)*. 2011, pp. 405–410.

[183] X. Li, J. Komulainen, G. Zhao, P.-C. Yuen, and M. Pietikäinen. "Generalized face anti-spoofing by detecting pulse from face videos." In: *Proceedings of the 23rd International Conference on Pattern Recognition (ICPR)*. 2016, pp. 4244–4249. DOI: 10.1109/ICPR.2016.7900300.

[184] R. Lienhart, A. Kuranov, and V. Pisarevsky. "Empirical Analysis of Detection Cascades of Boosted Classifiers for Rapid Object Detection." In: *Proceedings of the 25th DAGM Symposium on Pattern Recognition*. 2003, pp. 297–304. DOI: 10.1007/978-3-540-45243-0_39.

[185] J. S. Lim. *Two-dimensional signal and image processing*. Carl Hanser Verlag GmbH & Co. KG, 1990. Chap. 8. ISBN: 0-13-935322-4.

[186] Y.-C. Lin, N.-K. Chou, G.-Y. Lin, M.-H. Li, and Y.-H. Lin. "A Real-Time Contactless Pulse Rate and Motion Status Monitoring System Based on Complexion Tracking." In: *Sensors* 17.7 (2017). 1490. DOI: 10.3390/s17071490.

[187] S. G. Lipson, H. S. Lipson, and D. S. Tannhauser. *Optik*. 3rd ed. Cambridge University Press, 1995. Chap. 6. ISBN: 978-3-540-61912-3.

[188] T. Lister, P. A. Wright, and P. H. Chappell. "Optical properties of human skin." In: *Journal of Biomedical Optics* 17.9 (2012), pp. 090901–1–090901–15. DOI: 10.1117/1.JBO.17.9.090901.

[189] H. Liu, Y. Wang, and L. Wang. "The Effect of Light Conditions on Photoplethysmographic Image Acquisition Using a Commercial Camera." In: *IEEE Journal of Translational Engineering in Health and Medicine* 2 (2014), pp. 1–11. DOI: 10.1109/JTEHM.2014.2360200.

[190] S. Liu, P. C. Yuen, S. Zhang, and G. Zhao. "3D Mask Face Anti-spoofing with Remote Photoplethysmography." In: *14th European Conference on Computer Vision*. 2016, pp. 85–100. DOI: 10.1007/978-3-319-46478-7_6.

[191] W. Lovallo. "The Cold Pressor Test and Autonomic Function: A Review and Integration." In: *Psychophysiology* 12.3 (1975), pp. 268–282. DOI: 10.1111/j.1469-8986.1975.tb01289.x.

[192] W. Lu, H. Li, S. Tao, et al. "Research on the main elements influencing blood pressure measurement by pulse wave velocity." In: *Frontiers of medical and biological engineering : the international journal of the Japan Society of Medical Electronics and Biological Engineering* 4.3 (1992), pp. 189–199.

[193] B. D. Lucas and T. Kanade. "An Iterative Image Registration Technique with an Application to Stereo Vision." In: *Proceedings of the 7th International Joint Conference on Artificial Intelligence*. Vol. 2. 1981, pp. 674–679.

[194] C. Lueangwattana, T. Kondo, and H. Haneishi. "A comparative study of video signals for non-contact heart rate measurement." In: *12th International Conference on Electrical Engineering/Electronics, Computer, Telecommunications and Information Technology (ECTI-CON)*. 2015, pp. 1–5. DOI: 10.1109/ECTICon.2015.7206971.

[195] C. Maaoui and A. Pruski. "Unsupervised stress detection from remote physiological signal." In: *Proceedings of the IEEE International Conference on Industrial Technology*. 2018, pp. 1538–1543. DOI: 10.1109/ICIT.2018.8352409.

[196] R. Macwan, Y. Benezeth, and A. Mansouri. "Remote photoplethysmography with constrained ICA using periodicity and chrominance constraints." In: *BioMedical Engineering OnLine* 17.1 (2018), pp. 13–22. DOI: 10.1186/s12938-018-0450-3.

[197] Madhero88 and M. Komorniczak. *File:Skin layers.svg*. Creative Commons Attribution-Share Alike 3.0 Unported (https://creativecommons.org/licenses/by-sa/3.0/deed.en). URL: https://commons.wikimedia.org/wiki/File:Skin_layers.svg (visited on 06/26/2017).

[198] E. Magdalena Nowara, T. K. Marks, H. Mansour, and A. Veeraraghavan. "SparsePPG: Towards Driver Monitoring Using Camera-Based Vital Signs Estimation in Near-Infrared." In: *Proceedings of the IEEE Conference on Computer Vision and Pattern Recognition (CVPR) Workshops*. 2018, pp. 1272–1281.

[199] P. Magnan. "Detection of visible photons in CCD and CMOS: A comparative view." In: *Nuclear Instruments and Methods in Physics Research Section A: Accelerators, Spectrometers, Detectors and Associated Equipment* 504.1-3 (2003), pp. 199–212. DOI: 10.1016/S0168-9002(03)00792-7.

[200] T. M. Mahmoud. "A New Fast Skin Color Detection Technique." In: *Proceedings of the World Academy of Science: Engineering & Technology*. Vol. 43. 2008, pp. 501–505.

[201] Z. Marcinkevics, U. Rubins, J. Zaharans, et al. "Imaging photoplethysmography for clinical assessment of cutaneous microcirculation at two different depths." In: *Journal of Biomedical Optics* 21.3 (2016), p. 035005. DOI: 10.1117/1.JBO.21.3.035005.

[202] V. B. Markus Huelsbusch. "Contactless mapping of rhythmical phenomena in tissue perfusion using PPGI." In: *Proc. SPIE, Medical Imaging 2002: Physiology and Function from Multidimensional Images*. Vol. 4683. 2002, pp. 110–117. DOI: 10.1117/12.463573.

[203] L. F. C. Martinez, G. Paez, and M. Strojnik. "Optimal wavelength selection for noncontact reflection photoplethysmography." In: *Proc. SPIE, 22nd Congress of the International Commission for Optics: Light for the Development of the World*. Vol. 8011. 2011, pp. 801191–1–7. DOI: 10.1117/12.903190.

[204] MathWorks MATLAB Documentation. *Image Registration*. URL: https://mathworks.com/help/vision/image-registration-1.html?s_tid=srchtitle (visited on 07/26/2018).

[205] MathWorks MATLAB Documentation. *Texture Analysis*. URL: https://de.mathworks.com/help/images/texture-analysis.html?searchHighlight=TextureAnalysis&s_tid=doc_srchtitle (visited on 07/25/2018).

[206] MathWorks MATLAB Documentation. *imadjust*. URL: https://de.mathworks.com/help/images/ref/imadjust.html (visited on 08/06/2018).

[207] C. R. Maurer, R. Qi, and V. Raghavan. "A linear time algorithm for computing exact Euclidean distance transforms of binary images in arbitrary dimensions." In: *IEEE Transactions on Pattern Analysis and Machine Intelligence* 25.2 (2003), pp. 265–270. DOI: 10.1109/TPAMI.2003.1177156.

[208] L. K. McCorry. "Physiology of the Autonomic Nervous System." In: *American Journal of Pharmaceutical Education* 71.4 (2007), p. 78. DOI: 10.5688/aj710478.

[209] D. J. McDuff, J. R. Estepp, A. M. Piasecki, and E. B. Blackford. "A survey of remote optical photoplethysmographic imaging methods." In: *37th Annual International Conference of the IEEE Engineering in Medicine and Biology Society (EMBC)*. 2015, pp. 6398–6404. DOI: 10.1109/EMBC.2015.7319857.

[210] D. McDuff, E. Blackford, and J. Estepp. "Fusing Partial Camera Signals for Non-Contact Pulse Rate Variability Measurement." In: *IEEE Transactions on Biomedical Engineering* 65.8 (2018), pp. 1725–1739. DOI: 10.1109/TBME.2017.2771518.

[211] D. J. McDuff, J. Hernandez, S. Gontarek, and R. W. Picard. "COGCAM: Contact-free Measurement of Cognitive Stress During Computer Tasks with a Digital Camera." In: *Proceedings of the CHI Conference on Human Factors in Computing Systems*. 2016, pp. 4000–4004. DOI: 10.1145/2858036.2858247.

[212] D. McDuff. "Deep Super Resolution for Recovering Physiological Information From Videos." In: *Proceedings of the IEEE Conference on Computer Vision and Pattern Recognition (CVPR) Workshops*. 2018, pp. 1367–1374.

[213] D. McDuff, S. Gontarek, and R. W. Picard. "Improvements in Remote Cardiopulmonary Measurement Using a Five Band Digital Camera." In: *IEEE Transactions on Biomedical Engineering* 61.10 (2014), pp. 2593–2601. DOI: 10.1109/TBME.2014.2323695.

[214] J. A. McGrath and J. Uitto. "Anatomy and Organization of Human Skin." In: *Rook's Textbook of Dermatology*. Wiley-Blackwell, 2010, pp. 1–53. DOI: 10.1002/9781444317633.ch3.

[215] A. Melchor Rodríguez and J. Ramos-Castro. "Pulse rate variability analysis by video using face detection and tracking algorithms." In: *Proceedings of the 37th Annual International Conference of the IEEE Engineering in Medicine and Biology Society (EMBC)*. 2015, pp. 5696–5699. DOI: 10.1109/EMBC.2015.7319685.

[216] A. Melchor Rodríguez and J. Ramos-Castro. "Video pulse rate variability analysis in stationary and motion conditions." In: *BioMedical Engineering OnLine* 17.1 (2018), p. 11. DOI: 10.1186/s12938-018-0437-0.

[217] MidOpt - Midwest Optical Systems. *BP850 Near-IR Bandpass Filter*. (The right of use for the images was obtained). URL: http://midopt.com/filters/bp850/ (visited on 03/22/2018).

[218] S. C. Millasseau, F. G. Guigui, R. P. Kelly, et al. "Noninvasive Assessment of the Digital Volume Pulse." In: *Hypertension* 36.6 (2000), pp. 952–956. DOI: 10.1161/01.HYP.36.6.952.

[219] N. Minkley, T. P. Schröder, O. T. Wolf, and W. H. Kirchner. "The socially evaluated cold-pressor test (SECPT) for groups: Effects of repeated administration of a combined physiological and psychological stressor." In: *Psychoneuroendocrinology* 45 (2014), pp. 119–127. DOI: 10.1016/j.psyneuen.2014.03.022.

[220] D. Mishra, S. Chakraborty, and M. Sarkar. "Reflection based blood pulsation measurement using linear polarization of light." In: *2015 IEEE SENSORS*. 2015, pp. 1–4. DOI: 10.1109/ICSENS.2015.7370457.

[221] D. Mishra, G. Gogna, A. Barsaiyan, and M. Sarkar. "Blood Pulsation Measurement Using Linearly Polarized Light." In: *IEEE Sensors Journal* 15.8 (2015), pp. 4488–4495. DOI: 10.1109/JSEN.2015.2421553.

[222] D. Mishra, N. Priyadarshini, S. Chakraborty, and M. Sarkar. "Blood Oxygen Saturation Measurement Using Polarization-Dependent Optical Sectioning." In: *IEEE Sensors Journal* 17.12 (2017), pp. 3900–3908. DOI: 10.1109/JSEN.2017.2698520.

[223] L. A. Mitchell. "Cold Pressor Test." In: *Encyclopedia of Behavioral Medicine*. Ed. by M. D. Gellman and J. R. Turner. New York, NY: Springer New York, 2013, pp. 455–456. DOI: 10.1007/978-1-4419-1005-9_239.

[224] R. Mitsuhashi, G. Okada, K. Kurita, et al. "Noncontact pulse wave detection by two-band infrared video-based measurement on face without visible lighting." In: *Artificial Life and Robotics* 23.3 (2018), pp. 345–352. DOI: 10.1007/s10015-018-0430-5.

[225] A. V. Moço, S. Stuijk, and G. de Haan. "Ballistocardiographic Artifacts in PPG Imaging." In: *IEEE Transactions on Biomedical Engineering* 63.9 (2016), pp. 1804–1811. DOI: 10.1109/TBME.2015.2502398.

[226] A. V. Moço, S. Stuijk, and G. de Haan. "Motion robust PPG-imaging through color channel mapping." In: *Biomedical Optics Express* 7.5 (2016), pp. 1737–1754. DOI: 10.1364/BOE.7.001737.

[227] A. V. Moço, S. Stuijk, M. van Gastel, and G. de Haan. "Impairing Factors in Remote-PPG Pulse Transit Time Measurements on the Face." In: *The IEEE Conference on Computer Vision and Pattern Recognition (CVPR) Workshops*. 2018, pp. 1358–1366.

[228] A. V. Moço, S. Stuijk, and G. de Haan. "Skin inhomogeneity as a source of error in remote PPG-imaging." In: *Biomedical Optics Express* 7.11 (2016), pp. 4718–4733. DOI: 10.1364/BOE.7.004718.

[229] A. V. Moço, S. Stuijk, and G. de Haan. "New insights into the origin of remote PPG signals in visible light and infrared." In: *Scientific Reports* 8.1 (2018), p. 8501. DOI: 10.1038/s41598-018-26068-2.

[230] C. Mørk, K. Kvernebo, C. L. Asker, and E. G. Salerud. "Reduced Skin Capillary Density During Attacks of Erythromelalgia Implies Arteriovenous Shunting as Pathogenetic Mechanism." In: *Journal of Investigative Dermatology* 119.4 (2002), pp. 949 –953. DOI: 10.1046/j.1523-1747.2002.00218.x.

[231] K. Murakami, M. Yoshioka, and J. Ozawa. "Non-contact pulse transit time measurement using imaging camera, and its relation to blood pressure." In: *14th IAPR International Conference on Machine Vision Applications (MVA)*. 2015, pp. 414–417. DOI: 10.1109/MVA.2015.7153099.

[232] K. Nakajima, T. Tamura, and H. Miike. "Monitoring of heart and respiratory rates by photoplethysmography using a digital filtering technique." In: *Medical Engineering & Physics* 18.5 (1996), pp. 365–372. DOI: 10.1016/1350-4533(95)00066-6.

[233] J. Nakamura, ed. *Image sensors and signal processing for digital still cameras*. Taylor & Francis Group, 2006. Chap. 3,5. ISBN: 978-0-8493-3545-7.

[234] K. Nakano, R. Satoh, A. Hoshi, et al. "Non-contact imaging of venous compliance in humans using an RGB camera." In: *Optical Review* 22.2 (2015), pp. 335–341. DOI: 10.1007/s10043-015-0041-5.

[235] J. E. Naschitz, S. Bezobchuk, R. Mussafia-Priselac, et al. "Pulse Transit Time by R-Wave-Gated Infrared Photoplethysmography: Review of the Literature and Personal Experience." In: *Journal of Clinical Monitoring and Computing* 18.5-6 (2004), pp. 333–342. DOI: 10.1007/s10877-005-4300-z.

[236] J. A. Nijboer and J. C. Dorlas. "Comparison of plethysmograms taken from finger and pinna during anaesthesia." In: *BJA: British Journal of Anaesthesia* 57.5 (1985), pp. 531–534. DOI: 10.1093/bja/57.5.531.

[237] J. A. Nijboer, J. C. Dorlas, and H. F. Mahieu. "Photoelectric plethysmography-some fundamental aspects of the reflection and transmission methods." In: *Clinical Physics and Physiological Measurement* 2.3 (1981), pp. 205–215. DOI: 10.1088/0143-0815/2/3/004.

[238] L. Nilsson, A. Johansson, and S. Kalman. "Respiration can be monitored by photoplethysmography with high sensitivity and specificity regardless of anaesthesia and ventilatory mode." In: *Acta Anaesthesiologica Scandinavica* 49.8 (2005), pp. 1157–1162. DOI: 10.1111/j.1399-6576.2005.00721.x.

[239] L. Nilsson, A. Johansson, and S. Kalman. "Monitoring of respiratory rate in postoperative care using a new photoplethysmographic technique." In: *Journal of Clinical Monitoring and Computing* 16.4 (2000), pp. 309–315. DOI: 10.1023/A:1011424732717.

[240] M. Nitzan, B. Khanokh, and Y. Slovik. "The difference in pulse transit time to the toe and finger measured by photoplethysmography." In: *Physiological Measurement* 23.1 (2002), pp. 85–93. DOI: 10.1088/0967-3334/23/1/308.

[241] M. Nitzan, A. Babchenko, A. Milston, et al. "Measurement of the variability of the skin blood volume using dynamic spectroscopy." In: *Applied Surface Science* 106 (1996), pp. 478–482. DOI: 10.1016/S0169-4332(96)00387-X.

[242] M. Nitzan, C. Rosenfeld, A. T. Weiss, et al. "Effects of external pressure on arteries distal to the cuff during sphygmomanometry." In: *IEEE Transactions on Biomedical Engineering* 52.6 (2005), pp. 1120–1127. DOI: 10.1109/TBME.2005.846710.

[243] M. Nitzan, H. de Boer, S. Turivnenko, A. Babchenko, and D. Sapoznikov. "Power spectrum analysis of the spontaneous fluctuations in the photoplethysmographic signal." In: *Journal of Basic and Clinical Physiology and Pharmacology* 5.3-4 (1994). DOI: 10.1515/JBCPP.1994.5.3-4.269.

[244] M. Nitzan, S. Turivnenko, A. Milston, A. Babchenko, and Y. Mahler. "Low-frequency variability in the blood volume and in the blood volume pulse measured by photoplethysmography." In: *Journal of Biomedical Optics* 1.2 (1996), pp. 223–229. DOI: 10.1117/12.231366.

[245] E. M. Nowara, A. Sabharwal, and A. Veeraraghavan. "PPGSecure: Biometric Presentation Attack Detection Using Photopletysmograms." In: *12th IEEE International Conference on Automatic Face Gesture Recognition*. 2017, pp. 56–62. DOI: 10.1109/FG.2017.16.

[246] J. O'Doherty, J. Henricson, C. Anderson, et al. "Sub-epidermal imaging using polarized light spectroscopy for assessment of skin microcirculation." In: *Skin Research and Technology* 13.4 (2007), pp. 472–484. DOI: 10.1111/j.1600-0846.2007.00253.x.

[247] M. F. O'Rourke, A. Pauca, and X.-J. Jiang. "Pulse wave analysis." In: *British Journal of Clinical Pharmacology* 51.6 (2001), pp. 507–522. DOI: 10/b6v2cp.

[248] S. Osher and R. Fedkiw. *Level Set Methods and Dynamic Implicit Surfaces*. 1st ed. Berlin: Springer-Verlag, 2003. Chap. 1,3,6,7,12. ISBN: 0-387-95482-1.

[249] E. B. Page. “Ordered Hypotheses for Multiple Treatments: A Significance Test for Linear Ranks.” In: *Journal of the American Statistical Association* 58.301 (1963), pp. 216–230. DOI: 10.1080/01621459.1963.10500843.

[250] P. Palatini and S. Julius. “Elevated Heart Rate: A Major Risk Factor for Cardiovascular Disease.” In: *Clinical and Experimental Hypertension* 26.7-8 (2004), pp. 637–644. DOI: 10.1081/CEH-200031959.

[251] P. Palatini and S. Julius. “Heart rate and the cardiovascular risk.” In: *Journal of hypertension* 15.1 (1997), pp. 3–17.

[252] C. Park and H. Choi. “Motion artifact reduction in PPG signals from face: Face tracking & stochastic state space modeling approach.” In: *36th Annual International Conference of the IEEE Engineering in Medicine and Biology Society*. 2014, pp. 3280–3283. DOI: 10.1109/EMBC.2014.6944323.

[253] S. B. Park, G. H. Kim, J. H. Han, H. J. Baek, and J. H. Kim. “Remote Pulse Rate Measurement from Near-Infrared Videos.” In: *IEEE Signal Processing Letters* 25.8 (2018), pp. 1271–1275. DOI: 10.1109/LSP.2018.2842639.

[254] O. R. Patil, Y. Gao, B. Li, and Z. Jin. “CamBP: A Camera-based, Non-contact Blood Pressure Monitor.” In: *Proceedings of the ACM International Joint Conference on Pervasive and Ubiquitous Computing*. 2017, pp. 524–529. DOI: 10.1145/3123024.3124428.

[255] R. A. Payne. “Pulse transit time measured from the ECG: an unreliable marker of beat-to-beat blood pressure.” In: *Journal of Applied Physiology* 100.1 (2006), pp. 136–141. DOI: 10.1152/japplphysiol.00657.2005.

[256] J. Peñáz. “Photoelectric measurement of blood pressure, volume and flow in the finger.” In: *Digest of the 10th international conference on medical and biological engineering, Dresden, East Germany*. 1973, p. 104.

[257] J. Peñáz. “Mayer waves: History and methodology.” In: *Automedica* 2.3 (1978), pp. 135–141.

[258] S. L. Phung, A. Bouzerdoum, and D. Chai. “Skin segmentation using color pixel classification: analysis and comparison.” In: *IEEE Transactions on Pattern Analysis and Machine Intelligence* 27.1 (2005), pp. 148–154. DOI: 10.1109/TPAMI.2005.17.

[259] S. L. Phung, A. Bouzerdoum, and D. Chai. “A novel skin color model in YCbCr color space and its application to human face detection.” In: *Proceedings of the International Conference on Image Processing*. Vol. 1. 2002, pp. I–289–292. DOI: 10.1109/ICIP.2002.1038016.

[260] C. Pilz, S. Zaunseder, J. Krajewski, and V. Blazek. “Local Group Invariance for Heart Rate Estimation from Face Videos in the Wild.” In: *Proceedings of the IEEE Conference on Computer Vision and Pattern Recognition (CVPR) Workshops*. 2018, pp. 1254–1262.

[261] L.-M. Po, L. Feng, Y. Li, et al. “Block-based adaptive ROI for remote photoplethysmography.” In: *Multimedia Tools and Applications* 77.6 (2018), pp. 6503–6529. DOI: 10.1007/s11042-017-4563-7.

[262] M.-Z. Poh, D. J. McDuff, and R. W. Picard. “Non-contact, automated cardiac pulse measurements using video imaging and blind source separation.” In: *Optics Express* 18.10 (2010), pp. 795–805. DOI: 10.1364/OE.18.010762.

[263] M.-Z. Poh, D. J. McDuff, and R. W. Picard. "Advancements in Noncontact, Multiparameter Physiological Measurements Using a Webcam." In: *IEEE Transactions on Biomedical Engineering* 58.1 (2011), pp. 7–11. DOI: 10.1109/TBME.2010.2086456.

[264] S. K. A. Prakash and C. S. Tucker. "Bounded Kalman filter method for motion-robust, non-contact heart rate estimation." In: *Biomedical Optics Express* 9.2 (2018), pp. 873–897. DOI: 10.1364/BOE.9.000873.

[265] H. Qi, Z. Guo, X. Chen, Z. Shen, and Z. J. Wang. "Video-based human heart rate measurement using joint blind source separation." In: *Biomedical Signal Processing and Control* 31 (2017), pp. 309–320. DOI: 10.1016/j.bspc.2016.08.020.

[266] M. Ramsey. "Blood pressure monitoring: Automated oscillometric devices." In: *Journal of Clinical Monitoring* 7.1 (1991), pp. 56–67. DOI: 10.1007/BF01617900.

[267] M. Rapczynski, P. Werner, and A. Al-Hamadi. "Continuous low latency heart rate estimation from painful faces in real time." In: *Proceedings of the 23rd International Conference on Pattern Recognition (ICPR)*. 2016, pp. 1165–1170. DOI: 10.1109/ICPR.2016.7899794.

[268] B. Rasch, M. Friese, W. Hofmann, and E. Naumann. *Quantitative Methoden 1: Einführung in die Statistik für Psychologen und Sozialwissenschaftler*. 3rd ed. Springer-Verlag, 2010. Chap. 4.2. ISBN: 978-3-642-05271-2.

[269] S. Rasche, A. Trumpp, T. Waldow, et al. "Camera-based photoplethysmography in critical care patients." In: *Clinical Hemorheology and Microcirculation* 64.1 (2016), pp. 77–90. DOI: 10.3233/CH-162048.

[270] S. Rawlani and S. Rawlani. *Textbook of General Anatomy*. 2nd ed. Jaypee Brothers Medical Publishers (P) Ltd, 2013. Chap. 10. ISBN: 978-93-5090-507-4.

[271] RefractiveIndex.INFO. *Refractive index database*. URL: https://refractiveindex.info/?shelf=glass&book=BK7&page=SCHOTT (visited on 06/07/2018).

[272] A. Reisner, P. A. Shaltis, D. McCombie, and H. H. Asada. "Utility of the Photoplethysmogram in Circulatory Monitoring." In: *Anesthesiology* 108.5 (2008), pp. 950–958. DOI: 10.1097/ALN.0b013e31816c89e1.

[273] A. K. L. Reyners, R. A. Tio, F. G. Vlutters, et al. "Re-evaluation of the cold face test in humans." In: *European Journal of Applied Physiology* 82.5-6 (2000), pp. 487–492. DOI: 10.1007/s004210000217.

[274] J.-P. Ritz, A. Roggan, C. Isbert, et al. "Optical properties of native and coagulated porcine liver tissue between 400 and 2400 nm." In: *Lasers in Surgery and Medicine* 29.3 (2001), pp. 205–212. DOI: 10.1002/lsm.1134.

[275] V. Roberts. "Photoplethysmography- fundamental aspects of the optical properties of blood in motion." In: *Transactions of the Institute of Measurement and Control* 4.2 (1982), pp. 101–106. DOI: 10.1177/014233128200400205.

[276] K. Robertson and J. L. Rees. "Variation in Epidermal Morphology in Human Skin at Different Body Sites as Measured by Reflectance Confocal Microscopy." In: *Acta Dermato Venereologica* 90.4 (2010), pp. 368–373. DOI: 10.2340/00015555-0875.

[277] T. D. Rossing and C. J. Chiaverina. *Light science : physics and the visual arts*. Springer Science & Business Media, 1999. Chap. 8. ISBN: 0-387-98827-0.

[278] C. Rother, V. Kolmogorov, and A. Blake. "GrabCut -Interactive Foreground Extraction using Iterated Graph Cuts." In: *ACM Transactions on Graphics (SIGGRAPH)*. 2004.

[279] P. V. Rouast, M. T. P. Adam, D. J. Cornforth, E. Lux, and C. Weinhardt. "Using Contactless Heart Rate Measurements for Real-Time Assessment of Affective States." In: *Information Systems and Neuroscience*. 2017, pp. 157–163. DOI: 10.1007/978-3-319-41402-7_20.

[280] P. V. Rouast, M. T. P. Adam, R. Chiong, D. Cornforth, and E. Lux. "Remote heart rate measurement using low-cost RGB face video: a technical literature review." In: *Frontiers of Computer Science* 12.5 (2018), pp. 858–872. DOI: 10.1007/s11704-016-6243-6.

[281] U. Rubins, V. Upmalis, O. Rubenis, D. Jakovels, and J. Spigulis. "Real-Time Photoplethysmography Imaging System." In: *Proceedings of the 15th Nordic-Baltic Conference on Biomedical Engineering and Medical Physics*. 2011, pp. 183–186. DOI: 10.1007/978-3-642-21683-1_46.

[282] U. Rubins, A. Miscuks, and M. Lange. "Simple and convenient remote photoplethysmography system for monitoring regional anesthesia effectiveness." In: *EMBEC & NBC 2017*. 2017, pp. 378–381. DOI: 10.1007/978-981-10-5122-7_95.

[283] U. Rubins, J. Spigulis, and A. Miscuks. "Photoplethysmography imaging algorithm for continuous monitoring of regional anesthesia." In: *Proceedings of the 14th ACM/IEEE Symposium on Embedded Systems for Real-Time Multimedia*. 2016, pp. 67–71. DOI: 10.1145/2993452.2994308.

[284] A. D. Ryer. *Light Measurement Handbook*. International Light, 1997. Chap. 1,3. ISBN: 0-9658356-9-3.

[285] E. Salomatina, B. Jiang, J. Novak, and A. N. Yaroslavsky. "Optical properties of normal and cancerous human skin in the visible and near-infrared spectral range." In: *Journal of Biomedical Optics* 11.6 (2006), pp. 064026–064026–9. DOI: 10.1117/1.2398928.

[286] R. Sameni. *OSET - The Open-Source Electrophysiological Toolbox*. (version 2.1, 2010). URL: http://www.oset.ir.

[287] J. L. Sandell and T. C. Zhu. "A review of in-vivo optical properties of human tissues and its impact on PDT." In: *Journal of Biophotonics* 4.11-12 (2011), pp. 773–787. DOI: 10.1002/jbio.201100062.

[288] L. Scalise, N. Bernacchia, I. Ercoli, and P. Marchionni. "Heart rate measurement in neonatal patients using a webcamera." In: *IEEE International Symposium on Medical Measurements and Applications Proceedings*. 2012, pp. 1–4. DOI: 10.1109/MeMeA.2012.6226654.

[289] J. Schell. "Charakterisierung der kardiovaskulären Regulation anhand von Kameraaufnahmen." Diplomarbeit. Germany: TU Dresden, 2016.

[290] A. Schloegl. *Refractive index database*. URL: http://biosig.sourceforge.net/index.html (visited on 08/16/2018).

[291] R. F. Schmidt and F. Lang. *Physiologie des Menschen: Mit Pathophysiologie*. 30th ed. Springer Medizin Verlag, 2007. Chap. 20, 23, 26, 28, 39. ISBN: 978-3-540-32908-4.

[292] Schneider-Kreuznach. *Cinegon 1.8/16*. (The right of use for the images was obtained). URL: https://schneiderkreuznach.com/application/files/2315/1843/3983/Cinegon-1.8-16.pdf (visited on 03/21/2018).

[293] Schneider-Kreuznach. *Polarisatoren*. "Datenblatt-polarisatoren-de.pdf". URL: https://schneiderkreuznach.com/de/unternehmen/support/downloads (visited on 05/07/2018).

[294] L. Schwabe, L. Haddad, and H. Schachinger. "HPA axis activation by a socially evaluated cold-pressor test." In: *Psychoneuroendocrinology* 33.6 (2008), pp. 890–895. DOI: 10.1016/j.psyneuen.2008.03.001.

[295] A. Secerbegovic, J. Bergsland, P. S. Halvorsen, et al. "Blood pressure estimation using video plethysmography." In: *IEEE 13th International Symposium on Biomedical Imaging (ISBI)*. 2016, pp. 461–464. DOI: 10.1109/ISBI.2016.7493307.

[296] Seoul Semiconductor Co., Ltd. *SMD-LED SFT722N-S*. URL: http://www.produktinfo.conrad.com/datenblaetter/1100000-1199999/001125320-da-01-en-LED_ROT_GRN_BLA_KLAR_SFT722N_S_SMD_6_SSI.pdf (visited on 05/07/2018).

[297] L. Shan and M. Yu. "Video-based heart rate measurement using head motion tracking and ICA." In: *6th International Congress on Image and Signal Processing*. Vol. 1. 2013, pp. 160–164. DOI: 10.1109/CISP.2013.6743978.

[298] D. Shao, Y. Yang, C. Liu, et al. "Noncontact Monitoring Breathing Pattern, Exhalation Flow Rate and Pulse Transit Time." In: *IEEE Transactions on Biomedical Engineering* 61.11 (2014), pp. 2760–2767. DOI: 10.1109/TBME.2014.2327024.

[299] D. Shao, C. Liu, F. Tsow, et al. "Noncontact Monitoring of Blood Oxygen Saturation Using Camera and Dual-Wavelength Imaging System." In: *IEEE Transactions on Biomedical Engineering* 63.6 (2016), pp. 1091–1098. DOI: 10.1109/TBME.2015.2481896.

[300] D. Shao, Y. Yang, F. Tsow, C. Liu, and N. Tao. "Non-Contact Simultaneous Photoplethysmogram and Ballistocardiogram Video Recording towards Real-Time Blood Pressure and Abnormal Heart Rhythm Monitoring." In: *12th IEEE International Conference on Automatic Face Gesture Recognition*. 2017, pp. 273–277. DOI: 10.1109/FG.2017.42.

[301] D. Shao, F. Tsow, C. Liu, Y. Yang, and N. Tao. "Simultaneous Monitoring of Ballistocardiogram and Photoplethysmogram Using a Camera." In: *IEEE Transactions on Biomedical Engineering* 64.5 (2017), pp. 1003–1010. DOI: 10.1109/TBME.2016.2585109.

[302] K. H. Shelley, D. Tamai, D. Jablonka, et al. "The Effect of Venous Pulsation on the Forehead Pulse Oximeter Wave Form as a Possible Source of Error in Spo2 Calculation." In: *Anesthesia & Analgesia* 100.3 (2005), pp. 743–747. DOI: 10.1213/01.ANE.0000145063.01043.4B.

[303] J. Shi and C. Tomasi. "Good features to track." In: *Proceedings of the IEEE Conference on Computer Vision and Pattern Recognition*. 1994, pp. 593–600. DOI: 10.1109/CVPR.1994.323794.

[304] V. Shusterman, K. P. Anderson, and O. Barnea. "Spontaneous skin temperature oscillations in normal human subjects." In: *The American journal of physiology* 273.3-2 (1997), R1173–81.

[305] I. S. Sidorov, M. A. Volynsky, and A. A. Kamshilin. "Influence of polarization filtration on the information readout from pulsating blood vessels." In: *Biomedical Optics Express* 7.7 (2016), pp. 2469–2474. DOI: 10.1364/BOE.7.002469.

[306] I. S. Sidorov, R. V. Romashko, V. T. Koval, R. Giniatullin, and A. A. Kamshilin. "Origin of Infrared Light Modulation in Reflectance-Mode Photoplethysmography." In: *PLOS ONE* 11.10 (2016), pp. 1–11. DOI: 10.1371/journal.pone.0165413.

[307] D. U. Silverthorn and J. Michael. "Cold stress and the cold pressor test." In: *Advances in Physiology Education* 37.1 (2013), pp. 93–96. DOI: 10.1152/advan.00002.2013.

[308] E. Simonson, S. Koff, A. Keys, and J. Minckler. "Contour of the toe pulse, reactive hyperemia, and pulse transmission velocity: Group and repeat variability, effect of age, exercise, and disease." In: *American Heart Journal* 50.2 (1955), pp. 260–279. DOI: 10.1016/0002-8703(55)90322-7.

[309] S. Singh. *Polarization and Laser*. Discovery Publishing House, 2009. Chap. 2. ISBN: 978-81-8356-415-1.

[310] N. Skoluda, J. Strahler, W. Schlotz, et al. "Intra-individual psychological and physiological responses to acute laboratory stressors of different intensity." In: *Psychoneuroendocrinology* 51 (2015), pp. 227–236. DOI: 10.1016/j.psyneuen.2014.10.002.

[311] N. Spicher, T. Lovelace, and M. Kukuk. "Feasibility of Photoplethysmography Imaging of the Sole of the Foot." In: *Proceedings of the 13th Annual IEEE International Symposium on Medical Measurements & Applications*. 2018, pp. 1–7.

[312] N. Spicher, S. Maderwald, M. E. Ladd, and M. Kukuk. "Heart rate monitoring in ultra-high-field MRI using frequency information obtained from video signals of the human skin compared to electrocardiography and pulse oximetry." In: *Current Directions in Biomedical Engineering* 1.1 (2015), pp. 69–72. DOI: 10.1515/cdbme-2015-0018.

[313] Spitta Medizin & Sport. *Prävalenz von Herz-Kreislauf-Erkrankungen in Deutschland*. URL: https://www.spitta-medizin.de/news/sport/sportmedizin/story/praevalenz-von-herz-kreislauf-erkrankungen-in-deutschland__239.html (visited on 11/14/2018).

[314] H. M. Stauss. "Heart rate variability." In: *American Journal of Physiology - Regulatory, Integrative and Comparative Physiology* 285.5 (2003), R927–R931. DOI: 10.1152/ajpregu.00452.2003.

[315] B. Stemper, M. J. Hilz, U. Rauhut, and B. Neundörfer. "Evaluation of cold face test bradycardia by means of spectral analysis." In: *Clinical Autonomic Research* 12.2 (2002), pp. 78–83. DOI: 10.1007/s102860200024.

[316] M. A. C. Stephens and G. Wand. "Stress and the HPA Axis: Role of Glucocorticoids in Alcohol Dependence." In: *Alcohol Research : Current Reviews* 34.4 (2012), 468—483.

[317] R. Stricker, S. Müller, and H. Gross. "Non-contact video-based pulse rate measurement on a mobile service robot." In: *Proceedings of the 23rd IEEE International Symposium on Robot and Human Interactive Communication*. 2014, pp. 1056–1062. DOI: 10.1109/ROMAN.2014.6926392.

[318] N. Sugita, K. Obara, M. Yoshizawa, et al. "Techniques for estimating blood pressure variation using video images." In: *37th Annual International Conference of the IEEE Engineering in Medicine and Biology Society (EMBC)*. 2015, pp. 4218–4221. DOI: 10.1109/EMBC.2015.7319325.

[319] N. Sugita, M. Yoshizawa, M. Abe, et al. "Contactless Technique for Measuring Blood-Pressure Variability from One Region in Video Plethysmography." In: *Journal of Medical and Biological Engineering* (2018). DOI: 10.1007/s40846-018-0388-8.

[320] K. H. Suh and E. C. Lee. "Contactless physiological signals extraction based on skin color magnification." In: *Journal of Electronic Imaging* 26.6 (2017), p. 063003. DOI: 10.1117/1.JEI.26.6.063003.

[321] Y. Sun, C. Papin, V. Azorin-Peris, et al. "Use of ambient light in remote photoplethysmographic systems: comparison between a high-performance camera and a low-cost webcam." In: *Journal of biomedical optics* 17.3 (2012), pp. 37005–1–10. DOI: 10.1117/1.JBO.17.3.037005.

[322] Y. Sun, S. Hu, V. Azorin-Peris, et al. "Motion-compensated noncontact imaging photoplethysmography to monitor cardiorespiratory status during exercise." In: *Journal of Biomedical Optics* 16.7 (2011), p. 077010. DOI: 10.1117/1.3602852.

[323] Y. Sun, S. Hu, V. Azorin-Peris, R. Kalawsky, and S. Greenwald. "Noncontact imaging photoplethysmography to effectively access pulse rate variability." In: *Journal of Biomedical Optics* 18.6 (2013), p. 061205. DOI: 10.1117/1.JBO.18.6.061205.

[324] S. Suzuki and K. Oguri. "Cuffless blood pressure estimation by error-correcting output coding method based on an aggregation of AdaBoost with a photoplethysmograph sensor." In: *2009 Annual International Conference of the IEEE Engineering in Medicine and Biology Society*. 2009, pp. 6765–6768. DOI: 10.1109/IEMBS.2009.5332505.

[325] L. O. Svaasand, L. T. Norvang, E. J. Fiskerstrand, et al. "Tissue parameters determining the visual appearance of normal skin and port-wine stains." In: *Journal of Biomedical Optics* 10.1 (1995), pp. 55–65. DOI: 10.1007/BF02133165.

[326] C. Takano and Y. Ohta. "Heart rate measurement based on a time-lapse image." In: *Medical Engineering & Physics* 29.8 (2007), pp. 853–857. DOI: 10.1016/j.medengphy.2006.09.006.

[327] C. Tang, J. Lu, and J. Liu. "Non-Contact Heart Rate Monitoring by Combining Convolutional Neural Network Skin Detection and Remote Photoplethysmography via a Low-Cost Camera." In: *Proceedings of the IEEE Conference on Computer Vision and Pattern Recognition (CVPR) Workshops*. 2018, pp. 1309–1315.

[328] L. Tarassenko, M. Villarroel, A. Guazzi, et al. "Non-contact video-based vital sign monitoring using ambient light and auto-regressive models." In: *Physiological Measurement* 35.5 (2014), pp. 807–831. DOI: 10.1088/0967-3334/35/5/807.

[329] E. A. Tarbox, C. Rios, B. Kaur, et al. "Motion correction for improved estimation of heart rate using a visual spectrum camera." In: *Proc. SPIE, Smart Biomedical and Physiological Sensor Technology XIV*. Vol. 10216. 2017, p. 1021607. DOI: 10.1117/12.2262932.

[330] Task Force of the European Society of Cardiology the North American Society of Pacing and Electrophysiology. "Heart Rate Variability." In: *Circulation* 93.5 (1996), pp. 1043–1065. DOI: 10.1161/01.CIR.93.5.1043.

[331] H. E. Tasli, A. Gudi, and M. den Uyl. "Remote PPG based vital sign measurement using adaptive facial regions." In: *Proceedings of the IEEE International Conference on Image Processing (ICIP)*. 2014, pp. 1410–1414. DOI: 10.1109/ICIP.2014.7025282.

[332] X. F. Teng and Y. T. Zhang. "Continuous and noninvasive estimation of arterial blood pressure using a photoplethysmographic approach." In: *Proceedings of the 25th Annual International Conference of the IEEE Engineering in Medicine and Biology Society*. 2003, pp. 3153–3156. DOI: 10.1109/IEMBS.2003.1280811.

[333] X. F. Teng and Y. T. Zhang. "The effect of contacting force on photoplethysmographic signals." In: *Physiological Measurement* 25.5 (2004), pp. 1323–1335. DOI: 10.1088/0967-3334/25/5/020.

[334] V. Teplov, E. Nippolainen, A. A. Makarenko, R. Giniatullin, and A. A. Kamshilin. "Ambiguity of mapping the relative phase of blood pulsations." In: *Biomedical Optics Express* 5.9 (2014), pp. 3123–3139. DOI: 10.1364/BOE.5.003123.

[335] C. Tomasi and T. Kanade. *Detection and Tracking of Point Features*. Tech. rep. MU-CS-91-132. Carnegie Mellon University, 1991.

[336] A. Trumpp, J. Schell, H. Malberg, and S. Zaunseder. "Vasomotor assessment by camera-based photoplethysmography." In: *Current Directions in Biomedical Engineering*. Vol. 2. 1. 2016, pp. 199–202. DOI: 10.1515/cdbme-2016-0045.

[337] A. Trumpp, S. Rasche, D. Wedekind, et al. "Relation between pulse pressure and the pulsation strength in camera-based photoplethysmograms." In: *Current Directions in Biomedical Engineering*. Vol. 3. 2. 2017, pp. 489–492. DOI: 10.1515/cdbme-2017-0184.

[338] A. Trumpp, S. Rasche, D. Wedekind, et al. "Skin Detection and Tracking for Camera-Based Photoplethysmography Using a Bayesian Classifier and Level Set Segmentation." In: *Bildverarbeitung für die Medizin 2017, Informatik aktuell*. 2017, pp. 43–48. DOI: 10.1007/978-3-662-54345-0_16.

[339] A. Trumpp, P. L. Bauer, S. Rasche, H. Malberg, and S. Zaunseder. "The value of polarization in camera-based photoplethysmography." In: *Biomedical Optics Express* 8.6 (2017), pp. 2822–2834. DOI: 10.1364/BOE.8.002822.

[340] A. Trumpp, J. Lohr, D. Wedekind, et al. "Camera-based photoplethysmography in an intraoperative setting." In: *BioMedical Engineering OnLine* 17.1 (2018), p. 33. DOI: 10.1186/s12938-018-0467-7.

[341] G. R. Tsouri and Z. Li. "On the benefits of alternative color spaces for noncontact heart rate measurements using standard red-green-blue cameras." In: *Journal of Biomedical Optics* 20.4 (2015), p. 048002. DOI: 10.1117/1.JBO.20.4.048002.

[342] G. R. Tsouri, S. Kyal, S. Dianat, and L. K. Mestha. "Constrained independent component analysis approach to nonobtrusive pulse rate measurements." In: *Journal of Biomedical Optics* 17.7 (2012), p. 077011. DOI: 10.1117/1.JBO.17.7.077011.

[343] S. Tulyakov, X. Alameda-Pineda, E. Ricci, et al. "Self-Adaptive Matrix Completion for Heart Rate Estimation from Face Videos under Realistic Conditions." In: *Proceedings of the IEEE Conference on Computer Vision and Pattern Recognition (CVPR)*. 2016, pp. 2396–2404. DOI: 10.1109/CVPR.2016.263.

[344] E. Tur, M. Tur, H. I. Maibach, and R. H. Guy. "Basal Perfusion of the Cutaneous Microcirculation: Measurements as a Function of Anatomic Position." In: *Journal of Investigative Dermatology* 81.5 (1983), pp. 442–446. DOI: 10.1111/1523-1747.ep12522619.

[345] University of Colorado (Mechanical Engineering). *Anatomy & Physiology for Engineers*. URL: http://www.colorado.edu/MCEN/MCEN4278/index_files/Lecture1.pdf (visited on 06/21/2017).

[346] Untamed Science. *How to Avoid Flickering Video with Fluorescent lights*. URL: http://www.untamedscience.com/filmmaking/production-shooting/flickering-video-fluorescent-lights/ (visited on 04/03/2018).

[347] W. Verkruijsse and M. Bodlaender. *A novel biometric signature: multi-site, remote (> 100 m) photo-plethysmography using ambient light*. Tech. rep. Philips Research, 2010.

[348] W. Verkruysse, L. O. Svaasand, and J. S. Nelson. "Remote plethysmographic imaging using ambient light." In: *Optics Express* 16.26 (2008), pp. 21434–21445. DOI: 10.1364/OE.16.021434.

[349] W. Verkruysse, M. Bartula, E. Bresch, et al. "Calibration of Contactless Pulse Oximetry." In: *Anesthesia & Analgesia* 124.1 (2017), pp. 136–145. DOI: 10/gfgxv6.

[350] L. A. Vese and T. F. Chan. "A Multiphase Level Set Framework for Image Segmentation Using the Mumford and Shah Model." In: *International Journal of Computer Vision* 50.3 (2002), pp. 271–293. DOI: 10.1023/A:1020874308076.

[351] V. Vezhnevets, V. Sazonov, and A. Andreeva. "A Survey on Pixel-Based Skin Color Detection Techniques." In: *Proceedings of the Graphicon*. Vol. 3. 2003, pp. 85–92.

[352] M. Villarroel, J. Jorge, C. Pugh, and L. Tarassenko. "Non-Contact Vital Sign Monitoring in the Clinic." In: *12th IEEE International Conference on Automatic Face Gesture Recognition*. 2017, pp. 278–285. DOI: 10.1109/FG.2017.43.

[353] M. Villarroel, A. Guazzi, J. Jorge, et al. "Continuous non-contact vital sign monitoring in neonatal intensive care unit." In: *Healthcare Technology Letters* 1.3 (2014), pp. 87–91. DOI: 10.1049/htl.2014.0077.

[354] P. Viola and M. Jones. "Rapid object detection using a boosted cascade of simple features." In: *Proceedings of the IEEE Computer Society Conference on Computer Vision and Pattern Recognition*. Vol. 1. 2001, pp. I–511–518. DOI: 10.1109/CVPR.2001.990517.

[355] T. Vogels, M. van Gastel, W. Wang, and G. de Haan. "Fully-Automatic Camera-Based Pulse-Oximetry During Sleep." In: *Proceedings of the IEEE Conference on Computer Vision and Pattern Recognition (CVPR) Workshops*. 2018, pp. 1349–1357.

[356] M. V. Volkov, A. V. Potemkin, N. B. Margaryants, et al. "Analysis of light intensity modulation by red blood cells motion in capillaries." In: *Diffuse Optical Spectroscopy and Imaging VI*. Vol. 10412. Proc. SPIE, 2017, pp. 1–3. DOI: 10.1117/12.2284798.

[357] M. V. Volkov, N. B. Margaryants, A. V. Potemkin, et al. "Video capillaroscopy clarifies mechanism of the photoplethysmographic waveform appearance." In: *Scientific Reports* 7.1 (2017), p. 13298. DOI: 10.1038/s41598-017-13552-4.

[358] M. A. Volynsky, O. V. Mamontov, I. S. Sidorov, and A. A. Kamshilin. "Pulse wave transit time measured by imaging photoplethysmography in upper extremities." In: *Journal of Physics: Conference Series* 737.1 (2016), p. 012053.

[359] T. G. M. Vrijkotte, L. J. P. Van Doornen, and E. J. C. De Geus. "Effects of work stress on ambulatory blood pressure, heart rate, and heart rate variability." In: *Hypertension* 35.4 (2000), pp. 880–886. DOI: 10.1161/01.HYP.35.4.880.

[360] M. L. Wallace, J. A. Ricco, and B. Barrett. "Screening strategies for cardiovascular disease in asymptomatic adults." In: *Primary Care: Clinics in Office Practice* 41.2 (2014), pp. 371–397. DOI: 10.1016/j.pop.2014.02.010.

[361] S. Walsh and E. King. *Pulse Diagnosis*. Elsevier, 2008. Chap. 6. ISBN: 978-0-443-10248-6.

[362] W. Wang, S. Stuijk, and G. de Haan. "Exploiting Spatial Redundancy of Image Sensor for Motion Robust rPPG." In: *IEEE Transactions on Biomedical Engineering* 62.2 (2015), pp. 415–425. DOI: 10.1109/TBME.2014.2356291.

[363] W. Wang, S. Stuijk, and G. de Haan. "Unsupervised Subject Detection via Remote PPG." In: *IEEE Transactions on Biomedical Engineering* 62.11 (2015), pp. 2629–2637. DOI: 10.1109/TBME.2015.2438321.

[364] W. Wang, S. Stuijk, and G. de Haan. "A Novel Algorithm for Remote Photoplethysmography: Spatial Subspace Rotation." In: *IEEE Transactions on Biomedical Engineering* 63.9 (2016), pp. 1974–1984. DOI: 10.1109/TBME.2015.2508602.

[365] W. Wang, S. Stuijk, and G. de Haan. "Living-Skin Classification via Remote-PPG." In: *IEEE Transactions on Biomedical Engineering* 64.12 (2017), pp. 2781–2792. DOI: 10.1109/TBME.2017.2676160.

[366] W. Wang, A. den Brinker, S. Stuijk, and G. de Haan. "Algorithmic Principles of Remote-PPG." In: *IEEE Transactions on Biomedical Engineering* 64.7 (2016), pp. 1479–1491. DOI: 10.1109/TBME.2016.2609282.

[367] W. Wang, A. C. den Brinker, S. Stuijk, and G. de Haan. "Amplitude-selective filtering for remote-PPG." In: *Biomedical Optics Express* 8.3 (2017), pp. 1965–1980. DOI: 10.1364/BOE.8.001965.

[368] W. Wang, A. C. den Brinker, S. Stuijk, and G. de Haan. "Robust heart rate from fitness videos." In: *Physiological Measurement* 38.6 (2017), pp. 1023–1044. DOI: 10.1088/1361-6579/aa6d02.

[369] J. G. Webster, ed. *Design of Pulse Oximeters*. Taylor & Francis Group, 1997. Chap. 5,6,7. ISBN: 9780750304672.

[370] D. Wedekind, A. Trumpp, F. Gaetjen, et al. "Assessment of blind source separation techniques for video-based cardiac pulse extraction." In: *Journal of Biomedical Optics* 22.3 (2017), p. 035002. DOI: 10.1117/1.JBO.22.3.035002.

[371] L. Wei, Y. Tian, Y. Wang, T. Ebrahimi, and T. Huang. "Automatic Webcam-Based Human Heart Rate Measurements Using Laplacian Eigenmap." In: *Proceedings of the 11th Asian Conference on Computer Vision*. 2013, pp. 281–292. DOI: 10.1007/978-3-642-37444-9_22.

[372] J. Weinman, A. Hayat, and G. Raviv. "Reflection photoplethysmography of arterial-blood-volume pulses." In: *Medical & Biological Engineering & Computing* 15.1 (1977), pp. 22–31. DOI: 10.1007/BF02441571.

[373] T. F. Whayne and T. Killip. "Simulated diving in man: comparison of facial stimuli and response in arrhythmia." In: *Journal of Applied Physiology* 22.4 (1967), pp. 800–807. DOI: 10.1152/jappl.1967.22.4.800.

[374] J. T. Whitton and J. Everall. "The thickness of the epidermis." In: *British Journal of Dermatology* 89.5 (1973), pp. 467–476. DOI: 10.1111/j.1365-2133.1973.tb03007.x.

[375] C. Wiede, J. Richter, and G. Hirtz. "Signal fusion based on intensity and motion variations for remote heart rate determination." In: *Proceedings of the IEEE International Conference on Imaging Systems and Techniques (IST)*. 2016, pp. 526–531. DOI: 10.1109/IST.2016.7738282.

[376] F. P. Wieringa, F Mastik, and A. F. W. van der Steen. "Contactless multiple wavelength photoplethysmographic imaging: a first step toward "SpO2 Camera" Technology." In: *Annals of biomedical engineering* 33.8 (2005), pp. 1034–1041. DOI: 10.1007/s10439-005-5763-2.

[377] M. Y. M. Wong, E. Pickwell-MacPherson, and Y. T. Zhang. "Contactless and continuous monitoring of heart rate based on photoplethysmography on a mattress." In: *Physiological Measurement* 31.7 (2010), pp. 1065–1074. DOI: 10.1109/IEMBS.2008.4649890.

[378] World Health Organization (WHO). *A global brief on hypertension*. URL: http://www.who.int/campaigns/world-health-day/2013/en/ (visited on 05/10/2017).

[379] World Health Organization (WHO). *Cardiovascular disease*. URL: http://www.euro.who.int/en/health-topics/noncommunicable-diseases/cardiovascular-diseases/data-and-statistics (visited on 11/13/2018).

[380] B.-F. Wu, Y.-W. Chu, P.-W. Huang, M.-L. Chung, and T.-M. Lin. "A Motion Robust Remote-PPG Approach to Driver's Health State Monitoring." In: *Asian Conference on Computer Vision*. 2017, pp. 463–476. DOI: 10.1007/978-3-319-54407-6_31.

[381] T. Wu, V. Blazek, and H. J. Schmitt. "Photoplethysmography imaging: a new noninvasive and noncontact method for mapping of the dermal perfusion changes." In: *Proc. SPIE, Optical Techniques and Instrumentation for the Measurement of Blood Composition, Structure, and Dynamics*. Vol. 4163. 2000, pp. 62–70. DOI: 10.1117/12.407646.

[382] B. Xu, H. Madhu, and L. K. Mestha. "A study of the effect of subject motion to pulse rate estimation." In: *Proceedings of the 38th Annual International Conference of the IEEE Engineering in Medicine and Biology Society (EMBC)*. 2016, pp. 4901–4904. DOI: 10.1109/EMBC.2016.7591826.

[383] S. Xu, L. Sun, and G. K. Rohde. "Robust efficient estimation of heart rate pulse from video." In: *Biomedical Optics Express* 5.4 (2014), pp. 1124–1135. DOI: 10.1364/BOE.5.001124.

[384] B. P. Yan, W. H. S. Lai, C. K. Y. Chan, et al. "Contact-Free Screening of Atrial Fibrillation by a Smartphone Using Facial Pulsatile Photoplethysmographic Signals." In: *Journal of the American Heart Association* 7.8 (2018). DOI: 10.1161/JAHA.118.008585.

[385] Y.-s. Yan, C. C. Poon, and Y.-t. Zhang. "Reduction of motion artifact in pulse oximetry by smoothed pseudo Wigner-Ville distribution." In: *Journal of NeuroEngineering and Rehabilitation* 2.3 (2005), pp. 1–9. DOI: 10.1186/1743-0003-2-3.

[386] Y. Yang, C. Liu, H. Yu, et al. "Motion robust remote photoplethysmography in CIELab color space." In: *Journal of Biomedical Optics* 21.11 (2016), p. 117001. DOI: 10.1117/1.JBO.21.11.117001.

[387] M. Yoshizawa, N. Sugita, M. Abe, et al. "Non-contact blood pressure estimation using video pulse waves for ubiquitous health monitoring." In: *Proceesings of the IEEE 6th Global Conference on Consumer Electronics (GCCE)*. 2017, pp. 1–3. DOI: 10.1109/GCCE.2017.8229429.

[388] Q. Yousef, M. B. I. Reaz, and M. A. M. Ali. "The Analysis of PPG Morphology: Investigating the Effects of Aging on Arterial Compliance." In: *Measurement Science Review* 12.6 (2012), pp. 266–271. DOI: 10.2478/v10048-012-0036-3.

[389] C. Yu, Z. Liu, T. McKenna, A. T. Reisner, and J. Reifman. "A Method for Automatic Identification of Reliable Heart Rates Calculated from ECG and PPG Waveforms." In: *Journal of the American Medical Informatics Association* 13.3 (2006), pp. 309–320. DOI: 10.1197/jamia.M1925.

[390] S. Yu, X. You, X. Jiang, et al. “Human Heart Rate Estimation Using Ordinary Cameras under Natural Movement.” In: *Proceedings of the IEEE International Conference on Systems, Man, and Cybernetics*. 2015, pp. 1041–1046. DOI: 10.1109/SMC.2015.188.

[391] Y.-P. Yu, P. Raveendran, and C.-L. Lim. “Dynamic heart rate measurements from video sequences.” In: *Biomedical Optics Express* 6.7 (2015), pp. 2466–2480. DOI: 10.1364/BOE.6.002466.

[392] N. Zaproudina, V. Teplov, E. Nippolainen, et al. “Asynchronicity of Facial Blood Perfusion in Migraine.” In: *PLoS ONE* 8.12 (2013), e80189. DOI: 10.1371/journal.pone.0080189.

[393] S. Zaunseder, A. Trumpp, D. Wedekind, and H. Malberg. “Cardiovascular assessment by imaging photoplethysmography – a review.” In: *Biomedical Engineering / Biomedizinische Technik* 63.5 (2018), pp. 617–634. DOI: 10.1515/bmt-2017-0119.

[394] S. Zaunseder, A. Trumpp, H. Ernst, M. Förster, and H. Malberg. “Spatio-temporal analysis of blood perfusion by imaging photoplethysmography.” In: *Proc. SPIE, Optical Diagnostics and Sensing XVIII: Toward Point-of-Care Diagnostics*. Vol. 10501. 2018, p. 105010X. DOI: 10.1117/12.2289896.

[395] Q. Zhang, Q. Wu, Y. Zhou, et al. “Webcam-based, non-contact, real-time measurement for the physiological parameters of drivers.” In: *Measurement* 100 (2017), pp. 311–321. DOI: 10.1016/j.measurement.2017.01.007.

[396] Z. Zhang. “Photoplethysmography-Based Heart Rate Monitoring in Physical Activities via Joint Sparse Spectrum Reconstruction.” In: *IEEE Transactions on Biomedical Engineering* 62.8 (2015), pp. 1902–1910. DOI: 10.1109/TBME.2015.2406332.

[397] D. Zheng, J. Allen, and A. Murray. “Effect of external cuff pressure on arterial compliance.” In: *Computers in Cardiology*. 2005, pp. 315–318. DOI: 10.1109/CIC.2005.1588100.

[398] K. Zilles and B. N. Tillmann. *Anatomie*. Springer Medizin Verlag Heidelberg, 2010. Chap. 4, 16. ISBN: 978-3-540-69481-6.

[399] G. Zonios and A. Dimou. “Modeling diffuse reflectance from semi-infinite turbid media: application to the study of skin optical properties.” In: *Optics Express* 14.19 (2006), pp. 8661–8674. DOI: 10.1364/OE.14.008661.

[400] G. de Haan and V. Jeanne. “Robust Pulse Rate From Chrominance-Based rPPG.” In: *IEEE Transactions on Biomedical Engineering* 60.10 (2013), pp. 2878–2886. DOI: 10.1109/TBME.2013.2266196.

[401] G. de Haan and A. van Leest. “Improved motion robustness of remote-PPG by using the blood volume pulse signature.” In: *Physiological measurement* 35.9 (2014), pp. 1913–1926. DOI: 10.1088/0967-3334/35/9/1913.

[402] M. van Gastel, S. Stuijk, and G. de Haan. “Motion Robust Remote-PPG in Infrared.” In: *IEEE Transactions on Biomedical Engineering* 62.5 (2015), pp. 1425–1433. DOI: 10.1109/TBME.2015.2390261.

[403] M. van Gastel, S. Stuijk, and G. de Haan. “Robust respiration detection from remote photoplethysmography.” In: *Biomedical Optics Express* 7.12 (2016), pp. 4941–4957. DOI: 10.1364/BOE.7.004941.

[404] C. M. A. van Ravenswaaij-Arts, L. A. A. Kollee, J. C. W. Hopman, G. B. A. Stoelinga, and H. P. van Geijn. “Heart rate variability.” In: *Annals of Internal Medicine* 118.6 (1993), pp. 436–447. DOI: 10.7326/0003-4819-118-6-199303150-00008.

DECLARATION

I hereby declare that this dissertation is the product of my original work and contains nothing which is the result of work carried out in collaboration with others except as declared in the acknowledgement and specified in the text. I further state that no part of my thesis has already been or will be submitted to another university with the purpose of earning another degree or qualification.

Dresden, March 24, 2019

Alexander Trumpp

COLOPHON

This document was created using the typographical look-and-feel `classicthesis` developed by André Miede:

`http://www.miede.de/`

An available template was downloaded and in some extent adapted to personal preferences:

`https://www.ctan.org/pkg/classicthesis?lang=de`

Final Version as of March 24, 2019 (`classicthesis` draft version 1.0).